High Performance Lead–free Piezoelectric Materials

Shashaank Gupta

Dissertation submitted to the faculty of the
Virginia Polytechnic Institute and State University
in partial fulfillment of the requirements for the degree of
Doctor of Philosophy
In
Materials Science and Engineering

Shashank Priya (Committee Chair)

Carlos Suchicital

Dwight Viehland

Jean Heremans

7th May 2013

Blacksburg, VA 24061

Abstract

Piezoelectric materials find applications in number of devices requiring inter-conversion of mechanical and electrical energy. These devices include sensors, actuators and energy harvesting devices. A number of lead-based perovskite compositions (PZT, PMN-PT, PZN-PT etc.) have dominated the field in last few decades owing to their giant piezoresponse and high degree of compositional tunability resulting in desired electromechanical response. With increasing environmental concern, rapidly in the last decade, focus has now shifted towards developing a better understanding of lead-free piezoelectric compositions. Sodium potassium niobate ($K_xNa_{1-x}NbO_3$, abbreviated as KNN) is one of the most interesting candidates in the class of lead-free piezoelectrics. Absence of any toxic element makes it quite appealing among all the other lead-free candidates. KNN has high Curie temperature of 400°C which is even higher than that of PZT but possess an intermediate phase transition that limits its operating range. Thus modifying the phase transition temperature is of significance for this material to become practical and this is one of the issues addressed in this thesis.

This thesis focuses on the fundamental understanding of the crystallographic nature, domain structure and domain dynamics of KNN. Since compositions close to $x = 0.5$ are of primary interest because of their superior piezoelectric activity among other compositions ($0 < x < 1$), detailed crystallographic and domain structure studies were conducted to provide explanation for the observed electromechanical response. Investigations were conducted on random, textured and single crystals to collect comprehensive information for elucidating the fundamental behavior.

$K_{0.5}Na_{0.5}NbO_3$ single crystals were grown by the flux method and characterized for their ferroelectric and piezoelectric behavior. Dynamical scaling analysis was performed to reveal the origin of their moderate piezoelectric performance. Optical birefringence technique used to reveal the macro-level crystallographic nature of x = 0.4, 0.5 and 0.6 crystals. The results indicated these compositions to be monoclinic M_C, monoclinic $M_{A/B}$ and orthorhombic structures respectively. Contrary to this finding, pair distribution function analysis performed on the same composition crystals indicated them to be monoclinic M_c structure at local scale. Linear birefringence and piezoresponse force microscopy (PFM) was used to reveal the domain structure at macro and micros scales respectively.

A modified sintering technique was developed to achieve > 99% density for KNN ceramics. These high density ceramics were characterized for their dielectric, ferroelectric and piezoelectric properties and a significant improvement was obtained. Higher densities of the ceramics also lead to the superior ferroelectric fatigue behavior.

Highly textured KNN ceramics (Lotgering factor ~ 88 %) were synthesized using TGG method. A sintering technique similar to that employed for synthesis of random ceramics, was used to sinter the textured KNN ceramics as well. Piezoresponse force microscopy (PFM) results suggested that the textured ceramics had much larger domain size, ~6μm,as compared to 2μm domain size for random ceramics. Local switching behavior was studied using switching spectroscopy (SS-PFM) which revealed about 2.5X improvement of local piezoresponse in textured ceramics as compared to the random counterpart.

Acknowledgements

First of all I would like to express my gratefulness to my supervisors Prof. Shashank Priya for giving me an opportunity to work under his valuable guidance. His support, encouragement and patience in last three and half years was a great help, without which it would have not been possible to conduct this research. I am thankful to my other PhD advisory committee members Dr. Carlos Suchicital, Dr. Dwight Viehland and Dr. Jean Heremans for their time and valuable suggestions, which helped in improving the quality of present work.

I would like to thank Prof. Pam Thomas at University of Warwick, England to give me an opportunity to join their group as a visiting student to perform linear birefringence study on KNN single crystals. I am also thankful to Prof. Valeri Petkov from Central Michigan University for his help in pair distribution function analysis (PDF) of KNN crystals. Dr. S. Kalinin and his group at Oak Ridge National Lab (ORNL) is also acknowledged for their help in conducting some of the PFM studies on KNN textured and single crystals.

I express my thankfulness to all my friends at EMDL for their continuous support and friendly behavior in last three and half years. Especially the help of Dr. Yongke Yan and Deepam Maurya in writing introduction chapter of this thesis is appreciated. I would also like to thank Beth, Ai, Justin and Erin for their constant support in during last three half years.

Contents

List of Figures

List of Tables

List of Abbreviations and Symbols

KNN	$K_xNa_{1-x}NbO_3$
MPB	Morphotropic Phase Boundary
PPB	Polymorphic Phase Boundary
PZT	$PbTi_xZr_{1-x}O_3$
XRD	X-ray Diffraction
EDX	Energy Dispersive X-ray
EBSD	Electron Back Scattered Diffraction Analysis
SEM	Scanning Electron Microscopy
LS	$LiSbO_3$
LT	$LiTaO_3$
SPS	Spark Plasma Sintering
HP	Hot Pressing
KCN	$K_4CuNb_8O_{23}$
KCT	$K_{5.4}Cu_{1.3}Ta_{10}O_{29}$
T_{o-t}	Orthorhombic – Tetragonal Transition Temperature
T_c	Curie Temperature
Q_M	Mechanical quality factor
ST	$SrTiO_3$
EPR	Electron paramagnetic resonance
KNLN	$Li_x(Na_{0.5}K_{0.5})_{(1-x)}NbO_3$
d_{33}	Longitudinal Coupling Coefficient
k_p	Planner Coupling Coefficient
NKN-LS	$(Na_{0.5}K_{0.5}Nb)_{(1-x)}(LiSb)_xO_3$

AE	Alkali Earth elements
K or $\varepsilon_{33}^{T}/\varepsilon_0$	Dielectric Constant
CT	$CaTiO_3$
RT	Room Temperature
BT	$BaTiO_3$
LF4	$(K_{0.44}Na_{0.52}Li_{0.04})(Nb_{0.84}Ta_{0.10}Sb_{0.06})O_3$
TGG	Template Grain Growth
RTGG	Reactive Template Grain Growth
LF4T	Textured $(K_{0.44}Na_{0.52}Li_{0.04})(Nb_{0.84}Ta_{0.10}Sb_{0.06})O_3$
G	Piezoelectric Voltage Coefficient
F/f	Lotgering Factor
SSCG	Solid state single crystal growth
P_r	Remanent Polarization
P_s	Saturation Polarization
KT	$KTaO_3$
TEM	Transmission Electron Microscopy
PDF	Pair Distribution Function
PFM	Piezoresponse Force Microscopy
SS-PFM	Switching Spectroscopy-PFM
E_c	Coercive field
tan δ	Dielectric Loss
L - D Theory	Landau – Devonshire Theory
F	Frequency
°C	Curie Constant / Capacitance
X	Dielectric Susceptibility

T	Temperature / Tetragonal
<A>	Area under ferroelectric loop
E_0	Amplitude of electric Field
m/n	Switching Parameter
R	Rhombohedral
O	Orthorhombic
M	Monoclinic
PMN-PT	$PbMg_{1/3}Nb_{2/3}O_3$- $PbTiO_3$
NBT	$Na_{0.5}Bi_{0.5}TiO_3$
FE	Ferroelectric
PE	Paraelectric
n	Refractive Index
ϕ	Orientation of Optical Indicatrix
I_o	Incident intensity
I	Transmitted Intensity
σ	Electric Conductivity
TDGL	Time dependent Ginzburg – Landau
2D	Two Dimentional
LPS	Liquid Phase Sintering
I	Leakage Current
V	Voltage
d_h	Hydrostatic piezoelectric coefficient
R	Resistance
Q	Electrostriction coefficient
J	Current Density

BNKN	$Bi_{2.5}Na_{1.75}K_{1.75}Nb_5O_{18}$

Chapter 1

Introduction

Piezoelectric materials play important role in several applications including ultrasonic medical imaging, ultrasonic nondestructive testing, speakers, resonators, gas igniters, gyroscope, pressure sensors etc.[1-4] These materials also find applications in areas such as micromotors, energy harvesting devices, transformers, magnetoelectric sensors and high power transformers.[5-7] Potassium sodium niobate ($Na_{(1-x)}K_xNbO_3$, abbreviated as KNN) is considered as one of the leading piezoelectric materials owing to its environment friendly nature (no-lead) and the high Curie temperature.[8,9] Compositions close to the equimolar ratio of sodium and potassium ($Na_{0.5}K_{0.5}NbO_3$) are of greater interest in this system because of their superior piezoelectric and ferroelectric properties. In this thesis, emphasis was given on the synthesis of single crystal, random ceramic and textured ceramic of KNN and a comparative analysis was performed in terms of crystal structure, domain structure and electromechanical properties. In this chapter, brief review of the significant research reported in literature on KNN is presented. The discussion includes the techniques utilized for the processing of random ceramic and its derivatives, textured polycrystalline ceramics and the single crystals.

1.1 Crystal Structure of $K_xNa_{(1-x)}NbO_3$

In order to develop the structure – property relationship for the ferroelectric and piezoelectric perovskites, crystallographic information is necessary. First attempt towards developing the complete phase diagram for KNN was made in the classic book by Jaffe et al.[4]

This phase diagram is reproduced in Figure 1.1. The diagram was primarily based upon the findings of the previous investigators that performed investigations on number of KNN compositions by dielectric, thermal and crystallographic analyses.[10] Due to their technological importance, the crystal structure of compositions close to x = 0.5 is of utmost importance. According to the phase diagram of Jaffe et al., a phase boundary exists at x = 0.5 separating two distinct orthorhombic phases. On heating above 200°C, the compositions in the vicinity of x = 0.5 (0.4 < x < 0.6) go through phase transformation to the tetragonal structure. Above 400°C, ferroelectric tetragonal to paraelectric cubic transformation occurs.[4]

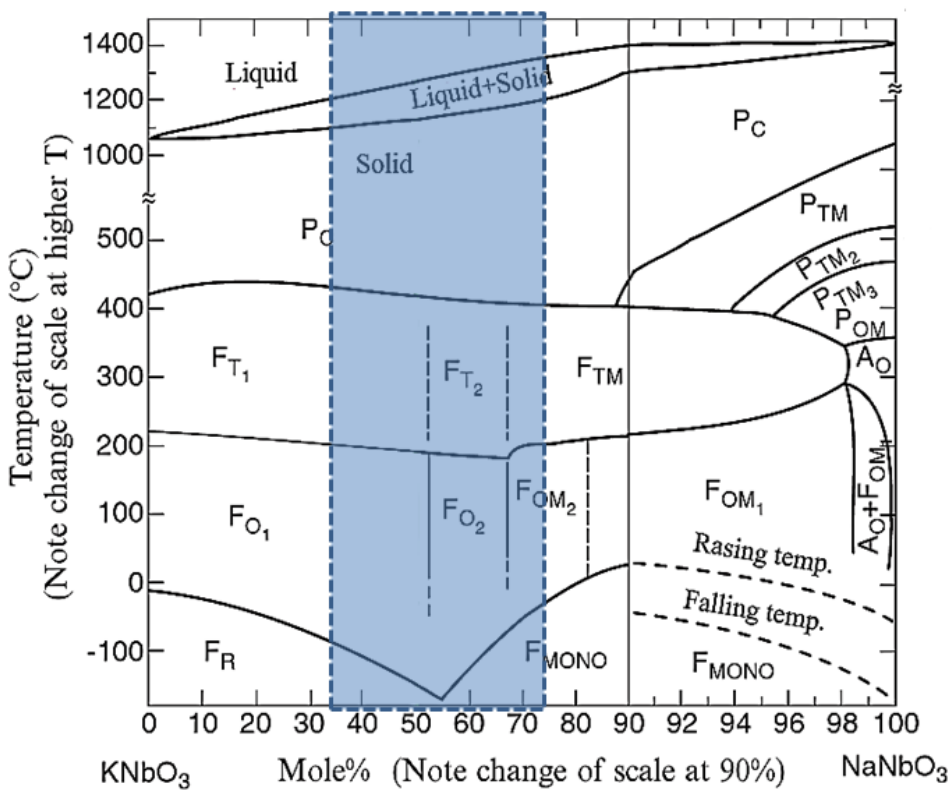

Figure 1.1 Phase diagram of KNN illustrating the presence of two distinct orthorhombic phases at the phase boundary of x = 0.5.

Contrary to the phase diagram given by Jaffe et al., later crystallographic studies performed on the polycrystalline KNN powder found no abrupt variation of lattice parameters across the x = 0.5, when refinement was performed for monoclinic Pm space group (Figure 1.2).[11,12]

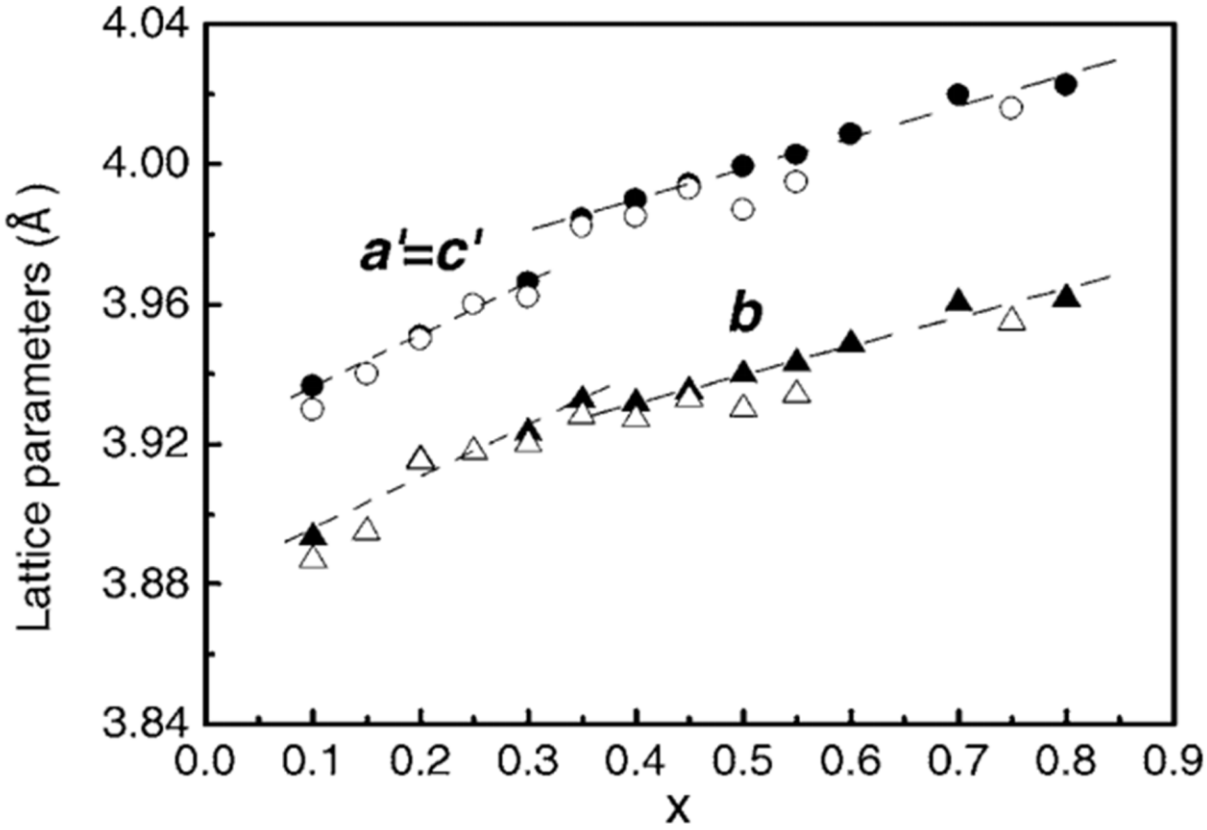

Figure 1.2 Evolution of lattice parameters for KNN in monoclinic settings across x = 0, taken from reference 11 (Reprint from references 11 © 2008 American Institute of Physics).

Wang et al. have also refined the lattice parameters of $Na_{0.5}K_{0.5}NbO_3$ ceramic in monoclinic setting and found the lattice parameters to be a = b = 4.003Å, c = 3.943Å and β = 90.36°.[13] Figure 1.3 shows the unit cell of $Na_{0.5}K_{0.5}NbO_3$ in monoclinic and orthorhombic setting.

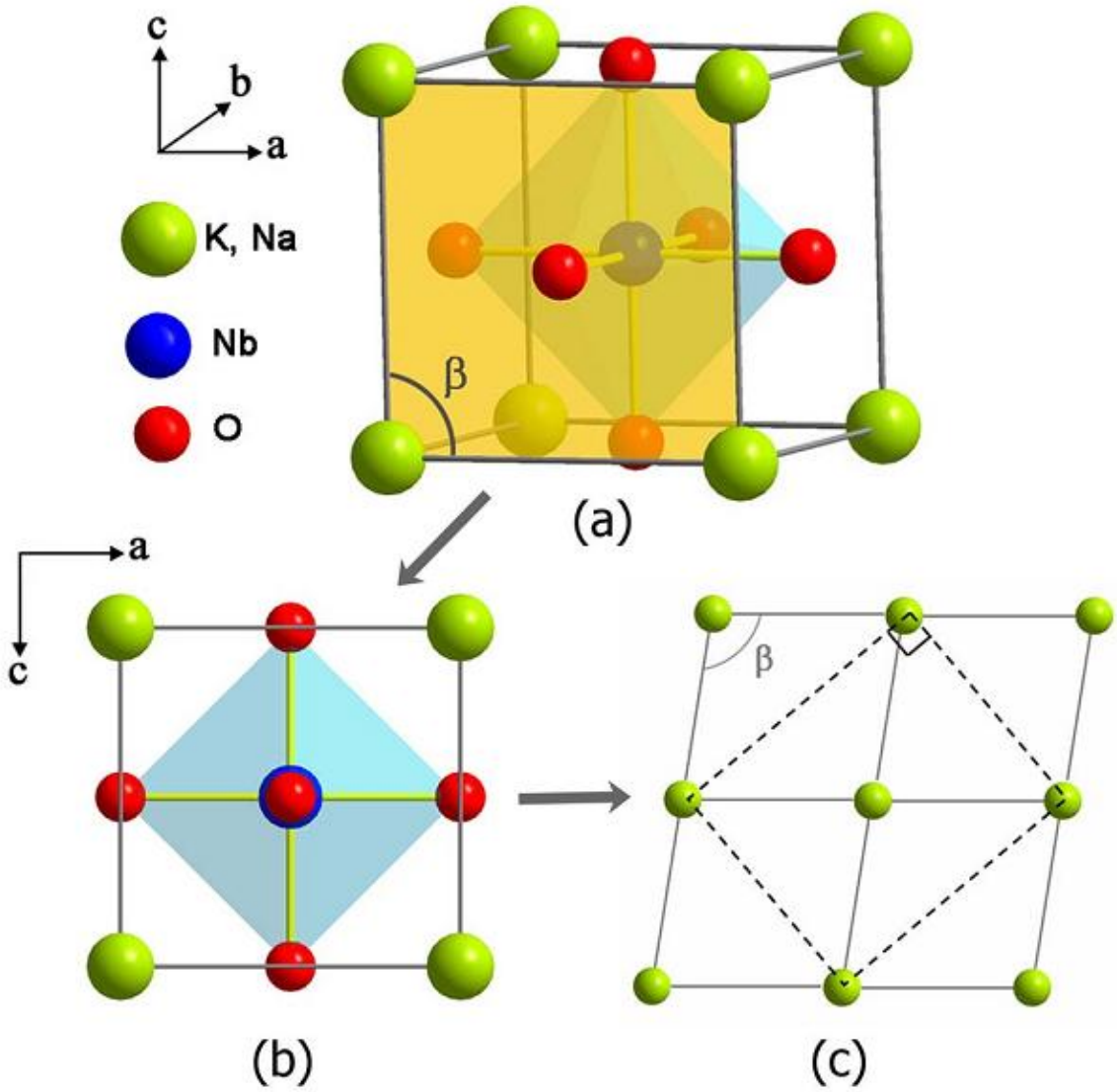

Figure 1.3 Unit cell of $Na_{0.5}K_{0.5}NbO_3$ (a) primitive monoclinic setting and (b) its projection along b axis (c) non-primitive orthorhombic setting of the same unit cell (Reprint from reference 13 © 2007 American Institute of Physics).

In a recent studies performed by Baker and coworkers, a comprehensive phase diagram for $K_xNa_{(1-x)}NbO_3$ was presented in the temperature range of -250℃ to 500℃.[14,15] Illustrated in the Figure 1.4. This phase diagram provides the insight about the different crystallographic phases present for the different compositions along with their space group and oxygen octahedral tilt information.[14-16] Similar to the phase diagram given by Jaffe et al., this phase diagram shows the presence of phase boundary at x = 0.5. In contrast, this diagram suggested the presence of orthorhombic (Amm2) and monoclinic (Pm) crystallographic phases on either side of the x=0.5 composition. Detailed analysis of two compositions on either side of x=0.5 revealed that they belong to $a_+^0 b_0^0 c_+^0$ and $a_+^0 b_+^0 c_0^0$ octahedral tilt system (Glazer Notation).[17]

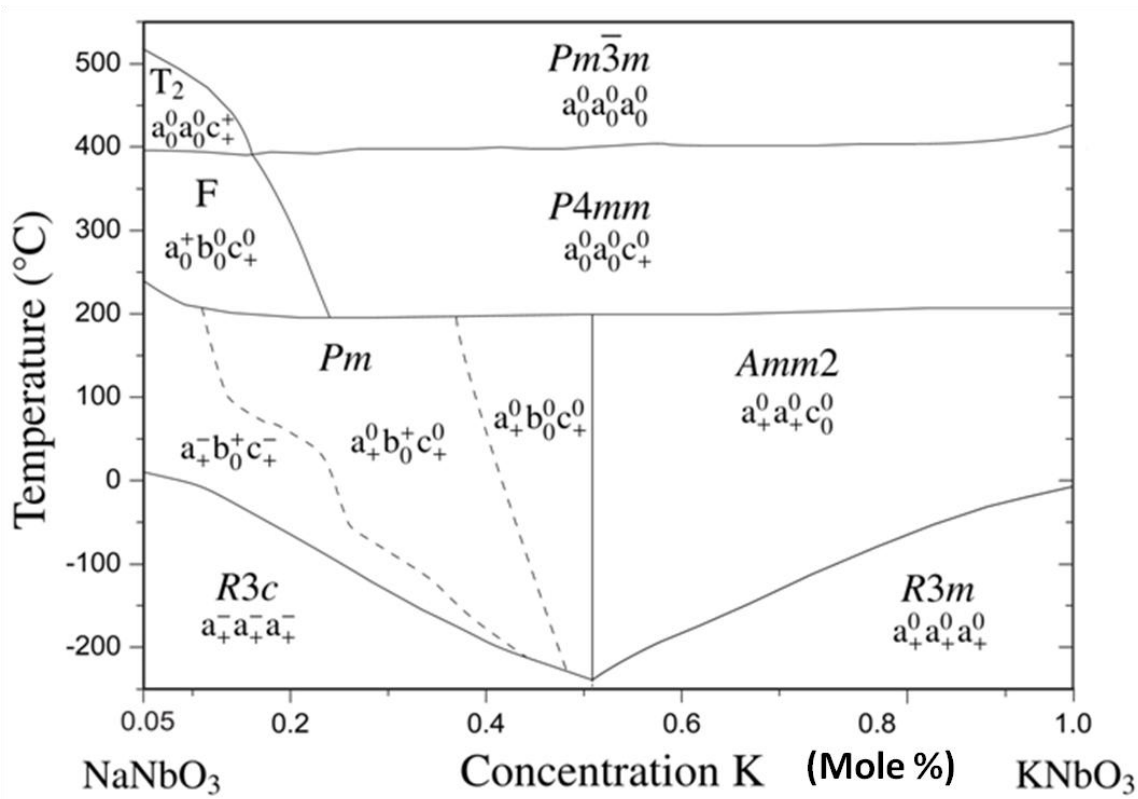

Figure 1.4 Comprehensive phase diagram of $K_xNa_{(1-x)}NbO_3$ after Baker and coworkers (Reprint from reference 14 © 2009 American Institute of Physics).

.

In agreement with the previous investigations, at high temperature compositions with x > 0.25 were reported to go through a transition to the tetragonal phase, represented by an almost composition independent polymorphic phase boundary (PPB) at 200°C. This high temperature tetragonal phase was reported to possess P4mm space group with $a_0^0 b_0^0 c_+^0$ tilt system. At 400°C, a ferroelectric to paraelectric phase transition with $Pm\bar{3}m$ space group was observed for all compositions.

1.2 Processing of KNN-based Ceramics

The solid state reaction route is the most common and convenient way to synthesize KNN. [11, 18 - 21] Generally sodium carbonate (Na_2CO_3, Molecular Weight – 105.99), potassium carbonate (K_2CO_3, Molecular Weight – 138.21) and niobium oxide (Nb_2O_5, Molecular Weight - 265.81) are used as the starting materials. The melting points of these precursors are 851℃, 891℃ and 1520℃ respectively. Since the normal sintering temperature for KNN is close to the melting point of two alkali precursors, there is always the problem of volatilization during calcination and hence the deficiency of the A-site ions.[18, 22, 23] The effects of the calcination temperature, dwell time and the excess of the alkali carbonates on phase formation and microstructure of the KNN have been studied extensively. [18, 24, 25] Bomlai and coworkers[18] studied the effect of the calcination temperatures and time on the phase formation of KNN. They found that a perovskite phase can be achieved at temperatures as low as 600℃ but broad XRD peaks without orthorhombic splitting suggested the absence of a compositional homogeneity. They tried different combinations of dwell time and temperature and found that the samples calcined at 900℃ for 6 hours had the perovskite phase with orthorhombic splitting. They also found that a single phase orthorhombic perovskite KNN can be formed at only 800℃, if 5% excess of the

alkali carbonates is used. Scanning electron micrographs showed that the samples with excess of alkali precursors (3% or less) had submicron grain size with equiaxed geometry, while samples with 5% excess had a cubical shape with crystal size increasing with calcination temperature and reaching to 2.5μm at 900℃, 2h. This type of grain growth was due to the secondary crystallization involving consumption of the small grains by the large ones. Excess of alkali precursors left after volatilization gave rise to the liquid phase which promoted the secondary crystallization.

The effect of Na / K ratios on the electromechanical properties of sodium potassium niobate was studied by Wu et al.[11] They synthesized $KxNa1\text{-}xNbO_3$ composition with $0.1 \geq x \geq 0.8$ and noticed a sharp change in the lattice parameters of KNN at $x = 0.35$, in contrast to many other reports suggesting the presence of morphotropic phase boundary (MPB) at $x = 0.5$. It was suggested that the broad peak in the piezoelectric properties in the range $0.4 \geq x \geq 0.6$ was not because of the presence of any MPB, but because of the uni-modal grain size distribution in this range.[11] Hagh and coworkers[21] synthesized the $K_{0.5}Na_{0.5}NbO_3$ - $LiSbO_3$ - $LiTaO_3$ (KNN-LS-LT) system by two alternative methods, namely perovskite and mixed oxides roots, and studied the effect of humidity and oxygen flow rate during sintering. It was found that the piezoelectric properties of ceramic samples synthesized by both processing roots were sensitive to the humidity and for best results precursors need to be preheated (dried) in inert atmosphere before formulation of the desired composition. They concluded that the mixed oxide root is the most suitable technique to synthesize KNN-based ceramics followed by sintering in the oxygen atmosphere.[21]

One of the challenges in commercialization KNN ceramic is its low sinterability. Lower relative density of piezoelectric ceramics not only leads to poor electromechanical coupling but

also gives rise to the high electrical conductivity which presents difficulty in poling. This problem is mainly attributed to the high volatilization of alkali elements at the sintering temperature, which is higher than 1100°C for normal solid state sintering.[22, 23] the evolution of cubical shaped KNN grains also contributes to this problem as a higher packing density is difficult to be achieved with such particle shape.[27] Significant research has been done to understand the problem of sintering in KNN and other members of the alkali-based perovskite family.[23, 28] Jenko et al.[22] studied the effect of sintering temperature on the microstructure, composition and phase formation of KNN ceramics. They found that the samples sintered at 1100°C for 24 hours had the presence of a niobium rich second phase having Na / K and (Na+K) / Nb atomic ratios to be 0.3 and 0.6 respectively. This analysis clearly indicated that volatilization of sodium is faster than that of potassium ions. Ahn and coworkers have reported an extensive study on the sintering mechanism of KNN based ceramics.[23] In their work three stages of sintering were identified. Microstructures of these samples at each stage of sintering along with the descriptive schematics are shown in Figure 1.5. Figure 1.5 (a) shows the morphology of the as calcined KNN powder to be cubical with particle size of 200 nm. This geometry of particles is distorted during ball milling, reducing the particle size further to 100 – 200 nm (Figure 1.5 (b)). In the first step of the process, random shaped ball-milled particles rearranged to form the cubical particles consisting of stacks of plate like particles (Figure 1.5 (c), (d) and (c-s)). Presence of plate-like particles was attributed to non-isotropic interfacial energy for lower liquid content. This stage of sintering lasted until the cross-section of neck reached a threshold after which further thermal activation energy was required for densification. Presence of liquid phase was also evident from the microstructure shown in figure 1.5 (c). According to the authors, formation of liquid phase is critical for the densification of KNN based ceramics due

to the non-uniform cubical shape of the particles. Presence of a liquid phase at grain boundaries not only provided a medium for the transport of the matter leading to a more effective packing but also wetting of the plates can result in bridging of the porosity. EDX analysis was performed to identify the composition of this liquid phase and results showed it to be sodium deficient. Based on the EDX results, authors proposed a chemical reaction (Equation 1.1) leading to the formation of a liquid phase due to evaporation of Na_2O.

$$0.995(K_{0.48}Na_{0.48}Li_{0.04})NbO_3\ 0.005BaTiO_3$$

$$\rightarrow 0.995(K_{0.48}Na_{0.025}Li_{0.04})NbO_{2.7725}0.005BaTiO_3 + 0.226Na_2O \uparrow \qquad (1.1)$$

In the second stage of sintering rapid grain growth takes place, which is assisted by the presence of a liquid phase. An elongated plate like structure was observed at the end of second stage of sintering (Figure 1.5 (c) & (d)) which was attributed to the grain accommodation process. According to the authors[23] insufficient amount of liquid phase was responsible for this kind of morphology as in these circumstances grains tend to undergo a considerable change in shape in order to flatten their contact region with neighboring grains. In the final stage of sintering coarsening became the dominant process. As is evident from Figure 1.5 (e) and (f), the rate of coarsening was higher at higher temperatures as solubility of solute as well as their diffusion increased with temperature. Variation of density and average grain size of KNN were plotted as a function of sintering temperature and are shown in Figure 1.6 (a). Variation of density with sintering temperature was similar to what has been reported for liquid assisted sintering and is consistent with microstructures showing presence of liquid phase at the grain boundaries. Grain size variation with sintering temperature was modeled for Ostwald ripening mechanism.

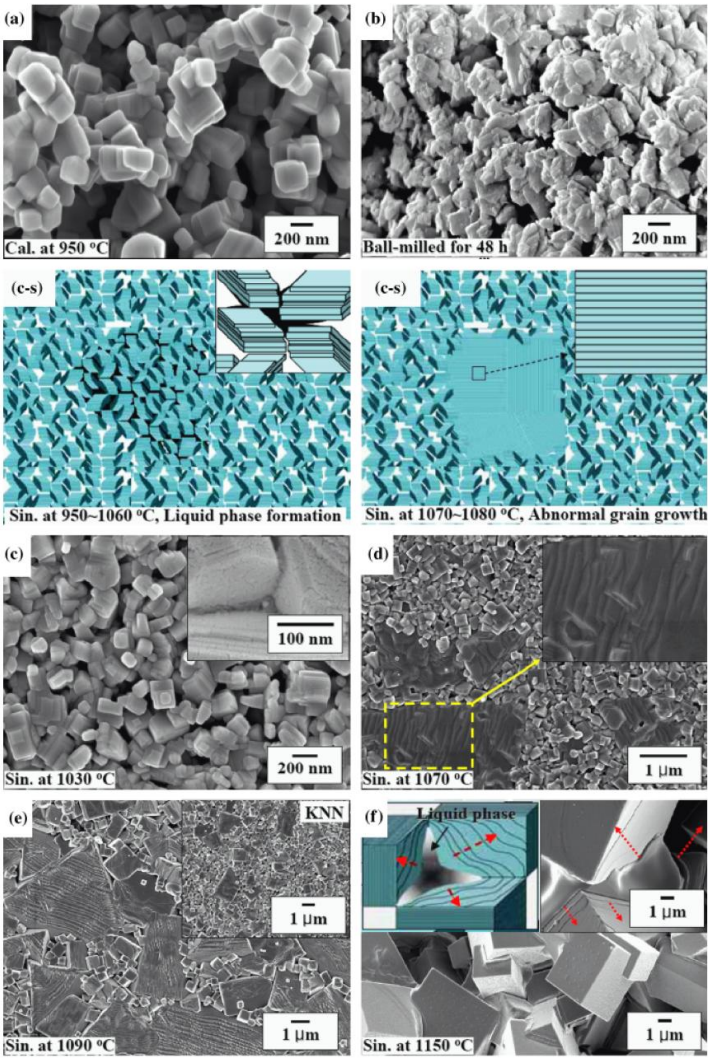

Figure 1.5 Microstructures of KNN-based ceramic samples at different stages of processing (a) calcined powders at 950°C for 180 min, (b) KNN powder ball milled for 48h after calcination (c) Sintered at 1030°C, 0 min, (d) Sintered at 1070°C, 0 min, (c-s) Schematics showing the simplified view of (c) and (d) to explain the sintering model in KNN, (e) Sintered at 1090°C, 0 min, Inset of figure (e) shows KNN specimen sintered at 1100°C for 0 min (f) sintered at 1150°C, 0 min; Left insets: Schematic diagram showing the presence of liquid phase and Right inset: magnified view of area in (e) showing liquid phase (Reprint from reference 23 © 2009 The American Ceramic Society).

Lifshitz, Slyozov and Wagner's equation relating the grain size with sintering time and temperature can be used for analyzing the sitering kinetics and is given by Equation 1.2.

$$G^m = G_o^{\,m} + Kt \tag{1.2}$$

where G_o is the initial grain size, K and m are respectively temperature and coarsening mechanism dependent parameters. Figure 1.6 (b) shows the variation of grain size for different compositions with sintering time. The value of parameter m was found to be 3 for all three compositions indicating the diffusion controlled mechanism of coarsening for all of them.

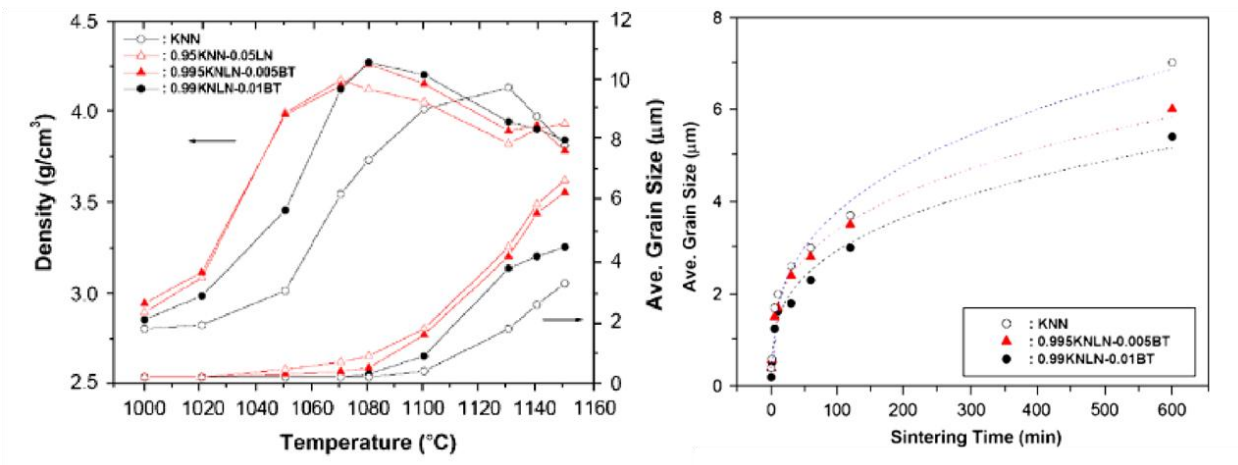

(a) (b)

Figure 1.6 Variation of density and average grain size with sintering temperature for various KNN based ceramics (b) Average grain size plotted as a function of sintering time at 1080°C. Dashed line shows fitting to data points according to equation (1.2) with m = 3. (Reprint from reference 23 © 2009 The American Ceramic Society).

A significant fraction of research on KNN based ceramics is focused on rectifying the problem of low sinterability.[20, 29 - 33] This includes the application of different nonconventional sintering techniques as well as use of different sintering additives. Ruzhong et

al. studied the effect of particle size on the sintering of KNN as driving force for sintering is higher for smaller particle size.[34] They achieved about 98.5% density at 1100℃ by using attrition milled powder of size 70 nm, in contrast to 94% density achieved for the traditionally ball milled powder at the same temperature.[34] The problem of volatility can also be controlled up to some extent by performing the sintering in sealed crucibles with muffling of samples by the same composition powder.[33, 35, 36] Mechano-chemical activation or synthesis by high energy ball milling can reduce the processing temperature which resulted in the reduction of loss of volatile constituents. However, there was increased possibility of the contamination during the processing.[37]

Spark plasma sintering (SPS) is another common technique used for sintering KNN.[38] Density of up to 99% of theoretical density could be achieved with grains of size of 200 – 500 nm. Samples sintered by the SPS method required an annealing at 900 ℃ to eliminate the oxygen vacancies that resulted in good saturated ferroelectric loops. But due to the fine grain size, samples had relatively low saturation polarization value of about 6.5 $\mu C/cm^2$.[38] The piezoelectric coefficient (d_{33}) and planar electromechanical coupling factor (k_p) were found to be 148 pC/N and 0.389 respectively for spark plasma sintered KNN samples. KNN samples synthesized by hot pressing and hot forging were also found to exhibit improved piezoelectric properties due to better densification.[31, 39, 40] Kosec et al.[41] studied the effect of A-site vacancies on the sintering of KNN. These vacancies were created in two ways, by doping higher valance ion Mg^{+2} on A-site and by using the excess of Nb_2O_5. The shrinkage measurements done on Mg^{+2} doped samples revealed that A-site vacancies not only lowered the initial sintering temperature but also improved the final density. Similar effects were observed in samples prepared with the excess of niobium oxide.

Ruzhong[34] and Smelter[42] along with their coworkers studied the effect of different oxide additives on sintering behavior of KNN. In Ruzhong's study, ZnO and SnO_2 proved to be best additives but in different ways. SnO_2 on one hand helped in getting higher density at same sintering temperature (1100℃), ZnO on the other hand decreased the sintering temperature by 100℃ for the same relative density. Decrease in Curie point of SnO_2 doped KNN samples indicated the change in lattice parameters of KNN and hence diffusion of Sn^{+4} ions into the KNN lattice. Significant increase in the coercive field of these samples suggested the formation of oxygen vacancies by substitution of lower valance Sn^{+4} ions onto the Nb^{+5} site. According to the authors, these oxygen vacancies helped in getting higher density when sintering was done in air. In case of ZnO, no change was observed in lattice parameters and coercive field and lowering of sintering temperature was attributed to the liquid phase sintering. The advantages of ZnO doping were also confirmed by number of other studies as well.[43, 44]

Copper based sintering additives like $K_4CuNb_8O_{23}$ (KCN) and $K_{5.4}Cu_{1.3}Ta_{10}O_{29}$ (KCT) have been found to be very effective in improving the sinterability of KNN based ceramics.[45, 46] Matsubara et al. employed the sintering aid KCT with KNN and found that only 0.38 mole % was sufficient in achieving high density at sintering temperature of 1120℃.[46] X-ray diffraction analysis showed no peaks belonging to KCT suggesting the formation of a complete solid solution with KNN. KNN- KCT solid solution was found to have a decreased T_{o-t} and T_c as compared to KNN. This drop in transition temperatures helped in achieving improved piezoelectricity with the d_{33} value of 190 pC/N. Copper ions going onto Nb site acted as acceptors and along with higher density, helped in achieving higher mechanical quality factor (Q_M). According to the authors, the Q_M value was found to be 1300 which is at least 14 times higher than that for pure KNN. Because of improved density, there was a significant

improvement in the planar coupling coefficient as well. Copper oxide is another common sintering aid in this category.[47 - 50] Lin et al. studied the effect of CuO on sintering and piezoelectric properties of KNN.[48] The ceramic KNN- xCuO was synthesized by normal sintering route with x varying between 0 - 2 mole percent. Samples with pure orthorhombic perovskite structure and improved density were found to have slightly smaller bimodal grains as compared to pure KNN. At the same time, CuO doping also lead to significant decrease in piezoelectricity and orthorhombic to tetragonal transition temperature $T_{o\text{-}t}$. In another study, CuO was used as the sintering additive in 0.95KNN-0.05$SrTiO_3$ composition.[51] XRD analysis revealed the change in lattice parameters indicating the occupation of Nb^{+5} and Ti^{+4} sites by Cu^{+2} ions for addition of < 1 mol % of CuO. Samples sintered at 960℃ with 1.5 mol% of CuO were found to display larger grain size due to presence of liquid phase. Owing to the larger grain size, the samples with 1 – 2% CuO doping were found to exhibit optimum piezoelectric properties with d_{33} and k_p values of 200 pC/N and 0.35 respectively. Anti-ferroelectric like *P-E* hysteresis loops were found in >1 mole % Cu doped KNN ceramics which was attributed to the presence of defect dipoles. In a recent report, Eichel et al. have performed multi-frequency and multi-pulse electron paramagnetic resonance (EPR) spectroscopy on Cu-doped KNN system and confirmed the substitution of Cu^{2+} on B-site as acceptor.[52] Park et al. have reported enhanced Q_m ~ 3053 in KNN ceramics by co-doping of KCT and CuO.[53]

Liang et al. studied the effect of poling conditions on the piezoelectric properties of KNN ceramic.[26] They studied the variation of poling field, time and temperature on longitudinal piezoelectric coefficient and concluded that samples poled at fields of 4 kV/mm for 20 minutes at 140°C had the best piezoelectric properties. Mei et al. studied the effect of humidity on the piezoelectric properties of KNN and concluded that small amount of $ScTaO_4$ improved the

stability of piezoelectric properties in humid environment.[54] However, Sc is one of the most expensive elements and thus its questionable if this method will be used in practical processes.

1.3 Compositional Modification to KNN Ceramics

A large numbers of dopants on both A and B sites as well as different solid solutions have been studied in order to improve the piezoelectric properties of KNN.[55 - 67] Guo[68] et al. studied the effect of ithium doping on the piezoelectric properties of KNN by synthesizing the ceramics given as $Li_x(Na_{0.5}K_{0.5})_{(1-x)}NbO_3$ (KNLN) for x varying between 0.0 to 0.2. They observed the presence of MPB between orthorhombic and tetragonal phases in the range $0.05 < x < 0.07$. A sharp peak in the piezoelectric properties (d_{33} – 235 pC/N, k_p – 0.44) observed in this composition range also confirmed the presence of MPB. Temperature dependent dielectric response analysis conducted at MPB compositions revealed the shift of T_c and T_{o-t} to higher and lower temperatures respectively. Du studied the effect of poling temperature on the same lithium doped MPB compositions (x = 0.05, 0.06, 0.07) and found that a significant improvement in the piezoelectric properties can be achieved if poling is performed at the orthorhombic to tetragonal transition temperature T_{o-t}.[69] Zhang and coworkers [70] extended the work of Guo et al.[68] and studied the effect of antimony doping on B-site while the lithium doping at A-site was fixed at 0.058 mole %. For the doping range of 2 - 8 mole %, no MPB could be found and crystal structure remained to be orthorhombic. But the sample with 6 mole % antimony doping had the largest grains and hence best piezolelectric properties (d_{33} – 298 pC/N, k_p – 0.34 and dielectric constant (ε) - 945). The disadvantage of antimony doping was the drastic decrease in the T_{o-t} to 60℃ in contrast to only lithium doped samples. Zang et al. studied the solid solution of $LiSbO_3$ with KNN by synthesizing the composition $(Na_{0.5}K_{0.5}Nb)_{(1-x)}(LiSb)_xO_3$ for $0.048 < x < 0.056$.[71]

Though they did not discuss the room temperature crystal structure of these samples, the composition with x = 0.052 was found to exhibit the best d_{33}, dielectric constant and k_p values given as 286 pC/N, 1372 and 0.51 respectively. According to the authors, this improvement in the properties could be attributed to the decrease in the To-t temperature. Lin also conducted similar studies on NKN-LS system and found the presence of MPB between orthorhombic to tetragonal phases at x = 0.06 resulting in optimum piezoelectric properties.[72]

Yuanyu et al. synthesized the $0.995[(K_{0.5}Na_{0.5})_{0.94}Li_{0.06}]NbO_3 - 0.05AETiO_3$ (AE = alkali earth elements like Mg, Ba, Sr and Ca) compositions and found that only $CaTiO_3$ (CT) makes solid solution with $(K_{0.5}Na_{0.5})_{0.94}Li_{0.06}NbO_3$.[73] These KNLN – CT samples with large grain size and highest density (> 98%), were found to have tetragonal crystal structure at room temperature. Temperature dependent dielectric response study revealed the existence of $T_{o\text{-}t}$ below room temperature. Similar to the work of Du[74], poling conditions were optimized and KNLN – CT samples were found to have d_{33} and k_p values of 172 pC/N and 0.43 respectively. These properties were attributed to high density, bigger grain size and near RT existence of orthorhombic to tetragonal phase transition temperature $T_{o\text{-}t}$. Temperature dependent piezoelectric measurements also revealed the excellent stability with only 4% variation in d_{33} value in the temperature range of 10°C - 70°C. Li[75] and coworkers studied the effect of silver doping on KNN. Single phase orthorhombic perovskite structure could be achieved for $x \leq 0.3$. For this composition range, both Tc and To-t were found to be decreasing linearly with x and sample with x = 0.18 was found to be best piezoelectric properties with d_{33} = 186 pC/N and k_p = 0.425. It was stated that this improvement is related to the decrease in $T_{o\text{-}t}$. The sample with x = 0.18 was also found to have temperature independent nature of k_p from RT to $T_{o\text{-}t}$.

Cho et al. studied the effect of sodium deficiency on the microstructure and piezoelectric properties of 0.95KNN – 0.05$SrTiO_3$ (0.95KNN-0.05ST) ceramic which was found to have high porosity and hence poor piezoelectric properties.[76] The small deficiency (1.0%) of Na_2O lead to denser microstructure due to the formation of liquid phase at sintering temperature of 1080°C. The samples with density of 96 % were found to have d_{33} and k_p values of 220 and 0.40 respectively. Unlike Cho et al.'s study, Kosec et al.[77] achieved density higher than 95% for (1-x)KNN - xST samples for $0.1 \leq x \leq 0.33$. The samples with $0.15 \leq x \leq 0.25$ were found to have pseudo-cubic crystal structure with submicron sized grains. Temperature dependent dielectric response for x = 0.2 sample revealed the relaxor behavior with giant dielectric constant values and broad dispersive maxima.

Ahn et al. have synthesized the KNN – $BaTiO_3$ (KNN-xBT) solid solution and studied the piezoelectric and dielectric properties.[78,79] This system was found to have three morphotropic phase boundaries at room temperature. Orthorhombic to tetragonal transition at $0.0 \leq x \leq 0.1$, tetragonal to cubic at x = 0.2 and tetragonal to cubic at $x > 0.94$. Among these MPBs, orthorhombic to tetragonal transition at $0.0 \leq x \leq 0.1$ was found to provide best piezoelectric properties. Rietveld refinement performed on X-ray diffraction patterns revealed the coexistence of Bmm2 and P4mm space groups in the composition range $0.02 \leq x \leq 0.07$. Sintering conditions were optimized for 0.9KNN – 0.05 BT samples and it was found that muffled samples sintered at 1060°C for two hours had the optimum grain size and hence the best piezoelectric properties.[80] Different amounts of sintering additives CuO and MnO_2 were explored to suppress the volatilization of Na_2O by decreasing the sintering temperature and hence reducing the leakage current.[49] It was found that addition of 2 mol% CuO and 0.5 mol% MnO_2 reduces the sintering temperature to 950°C and improves the piezoelectric properties with d_{33} increasing from 220 to

248 pC/N. Effect of small amount of $BaTiO_3$ ($0.0 \leq x \leq 0.20$) was also studied on the $(K_{0.5}Na_{0.5})_{0.96}Li_{0.04}NbO_3$ composition.[81] Saito et al. have shown that KNN based composition given as $[(K_{0.44}Na_{0.52}Li_{0.04})(Nb_{0.84}Ta_{0.10}Sb_{0.06})O_3]$ has piezoelectric coefficient as high as 300 pC/N.[82]

1.4 Textured KNN Ceramics

Since the piezoelectric properties of KNN-based ceramics are far inferior to those of lead-based compositions, it is important to utilize the anisotropy in elastic, dielectric and piezoelectric properties in order to achieve desired performance. In case of relaxor ferroelectrics such as PMN-PT, [001] oriented crystals exhibit enhanced piezoelectric response for compositions near the MPB. But the application of single crystals is usually limited by the high production cost, small product size, and the compositional heterogeneity. It has been demonstrated that crystallographic texturing of polycrystalline ceramics offers significant enhancement in the piezoelectric response. Template grain growth (TGG) and reactive templated grain growth (RTGG) are two cost-effective methods to fabricate highly textured ceramics with enhanced properties comparable to those for single crystal. TGG is a process in which nucleation and growth of the ceramic in desired orientation take place on aligned single crystal template particles during the heat treatment, resulting in textured microstructure.

However in TGG process, due to the complex nature of few piezoelectric compositions, it is sometimes difficult to synthesize the homogeneous anisotropic shaped template of the same composition as matrix. The heterogeneous templates used in such cases, having different composition from the matrix materials can diminish the piezoelectric performance of ceramic.

To overcome this problem of template heterogeneity in the RTGG process, anisotropic particles of reactant composition are used that chemically react with the other reactant to form the end composition. These templates can be aligned and converted into the target material on reaction with matrix, while preserving their crystallographic orientation. Using TGG and RTGG process, several lead-based and lead-free piezoelectric ceramics have been fabricated in the last decade.[83-88]

A <001> oriented textured KNN-based ceramic synthesized by TGG process was first reported by Saito et al. in 2004.[82] They used $NaNbO_3$ platelets as reactive template for texturing KNN based ceramics. Figure 1.7 (a) and (b) shows the scanning electron micrograph (SEM) image and X-ray diffraction (XRD) profile for textured $(K_{0.44}Na_{0.52}Li_{0.04})$ $(Nb_{0.84}Ta_{0.10}Sb_{0.06})O_3$ ceramic (LF4T) in comparison to that of the random ceramic (LF4) with the same composition. It should be noted that the textured ceramic exhibits the brick-wall type microstructure with the grains aligned parallel to the tape-casting direction. As shown in Table 1.1, the overall performance of the textured KNN-based ceramics (LF4T) is comparable to the lead-based PZT ceramic (PZT4).

This work of Saito et al. trigged a significant amount of research on developing the texture controlled piezoelectric ceramics, including both lead-based and lead-free compositions. Table 1.2 lists the different KNN-based compositions textured in the last few years, along with their different piezoelectric properties.[82, 83, 85 - 88] Since high relative density of ceramic is desired for obtaining the grain growth on template crystal, different sintering additives were used to achieve high degree of texturing in KNN.[85, 86]

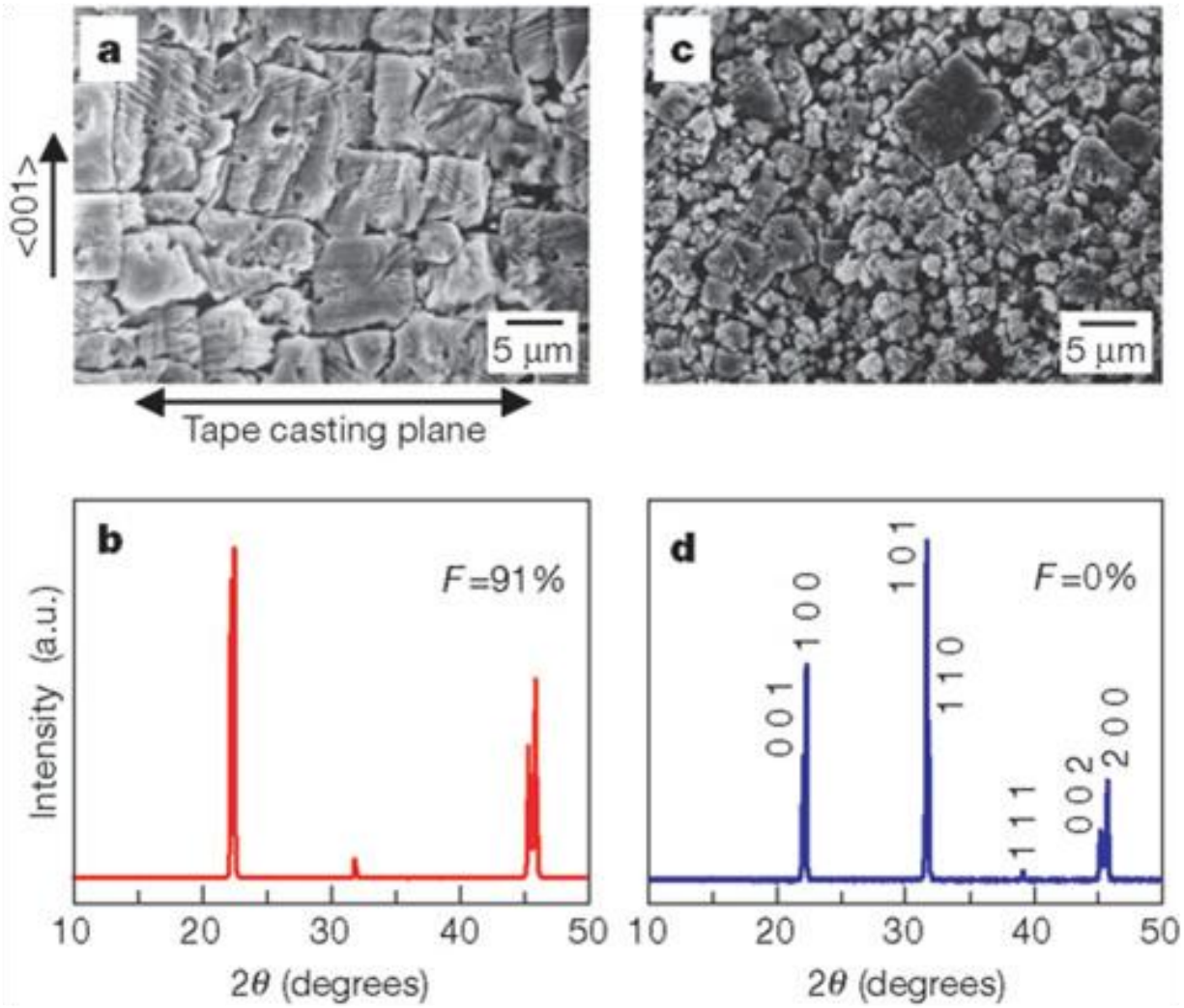

Figure 1.7 Microstructure and X-ray diffraction patterns (a) and (c) for textured and (b) & (d) for random ceramics (LF4 and LF4T) respectively (Reprint from reference 82 © 2004 Nature Publishing Group).

Table 1.1 Comparison of piezoelectric properties of random and textured $(K_{0.44}Na_{0.52}Li_{0.04})(Nb_{0.84}Ta_{0.10}Sb_{0.06})O_3$ composition (taken from reference 82).

Piezoelectric property		LF4T	PZT4
Curie temperature	T_c (^oC)	253	250
Piezoelectric coupling constant	k_p	0.61	0.60
Piezoelectric charge sensor constant	d_{31} (pC/N)	152	170
	d_{33} (pC/N)	416	410
Piezoelectric voltage constant	g_{31} (10^{-3}V m N^{-1})	11.0	8.3
	g_{33} (10^{-3}V m N^{-1})	29.9	20.2
Dielectric constant	$\varepsilon_{33}^T/\varepsilon_0$	1,570	2,300
Normalized strain	S_{max}/E_{max} (pm V^{-1})	750	700

Table 1.2 Piezoelectric properties of different textured KNN-based compositions

Composition	Template	Parameters	Random Ceramics	Textured Ceramics	Ref
$(K_{0.44}Na_{0.52}Li_{0.04})(Nb_{0.84}Ta_{0.10}Sb_{0.06})O_3$	$NaNbO_3$	S_m/E_m(pm/V)	400	750	82
		d_{33}(pC/N)	300	416	
		T_c(^oC)	253	253	
$(K_{0.5}Na_{0.5})NbO_3$-1.0 mol%CuO	$NaNbO_3$	k_p	0.38	0.54	86
		d_{33}(pC/N)	86	123	
$(K_{0.476}Na_{0.524})NbO_3$-1.0 mol%CuO	$NaNbO_3$	$-d_{31}$	28	47	
		k_p	0.31	0.58	85
		d_{33}(pC/N)	85	146	
$(K_{0.5}Na_{0.5})(Nb_{0.97}Sb_{0.03})O_3$	$NaNbO_3$	k_{31}	0.17	0.33	
		k_p	0.43	0.64	84
		d_{33}(pC/N)	148	208	
$(K_{0.5}Na_{0.5})_{0.98}Li_{0.02}NbO_3$	$NaNbO_3$	k_{31}	-	0.39	83
		d_{33}(pC/N)	114	192	
		$-d_{31}$	-	73	
$(K_{0.5}Na_{0.5})(Ta_{0.15}Nb_{0.85})O_3$	$NaNbO_3$	k_{31}	-	0.33	83
		d_{33}(pC/N)	151	184	
		$-d_{31}$	65	68	

Another effective way to achieve textured KNN-based ceramics with high density is by using non conventional sintering techniques such as hot pressing (HP) and spark plasma sintering (SPS). In an unpublished work of Yan, RTGG method was used to achieve textured KNN-LN ceramics by using 5 mol% $NaNbO_3$ seeds. Figure 1.8 (a) shows the sample after binder burnout at 600°C. This sample was sintered at 900°C for 5 min using SPS. During this process, heating rate and pressure values were 100°C/min and 50 MPa respectively. Spark plasma sintering was conducted at 1100°C for 1h to accelerate the oriented grain growth and the texture development. Figure 1.8 (b) shows the cross-sectional SEM image of the sample. The texture degree was calculated from XRD pattern (Fig. 1.9) using Lotgering factor and was found to be 86%.

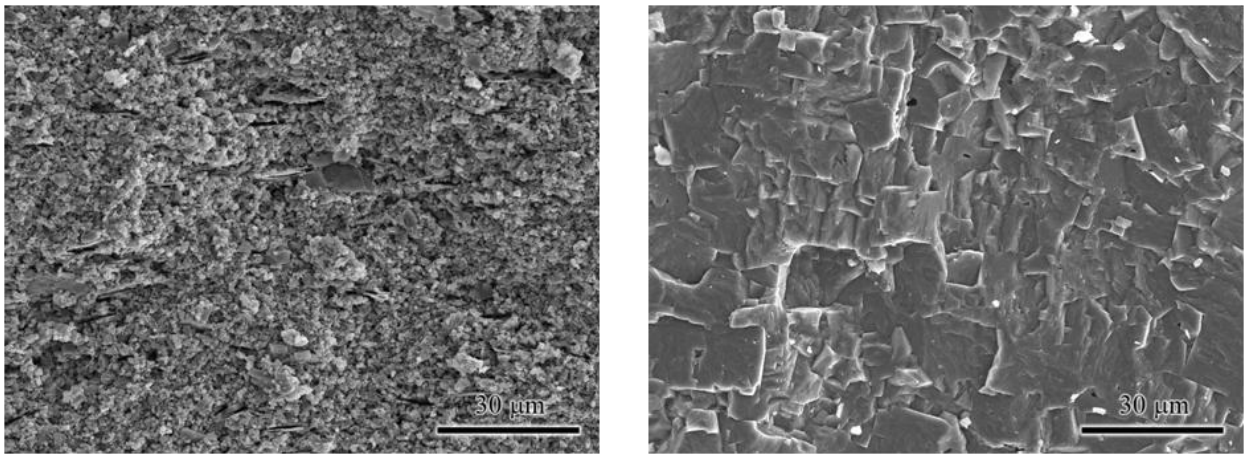

(a) (b)

Figure 1.8 SEM images of KNN-LN ceramics (a) green tape and (b) after sintering at 1100°C for 1h.

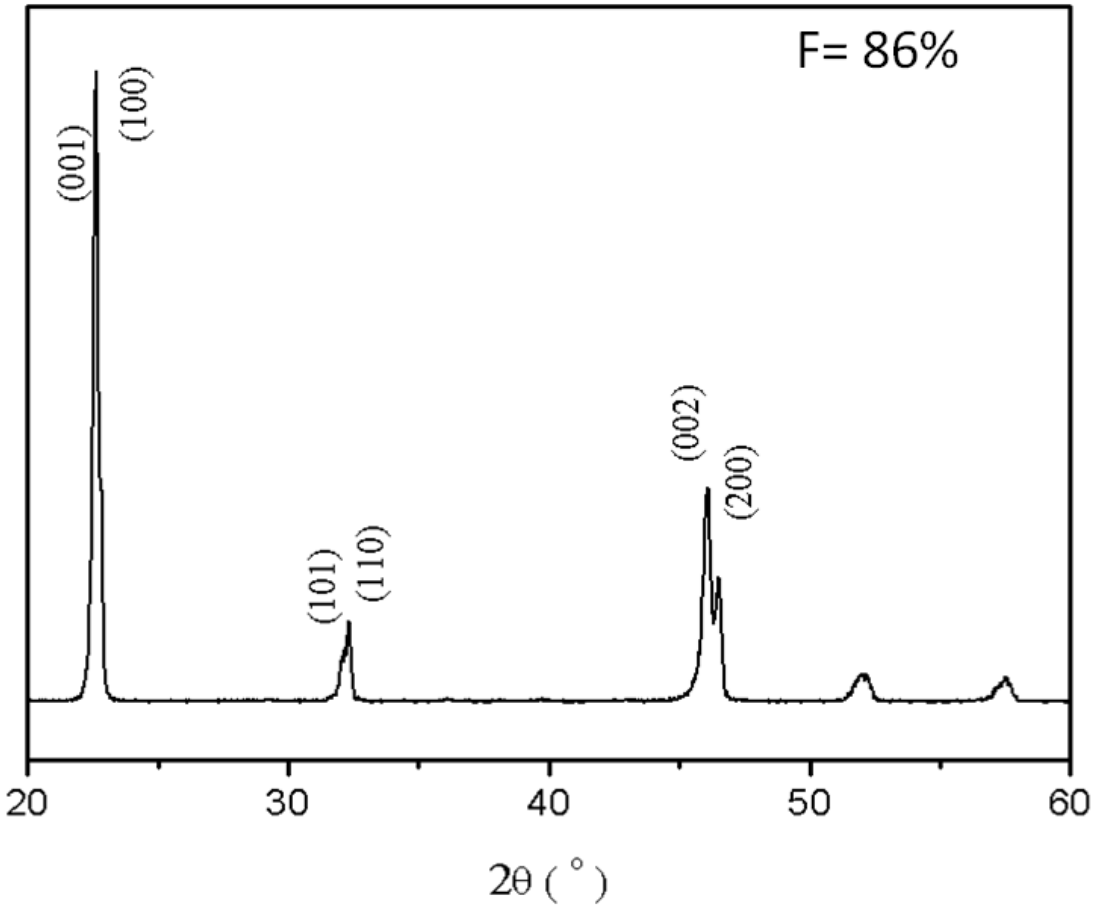

Figure 1.9 XRD pattern of textured KNN ceramic showing the Lotgering factor to be about 86%.

1.5 KNN-based single crystal

Compared to the volume of research done on random KNN ceramics, there are very few published reports related to the synthesis and characterization of KNN single crystals. Because of the presence of volatile components, it is difficult to grow good quality single crystals of KNN based compositions. Recently Kizaki et al.[89] have reported the synthesis of KNN single crystals of size 2 x 2 x 2 mm^3. In their work molten salt method was used to grow these crystals and mixture of NaF and KF salts was used as a flux. But due to the high conductivity of crystals ferroelectric and piezoelectric properties could not be measured. The reason for high

conductivity was proposed to be related to charge fluctuation of niobium ions (Nb^{+4} instead of Nb^{+5}). By doping 5 mole% manganese ions at B-site, significant improvement in resistivity of crystals was achieved with remanent polarization value of 40 μC/cm^2. Recently, Mn-doped KNN single crystals have been reported to show significant improvement in piezoelectric and dielectric properties.[90] The domain structures of pure and doped crystals is shown in Figure 1.10. Based on this figure, the improvement in piezoelectric and dielectric responses was attributed to the presence of higher domain density (lower domain size) in Mn-doped crystals.

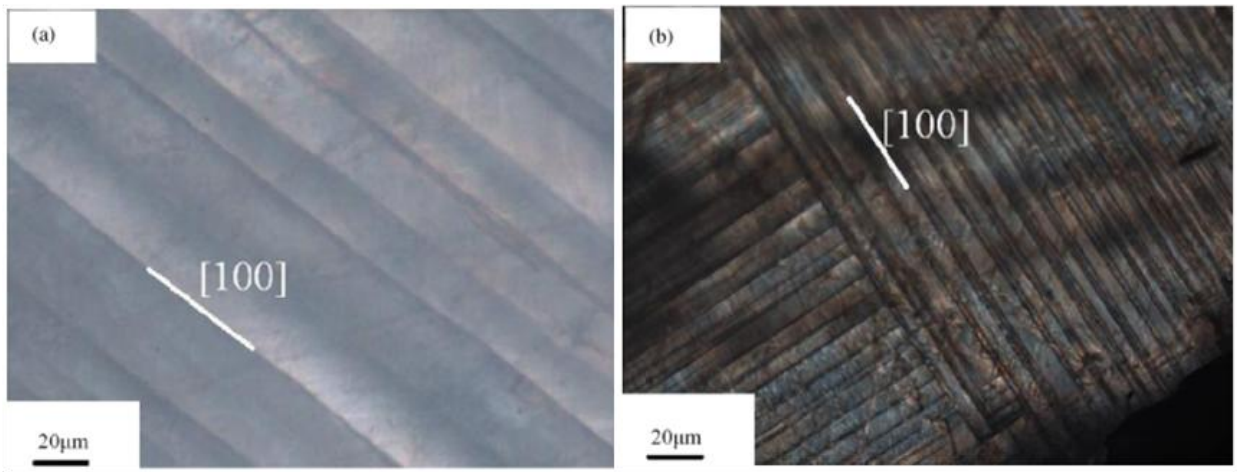

Figure 1.10 Domain structure of (a) pure and (b) 5 mole % Mn doped KNN single crystals.

Solid state single crystal growth (SSCG) method is an effective crystal growth technique to grow compositionally homogeneous single crystals of complex compositions. The principle of SSCG method is based on the abnormal grain growth in ceramics and it is suitable for growing the single crystals of materials with high melting temperature containing volatile components with the incongruent melting. This method was used to synthesize the KNN crystal using (110) oriented $KTaO_3$ crystal as seed. [91 - 93] The crystals had largest dimensions up to 4 mm but did not exhibit full density as shown in Figure 1.11.

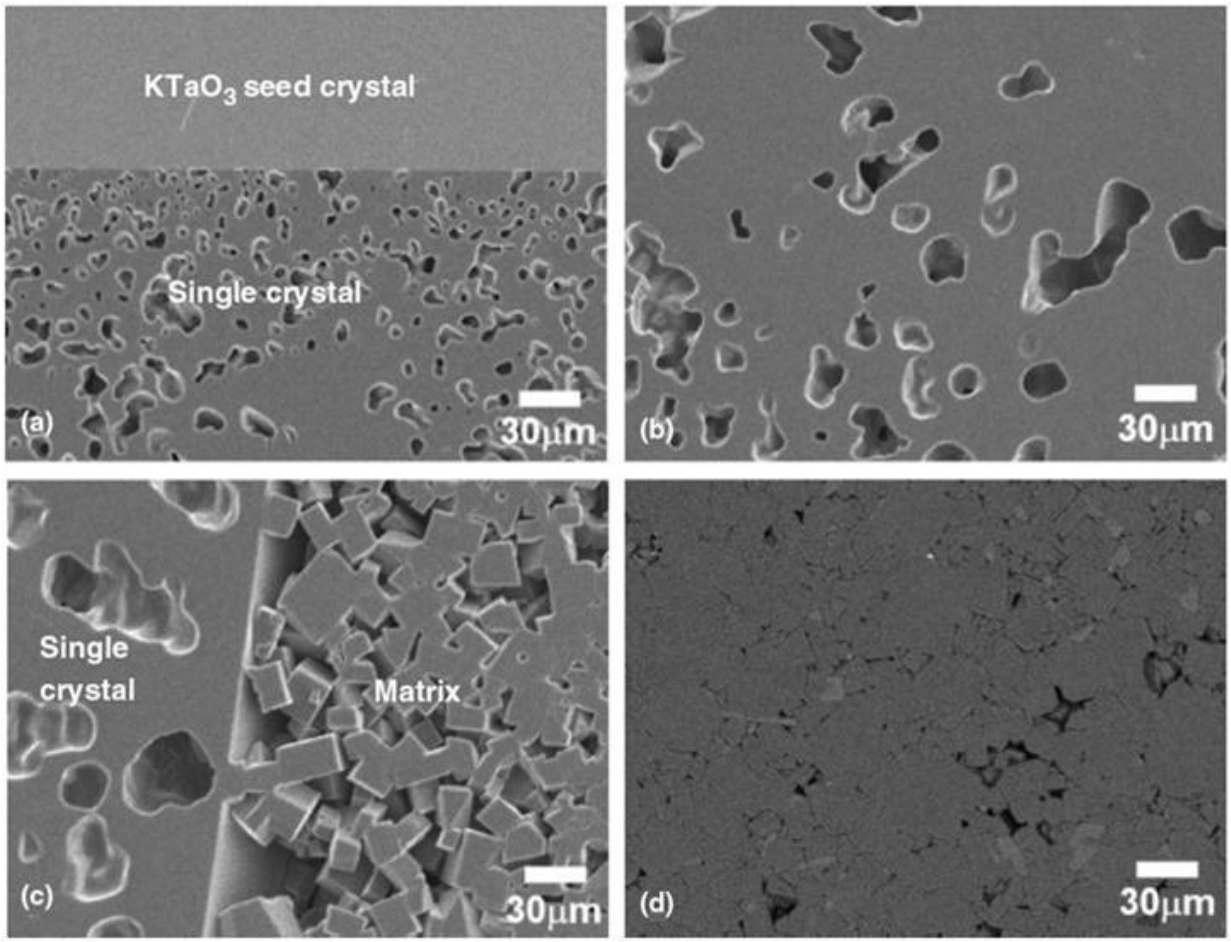

Figure 1.11 SEM images of $(K_{0.5}Na_{0.5})NbO_3$ single crystal grown in conventional furnace at 1100°C for 100h. (a) Secondary electron image of the seed crystal/single crystal boundary, (b) secondary electron image of the single crystal, (c) secondary electron image of the single crystal/matrix boundary, and (d) backscattered electron image of the matrix (Reprint from reference 91 © 2008 The American Ceramic Society)

Hot pressing instead of conventional sintering was found reduce the porosity of the grown crystals as shown in Figure 1.12.[91] Dielectric response as a function of temperature showed T_{o-t} and T_c to be 193℃ and 410℃ respectively that is consistent with the reported values for ceramics.[91] Crystals were found to have higher dielectric constant values in $[1\bar{3}1]$ direction as

compared to $[3\bar{2}3]$ direction.[92] Ferroelectric properties measured in $[1\bar{3}1]$ direction exhibited P_r of 17 μC/cm^2 at applied field of 60 kV/cm. Crystals were found to possess d_{33} value of 80 pC/N at 2 Hz which was attributed to the nano size (<300 nm) domains.

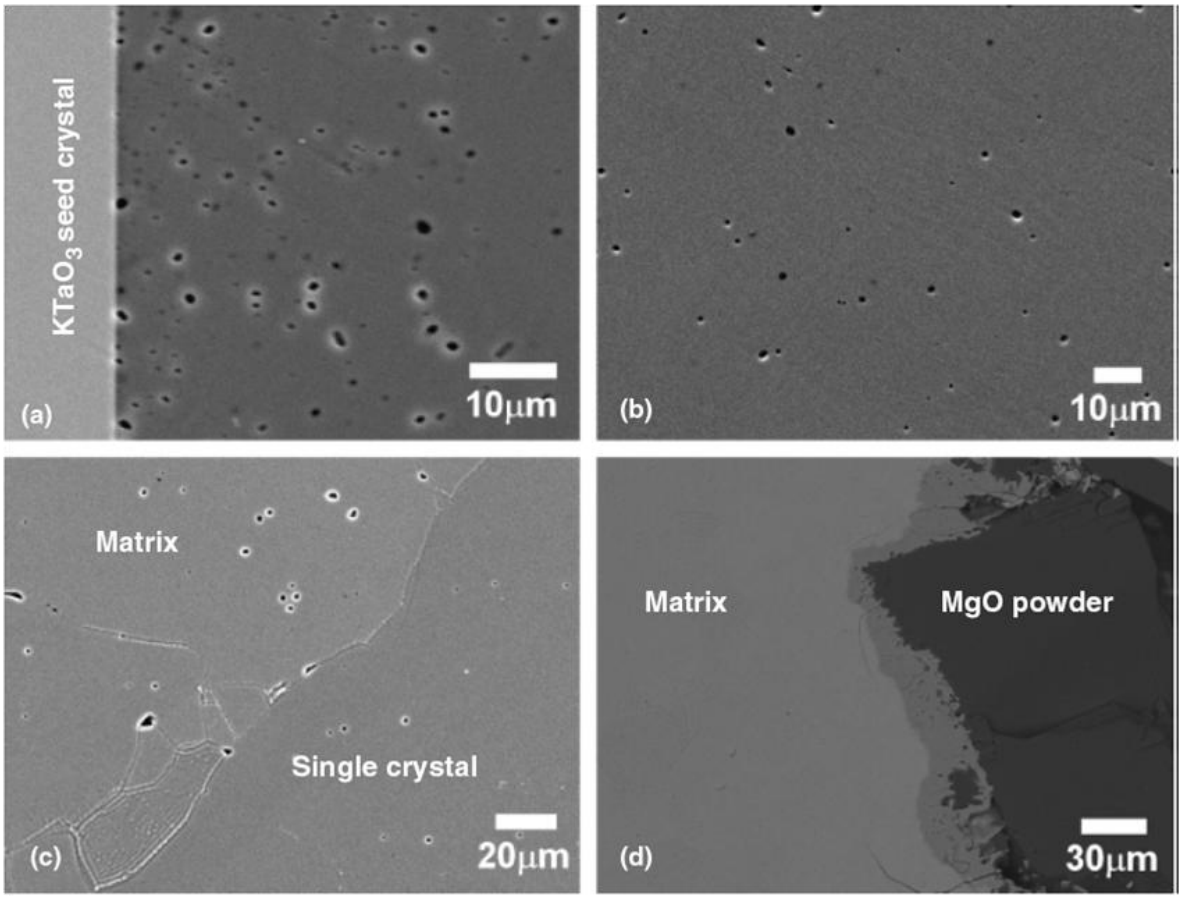

Figure 1.12 Scanning electron microscopy images of a single crystal of $(K_{0.5}Na_{0.5})NbO_3$ grown in a hot press using a two-stage treatment: 975°C-50 MPa for 2 h followed by 1100°C-50 MPa for 100h. (a) Secondary electron image of the seed crystal/single crystal boundary, (b) backscattered electron image of the single crystal, (c) secondary electron image of the single crystal/matrix boundary, and (d) backscattered electron image of the edge of the sample (Reprint from reference 91 © 2008 The American Ceramic Society).

Bencan et al.[93] investigated the chemical composition and the structure of KNN single crystals prepared by SSCG method. No compositional in-homogeneities, typically encountered in single crystals prepared by the conventional flux synthesis method were observed. According to XRD and TEM results, KNN single crystal had a monoclinic symmetry.[93] It can be seen in Figure 1.13, KNN single crystals grown by SSCG method were found to have large 90° domains with 100 millimeter thickness. These crystals were also found to have smaller 180° domains of thickness of few tens of nanometers.

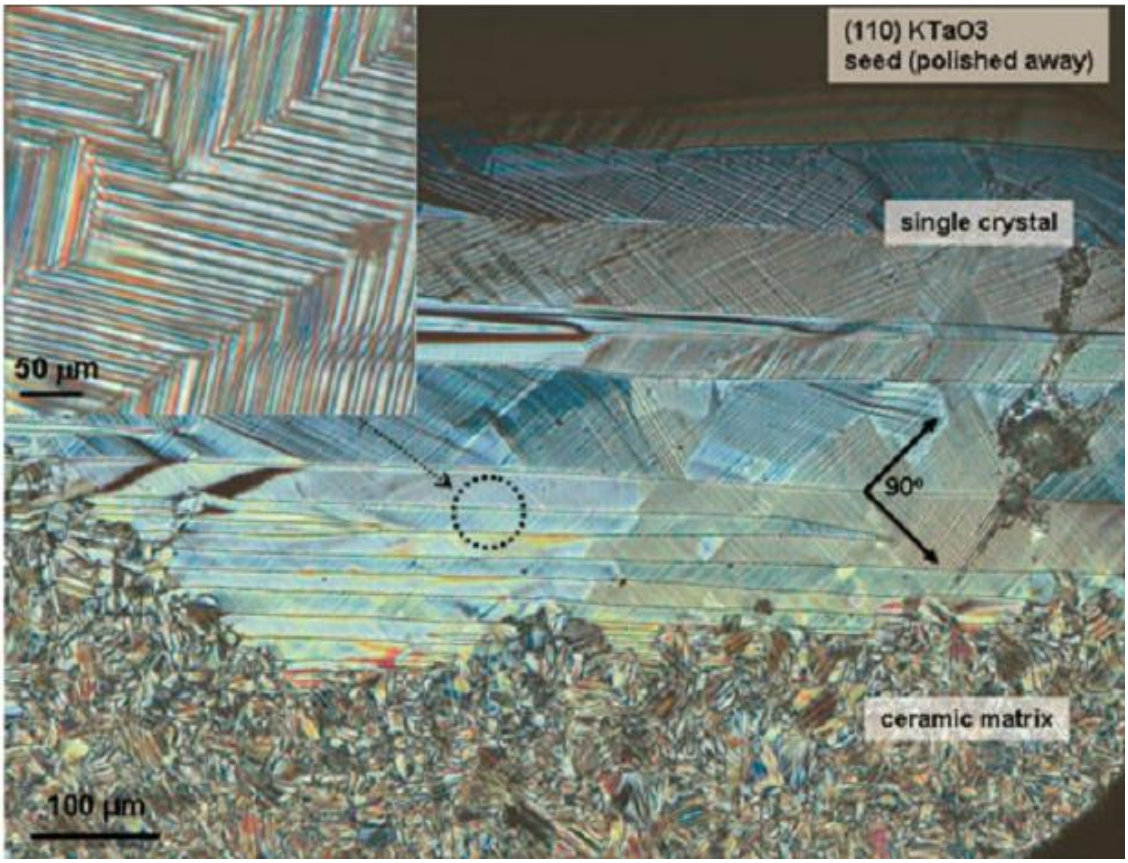

Figure 1.13 Optical micrograph showing the presence of 90° domains in KNN (x = 0.5) single crystal grown by SSCG method. Inset of the figure shows the larger view of area under circle (Reprint from reference 93 © 2009 Cambridge University Press).

Lin et al.[94] studied the domain structure of KNN crystals grown by Bridgman method using polarized light microscopy. At room temperature poled crystals were found to have the presence of 90^0 domains while un-poled crystals were found to exhibit 60^0, 90^0 and 120^0 domains. Temperature dependent study conducted on poled crystal was found to be consistent with the known transition temperatures of KNN. Domain structures of poled crystal at different temperatures are shown in Figure 1.14. A laminar domain structure having 90° boundaries oriented along $[100]_{pc}$ can be seen in orthorhombic phase field (Figures 1.14 (a) – (d)). At 213°C orthorhombic to tetragonal structure transformation was observed, which was at slightly higher temperature than one obtained by dielectric constant vs. temperature study. Above 213°C, 90° domains having extinction direction parallel to $[100]_{pc}$ were seen (Figures 1.14 (e) – (g)). With increasing temperature in tetragonal regime, domain structure started to appear complicated with the emergence of smaller domains. At 401°C cubic phase appeared, as illustrated by the total extinction in the area "A" in Figure 1.14 (g). In the temperature range of 401°C - 405°C, both tetragonal and cubic phases coexisted suggesting a diffuse phase transition.

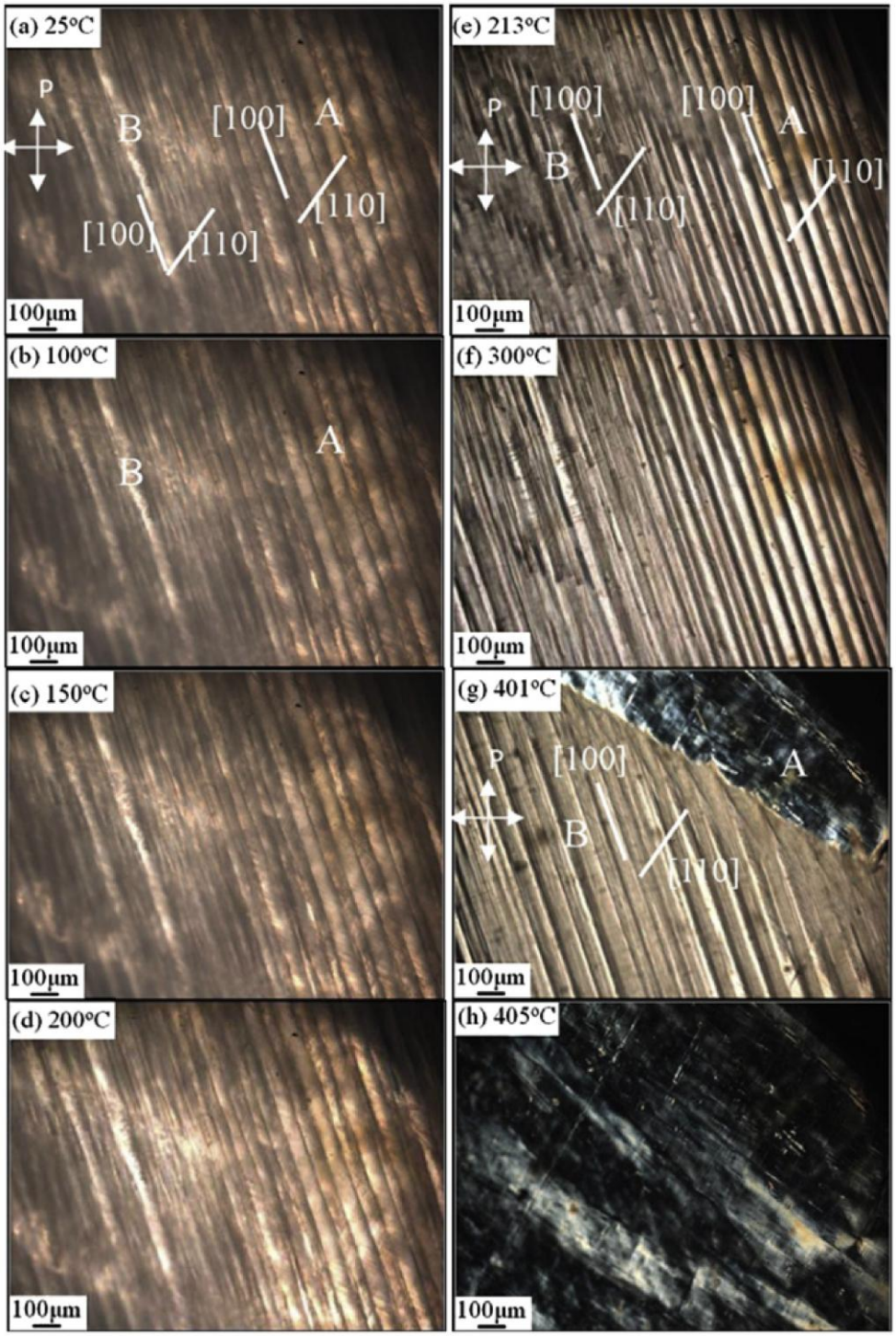

Figure 1.14 Domain structure of [001] oriented KNN single crystal of KNN at different temperatures. (a) 25°C, (b) 100°C, (c) 150°C, (d) 200°C, (e) 213°C, (f) 300°C, (g) 401°C, and (h) 405°C (Reprint from reference 94 © 2009 Elsevier).

Chapter 2

Research Objective

Lead-based perovskite compositions have dominated the application of piezoelectrics in last few decades owing to their excellent piezoelectric properties. Along with the interest from the application point of view, these materials have also been the focus of fundamental research where the goal has been to understand the role of domain size and structure, microstructure and crystal structure on superior piezoresponse of MPB compositions. All these prior studies have led to the advancement in the understanding of piezoelectrics.

Recently, there is increasing health concerns related to the use of lead-based piezoelectric materials in consumer devices. In the last decade, the focus of research has shifted towards replicating the properties of lead-based compositions in more environmental friendly lead-free perovskite compositions. Sodium potassium niobate ($K_xNa_{1-x}NbO_3$, abbreviated as KNN) is one of the leading candidates in this respect, though its properties are far inferior to that of the lead-based compositions. Compositions close to x = 0.5 are of greater interest because of superior piezoelectric and ferroelectric properties. Beside its environment friendly nature, high Curie temperature (420°C) and existence of a broad morphotropic phase boundary (MPB) at x = 0.5 makes it quite appealing for the device applications.

KNN has been known as a piezoelectric material for more than sixty years but little work has been done on providing the fundamental understanding that can be used to improve its performance. Processing of KNN in the form of polycrystalline ceramic, textured ceramic and single crystals has been difficult which limits the availability of high quality samples for

fundamental studies. In this thesis, emphasis was given towards developing the fundamental understanding of KNN system by correlating its domain morphology and crystal structure to the macroscopic piezoelectric properties. It is expected that the results reported in this thesis would not only help in explaining the underlying physics of KNN materials but also assist the development of new compositions and microstructure with superior properties. In this thesis, all three forms of KNN, namely polycrystalline ceramic, textured ceramic and single crystals were synthesized and investigated in order to make fundamental conclusions.

Single crystals are the most ideal form of a material to study due to the lack of boundaries and defects that can make the measurements and interpretation quite complex. High quality $K_xNa_{1-x}NbO_3$ single crystals with different compositions were grown by the flux method. Since ferroelectric and piezoelectric properties of a material depend upon its crystal structure (intrinsic contribution) and domain structure (extrinsic contribution), emphasis was given towards characterizing these two aspects. Along with the x = 0.5 composition, the compositions on either side of the boundary provide an opportunity to study the evolution of domain structure and crystallographic phase. To reveal the local crystallographic nature of KNN crystals across the MPB, pair distribution function (PDF) analysis was performed. The qualitative analysis of domain structure was performed by linear birefringence and piezoresponse force microscopy (PFM). Dynamic scaling analysis was conducted to understand the quantitative behavior of domains under the applied electric field. Optical birefringence was also used to reveal macroscopic crystallographic nature of KNN single crystals.

A modified sintering technique was developed to achieve > 99 % density for KNN ceramic with improved piezoelectric properties and excellent fatigue behavior. Texture controlled ceramics have been shown to be very effective in improving the properties of

piezoelectric compositions. Textured ceramics can provide electromechanical properties close to that found for the single crystals. They have the advantage of easier processing and flexibility of size and shape of samples. Switching spectroscopy (SS-PFM) was performed to reveal the difference in local switching behavior of textured and random KNN ceramic.

Chemical modifications in KNN have been attempted in order to tailor the specific coefficients. Lowering of polymorphic phase transition to room temperature has been a widely used technique to achieve high piezoelectric activity in KNN-based ceramics. In this thesis, compositions in the ternary system [xNBT – yBT – (1-x-y) KNN] were synthesized and it was found that some of these compositions had excellent stability of dielectric and piezoelectric behavior with temperature along with improved piezoelectric properties at room temperature.

An extension of the research was made by attempting to develop multiferroic ceramics. In order to achieve magnetoelectric behavior in alkali niobate based ceramics, paraelectric $NaNbO_3$ component of KNN was replaced by well known multiferroic material $BiFeO_3$. This modification lead to highly resistive $(Bi_{0.5}K_{0.5})(Nb_{0.5}Fe_{0.5})O_3$ composition having reasonable ferroelectric and magnetic behavior.

Chapter 3

Growth, Characterization and Dynamic Scaling Analysis of <100> oriented $K_{0.5}Na_{0.5}NbO_3$ Single Crystals

3.1 Growth of KNN single crystals by the flux method

Flux method is a solution growth technique for growing the single crystals. In this technique, the stoichiometric composition of ceramic is mixed with a salt having lower melting point. Good solubility of ceramic in the flux salt is desired for promoting the growth of large crystals. In the process, the mixture of salt along with ceramic powder is heated to the temperature being higher than melting point of salt but lower than that of ceramic. Holding this mixture at this temperature makes a homogeneous liquid – solid solution of two components. On cooling the solution from this temperature give rise to the decreases in solubility of liquid salt and results in nucleation of single crystals. With controlled rate of cooling, numbers of nucleation sites can be restricted and large size single crystals can be grown.

In this thesis, KNN ceramic were synthesized by conventional solid state synthesis route. High purity precursors (from Alfa Aesar) sodium and potassium carbonates along with niobium oxide (with purity > 99.5%) were ball milled in ethanol medium for 24h, prior to calcination at 850°C. Calcined powder of KNN ($K_{0.5}Na_{0.5}NbO_3$) was mixed with NaF and KF salts in the ratio of 10:3:2 and ball milled for 6 hours. After drying this solution was loaded in a platinum crucible, covered with a alumina plate and rapidly heated to 1080°C in a conventional box furnace. After holding the solution at 1080°C for 2h, it was allowed to cool down to room temperature by natural cooling rate. The gray colored cubical shaped crystals were found to grow uniformly in

the crucible. Figure 3.1 (a) shows the optical image of as grown gray color crystals in the re-solidified flux matrix. Figure 3.1 (b) shows one of the larger crystals.

(a) (b)

Figure 3.1 Optical images showing (a) as-grown KNN crystals in KF – NaF matrix, and (b) one of the large size crystal.

The maximum size of the crystals which could be achieved was about 6 x 6 x 2 mm^3. Figure 3.2 shows the X-ray diffraction analysis conducted on one of the higher surface area planes. Presence of split in the {100} and {200} family peaks confirmed the formation of perovskite phase. X-ray photoelectron spectroscopic (XPS) analysis done on one of the crystals indicated the composition to be close to $K_{0.49}Na_{0.51}NbO_3$.

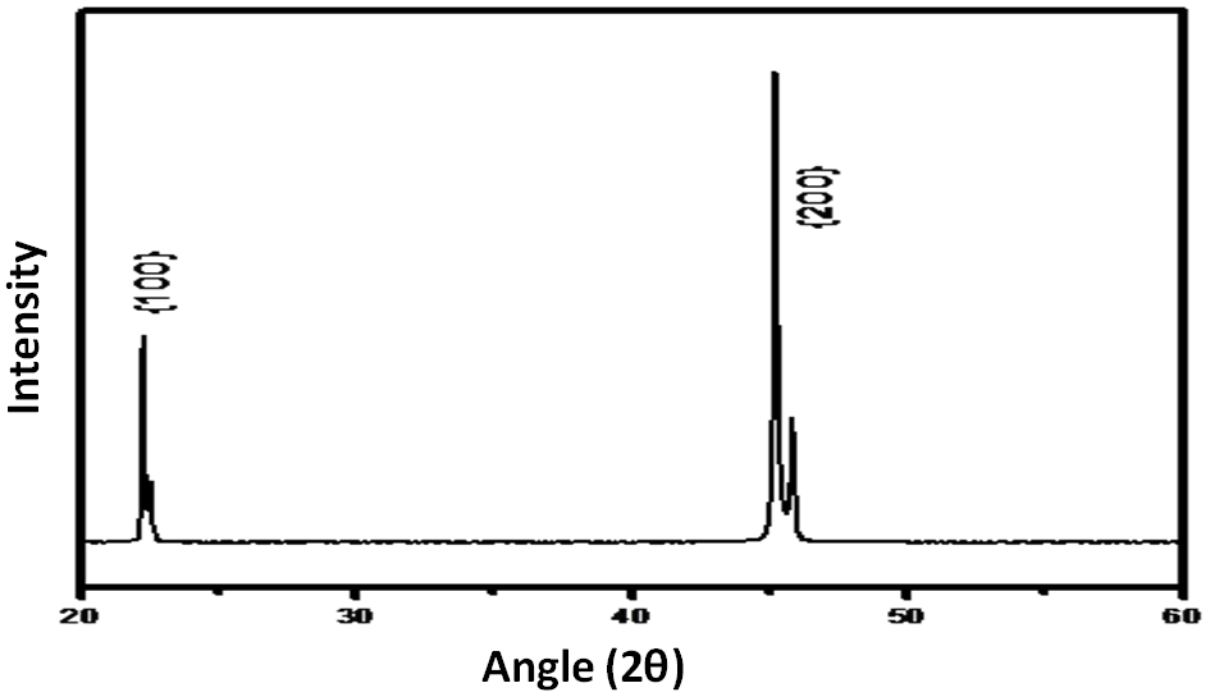

Figure 3.2 X-ray diffraction pattern obtained for one of the as-grown KNN crystal.

3.2 Crystal orientation, piezoelectric and dielectric characterization

Crystal-orientation analysis was conducted by electron backscattered diffraction analysis (EBSD) to confirm the crystallographic orientation of two opposite faces of these crystals. Figure 3.3 (a) and (b) shows the Kikuchi pattern obtained for one of the crystal faces along with indexing of bands. For this analysis, the known lattice parameters of $K_{0.5}Na_{0.5}NbO_3$ composition were used. Indexed Kikuchi pattern showed a high value of goodness of fit parameter and provided Euler's angle values to be (238°, 93°, and 181°). Corresponding crystallographic orientation of the crystal is shown in figure 3.3 (I) and confirms the pseudo cubic {100} orientation of crystal, being consistent with the conclusion of X-ray diffraction analysis. Similar values of Euler's angles were found for opposite faces of crystal suggesting that these two faces are parallel and exhibited {100} orientation.

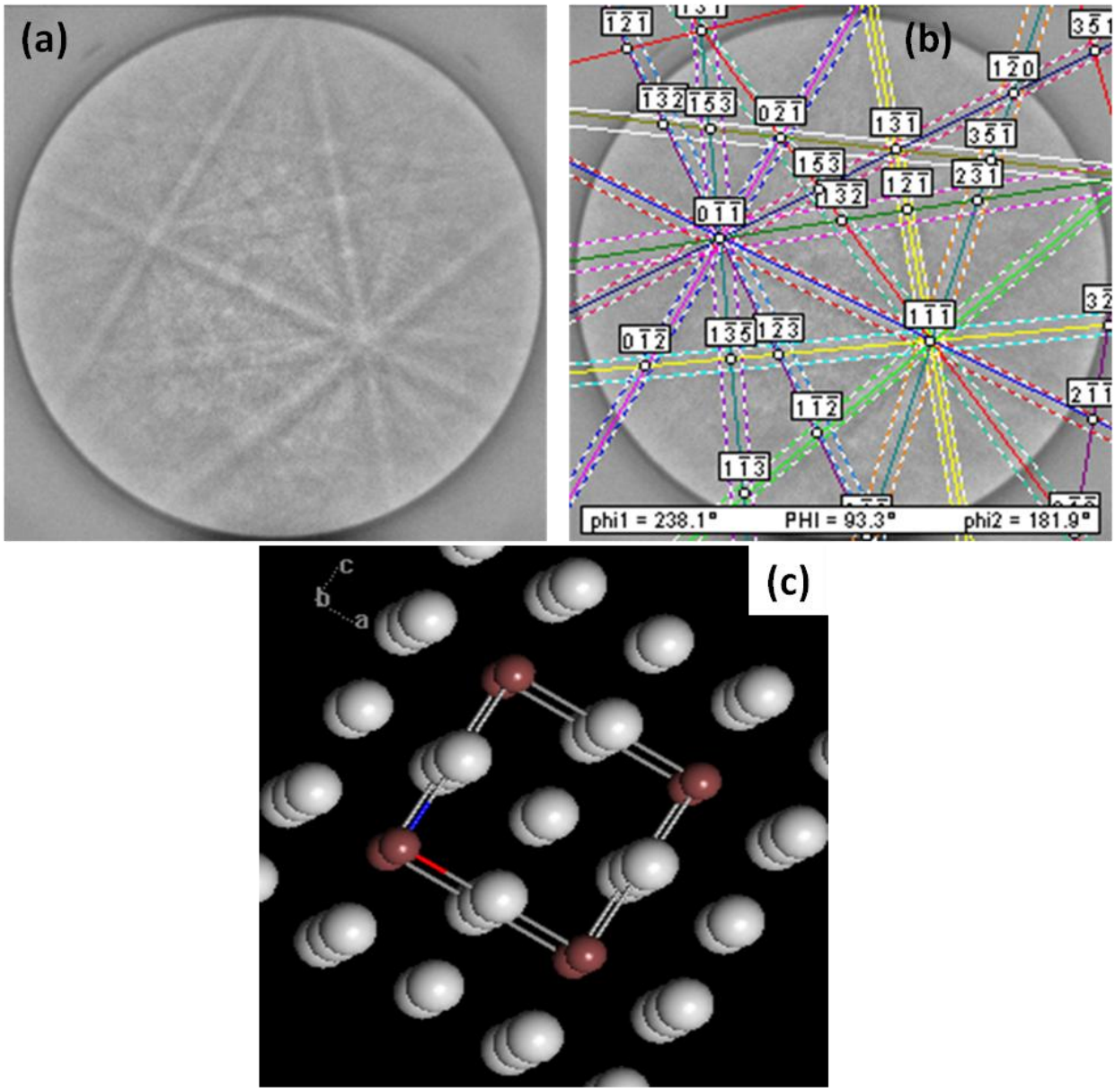

Figure 3.3 Orientation determination of KNN crystal (a) As obtained and (b) Indexed, electron backscattered diffraction patterns obtained on one of the faces of KNN crystal (I) corresponding crystallographic orientation of the crystal (Reprint from reference 95 © 2011 American Institute of Physics).

For electrical characterization, silver electrodes were fired at 650°I on the two opposite faces with higher area. As-grown crystals had high leakage and could neither be poled nor be

characterized for ferroelectric properties. This high leakage current was attributed to the presence of oxygen ion vacancies[89] in the lattice. Thus, the composition of as-grown crystals can be represented as $K_{0.5}Na_{0.5}NbO_{3-\delta}$. Gray color of the crystals also supported this argument which is generally associated with oxygen vacancies in perovskites.[89] The missing oxygen atoms give rise to $2e^-$ in the conduction band according to the Equation 3.1 and hence result in low resistivity.[96]

$$O^{--} \rightarrow V_o^{\bullet\bullet} + 2e^- \tag{3.1}$$

Annealing these crystals in air at 850°I helped in compensating the oxygen vacancies and the color was changed from gray to transparent. At 100 kHz, an annealed crystal was found to have ac resistivity value of 1.17 x 10^4 Ω.m in contrast to 1.32 x 10^2 Ω.m before annealing, confirming the improvement by two orders of magnitude. Activation energies calculated for these crystals were found to be 1.3 eV and 1.2 eV respectively, before and after annealing. These values lie in the range of reported values of activation energies for oxygen ion conduction in different perovskites.[97]

These highly resistive crystals were further characterized for their dielectric, ferroelectric and piezoelectric properties. Dielectric response vs. temperature plot shown in Figure 3.4 was used to determine the Curie temperature (T_c) and tetragonal to orthorhombic transition temperature (T_{o-t}) values, which were found to be 407°I and 200°I respectively. These values were in the expected range as reported previously.[91] At room temperature dielectric constant and loss values were found to be 226 and 0.08, being consistent with the inherent low permittivity of KNN.[9] For piezoelectric measurements the crystals were poled at 3 kV/mm at 130°C. Low-field piezoelectric coefficient (d_{33}) value was found to be 148 pc/N. Figure 3.6 shows the saturated ferroelectric hysteresis loops obtained on crystals. Well saturated loops confirmed the high resistive nature of these crystals. Remnant polarization (P_r) and coercive field (E_c) values were

found to be 18 μC/cm^2 and 22 kV/cm. Table 3.1 lists magnitude of the different parameters measured on KNN crystals.

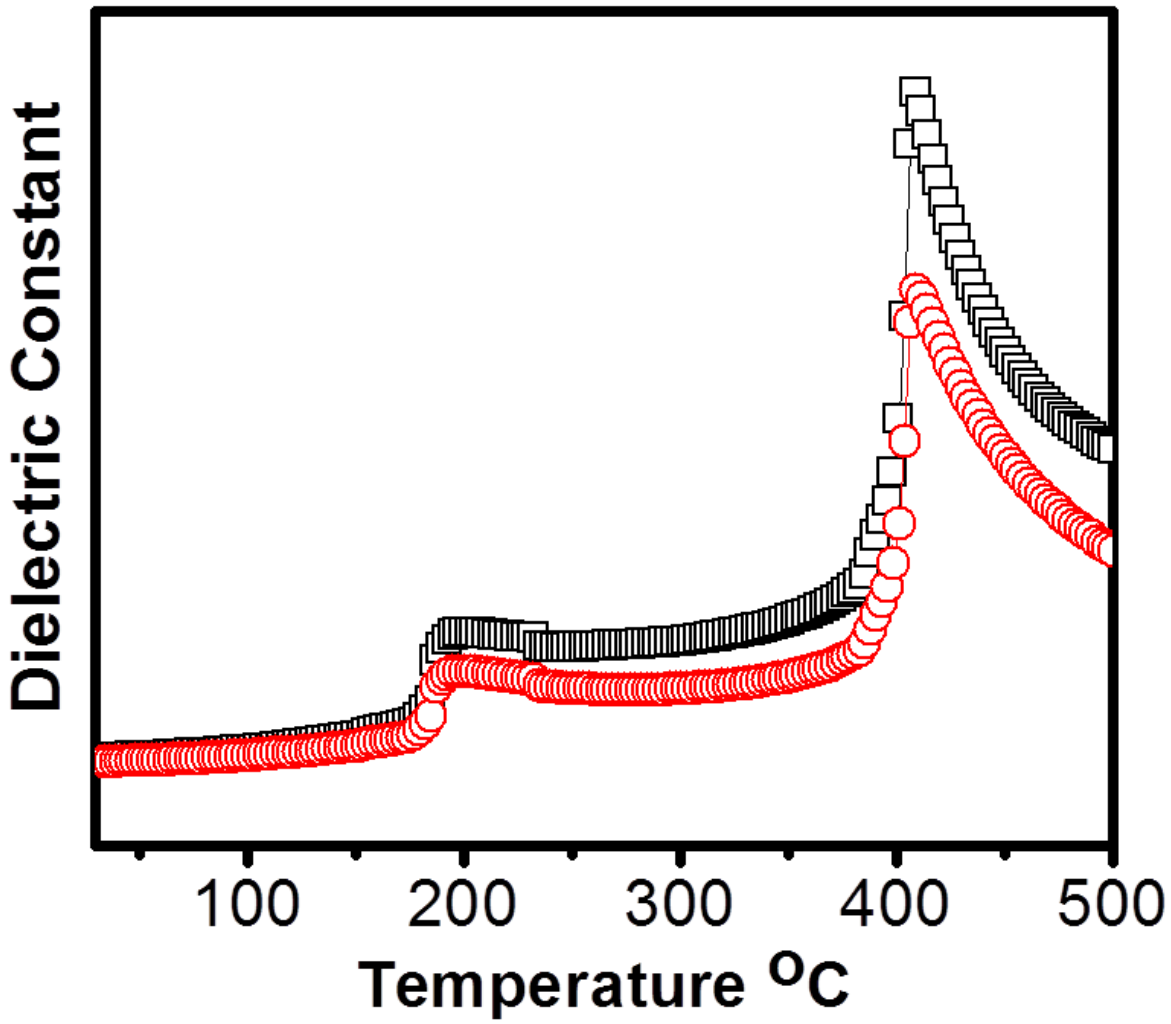

Figure 3.4 Variation of dielectric constant with temperature showing To-t and Tc to be 200°I and 407°I respectively.

Table 3.1 Ferroelectric, dielectric and piezoelectric properties of $K_{0.5}Na_{0.5}NbO_3$ single crystal

d_{33}	148 pC/N
Pr	18 μC/cm^2
E_c	20 – 22 kV/cm
K	226
tan δ	0.08
T_c	407°I
T_{o-t}	200°I

Landau – Devonshire theory was used to correlate the dielectric stiffness to the shape of ferroelectric loops. From Landau – Devonshire Theory (L-D)[98, 99], Gibbs free energy of a ferroelectric material given by Equation 3.2 can be differentiated with respect to polarization P to arrive at the expression for electric field (Equation 3.3):

$$G = \frac{1}{2}\alpha P^2 + \frac{1}{4}\beta P^4 + \frac{1}{6}\gamma P^6 - EP \tag{3.2}$$

$$E = \alpha P + \beta P^2 + \gamma\, P^4 \tag{3.3}$$

Neglecting the higher order terms this equation can be reduced to $E = \alpha P$, where:

$$\alpha = \frac{T_c - T_0}{2\,\epsilon_0\, C} \tag{3.4}$$

In this equation T_c and I are Curie temperature and Curie constant respectively. The Curie constant I can be calculated by plotting the dielectric susceptibility as a function of 1/ (T- T_c) according to the Equation $\chi = I / (T - T_c)$, $T > T_c$.

Figure 3.5 shows the plot of susceptibility χ vs. 1/ (T- T_c). The slope of the line gave the Curie constant magnitude of 4.2 x 10^4. Inset in the figure shows the variation of 1/Ɛ vs. T where extending the linear part of plot gave the magnitude of T_o to be 636K. Substituting these values in the expression for α (Equation 3.4) gave its value to be 5.5 X 10^7 m/F.

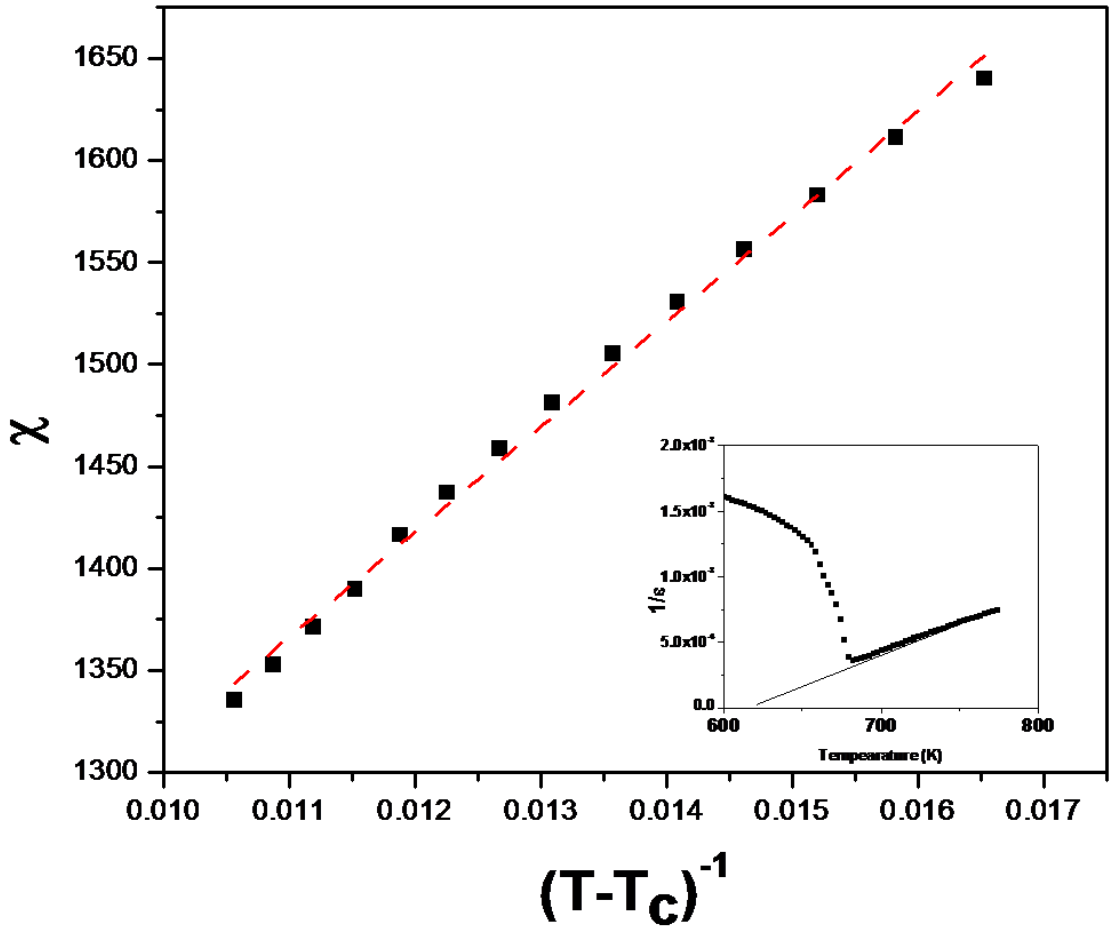

Figure 3.5 Variation of dielectric susceptibility with 1/ (T- T_c) at T > T_c gave the value of Curie constant to be 4.2 x 10^4. Inset of figure shows the 1/Ɛ vs. T plot (Reprint from reference 95 © 2011 American Institute of Physics).

According to the Landau – Khalatnikov simulation, which is a dynamic version of L – D theory, the parameter α is a measure of the effect on shape of ferroelectric loops and its higher

magnitude leads to square shaped ferroelectric loops.[100] The value of α obtained for KNN single crystals is on the higher side and explains the square shape of ferroelectric loops. [99, 100]

3.3 Dynamic ferroelectric Scaling

To reveal the dynamic response of domains to applied electric field, dynamic hysterics analysis based on $(\Phi^2)^2$ model was conducted on these crystals. Originally this technique was established for magnetic materials using Heisenberg model based on non-equilibrium statistical mechanical theory, but can be applied equally well to ferroelectrics as domain reversal dynamics have similarity in the two cases.[101 – 103] Dynamic hysteresis analysis relates the area under the ferroelectric loop <A> to the amplitude (E_0) and frequency *(f)* of applied electric field, according to power law relation given in Equation 3.5. [104, 105]

$$< A > \propto f^m E_o^n \tag{3.5}$$

In Equation 3.5, the parameters m and n are controlled by polarization switching mechanism in ferroelectrics. Theoretical calculations based on $(\Phi^2)^2$ model suggests the values of m and n to be -1 and 2 respectively at high frequencies and 1/3 and 2/3 at low frequencies.[101, 106] Experimentally it has been observed that the frequency (f_c) at which the equation $< A > \propto f^m E_o^n$ flips from one set of exponents to others, also depends upon the applied electric field and increases with increase in the applied electric field.[107] The exponent m in this relation refers to the switching time required by the domains at a given electric field. Its value is governed by the charged defect density and space charge density present in the sample and higher negative value means higher response time of domains. On the other hand, the exponent of electric field n is a measure of ability of domains to respond to the change in electric field

direction.[108] Higher value of n means sharper response of domains and hence higher value of polarization.[109]

Ferroelectric loops were obtained for electric fields varying from 10 kV/cm to 54 kV/cm, while frequency range covered during the measurement was 2 Hz – 200 Hz. Figure 3.6 (a) and (b) show the ferroelectric loops obtained at different f but fixed E_o (54 kV/cm) and different E_o but fixed frequency (f = 2 Hz). Similar loops were obtained for other possible combinations of E_o and f and the area under the loop (<A>) was calculated. Area under ferroelectric loops for different frequency and electric field values are given in appendix 1. Figure 3.7 (a) and (b) show the variation of hysteresis loop area with electric field (at different frequencies) and frequency (at different electric fields) respectively. From Figure 3.7 (a), the area of the curves obtained for E_o < 20 kV/cm decreases with increasing frequency, while for E_o > 20 kV/cm reverse trend was observed. On the other hand, Figure 3.7 (b) shows that over the whole frequency range the area under the loop <A> increases monotonically with applied electric field, though the rate of increase of <A> with E_o is higher for higher frequencies.

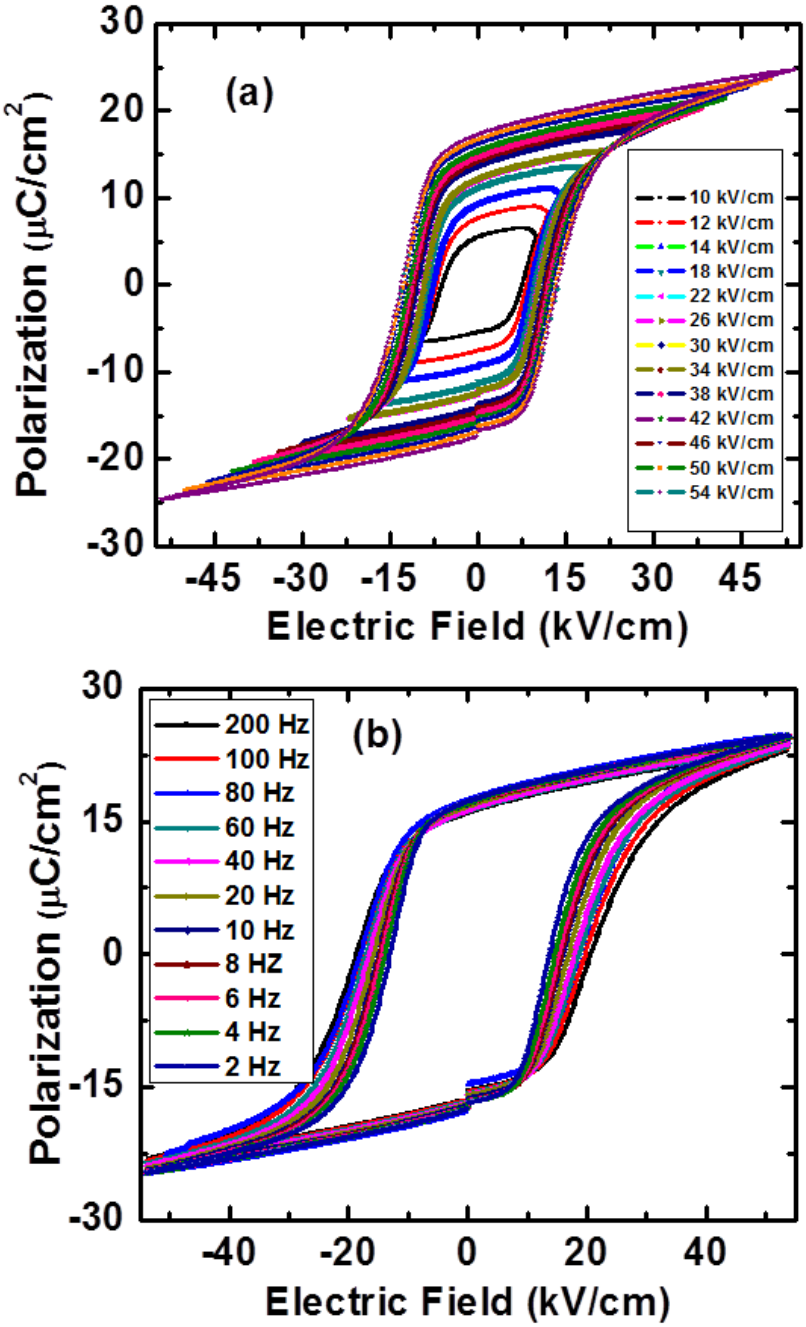

Figure 3.6 Hysteresis loops obtained for KNN single crystals (a) Varying electric fields at frequency of 2 Hz, and (b) Varying frequencies at applied field of 54 kV/cm (Reprint from reference 95 © 2011 American Institute of Physics).

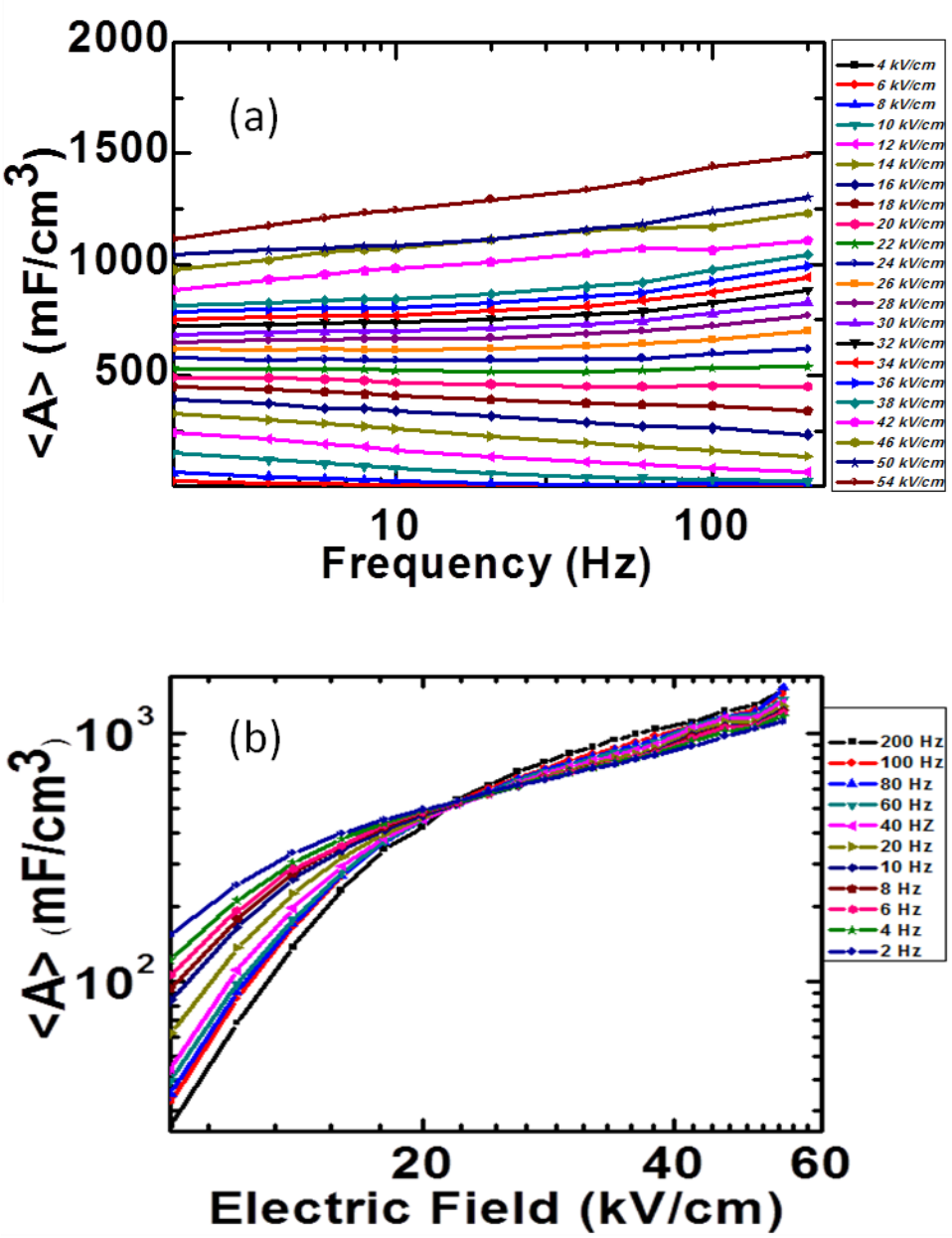

Figure 3.7 Variation of area <A> under ferroelectric loop (a) with frequency, at different E_o values, and (b) with electric field at different applied frequencies (Reprint from reference 95 © 2011 American Institute of Physics).

To obtain the value of m, i.e. the exponent expressing the variation of <A> with frequency, each of the plot in Figure 3.7 (a) was fitted to the equation $< A > \propto f^{m}$. Different values of m obtained

for different applied electric field are plotted in Figure 3.8(a). Clearly the plot can be divided into two parts, first with E_o < 20 kV/cm and other having E_o > 20 kV/cm. Except for the electric field range where two linear regions coincide (E_o ~ 20 kV/cm), fitting to the curves was excellent (R^2 > 0.97). Though generally the coercive field is frequency dependent, in our case where m vs. E_o plot is changing its slope, it can be considered as coercive field (E_c = 20 kV/cm). The two linear regions were further fitted to obtain the variation of m with applied electric field. It was found that for $E_o < E_c$, $m = 0.47E_o - 0.85$ (R^2 > 0.97) and field independent values of m was 0.04 (R^2 > 0.90) for $E_o > E_c$. Similarly, <A> vs. electric field curves in Figure 3.7 (b) were fitted for different frequencies to obtain the value of n according to the relation $< A > \propto E_o^n$. Again the data in Figure 3.8 (b) can be partitioned in two parts, one for $E_o < E_c$ and other having $E_o > E_c$.

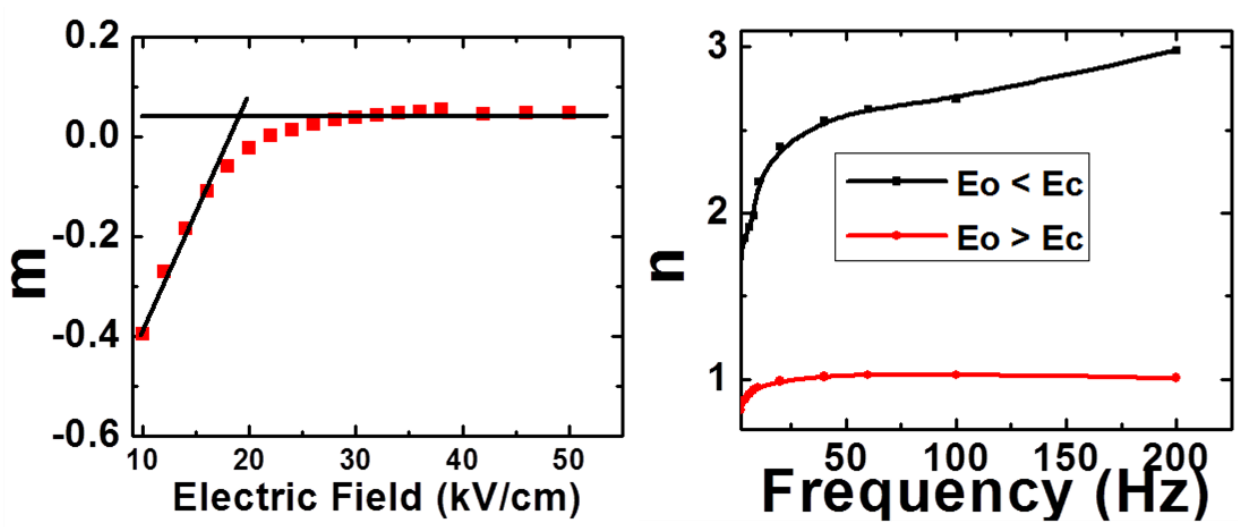

(a) (b)

Figure 3.8 Variations in the values of exponent (a) m with electric field and (b) n with frequency (Reprint from reference 95 © 2011 American Institute of Physics).

Values of m and n obtained by fitting the curves for different frequencies (R^2 > 0.97) are shown in the Figure 3.8 (a) and (b) respectively. These curves were further fitted to obtain the frequency dependence of exponent n. For $E_o < E_c$, $n = 1.45*f^{0.14}$ ($R^2 > 0.99$) and for $E_o > E_c$, $n = 1 - 0.25*\exp(-0.13f)$ ($R^2 > 0.98$). This value of n is complex but it can be seen that at f > 10 Hz it is almost constant and equal to 1.

Hence, the power law relations for $E_o < E_c$ and $E_o > E_c$ can be expressed by Equation (3.6) as:

$$< A > \propto f^{0.47E_o - 0.85} E_o^{1.45 f^{0.14}} \qquad E_o < E_c$$

$$< A > \propto f^{0.04} E_o \qquad E_o > E_c \qquad (3.6)$$

It can be clearly seen from these equations that the values of m and n are pretty complex for $E_o < E_c$ and do not match with theoretically predicted values by $(\Phi^2)^2$ and $(\Phi^2)^3$ models.[101, 106] Also the scaling behavior of minor loops is completely different from saturated loops. This kind of behavior is related to the variation in response of domains below and above coercive field.

The domains responding below the average coercive field of crystals are small in size and known as reversible domains.[103] On the other hand the irreversible domains are comparatively larger and respond at fields higher than E_c. In the case of relaxors, the non-linear hysteretic response below the coercive field is well-known phenomenon. Unpoled relaxor is a glassy state, however polarization irregularities are known to exist within a poled condition in the vicinity of randomly-quenched defects. Analogous to a random-field magnetic state, under applied field, clusters or diffuse domain walls can be nucleated in the vicinity of defects. According to this micro-heterogeneity or random-field model, poled single crystals is not simple single domain state, but rather may have many irregular small polar regions within single domain

conditions which respond to the field below coercivity. We anticipate a multi-polar state exists in the KNN crystal under the applied field due to the polymorphic transition from orthorhombic to tetragonal symmetry. For minor loops, electric field dependence of exponent m is similar to that observed for conventional ferroelectric such as $BaTiO_3$ single crystals.[105] The value of exponent n remains greater than 2 for most of the frequency range suggesting ease of domains in responding to changes in applied electric field direction. These values for m and n imply that for minor loops, <A> decay more slowly with f and increases much faster with E_o, as compared to theoretical predictions for magnetic materials.[101] This observation can be attributed to the fact that reversible domains responding to $E_o < E_C$, are kinetically easier to switch and hence less sensitive to frequency and more sensitive to field.[103] In case of $E_o > E_c$, m is almost independent of electric field with value close to zero. Hence the area of saturated loops is independent of frequency of applied field. The value of exponent n, which is constant at 1 for f > 8 Hz, is lower than theoretically predicted value of 2. Since the value of exponent n is the measure of ability of domains in following the electric field direction, lower value indicates poor ability of irreversible domains in this respect.[109] As a consequence, the lower value of n leads to lower hysteresis area as well as lower value of remnant polarization.[104] Also the near linear dependence of <A> to electric field also suggests occurrence of concurrent nucleation and domain boundary motion, phenomena very well known in $KNbO_3$ and $BaTiO_3$.[110] Linear electric field dependence of parameter m at sub-coercive fields and simultaneous nucleation of irreversible domain with domain boundary motion show KNN resembles the $BaTiO_3$ in polymorphism and dynamic scaling.

In summary, KNN single crystals were grown by flux method. Cubical shaped crystals were found to have (100) orientation on their two opposite faces. As-grown crystals

were annealed to improve the resistivity. Ferroelectric and piezoelectric characterization revealed the P_r and d_{33} values to be 18 μC/cm^2 and 148 pC/N respectively. Curie constant and second order parameter in Gibbs free energy expression were calculated to be 4.2 x 10^5 K and 5.5 x 10^7 m/F. Dynamic scaling analysis provided relationships of the form: $< A > \propto f^{0.47E_o - 0.85} E_o^{1.45 f^{0.14}}$ and $< A > \propto f^{0.04} E_o$ for $E_o < E_c$ and $E_o > E_c$ respectively. Poor ferroelectric nature of these crystals can be attributed to lower value of exponent n for saturated loops.

Chapter 4

Optical crystallographic Study of $K_xNa_{1-x}NbO_3$ (x = 0.4, 0.5 & 0.6) Single Crystals using Linear Birefringence

4.1 Introduction

High piezoelectric activity of MPB compositions in different distorted perovskite solid solutions is widely attributed to the simultaneous coexistence of two crystallographic phases which allow higher degree of freedom for the polarization vector to rotate towards the electric field direction. In the case of lead-based composition PZT, the discovery of the presence of a bridging monoclinic phase of Cm symmetry at the MPB between tetragonal (T) and rhombohedral (R) phases has gained a significant attention. It is believed that the intermediate monoclinic phases near the MPB allow the polarization vector to rotate in a plane, rather than having orientations fixed in R and T symmetries, imparting enhanced piezoelectric properties.[111, 112] Similar to PZT, bridging monoclinic phases close to the MPB have also been reported for PMN-PT single crystals.[113, 114] These findings have led to a reconsideration of the stable crystallographic structures at morphotropic and polymorphic phase boundaries (MPBs and PPBs) in different perovskite solid solutions.[114, 115] Recently, NBT crystals have also been reported to exhibit lower symmetry phase at a R → T transition at elevated temperatures.[116]

Figure 4.1 illustrates the schematic of a phase diagram of KNN for compositions close to x = 0.5. All prior studies broadly agree on the position of the different phase boundaries, although the crystallographic nature of the KNN compositions on either side of x = 0.5 have been a point of debate.

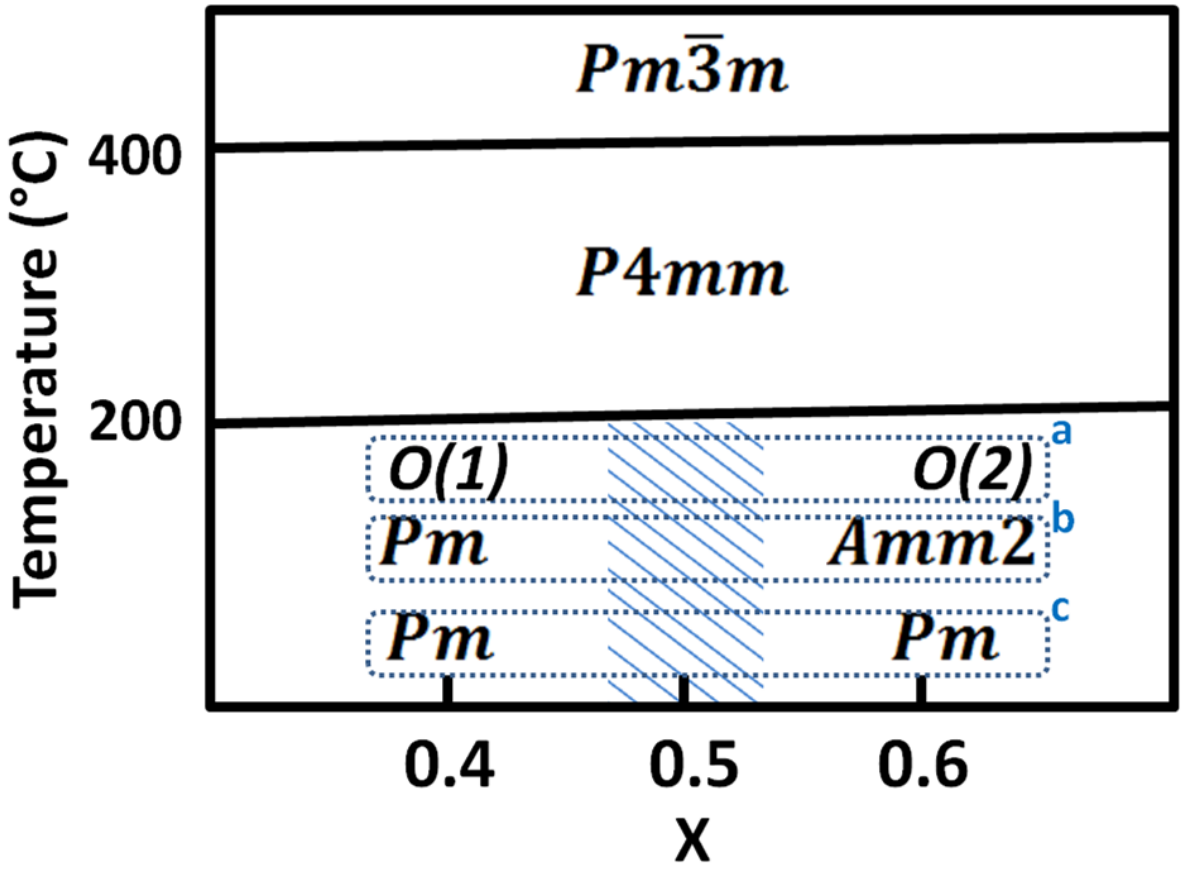

Figure 4.1 Schematic of phase diagram of KNN close to x = 0.5. a – Reference 1, b – Reference 14, c – Reference 16

According to the phase diagram provided in the classic textbook by Jaffe et al., the phase boundary at x = 0.5 separates two distinct orthorhombic (O) phases that exist at the K-rich and deficient sides.[4] Later, a number of investigations alternatively suggested the presence of a MPB at x = 0.5 separating potassium-deficient monoclinic *Pm* phase from a potassium-rich orthorhombic *Amm2* phase at room temperature.[14-16, 117, 118] Both of these phases existing at room temperature were found to lack oxygen octahedral tilts, which have been designated as $a^0b^0c^0$ in Glazer notation.[14, 17] On the contrary, in another investigation performed by fixing the space group to be *Pm* for 0.4 < x < 0.6, the refinement of lattice parameters illustrated no abrupt

changes on approaching x = 0.5, suggesting the presence of monoclinic phases on both side of this composition. Another study focusing on microstructure variation of KNN ceramic with composition, suggested that high piezoresponse near x = 0.5 could be due to favorable microstructure, rather than the presence of MPB.[11] Though, all previous studies of KNN solid solution agree that a nearly composition independent polymorphic phase boundary (PPB) exists near 200°C, above which KNN (x > 0.25) undergoes a transition to a tetragonal phase.[4, 12, 14-16, 117, 118] This high temperature T structure belongs to the *P4mm* space group and lacks oxygen octahedral tilts ($a^0b^0c^0$) similar to room temperature M and O phases.[14] At 400°C, a ferroelectric (FE) → paraelectric (PE) transition occurs and the new structure belongs to the cubic $Pm\bar{3}m$ space group.[16] These prior crystallographic investigations for compositions close to x = 0.5 have focused on determining the pseudo-cubic sub-cell lattice parameters by Rietveld refinement of x-ray and neutron diffraction data taken from polycrystalline powders.[4, 14-16, 117, 118] In such scenarios, distinguishing monoclinic symmetry ($a_p \neq c_p$, $\beta > 90$) from an orthorhombic one ($a_p = c_p$, $\beta > 90$) becomes difficult if two of the lattice parameters have close values, potentially resulting in discrepancies between investigations. To overcome this limitation of powder diffraction crystallography, and broaden our understanding of the nature of the crystallographic transformation at x = 0.5, and of the PPB (200°C) in KNN, we present a study focused on the optical birefringence crystallography of KNN (x = 0.4, 0.5 and 0.6) single crystals in the temperature range of 30°C – 600°C. Unlike Rietveld refinement of polycrystalline diffraction data, this technique can reveal the macroscopic symmetry irrespective of their lattice parameters. Optical birefringence also provides an opportunity to visualize large area domain structures, which along with macroscopic symmetry, can be used to construct an understanding of the structure – property relationship.[119]

4.2 Optical Crystallography

When plane polarized light is allowed to pass through an optically transparent medium, the refractive index of the medium is anisotropic, where the surface of rotation can be represented by an ellipsoid known as the optical indicatrix (Figure 4.2 (a)).[120, 121] This optical indicatrix, given in equation 4.1, is a single valued surface representing the mutual relationship amongst three mutually perpendicular principle refractive indices n_1, n_2 and n_3 along the principle axes Z_1, Z_2 and Z_3. The shape of the optical indicatrix (mutual relationship amongst three principle refractive indices) as well as its orientation with respect to the crystallographic axes depends on the symmetry of the crystal, and thus the phenomenon can be used as an effective tool for optical crystallography.[121]

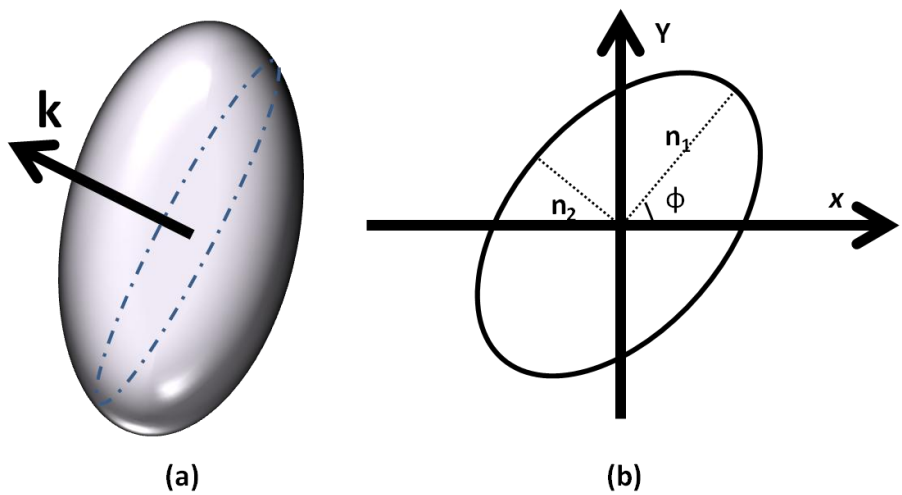

Figure 4.2 Optical indicatrix (a) for an anisotropic crystal, with vector k showing the direction of propagation of light (b) Ellipse representing the variation of refractive index of light propagating along k for different orientations of polarization vectors

The optical indicatrix itself has an *mmm* intrinsic symmetry with three mutually perpendicular mirror planes lying normal to thee principle axes Z_1, Z_2 and Z_3 respectively. According to Neumann's principle, the symmetry of a physical property should be contained in the symmetry elements of the crystal.[121] Orthorhombic crystals have three mutually perpendicular principle axes that coincide with the crystallographic axes [100], [010] and [001] respectively; whereas, monoclinic ones have a principle axes that is parallel to a two-fold axis along a unique b-axis. Triclinic crystals conversely have no fixed orientation of the indicatrix with respect to the crystallographic axes. For rhombohedral, hexagonal and tetragonal crystals (having symmetries higher than mmm), the shape of the optical indicatrix is altered to contain extra symmetry elements, and hence a more symmetric ellipsoid having two principle refractive indices values that are equal (i.e. $n_1 = n_2 \neq n_3$). In the case of tetragonal, rhombohedral and hexagonal crystals, n_3 has a unique value along the principle axis. This principle axis is collinear with 4-fold, 3-fold and 6-fold axes of rotations in these crystal systems. For cubic crystals, all the three principle values of the refractive index are equal ($n_1 = n_2 = n_3$), and the optical indicatrix surface reduces to a sphere. In the present investigation, when the direction of propagation of the polarized light (k) was fixed with respect to the single crystal and only the polarization vector of the wave was allowed to rotate, the optical indicatrix was reduced to an ellipse as shown in Figure 4.2 (b). Geometrically, this ellipse is the cross-sectional view of the optical indicatrix along the k and passing through the origin (Figure 2(a)). The difference between the refractive indices for two mutually perpendicular (slowest n_1 and fastest n_2) axes is defined as the optical birefringence, as given in equation 4.2. The angle φ in Figure 2(b) gives the inclination of the slow axis with respect to some arbitrary frame of reference. However, for an optically isotropic

material like glass, refractive index of light ray become equal for all directions of polarization vector and elliptical shape is reduced to a circle.[122]

$$\frac{Z_1}{n_1^2} + \frac{Z_2}{n_2^2} + \frac{Z_3}{n_3^2} = 1 \tag{4.1}$$

$$\Delta n = n_1 - n_2 \tag{4.2}$$

Non-cubic polar single crystals such as KNN or PZT always consist of a multi-domain state. Due to the symmetry of the crystal, these domains are constrained to have only few symmetry equivalent orientations with respect to each other. Figure 4.3 shows the allowed mutual orientations of crystallographic domains with respect to pseudo-cubic unit cell for T, R, O, M_A/M_B and M_C symmetries respectively. Since in this study the domains are on the $(100)_{pc}$ plane, only projections of these domains on the this plane can be seen, which are also depicted along with polarization vectors in pseudo-cubic cell. As we move towards the lower symmetry structures, the number of these allowed domain orientations are increased. In the case of optical studies of these different crystal structures, the misorientation between two domains results in a change of the orientation of the optical indicatrix by the same angle, and hence the nature of domain wall between them can be revealed. Considering Figure 4.3 (a) as an example, it can be seen for tetragonal crystals, that the domains can be oriented along only $[100]_{pc}$ while making an angle of 90° with respect to each other. Similarly by following Figures 4.3 (b) – (e), the allowed orientations of the different domains for the lower symmetry structures can be determined as well.

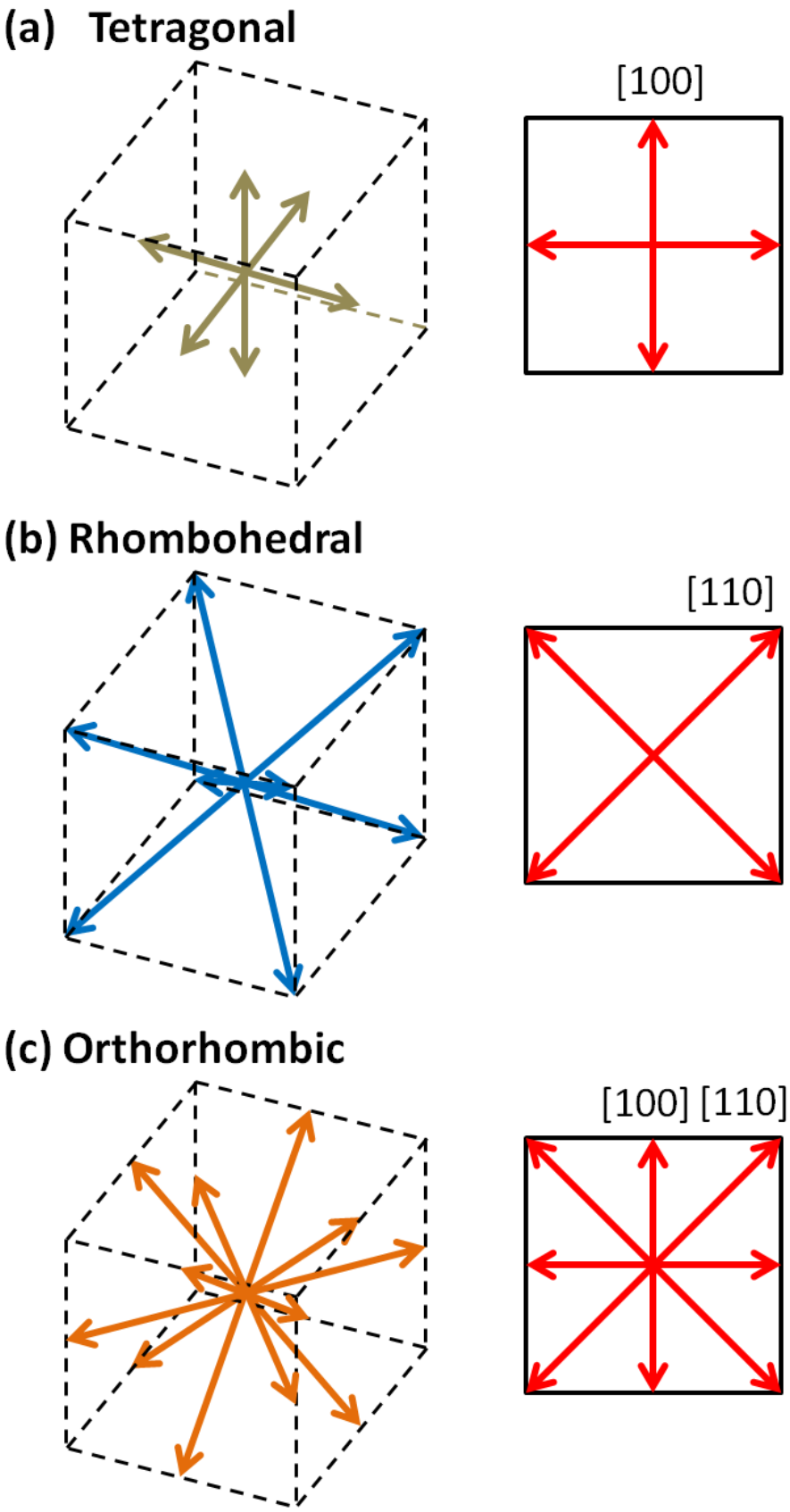
(a) Tetragonal
[100]
(b) Rhombohedral
[110]
(c) Orthorhombic
[100] [110]

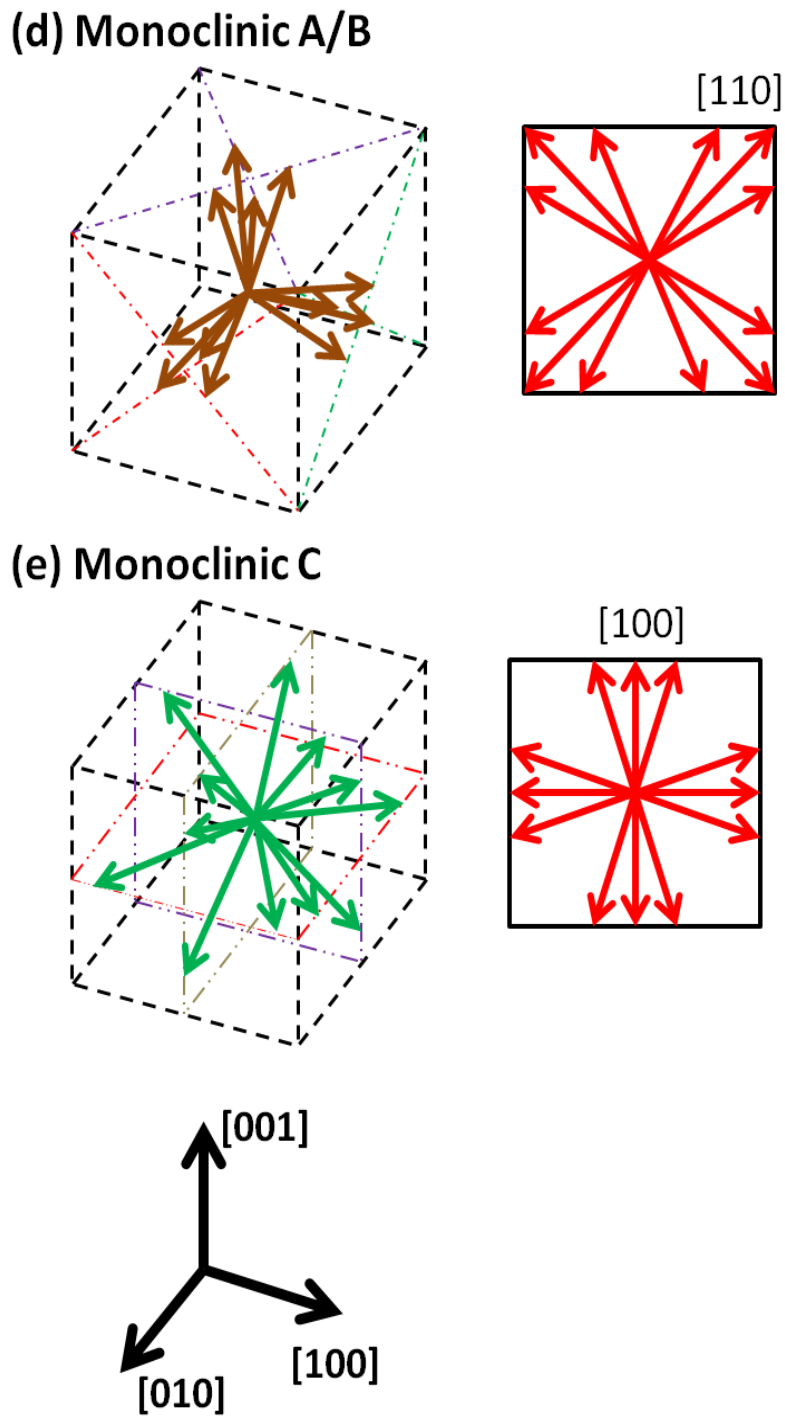

Figure 4.3 Schematics representing the possible orientations of polarization vectors for (a) tetragonal (b) rhombohedral (c) Orthorhombic (d) monoclinic M_A/M_B (e) monoclinic M_C symmetries in terms of pseudo cubic unit cells and their projections on $(100)_{pc}$ planes.

4.3 Birefringence Measurements

Figure 4.4 shows the schematic diagram of Metripol birefringence imaging system used for this study.[116, 122] Detailed descriptions and working principles of the Metripol Birefringence measurement system that was used in this study can be found in previous literatures.[123, 124] This instrument is based upon a rotating polarizer technique and consists of a monochromatic light source of wavelength 550 nm followed by a polarizer and sample stage. Elliptically polarized light passing through the sample goes into a circular analyzer having a λ/4 plate and a linear polarizer. The optical signal is then incident on a CCD detector that converts it to a proportional electric signal. The sample stage has a heating oven (LINKAM TP93) applicable over a temperature range of 25 °C to 600°C with an accuracy of 0.1°C. This instrument provides an opportunity to study the phase transformation behavior of ferroelectric crystals via the evolution of linear birefringence and domain structure changes with temperature.

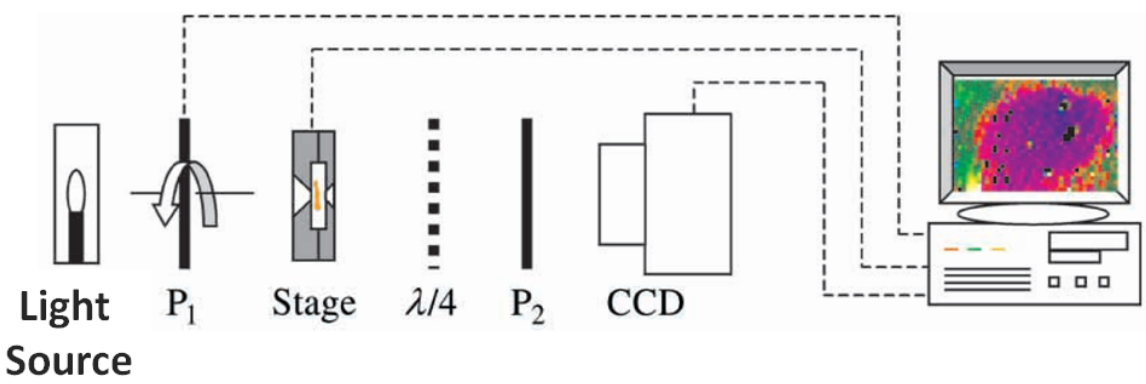

Figure 4.4 Schematic diagram of Metripol birefringence imaging system. In this figure P_1 represents the polarized, while P_2 along with λ/4 plate work as a analyser (Reprint from reference 122 © 2000 International Union of Crystallography).

The intensity of the transmitted polarized light at each point (pixel) of the CCD detector can be determined by Equation 4.3.[124] In this equation I_o and φ are the transmittance of the sample and the angle between the minor axis of the indicatrix with an arbitrary coordination axis, respectively, δ is the phase difference introduced by the crystal to the transmitted light ray, and is related to the birefringence Δn according to equation (4.4), and L is the thickness of the crystal and λ is the wavelength of light used.

$$I = I_o/2[1 + Sin(2\alpha - 2\varphi)Sin\delta] \quad (4.3)$$

$$\delta = 2\pi L\Delta n/\lambda \quad (4.4)$$

To determine the values of all three components I_o, |Sinδ| and φ in equation (4.3), the intensity of the transmitted light is measured for different values of the rotation angle α which the polarizer makes from a fixed reference. Data is collected in the form of three false color images for transmittance (I_o), |Sinδ| and φ for each corresponding point (pixel) of the single crystal.

4.4 Crystal Growth and Orientation Determination

In order to reveal the crystallographic transformation across the boundary at x = 0.5, three compositions of $K_xNa_{1-x}NbO_3$ crystals (x = 0.4, 0.5 and 0.6) were chosen for this study. Crystal growth technique is similar to one described in chapter 3. These crystals were annealed in air at 1000°C for compositional homogenization, followed by compositional verification by energy dispersive X-ray (EDX) analysis. EDX was performed on different portions of the same crystals to confirm compositional homogeneity. Figure 4.5 shows the atomic mole % of Na and K ions in the crystals of three batches (x = 0.4, 0.5 and 0.6). For optical birefringence study,

crystals with higher transparency were chosen from each batch of x = 0.4, 0.5 and 0.6 respectively.

Similar to findings for x = 0.5 crystals described in chapter 3, electron backscattered diffraction (EBSD)[95] showed that these cubic shaped crystals had $\{100\}_{pc}$ facets, while detailed X-ray diffraction analysis (XRD) confirmed the large faces of these crystals to be $(001)_{pc}$. For optical birefringence studies, these crystals were polished to thicknesses of about 100 μm. After polishing, the crystals were annealed at 600°C to relieve any residual stress induced by polishing before birefringence data collection. Since the cooling rate through a phase transition range may affect the domain morphology, the crystals were cooled using the same rate of 1°/min. Birefringence data was collected over the temperature range of 30°C - 600°C on heating. During data collection, the heating rate was fixed at 1°/min and data was collected at 1°C step interval.

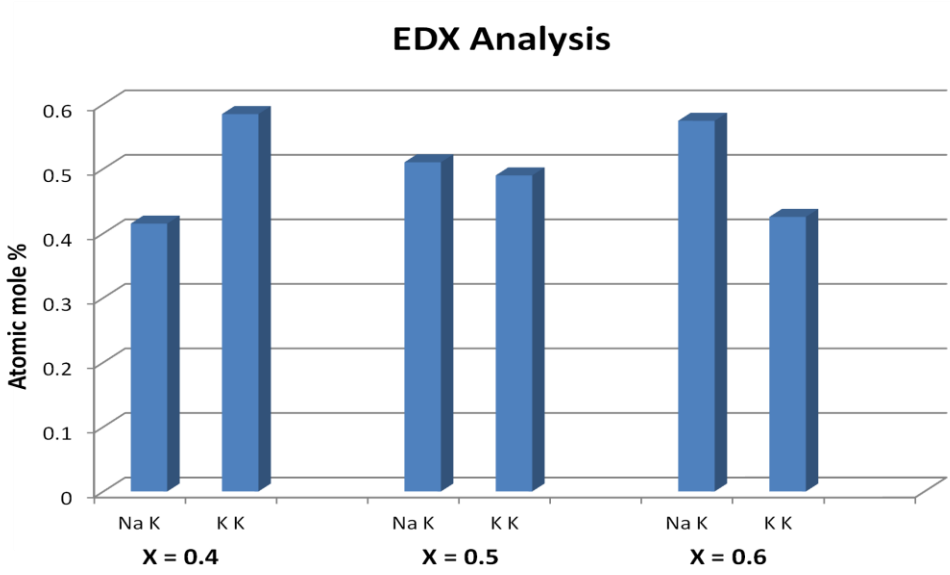

Figure 4.5 Energy dispersive X-ray (EDX) analysis performed on crystals intended to have composition x = 0.4, 0.5 and 0.6.

4.5 Results and Discussion

Figure 4.6 (a) illustrates the variation of low field longitudinal piezoelectric coefficient (d_{33}) and remanent polarization (P_r) across the phase boundary at x = 0.5. Similar to the findings for polycrystalline ceramic, maxima in the values of two parameters for single crystals suggest that superior piezoelectric and ferroelectric properties in ceramic close to x = 0.5 could not be attributed only to the difference in microstructure. Figure 4.6 (b) shows dielectric constant as a function of temperature for x = 0.4, 0.5 and 0.6 taken along the $(100)_{pc}$ axis in the temperature range 30°C – 500°C. For all compositions, two dielectric anomalies were evident near 200°C and 400°C, indicating the presence of three distinct phase fields over this temperature range. Previous studies suggested the existence of monoclinic or orthorhombic structures for these compositions from room temperature to 200°C, whereas a tetragonal structure was reported between 200°C – 400°C. On heating above 400°C, a transformation to a paraelectric cubic structure occurs. Figures 4.7, 4.8 and 4.9 respectively show orientation (φ) false color images from an area of about 2.5 mm X 1.9 mm for x = 0.4, 0.6 and 0.5 at different temperatures over the range 30°C – 380°C. In accordance with the dielectric data above in Figure 4.6, particular temperatures were chosen to capture the optical crystallographic state just below and above each phase transition. These images were used to obtain the orientation (φ) histograms for three compositions at different temperatures as shown in respectively in Figures 4.10, 4.11 and 4.12. Each of these images consisted of about 1.39 million (1360 X 1024) pixels, each representing a value of φ between 0° – 180°. Detailed description of procedure used to determine orientation histograms along with distributions of φ for three crystals is given in appendix 2.

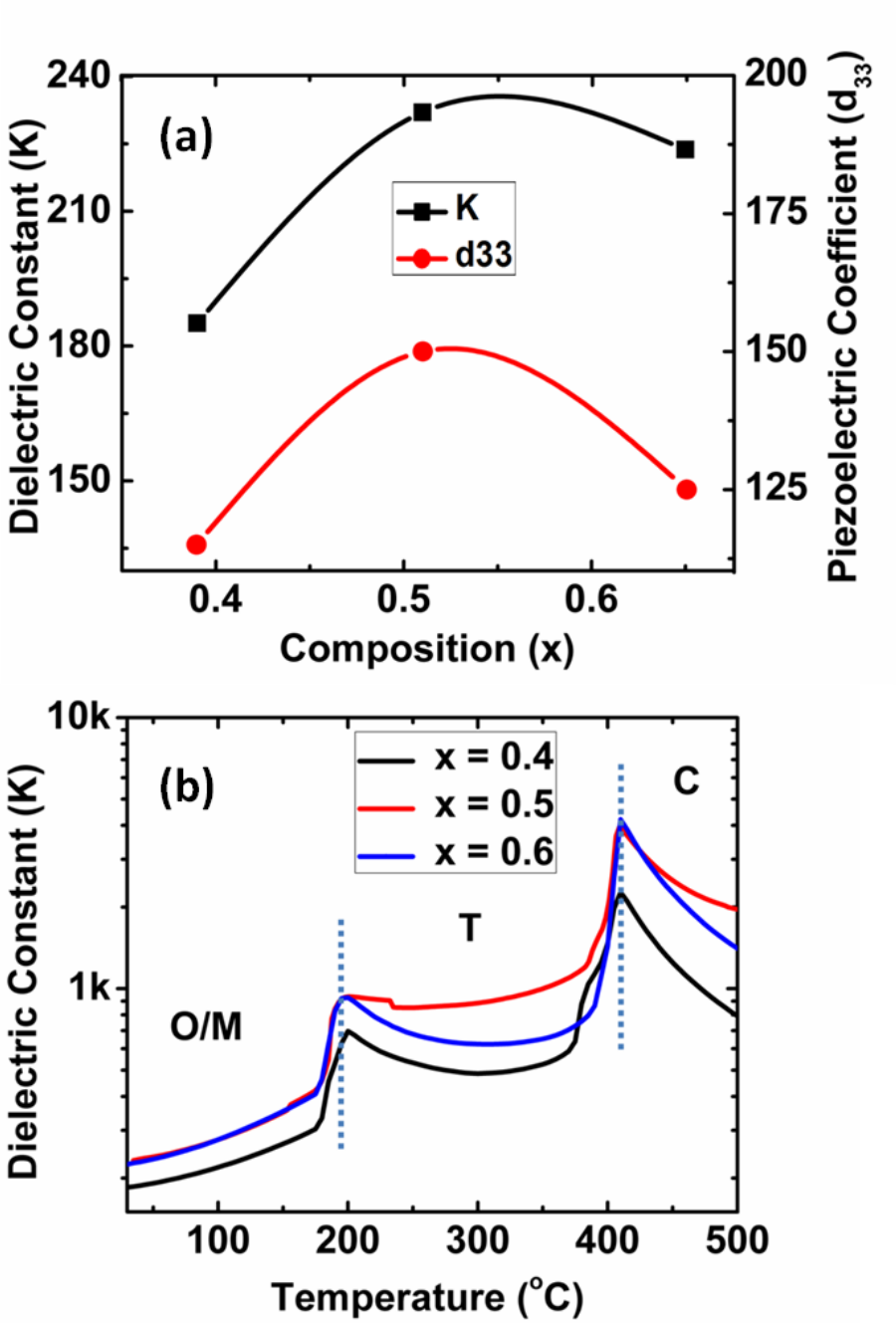

Figure 4.6 (a) Variation of d_{33} and K across the phase boundary at x = 0.5 (b) Temperature vs. dielectric constant values for x = 0.4, 0.5 and 0.6 KNN crystals along (001) planes.

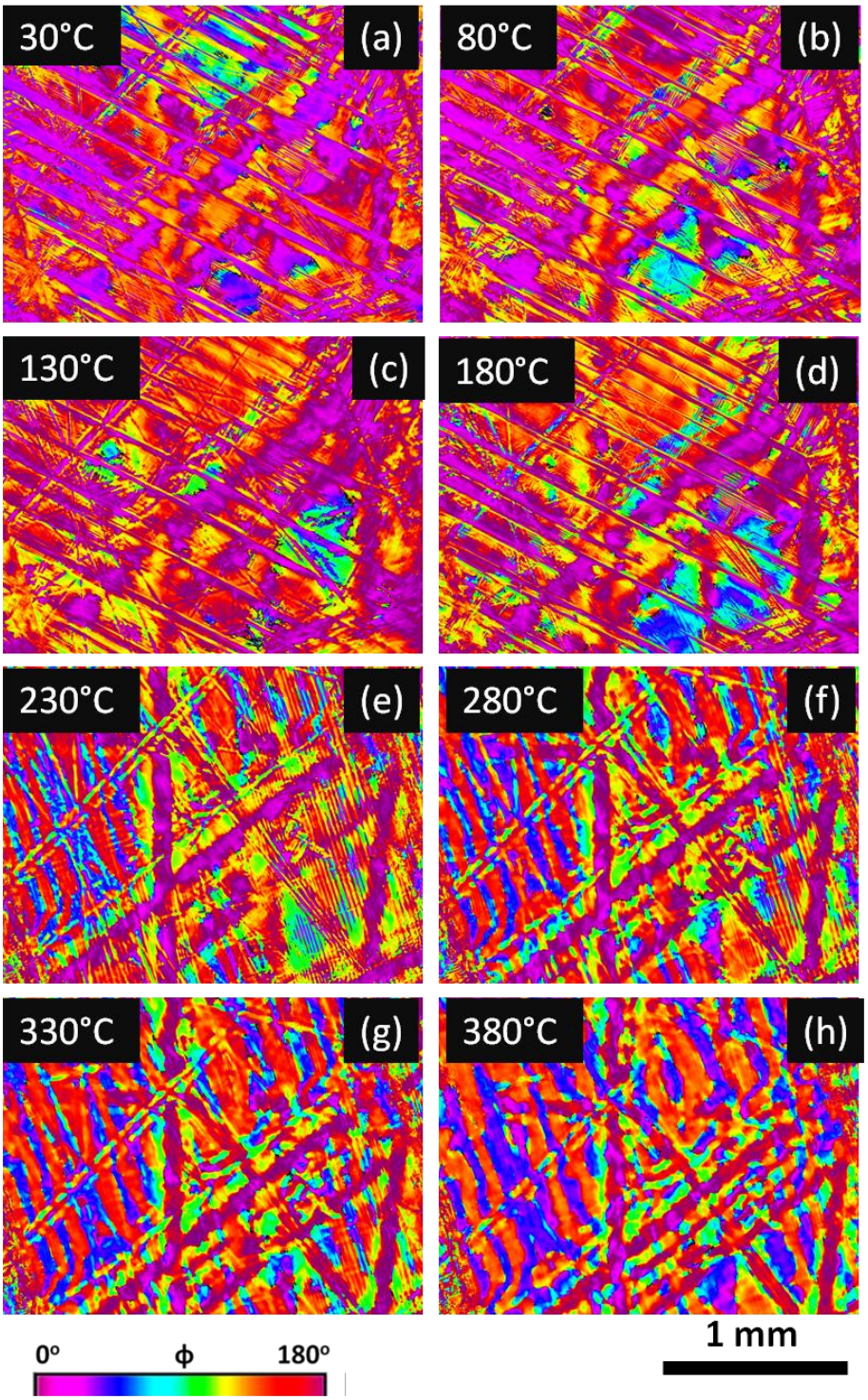

Figure 4.7 Orientation (false color images) for x = 0.4 KNN crystal at (a) 30°C, (b) 80°C, (c) 130°C, (d) 180°C, (e) 230°C, (f) 280°C, (g) 330°C, (h) 380°C

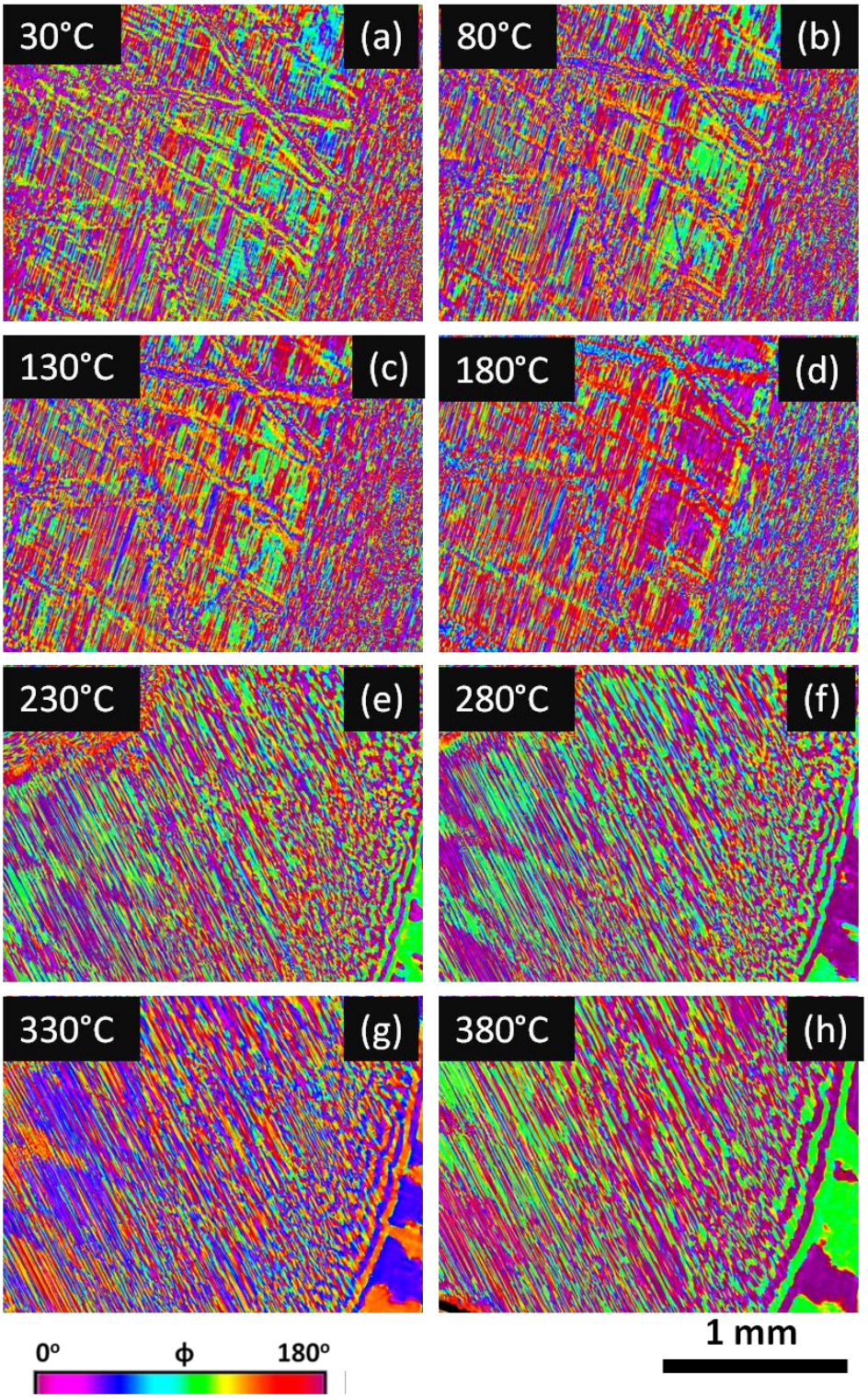

Figure 4.8 Orientation (false color images) for x = 0.6 KNN crystal at (a) 30°C, (b) 80°C, (c) 130°C, (d) 180°C, (e) 230°C, (f) 280°C, (g) 330°C, (h) 380°C

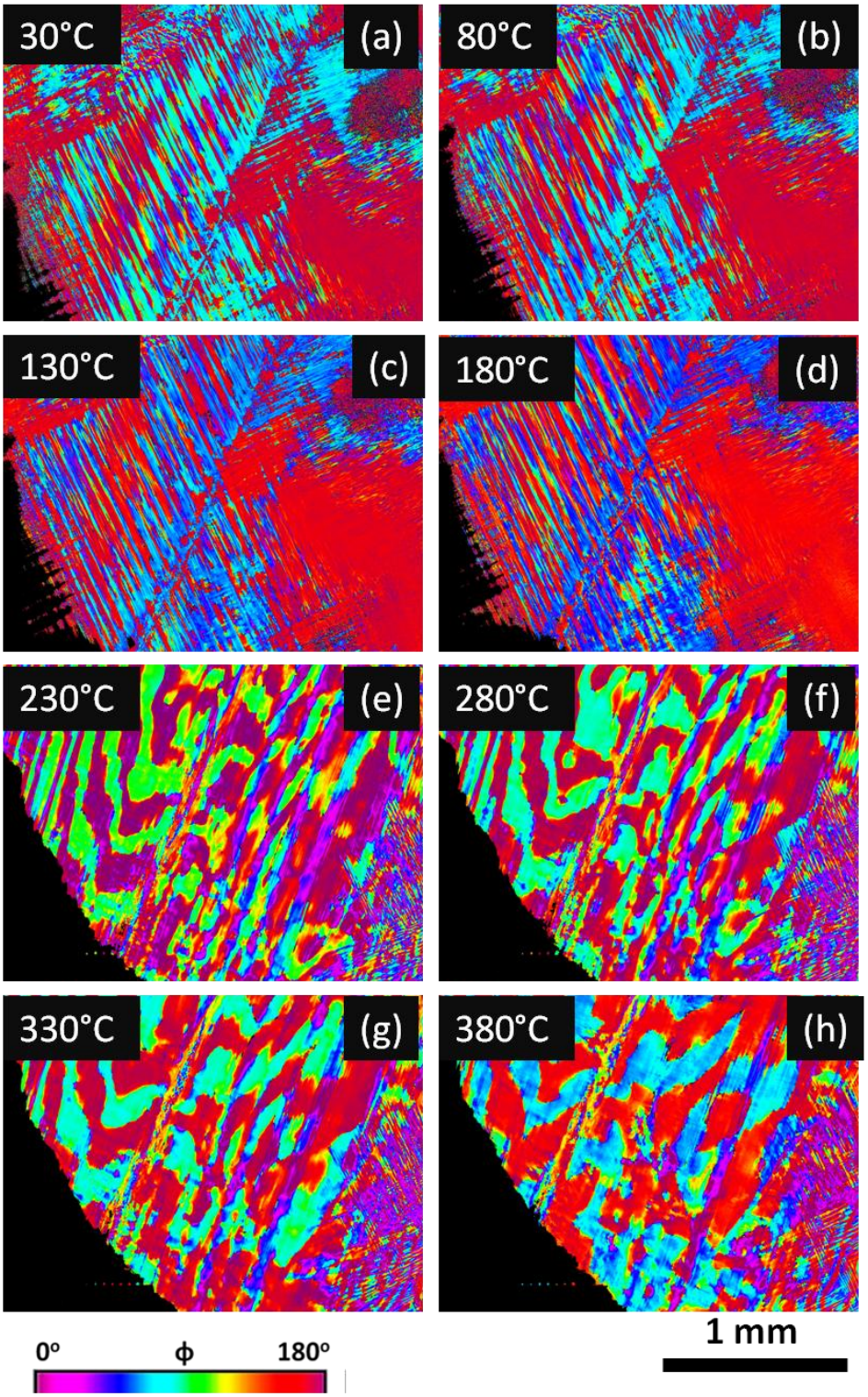

Figure 4.9 Orientation (false color images) for x = 0.5 KNN crystal at (a) 30°C, (b) 80°C, (c) 130°C, (d) 180°C, (e) 230°C, (f) 280°C, (g) 330°C, (h) 380°C

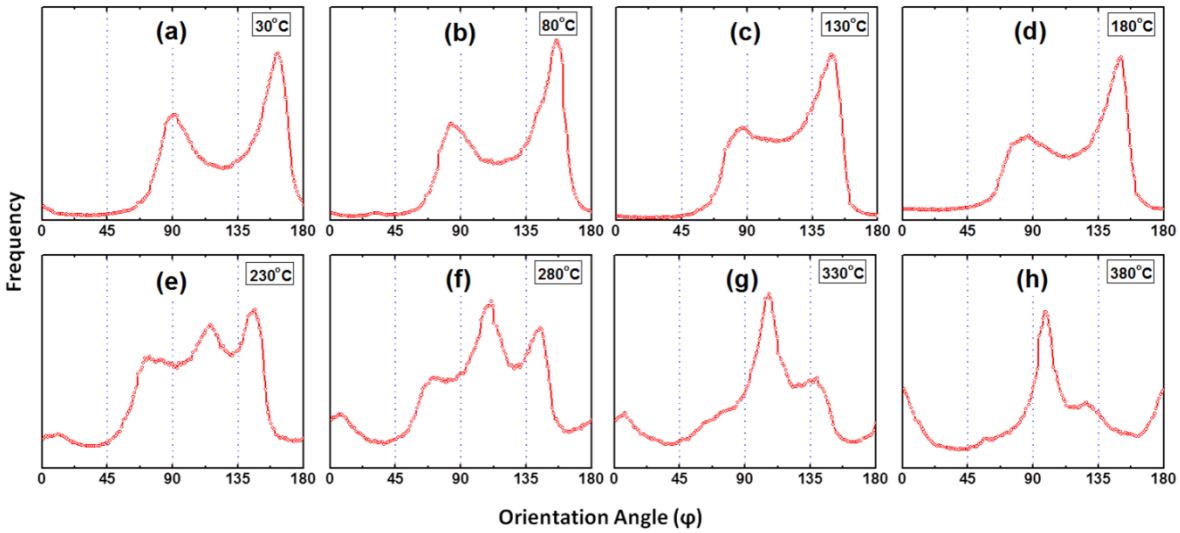

Figure 4.10 Orientation histograms for x = 0.4 KNN crystal at (a) 30°C, (b) 80°C, (c) 130°C, (d) 180°C, (e) 230°C, (f) 280°C, (g) 330°C, (h) 380°C

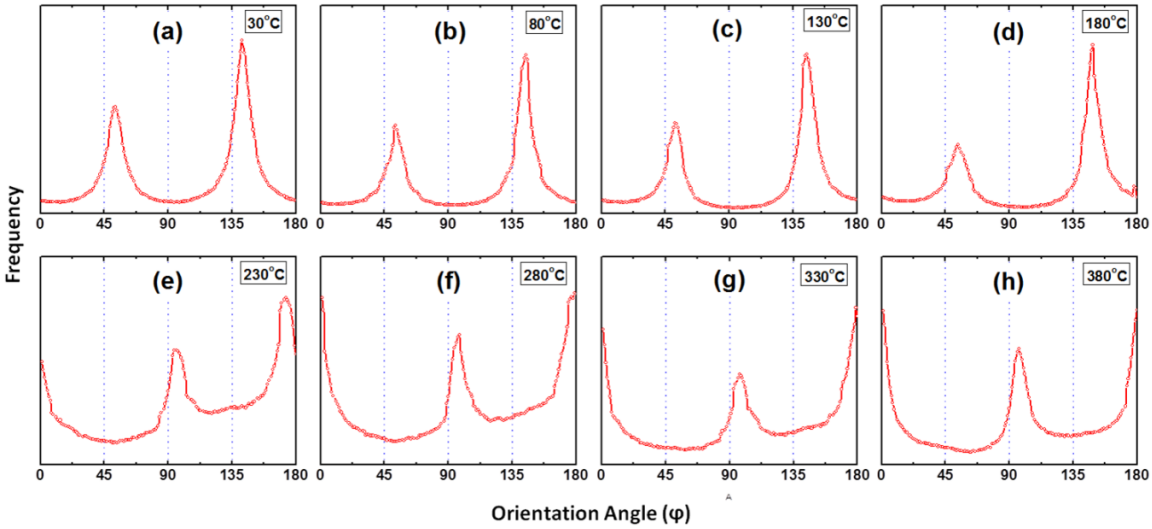

Figure 4.11 Orientation histograms for x = 0.6 KNN crystal at (a) 30°C, (b) 80°C, (c) 130°C, (d) 180°C, (e) 230°C, (f) 280°C, (g) 330°C, (h) 380°C

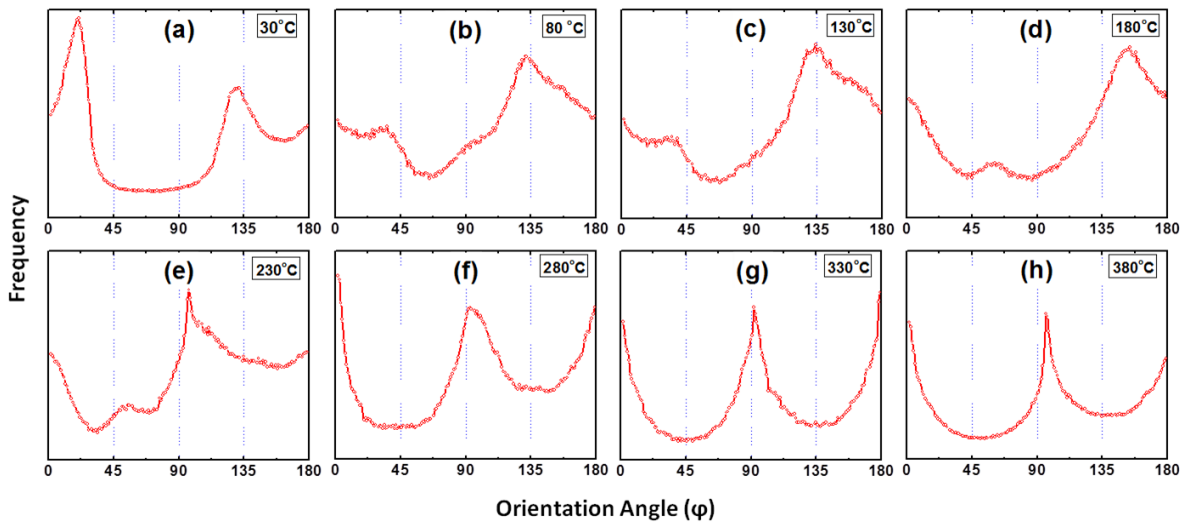

Figure 4.12 Orientation histograms for x = 0.5 KNN crystal at (a) 30°C, (b) 80°C, (c) 130°C, (d) 180°C, (e) 230°C, (f) 280°C, (g) 330°C, (h) 380°C

Histograms were obtained for different compositions during heating cycle at different temperatures. For the sake of simplification and better illustration of the relative shift of peaks corresponding to lower symmetry phases, the φ-axis for the orientation histograms was shifted in such a way that one of the peaks appearing at 380°C was shifted to either φ = 0° or 180°. This shift is equivalent to rotating the crystal on its axis, and does not result in any discrepancy or loss of information. Geometrically, this shift is equivalent to rotating the coordination axes in Fig. 4.2(b). Now, in this scenario two extreme values of φ (0° and 180°) represent the same $[100]_{pc}$ direction along the different opposite orientations. It is important to note that after a shift in the φ-axes in histograms (Figures 4.10 – 4.12), false color scales provided in Figures 4.7, 4.8 and 4.9 do not correspond to same absolute values of orientation for corresponding false color images. Since in Figures 4.10 – 4.12, the interest is only in illustrating the domain wall orientations with respect to $[100]_{pc}$, absolute values of φ are not relevant.

For x = 0.4, two peaks (φ = 17° and 90°) separated by Δ φ = 73° can be seen at room temperature (Figure 4.10 (a)). Following the Figure 4.3, one can see that such orientations of the polarization vectors with respect to $[100]_{pc}$ are only allowed for monoclinic M_C (Vanderbilt and Cohen Notation)[125] symmetry, and hence it can be inferred that x = 0.4 crystals have a stable M_C structure. This inference is consistent with previous findings of a *Pm* space group for KNN polycrystalline powders for x < 0.5.[16] With increasing temperature the presence of two peaks persisted to 180°C without any emergence of a new peak, suggesting that the M_C phase remains stable for x = 0.4, which is consistent with the dielectric data in Figure 4.6. On heating above 200°C, two additional peaks appeared which grew with increasing temperature at the expense of the two low temperature φ-peaks. Following the known phase diagram of KNN, above 200°C, all compositions studied in this investigation should have tetragonal 4mm symmetry. Accordingly, the two φ-peaks separated by 90° should be evident in the orientation histograms for all three compositions. However, for x = 0.4 at 380°C, the two major peaks had angles of $\varphi = 0^o$ and 99° with respect to the $[100]_{pc}$; not only were these peaks separated by an angle highly deviating from 90°, but they were also very broad relative to other tetragonal compositions subjected to similar birefringence investigations.[116] Furthermore, the two lower temperature peaks continued to appear as minor shoulders above the PPB. As for T phase, even superimposition of multiple domain cannot give rise to peaks other than at $\varphi = 0^o$ and 90°, these discrepancies suggest the coexistence of M_C and T phase above PPB for x = 0.4.[116]

For x = 0.6, at room temperature, two sharp peaks separated by Δ φ = 90° were apparent (Figure 4.11 (a)). These two peaks made an angle of φ = 90° with the $[100]_{pc}$. Following Fig. 4.3, these types of polarization directions can only be attributed to an O structure. Hence, on the basis of optical birefringence data, it can be inferred that the K-rich side of the

phase boundary has an orthorhombic crystal structure. This is important to note as previous different X-ray and neutron diffraction investigations were not in agreement with each other about the symmetry.[12, 118] On heating above the PPB at 200°C (Figure 4.11 (e) – (h))., the two orthorhombic-like φ-peaks disappeared and two new peaks appeared. New peaks were positioned at Δ φ = 45° from the orthorhombic-like peaks. These peaks were 90° apart from each other, as well as making 0° and 90° angles with $[100]_{pc}$ indicating a tetragonal symmetry. The presence of a weak peak at φ = 135° at 230°C may indicate that a minor amount of orthorhombic phase persists above the PPB. Note that as compared to x = 0.4, the volume fraction of this 2nd low-symmetry phase was minute and disappeared on heating to higher temperatures.

For x = 0.5, near the phase boundary, the presence of two peaks making angles of φ = 45° and 21° with respect to $[100]_{pc}$ direction were found (see Figure 4.12(a)), which were separated from each other by Δ φ = 66°. Following Figure 4.3, such orientations are consistent only with monoclinic M_A/M_B symmetries. This is an interesting observation, not only because previously no such phase has been reported for any KNN composition but also as the monoclinic *Pm* and orthorhombic O phases on the two sides of the phase boundary have a group-subgroup relationship.[110, 113] Similar to x = 0.4 and 0.6, a low intensity secondary peak belonging to a lower temperature phase persisted on heating above 230°C suggesting the persistence of a small fraction of the low-symmetry phase in the tetragonal phase field (Figure 4.12 (b) – (h)). Observation of the coexistence of lower symmetry phase within the high temperature tetragonal phase has not been reported previously for KNN, though modified KNN compositions having polymorphic phase boundaries below room temperature have been reported to have coexistence of tetragonal and orthorhombic phases at room temperature.[126]

When a ferroelectric crystal goes through the structural phase transformation, orientations of domain walls change in order to maintain strain compatibility between the neighboring domains.[127 - 129] During such transformations the lower symmetry phase has higher numbers of orientation states (OS) as compared to higher symmetry phase.[129, 130] The spontaneous strain tensor representing an OS is a second rank tensor, possessing all the symmetries of the point group of the crystal under consideration. If S and S′ represent the strain tensors (OS) of the parent and ferroelectric phases, strain compatibility condition can be represented as in Equation 4.5.[130]

$$(S_{ij} - S'_{ij})\, x_i\, x_j = 0 \qquad (4.5)$$

Strain tensors for different crystallographic point groups were determined previously and can be found in the classic work of Aizu.[131] Using the strain compatibility condition for different possible structural transformations, the orientations of domain walls were determined as listed in table 4.1.[127, 130, 132] Since for a particular structural transformation, domain walls can only have fixed orientations, the table can be utilized to identify the crystallographic information of crystal.

Table 4.1 Possible orientations of ferroelastic domain walls for different structural transformations

Structural Transformation	**Space Groups**	**Orientations of permissible domain walls**
Cubic → Tetragonal	$m\bar{3}m \rightarrow 4mm$ $432 \rightarrow 422$ $\bar{4}3m \rightarrow \bar{4}2m$	x = y, x = -y z = x, z = -x y = z, y = -z

	m3m → 4/mmm	
Tetragonal → Orthorhombic	422 → 222 4mm → mm2 $\bar{4}$2m → 222 $\bar{4}$2m → mm2 4/mmm → mmm	x = 0, y = 0
Tetragonal → Monoclinic	4 → 2 $\bar{4}$ → 2 4/m → 2/m	x = py, x = -y/p where $p = b + (a^2+b^2)^{1/2}/a$
Hexagonal → Orthorhombic	622 → 222 6mm → mm2 $\bar{6}$m2 → mm2 6/mmm → mmm	x = 0, y = 0 $x = \sqrt{3}\,y$, $y = -\sqrt{3}\,x$ $x = -\sqrt{3}\,y$, $y = \sqrt{3}\,x$
Trigonal – Monoclinic	32 → 3 3m → m $\bar{3}$m → 2/m	y = 0, z = -(a/c)x $y = \sqrt{3}\,x$, $a(x+\sqrt{3}\,y)-2cz = 0$ $y = \sqrt{3}\,x$, $a(x+\sqrt{3}\,y)-2cz = 0$
Orthorhombic → Monoclinic	222 → 2 mm2 → m mm2 → 2 mmm → 2/m	x = 0, z = 0

According to the table, any transformation from cubic ($m\bar{3}m$) to tetragonal (4mm, 422 and $\bar{4}2m$) symmetries must result in domain walls fixed only to {110} planes.[129, 130] Lower temperature T → O transitions can result in two types of domain walls, depending upon the relative orientations of T and O cells. For transformations in which the 2-fold axis of the O cell is along the 4-fold axis of the T cell (i.e. p-type transformation, according to Aizu's notations), [133] the walls are allowed to be oriented along {110 }planes. Moreover, if the 2-fold axis of the O cell is aligned to 45° angle to the 4-fold of T cell (i.e. s-type transformation) [133], the domain walls are fixed for being coplanar with the {100} crystallographic planes. For the T → M transformation, the domain wall orientations depend upon the relative orientation of T and M unit cells; but, unlike the previous transition cases mentioned above, the domain walls have complex orientations that depend upon the values of the elements of the strain tensor rather than being fixed to {100} or {110} planes.

Figures 4.13, 4.14 and 4.15 show φ and I_o snapshots for all the three compositions at varying temperatures. At room temperature, all the crystals exhibited the presence of stripe-like domains that extended throughout the sample area under the microscope, having lengths on the order of millimeters. Schematics are provided in these figures constructed from the false color images that represent the domain wall orientations in the crystals.

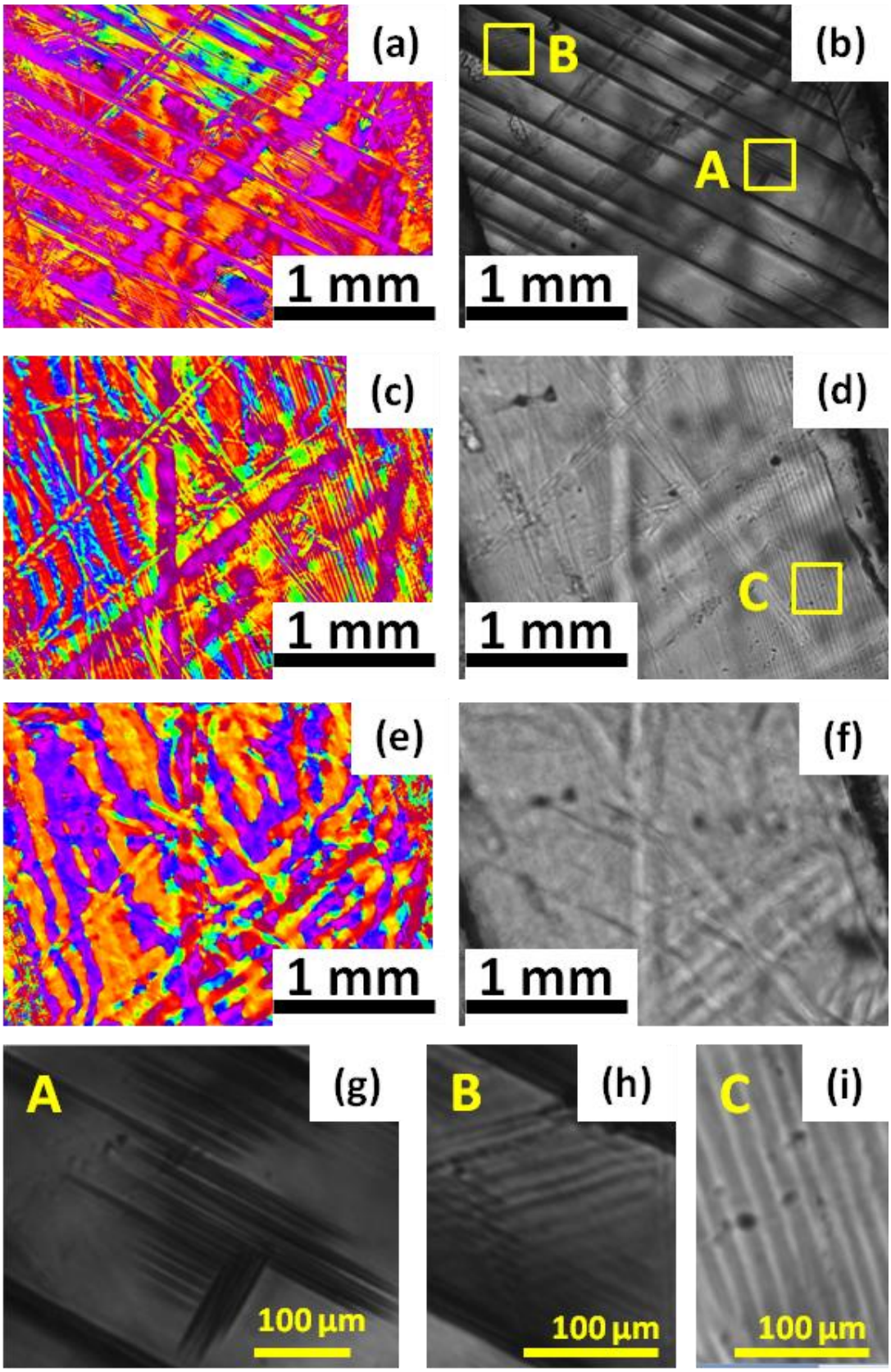
(a)
1 mm
(b)
B
A
1 mm
(c)
1 mm
(d)
C
1 mm
(e)
1 mm
(f)
1 mm
A
(g)
100 µm
B
(h)
100 µm
C
(i)
100 µm

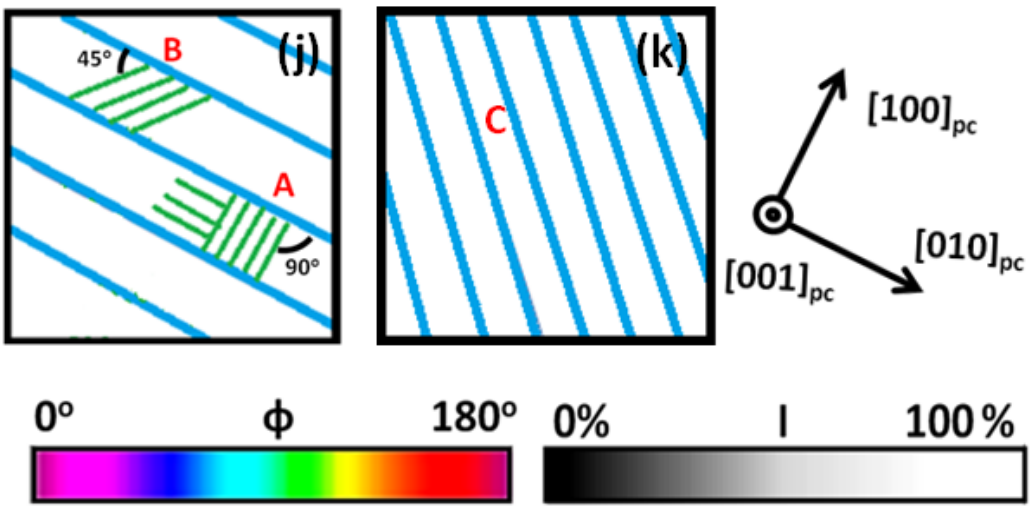

Figure 4.13 orientations of domain walls for x = 0.4 (a), (c), (e) φ, and (b), (d), (f) I_o false color images obtained at 30°C, 230°C and 430°C respectively. (g), (h) and (i) show the larger view of domains under the area A, B and C respectively shown in figure (b) and (d). (j) and (k) representing schematics of the domain wall orientations at respectively 30°C and 230°C (False color scale does not correspond to the same absolute φ value, though Δφ value between any two corresponding points is true).

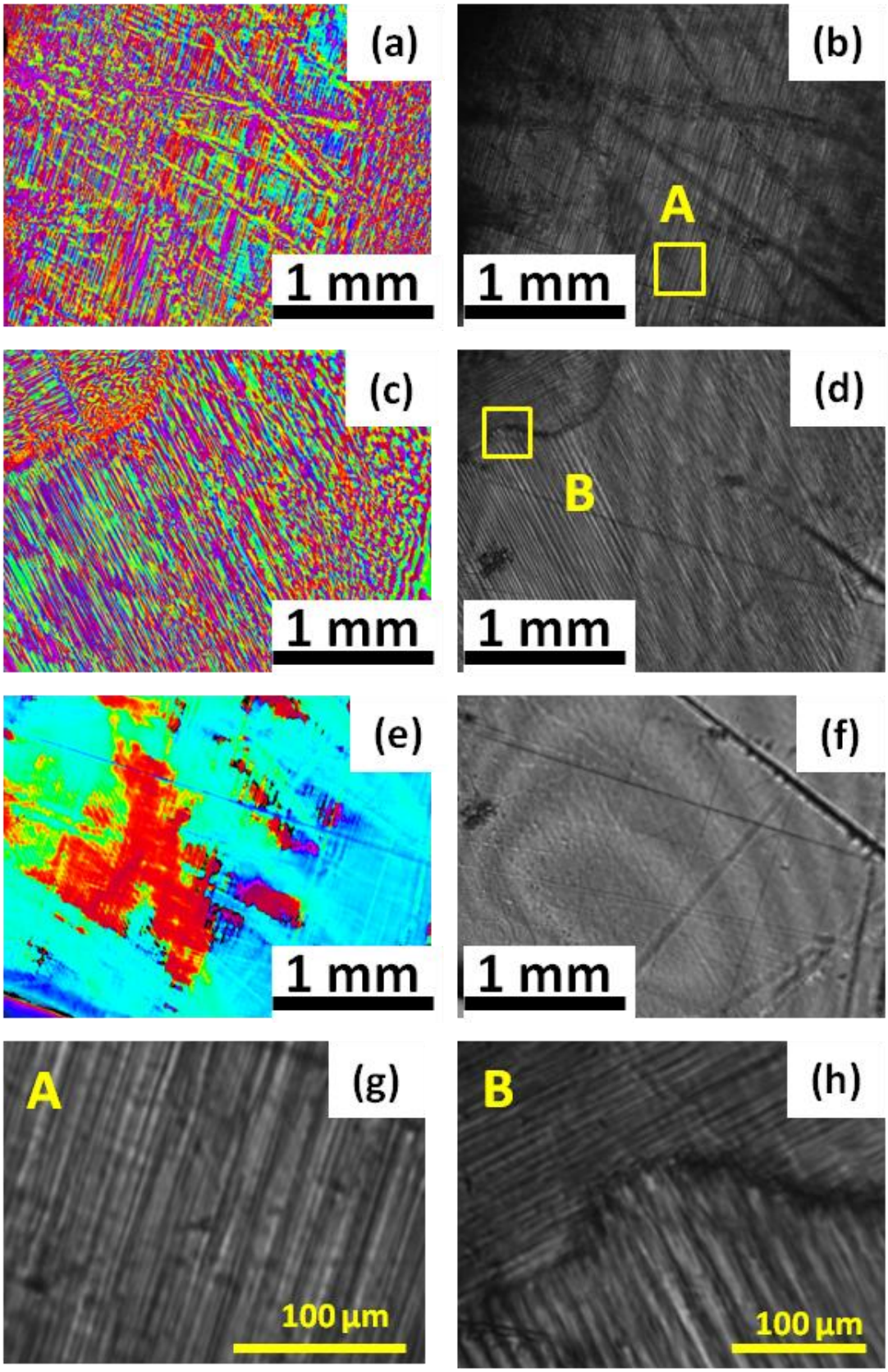
(a)
1 mm
(b)
A
1 mm
(c)
1 mm
(d)
B
1 mm
(e)
1 mm
(f)
1 mm
A
(g)
100 µm
B
(h)
100 µm

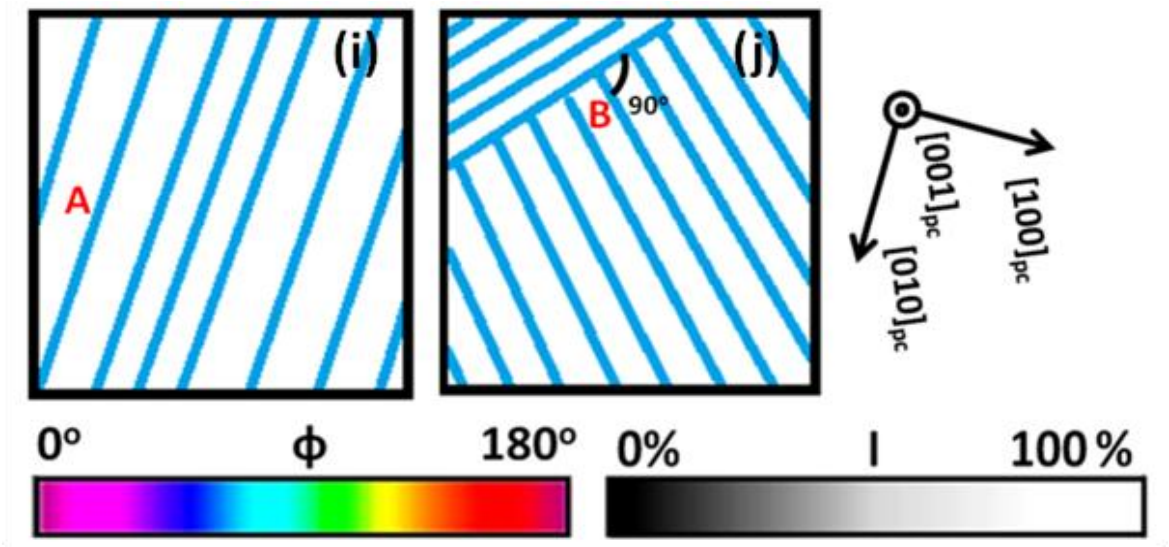

Figure 4.14 orientations of domain walls for x = 0.5 (a), (c), (e) ϕ, and (b), (d), (f) I_o false color images obtained at 30°C, 230°C and 430°C respectively. (g), and (h) show the larger view of domains under the area A and B respectively shown in figure (b) and (d). (i) and (j) represent the schematics of the domain wall orientations at 30°C and 230°C (False color scale does not correspond to same absolute ϕ value, though Δϕ value between any two corresponding points is true).

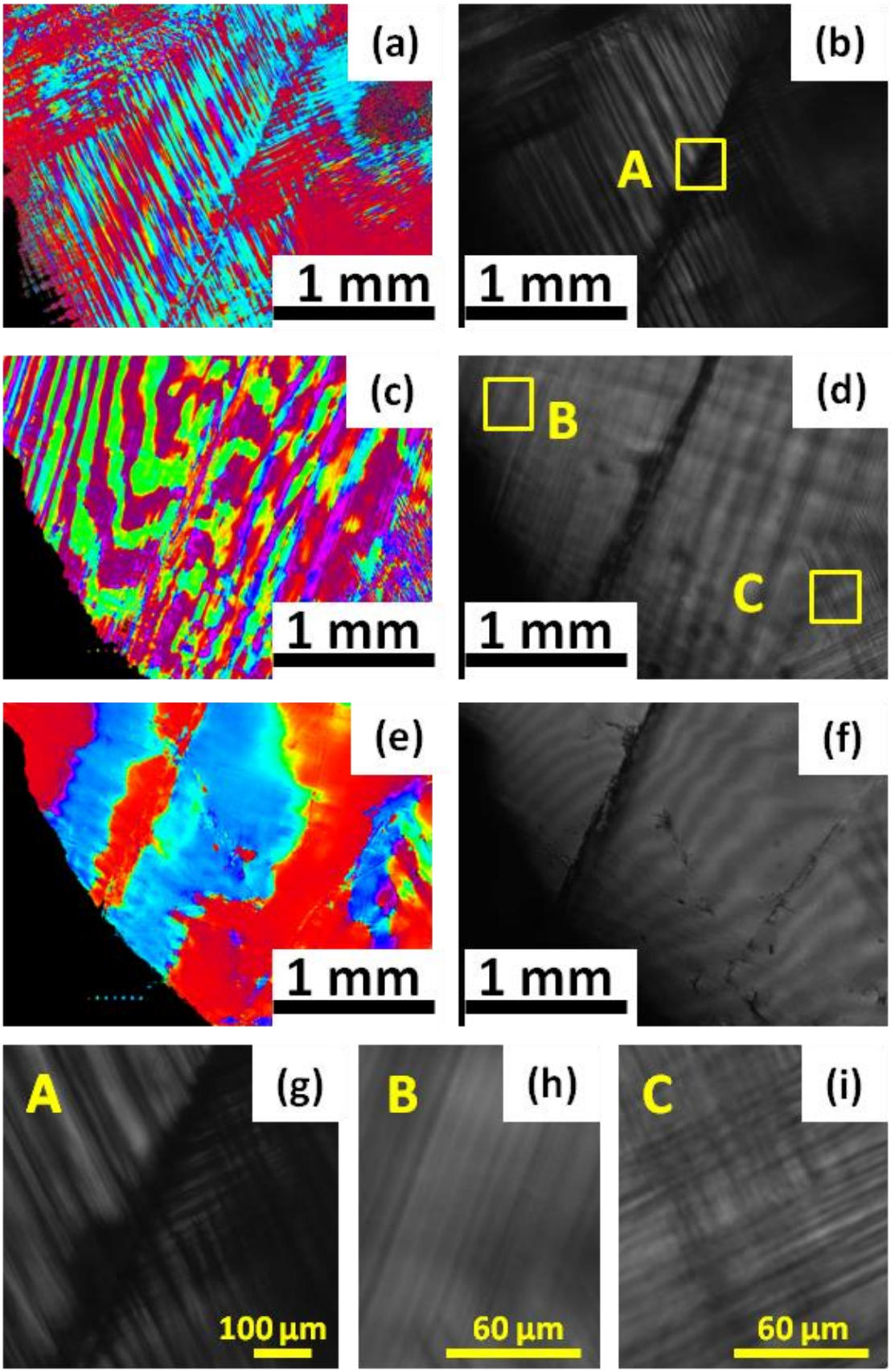
(a)
1 mm
(b)
A
1 mm
(c)
1 mm
(d)
B
C
1 mm
(e)
1 mm
(f)
1 mm
A
(g)
100 µm
B
(h)
60 µm
C
(i)
60 µm

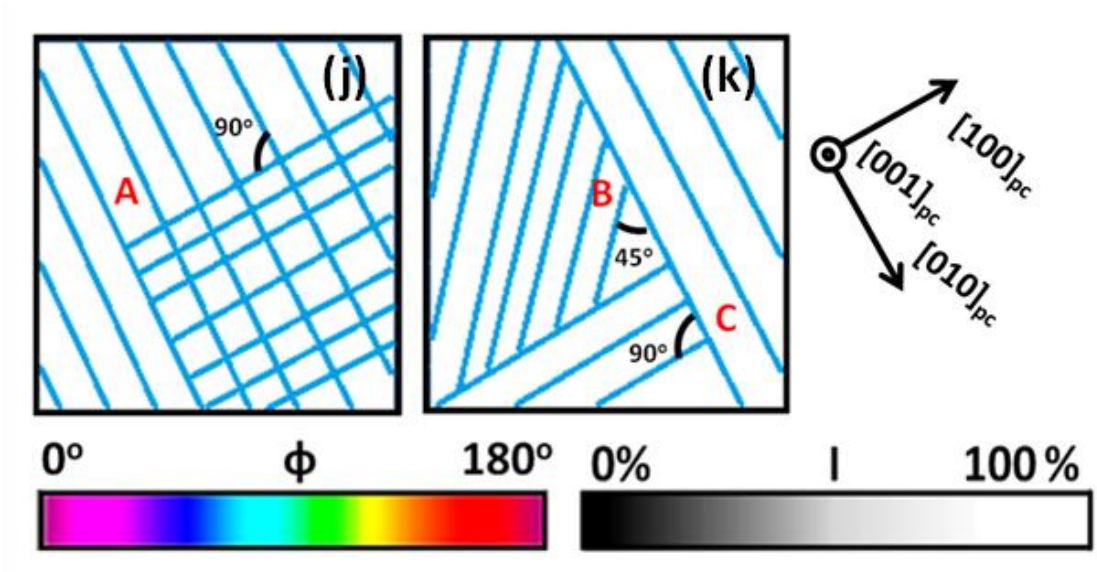

Figure 4.15 Domain wall orientations for x = 0.6: (a), (c), (e) show φ, and (b), (d), (f) show I_o false color images obtained at 30°C, 230°C and 430°C respectively. (g), (h) and (i) show the larger view of domains under the area A, B and C respectively shown in figure (b) and (d). (j) and (k) representing schematics of the domain wall orientations at respectively 30°C and 230°C (False color scale does not correspond to same absolute φ value, though Δφ value between any two corresponding points is true).

These schematics try to capture the domain wall orientations, but are not-to-scale with regards to the domain widths for the different crystals. Continuous domain walls extending to millimeters length confirmed that the crystals were compositionally homogeneous.

For x = 0.4, broad stripe-like domains extending through the entire snapshot image having widths of > 200 μm were evident, which made an angle of 0° with $[100]_{pc}$. These domains were found to have internal sub-domains as well, with domain walls making angles of 45° and 90° with one of the $[100]_{pc}$ directions. For better illustration of these domains, larger images of areas A and B are provided in Figures 4.13 (g) - (h). Following the compatibility

conditions, simultaneous wall angles of 0° and 45° with $[100]_{pc}$ are only possible for low symmetry monoclinic or triclinic phases. This finding is consistent with the above determination of M_C symmetry for this composition. At 230°C, above the PPB, only walls with angles of 45° to $[100]_{pc}$ were found, consistent with a higher symmetry T phase.

For x = 0.5 (see Fig. 4.13a-b), only walls making an angle of about 0° with $[100]_{pc}$ were evident. An angle of 0° between the walls and $[100]_{pc}$ is common amongst many symmetries, excluding tetragonal. Hence, the results are not definitive with regards to the crystallographic nature of this composition. Note that the finding does not contradict the possibility of M_A/M_B phase for this composition, as suggested above. On heating above 200°C (see Figs 4.13c-d) two types of T domain walls making angles of 45° and 135° with $[100]_{pc}$ became evident.

For x = 0.6 (see Figs 4.14a-b), two types of walls making angles of 0° and 90° with $[100]_{pc}$ were evident, consistent with O symmetry, as determined by the peak positions in the orientations histograms. With regards to the compatibility conditions, O domain walls parallel to $\{100\}_{pc}$ imply a s-type transformation, which in turn suggests a non-primitive nature for the O unit cell consistent with the Amm2 space group as previously reported for KNN.[14 - 16] On heating the crystal near the PPB to 200°C, most of the crystal area (except bottom right corner) in the false color images reveals a rotation of the domain walls by about 45°, however a small area (lower right) continues to have domain morphology with wall angles of 0° and 90° to $[100]_{pc}$, which cannot be attributed to the T symmetry. Thus, it can be inferred that this small area is an untransformed O region that persists into the T phase above PPB.

On comparing the images of the stripe like domains for the three compositions, it can be seen for x= 0.4 and x =0.6 that their domain width were quite large relative to that for x = 0.5. The widths for x = 0.4 and 0.6 were in the range of 80μm – 200μm with a broad size distribution. In contrast, near the boundary at x = 0.5, the widths were about 15μm – 18μm. These findings are similar to the previous investigations that demonstrated the presence of a more uniform domain structure of smaller dimensions for compositions close to the MPB as compared to the compositions away from it. For example, piezoresponse force microscopy (PFM) analysis performed on PMN-PT and NBT-BT crystals across their MPBs revealed the presence of more organized and smaller domains close to MPB.[134] Domain size also plays an important role in the dynamic response of piezoelectric properties. Theoretical calculation conducted on two-dimensional (2D) $BaTiO_3$ single crystals using a time dependent Ginzburg – Landau (TDGL) model indicated about a threefold increase in the longitudinal piezoresponse (d_{33}) on decreasing the domain size from 22.6 nm to 4.5 nm.[135] Experimental investigations have also shown an increased piezoresponse in $KNbO_3$ and $BaTiO_3$ with decreased domain size.[136, 137] Accordingly, the enhanced piezoelectric properties of KNN at x = 0.5 might be attributed to thermodynamic changes caused by a decreased domain size.

Figure 4.16 (a) shows the variation of the linear optical birefringence for multi-domain KNN (x = 0.4, 0.5 & 0.6) crystals in the temperature range of 30°C-600°C. These birefringence values were calculated using the averaged values of $|\mathrm{Sin}\delta|$ for the respective three crystals over an area of 1360 x 1024 pixels with the help of equation (4.4). Due to the anisotropic shape of domains and their small size, it was not possible to obtain temperature dependent linear birefringence plots for a single domain area. All three crystals exhibited two clear transitions at 200°C and 400°C, consistent with the dielectric data. Interestingly, for x = 0.5 the birefringence value was

quite high as compared to the other compositions x = 0.4 and x = 0.6 in both of the temperature ranges of 30°C–200°C and 200°C–400°C, whereas in the cubic phase they all exhibited similar nonzero values of birefringence. Also, the birefringence for x = 0.5 decreased continuously as moving towards higher symmetry phases, in contrast to x = 0.4 and x = 0.6 which exhibited contrary trends. This discrepancy in the values of linear birefringence could be attributed to complex multi-domain state of these crystals, as previously multi domain crystals of $PbTiO_3$ have been reported to have contrary and ambiguous linear birefringence data.[138, 139] For x = 0.5, high domain wall density could also be the source of high birefringence values in the temperature range of 30°C–200°C, as high stress induced at domain walls may lead to localized birefringence.[140]

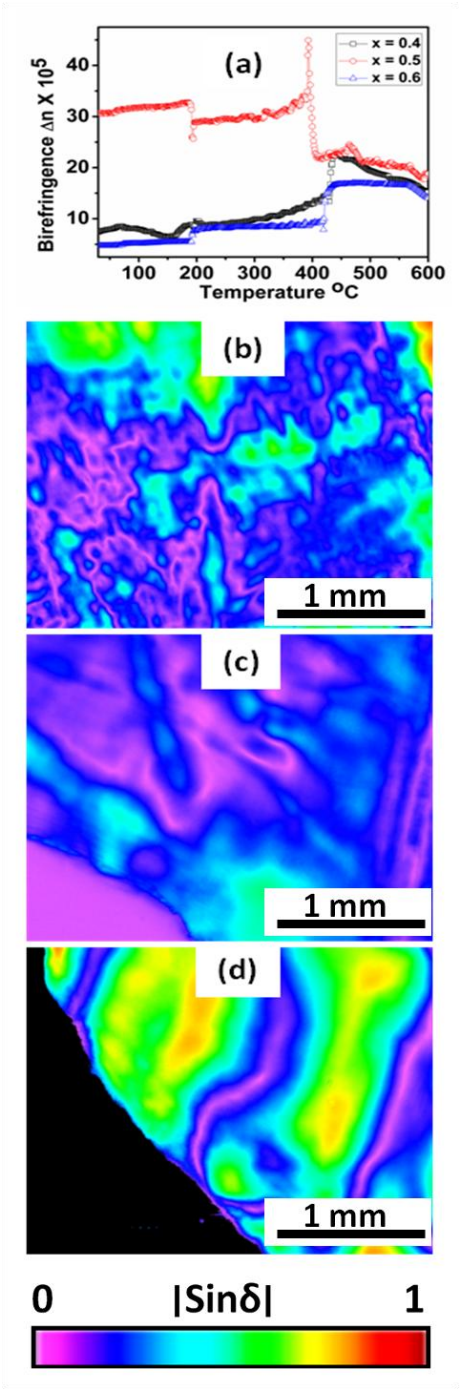

Figure 4.16 (a) variation of linear birefringence for x = 0.4, 0.5 and 0.6 with temperature in the range 30°C-600°C. (b) (c) and (d) false color images showing the nonzero values of **/**Sinδ**/** for x = 0.4, 0.5 and 0.6 respectively.

Interestingly, all the three composition crystals showed a non-zero birefringence of similar magnitude in the cubic phase, which decreased with increasing temperature but persisted up to 600°C (the upper limit of temperature which could be attained in the instrument used). Figures 4.16 (b) - (d) show the false color images of |Sinδ| for the three composition crystals, confirming the non-zero value at 600°C. This is an interesting finding as a crystal having $m\bar{3}m$ cubic symmetry should have zero birefringence.[120, 121] Non-zero birefringence for cubic crystals has been reported previously as well and number of mechanisms could contribute to this phenomenon.[139, 141] Presence of any local stress could be a source of photo-elastic effect, resulting in a non-zero birefringence in cubic phase field. Since these crystals are pre-heated at 600°C prior to birefringence study, possibility of any residual stress introduced during polishing is very rare. But high density of oxygen ion vacancies[95] produced during growth of these crystals could result in extended defects with localized stress.[142] Besides, deviation of crystal structure from ideal $m\bar{3}m$ symmetry could also result in non-zero birefringence. For example, $BaTiO_3$ was found to have non-zero birefringence in cubic phase[141, 143] and was reported to have the uncorrelated displacements of Ba ions amongst the eight equivalent <111> directions.[144]

6 Summary

In summary, KNN crystals for x = 0.4, 0.5 and 0.6 were investigated for their macroscopic symmetry and domain structure using an optical birefringence technique. At room temperature, crystals with compositions x = 0.4 and 0.6 were found to have monoclinic M_C and orthorhombic O symmetries. However, this investigation suggests the existence of a new monoclinic M_A/ M_B or triclinic phase near the MPB at x = 0.5. Figure 4.17 illustrates the phase diagram of KNN system drawn according to the findings in this optical crystallographic study. The composition x = 0.5 had more organized and smaller domains as compared to either the K or

Na rich sides. This suggests that domain size may play an important role in the superior ferroelectric and piezoelectric properties of KNN for x = 0.5. On heating above the PPB at 200°C, all three compositions exhibited a transformation to a T phase, though a relatively small fraction of the lower symmetry phase persisted in this temperature regime and diminished with increasing temperature. In the paraelectric cubic phase above 400°C, none of the crystals exhibited zero birefringence, suggesting a disordered m$\bar{3}$m cubic structure.

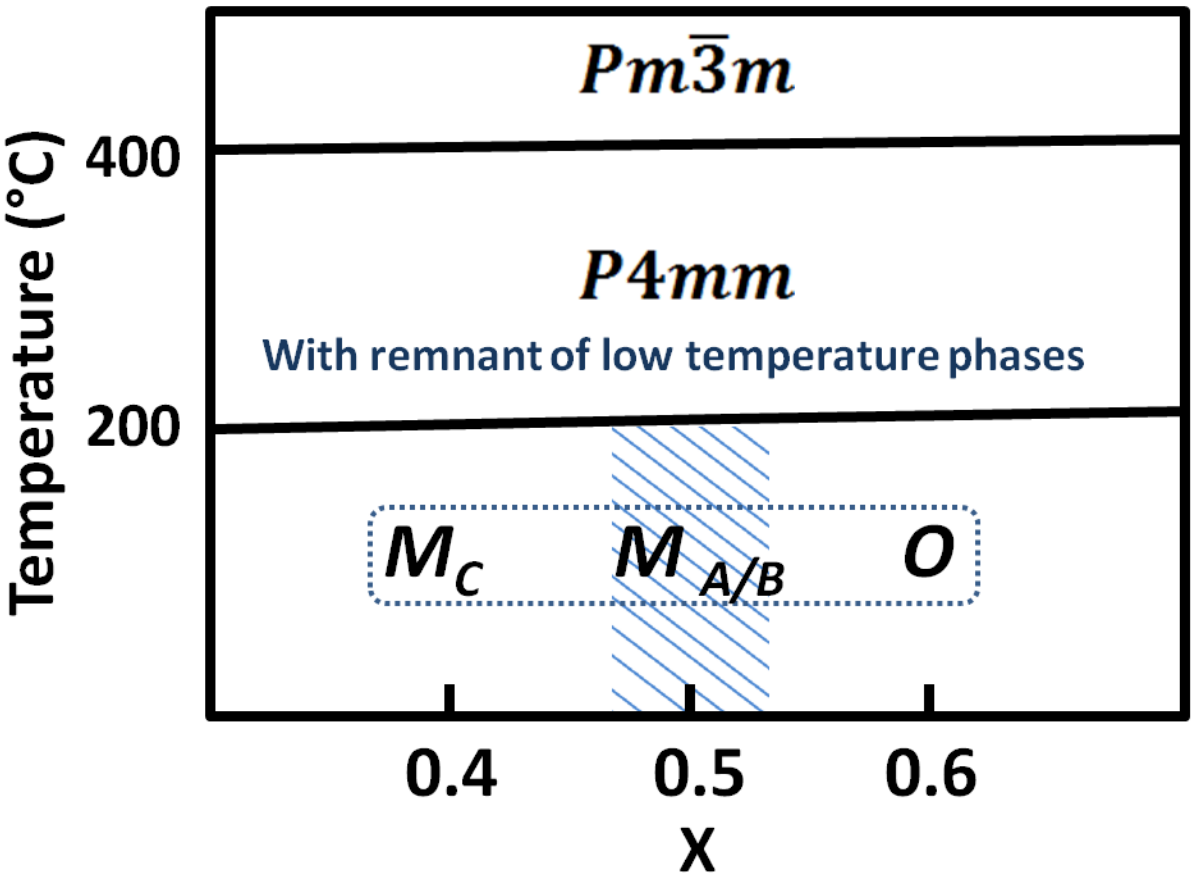

Figure 4.17 Phase diagram of KNN based upon the present optical crystallographic analysis

Chapter 5

Crystallographic Analysis and Microscopic Domain Structure of KNN Single Crystals

5.1 Domain structure study by piezoresponse force microscopy (PFM)

In conjunction with the advantage of having large field of view, the birefringence technique has limitation of resolution which prevents the investigation of finer details within domain structure. Piezoresponse force microscopy (PFM) is an effective technique to study the domain structure of ferroelectrics at the micron scale. PFM was performed on KNN crystals on either side of phase boundary at x = 0.5. Scanning probe microscopy based technique involves measurement of local response of a piezoelectric material with respect to a small AC signal applied through a conducting tip.[145]

For the PFM analysis, KNN crystals of lateral dimensions about 4 mm x 4 mm were polished with the help of an alumina paste to a surface finish of 0.5μm. After polishing, all crystals were annealed at 1000°C to homogenize the composition. This annealing also helps in relieving the stress produced on the crystal surfaces during polishing.[146] Prior to PFM analysis, both crystals were subjected to energy dispersive X-ray analysis to confirm their compositions. Figure 5.1 shows the EDX analysis performed on two crystals, showing crystal 1 and 2 to have composition x = 0.35 and 0.65 respectively.

Bruker Icon atomic force microscope was used to collect the PFM data on these crystals. Crystals were mounted on a conducting sample holder with the help of silver paste. Small areas of all the three composition crystals were scanned with a conductive silicon tip

having platinum coating. An AC signal of frequency about 15 kHz and amplitude of 10V was applied to the tip. Data was collected in contact mode on the area of size 10µm x 10 µm. Crystals were positioned in such a way that one of the [100] edges was parallel to the scanning direction.

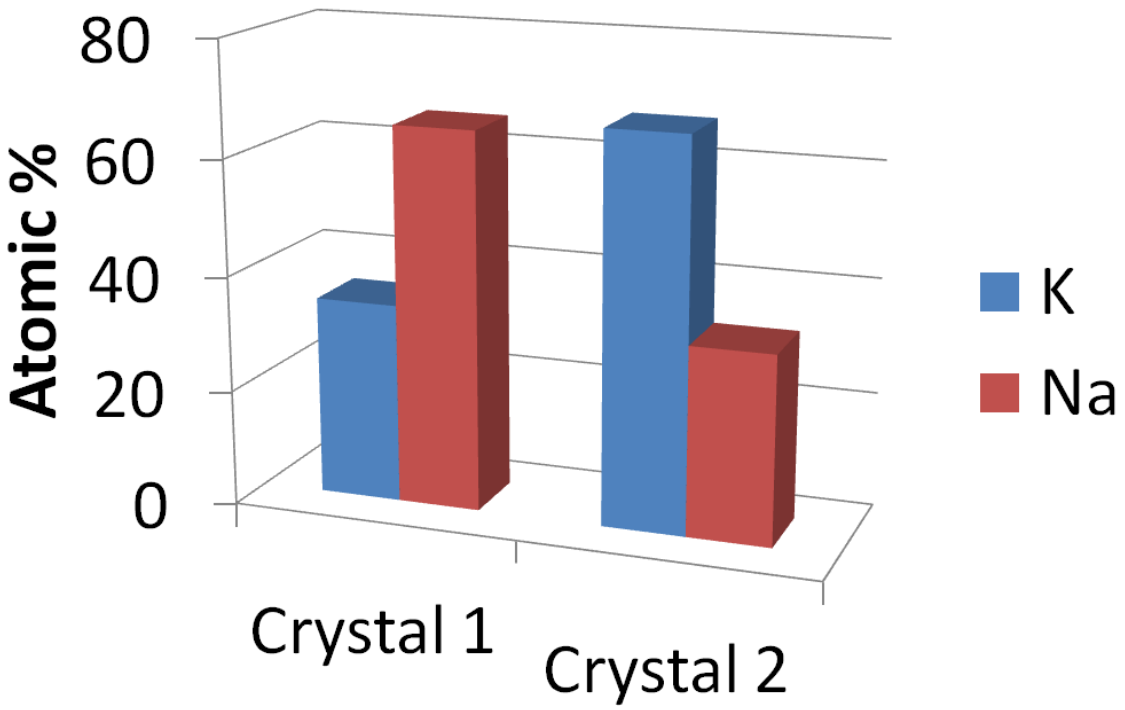

Figure 5.1 EDX analysis performed on crystal samples used for PFM investigation.

Figure 5.2 shows the PFM amplitude and phase images of KNN single crystals for x = 0.35 on $(100)_{pc}$ plane. For x = 0.35 crystal, stripe like domains of widths 1µm can be seen in amplitude as well as phase image. The domain wall separating these ferroelastic domains make an angle of 45° with the [100] edges of crystals. This orientation of ferroelastic domain walls is consistent with the monoclinic structure of this composition.[133,147]

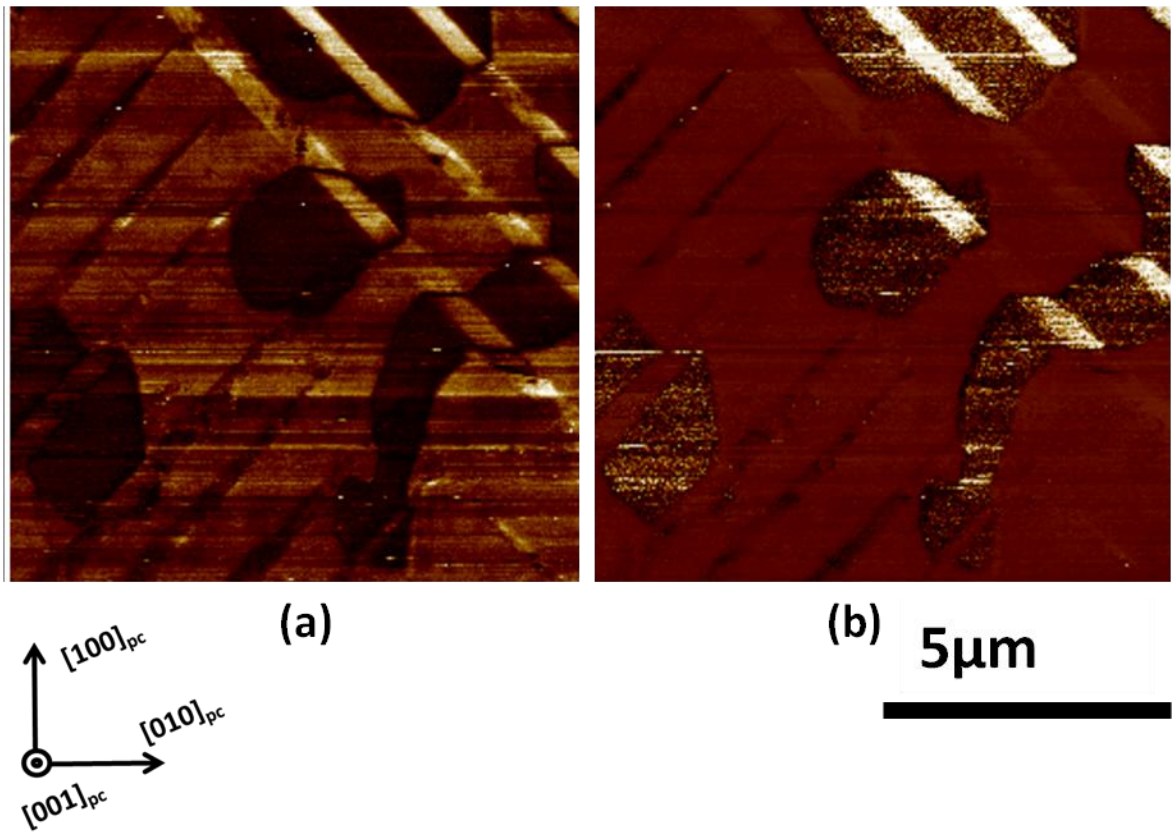

Figure 5.2 PFM images of KNN single crystals (a) amplitude and (b) phase for x = 0.35.

Beside the ferroelectric domain walls, x = 0.35 crystals were also found to have closed contour like domains with arbitrary domain wall orientations, suggesting them to be 180° domains walls.

Contrary to the x = 0.35 composition, the x = 0.65 crystal did not show the presence of any ferroelastic domain, as was evident by the absence of any well aligned domain wall in the PFM image. These ferroelectric domains had dimensions on the order of few micron which was quite large as compared to the ferroelectric domains seen for x = 0.35.

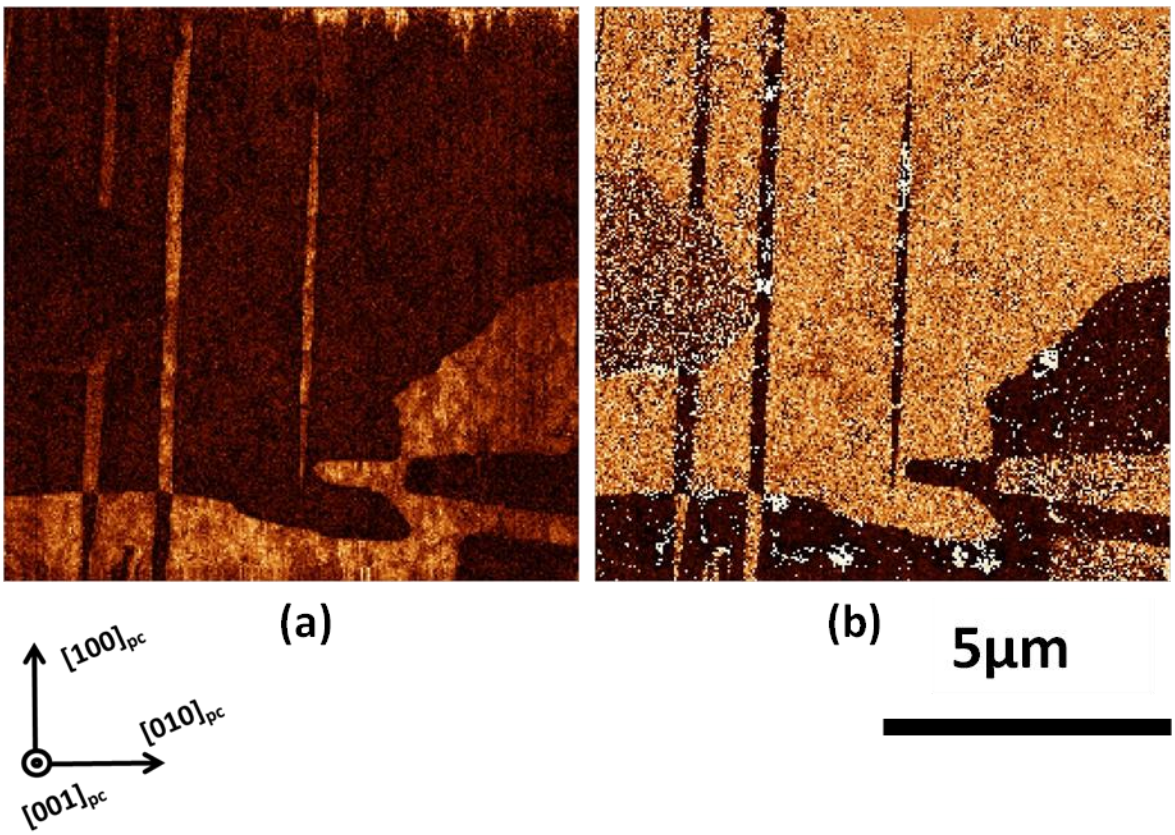

Figure 5.3 PFM images of KNN single crystals (a) amplitude and (b) phase for x = 0.65.

5.2 Crystallographic analysis of KNN crystals

Most of the crystallographic studies conducted on KNN materials in literature has utilized polycrystalline powder for Rietveld refinement investigations.[14, 16] This technique determines the crystallographic information about a composition by simply finding the best model for a powder diffraction pattern and hence there is finite fitting uncertainity. Also, it is difficult to extract the finer details of the structure by using powder diffraction analysis. In case of perovskites, this shortcoming is of greater importance as these finer details are of great importance in determining the structure – properties relationships. For example, tilt in oxygen octahedral in perovskites play

an important role in determining the piezoelectric nature of material and they can only be determined accurately by the crystallographic analysis of single crystals.[14] To achieve better understanding of crystallographic nature of KNN on potassium deficient side of phase boundary, the x = 0.35 composition crystal was used for crystallographic analysis. An Oxford diffractometer (Figure 5.4) with copper radiation and Gemini R goniometer was used to collect diffraction data on the crystal sample.

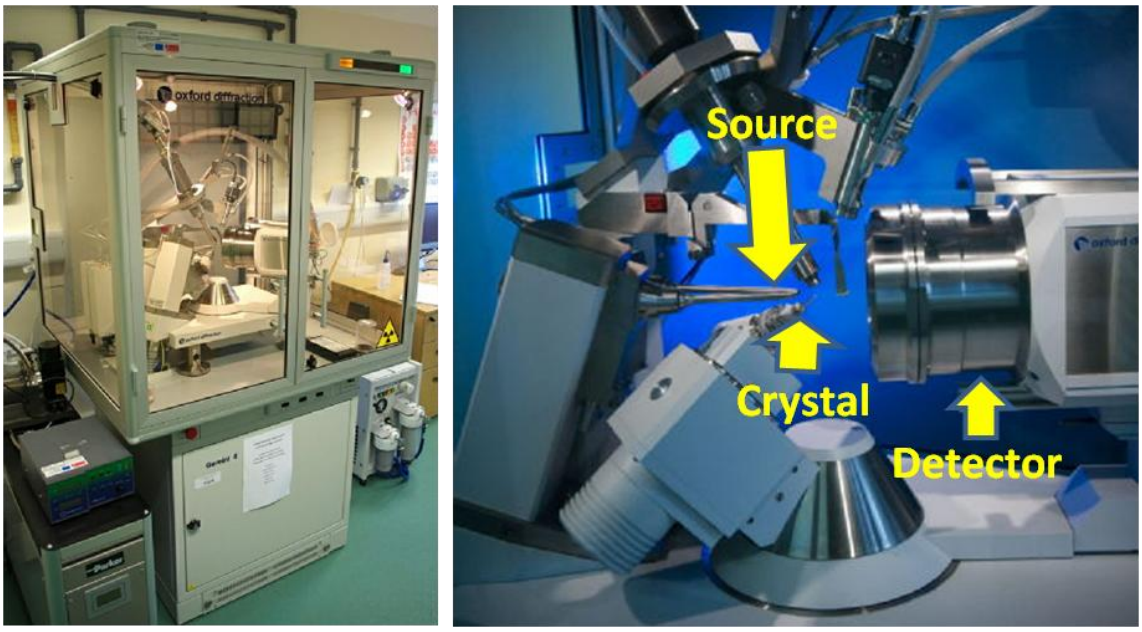

(a) (b)

Figure 5.4 (a) Oxford diffractometer and (b) Larger view of source and detector.

A small piece of transparent crystal having dimensions of the order of a few micrometers was used to collect the data in different orientations of a CCD detector. Figure 5.5 shows the KNN crystal loaded for the study along with one of the diffraction patterns. CrysAlis Pro software was used for data reduction followed by structure refinement by Olex2. The x = 0.35 composition crystal showed it to have monoclinic symmetry with Pm space group. This

finding of monoclinic symmetry for $K_{0.4}Na_{0.6}NbO_3$ crystals is consistent with the findings of the previous Rietveld refinement investigations performed on powder diffraction data.[11, 12]

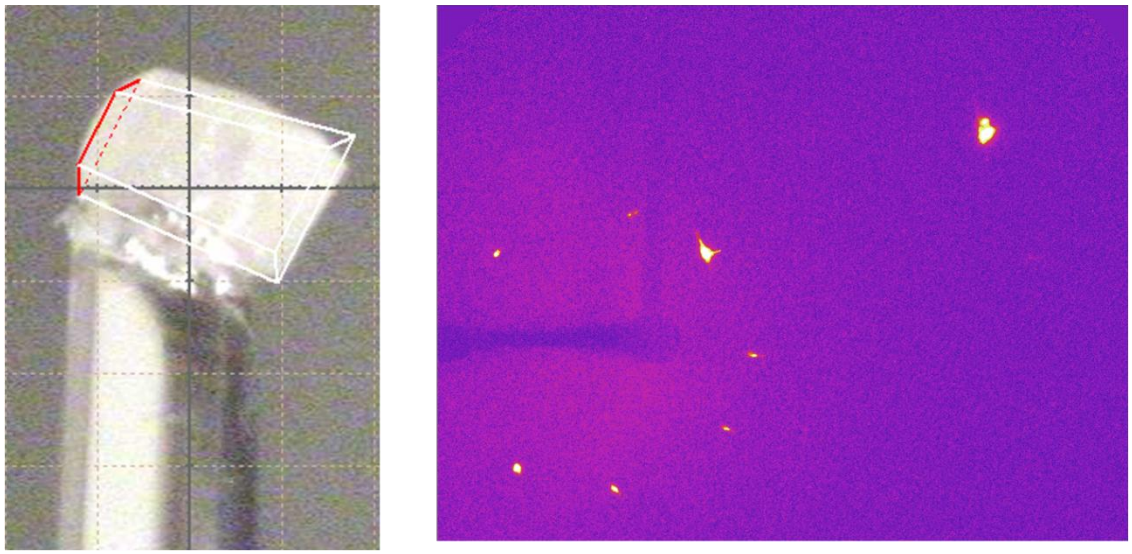

(a) (b)

Figure 5.5 Small KNN single crystal used for data collection (b) Diffraction pattern taken from one of the orientations.

5.3 Determination of local structure of KNN crystals using Pair Distribution Function (PDF) analysis

Reciprocal space X-ray diffraction analysis described above, considering a crystal to have ideal repetition of one unit cell, can provide only the average crystallographic information.[148] In case of complex solid solution ferroelectrics like KNN, where local crystallographic information is vital from the point of view of structure – property relationship, sometimes this averaging of crystal structure may be misinterpreted. Recently, in contrast to long known and universally accepted phenomena of phase transformation at Curie temperature (T_c), PZT was found to exhibit ferroelectric structure above T_c suggesting that transformation of structure at T_c is only

for long-range order.[148] Hence, atomic pair distribution function analysis (PDF) was performed to determine the local structure of x = 0.4, 0.5 and 0.6 composition KNN crystals.

In PDF technique, the reciprocal space powder diffraction data is Fourier transformed to real space to obtain the pair distribution function G(r).[148] Figure 5.6 shows the typical X-ray diffraction pattern in reciprocal space along with pair distribution function after Fourier transformation.

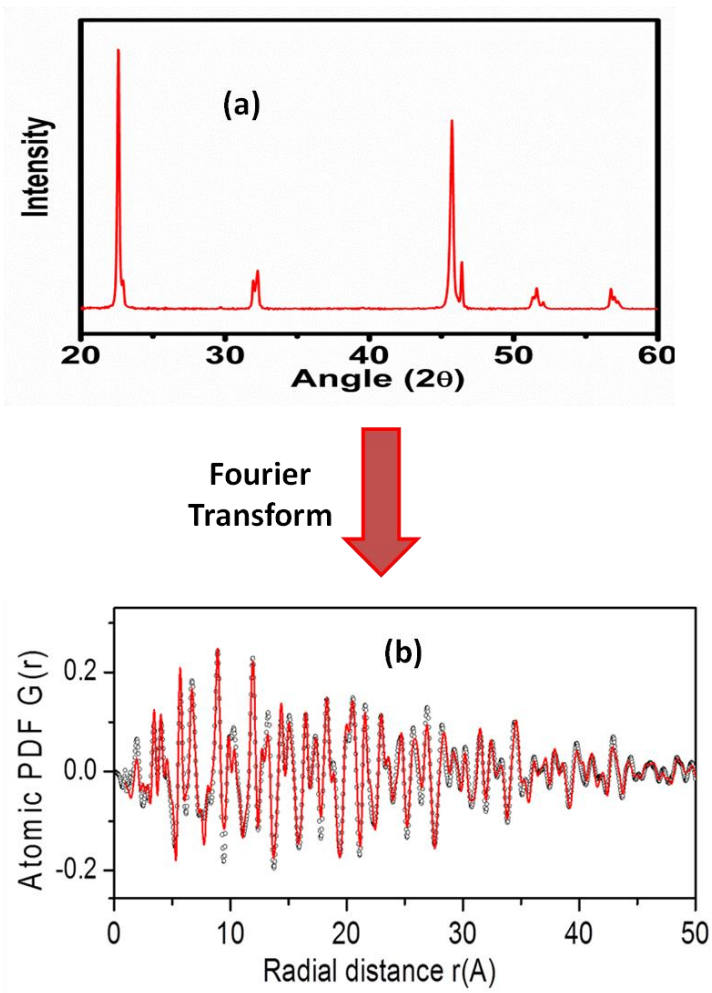

Figure 5.6 Conversion of (a) reciprocal space diffraction data to (b) real space data.

Figure 5.7 illustrates the pair distribution functions G(r) for three KNN compositions as a function of distance (r) from reference atom. In this technique by selecting the value of parameter r, number of unit cells over which average structure is to be determined, can be fixed. In present case, by determining the value of PDF for only 50Å, the structure is averaged for 10 – 15 pseudo-cubic unit cells, in contrast to normal X-ray diffraction analysis averaging the crystallographic data for millions of unit cells.

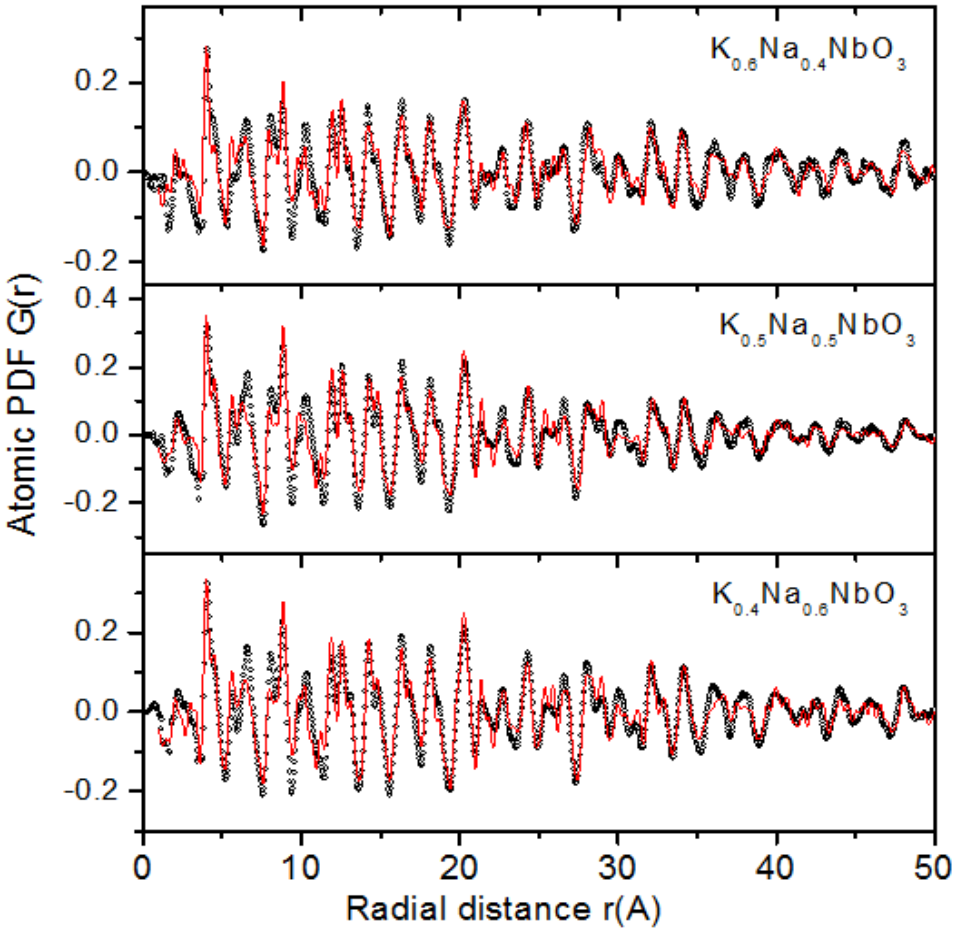

Figure 5.7 Atomic pair distribution function for x = 0.4, 0.5 and 0.6 crystals.

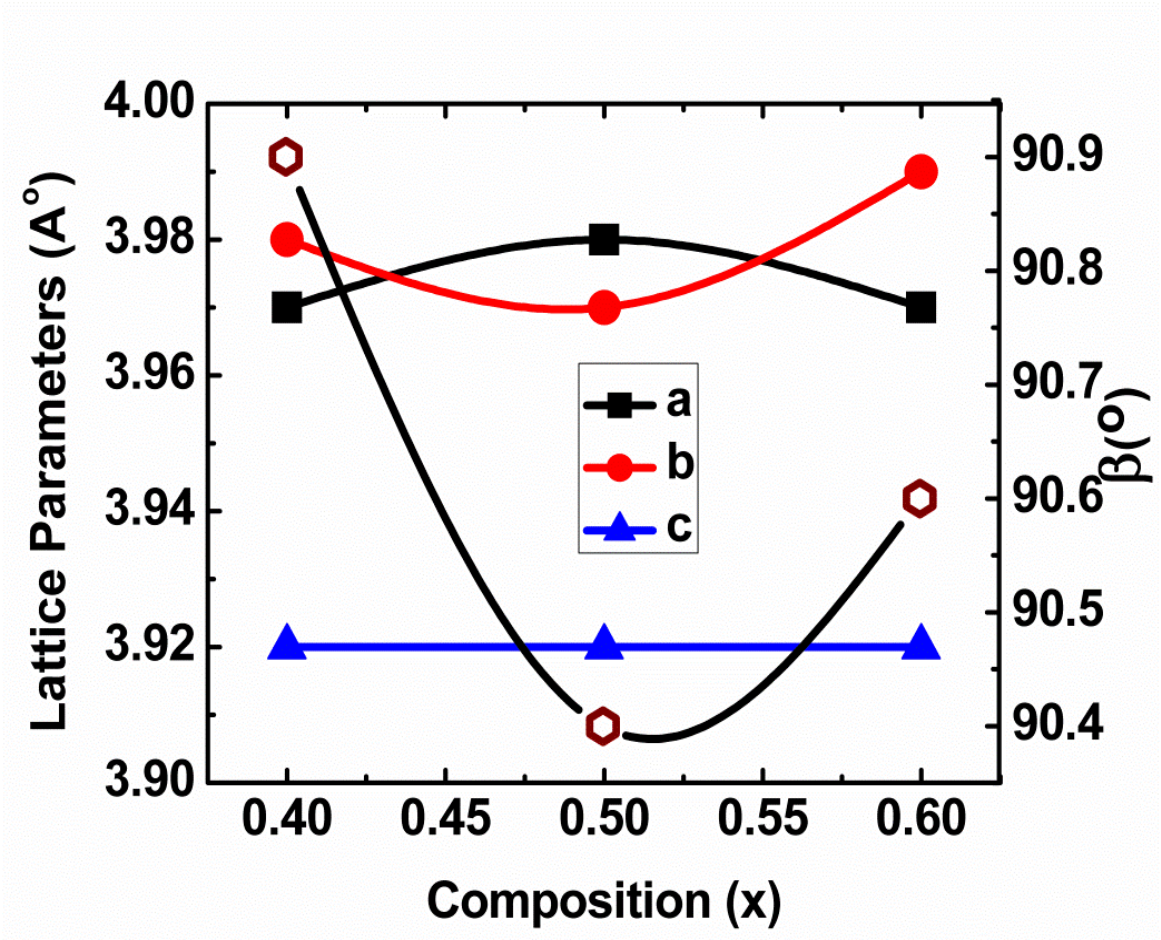

Figure 5.8 Variation of lattice parameters in the vicinity of x = 0.5.

Data refinement for three compositions suggests the monoclinic Pm symmetry for all of them. Though, if we carefully follow the variation of lattice parameters across the phase boundary (Figure 5.8), the point of inflation in lattice parameters can be seen close to the proposed phase boundary at x = 0.5. This observation is contrary to not only the known phase diagram of KNN, but also to our findings of macroscopic symmetry by optical birefringence study described in the previous chapter. Hence, it could be concluded that in KNN, proposed morphotropic phase boundary at x = 0.5 exists only for macroscopic symmetry, while local structure tends to remain

monoclinic across x = 0.5. Table 5.1 lists all the lattice parameters for x = 0.4, 0.5 and 0.6 crystals.

Table 5.1 Lattice parameters for x = 0.4, 0.5 and 0.6 KNN crystals

Composition	**a(Å)**	**b(Å)**	**c(Å)**	**β(^{o})**	**Space Group**
X = 0.4	3.97	3.98	3.92	90.9	*Pm*
X = 0.5	3.98	3.99	3.92	90.4	*Pm*
X = 0.6	3.97	3.97	3.92	90.6	*Pm*

Chapter 6

Sintering and Chemical Modification of KNN Ceramic

6.1 Sintering and Fatigue Behavior of $K_{0.5}Na_{0.5}NbO_3$ Ceramic

6.1.1 Introduction

Sodium potassium niobate ($K_{0.5}Na_{0.5}NbO_3$, abbreviated as KNN) is considered as one of the leading piezoelectric materials[1-3] owing to its environment friendly nature and high Curie temperature.[4, 8, 9, 95] Recently, significant improvement in piezoelectric properties of KNN has been achieved by means of compositional modifications, texturing, domain engineering and combination of these three strategies.[82, 149, 150] In spite of all its merits as a piezoelectric material, low sinterability and poor fatigue behavior of KNN restricts its use in commercial application.[151, 152] Figure 6.1 (a) shows the variation of the density of KNN ceramic as a function of sintering temperature. Density less than 92% of theoretical density was achieved by conventional solid state sintering at 1100°C.[152] Above this temperature, rapid grain growth took place and the density of ceramic started to decrease (Figure 6.1 (b) – (d)).[152] Besides, this sintering temperature is very close to melting point of KNN (1180°C - 1200°C) and processing at this temperature leads to rapid volatilization of lighter alkali elements, sodium and potassium, from the matrix.[153] The volatile nature of constituent elements also gives rise to instability of perovskite phase at high temperature and results in secondary tungsten bronze phase.[35] All these factors along with poor densification results in diminishing of piezoelectric and ferroelectric properties of KNN.[29, 34, 45, 154]

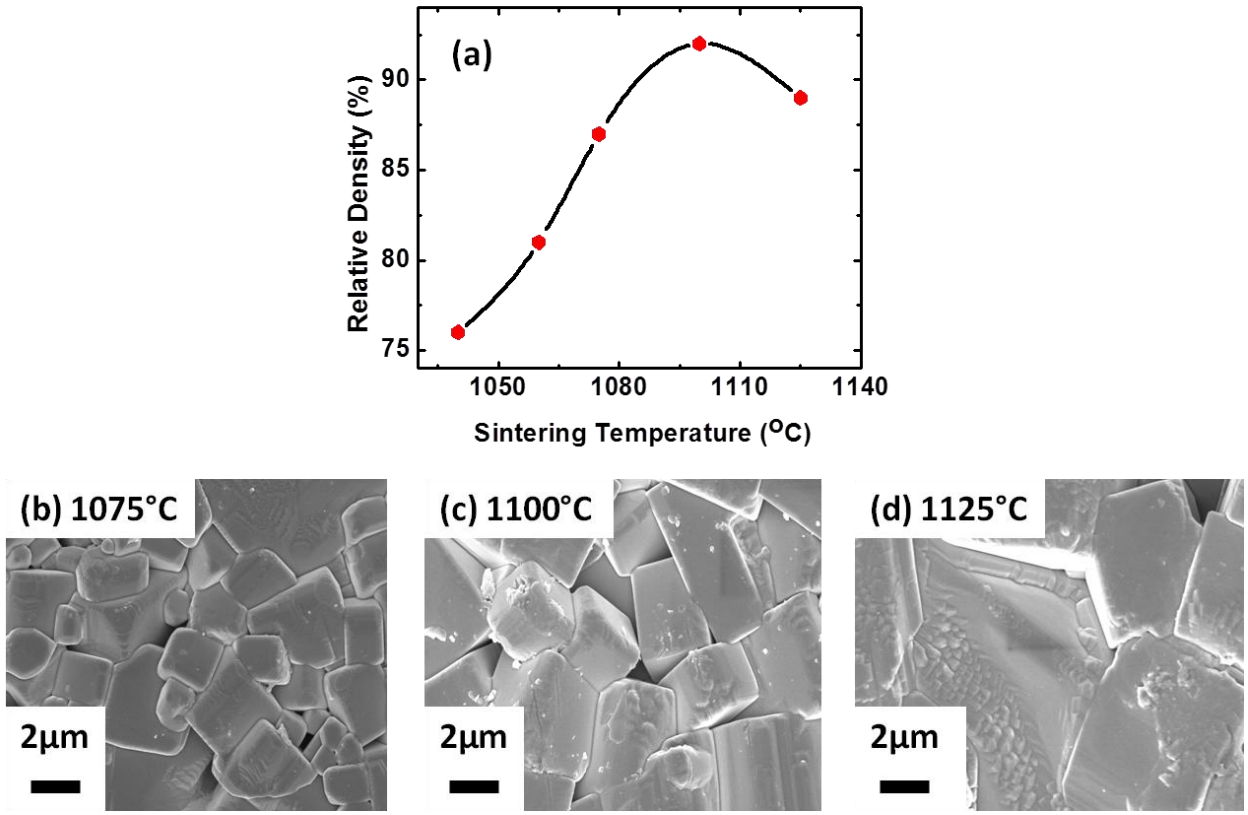

Figure 6.1Effect of sintering temperature on densification of KNN (a) Variation of density of KNN sintered by normal solid state sintering (b) (c) & (d) Variation of microstructure at different sintering temperatures

To address the problem of low sinterability in KNN, a number of techniques have been employed in the last few decades. Commonly, researchers have utilized different oxides as sintering additives that melt below the sintering temperature of KNN and provide higher density by means of liquid phase sintering (LPS).[27, 155, 156] ZnO, SnO_2 CuO, $K_{5.4}Cu_{1.3}Ta_{10}O_{29}$ (KCT), $K_4CuNb_8O_{23}$ (KCN) and MnO_2 are examples of the common sintering additives used with KNN-based compositions.[34, 45, 46] During high temperature sintering, most of these additives are known to diffuse in the KNN lattice and alter the stoichiometry of $K_{0.5}Na_{0.5}NbO_3$.[34] Besides in certain cases, depending upon the size and charge of cation, charge defects are created.[30] All these

alterations result in either decrease in piezoresponse or drop in transition temperatures, hence compromising the advantages of KNN.[30, 34]

To overcome the disadvantages of using sintering additives, different nonconventional processing techniques have been employed to achieve higher density in KNN ceramics. Effect of particle size on sinterability has been demonstrated by the use of attrition milling and high energy ball milling of KNN powder before compaction. Besides, sintering techniques like hot pressing (HP) and spark plasma sintering (SPM) have been employed to achieve high density in KNN ceramic.[38, 157] Among all these nonconventional processing techniques, SPS has been shown to be most effective in providing density as high as > 99 % of theoretical density.[38] This high density resulted in improved electromechanical coupling, but at the same time smaller grain size resulted in diminishing of ferroelectric behavior.[38] In spite of being more effective as compared to the conventional processes, all these nonconventional techniques are complicated and costly. Also the techniques such as SPS has limitation on the size of sample that can be synthesized.[38]

In this thesis, a modified two-fold sintering technique was developed to achieve > 99 % density in KNN ceramic without the incorporation of any foreign additive or non-conventional processing technique. These high density ceramics (referred as KNN-S, hereafter) exhibited significantly reduced lattice defects and demonstrated excellent piezoresponse as compared to the conventionally synthesized counterpart (referred as KNN-N, hereafter).

Apart from the magnitude, stability of the electromechanical properties against the cyclic electric loading is also a requirement for any device application of KNN. Systematic loss of the switchable polarization under cyclic external electric field is a well-known phenomenon in

ferroelectrics and is defined as a polarization fatigue.[158] This polarization loss simultaneously leads to a degradation of the dielectric and piezoelectric properties. Ferroelectric fatigue is known to occur through accumulation of charged defects resulting in pinning of domain walls,[159] defect cluster growth,[160] formation of space charge layer at ferroelectric – electrode interface,[161] micro-cracking due to strain incompatibility,[162] and electric field driven charge fluctuation of ions[163].[164] In case of KNN, few studies have investigated the fatigue behavior but the mechanism behind the loss of switchable polarization is not clear.[151, 165, 166] In this chapter, the fatigue behavior of KNN ceramics was studied under bipolar electric loading. Along with KNN-S and KNN-N, KNN ceramic sintered with sintering profile similar to KNN-S but having no incorporation of alkali carbonates during sintering (referred as KNN-N′ hereafter) were studied under cyclic loading to reveal their fatigue behavior. Impedance spectroscopic analysis was performed on KNN-S and KNN-N′ to correlate the nature of defects present along with their fatigue behavior.

6.1.2 Experimental Work

KNN ceramic powders were synthesized by conventional solid state synthesis process using high purity precursors (all from Alfa Aesar with > 99 % purity). Stoichiometric amounts of sodium carbonate (Na_2CO_3), potassium carbonate (K_2CO_3) and niobium oxide (Nb_2O_5) were ball milled in ethanol medium for 24 hours before calcination. Calcination was performed in an alumina crucible in the temperature range of 550°C - 800°C. After calcination, 0.5 mole% of sodium and potassium carbonate was added to the KNN powder as sintering additives, followed by second ball milling for another 24 hours. Prior to two-step sintering, KNN powder was sieved through the 90 μm mesh followed by compaction in different shapes under cold isostatic pressure of 20

kPa. To reveal the effect of incorporation of sodium and potassium carbonates as sintering additives and of the two step sintering profile, KNN samples were sintered in the temperature range of 1020°C – 1120°C by conventional single-step sintering process without presence of any sintering additives. To study the effect of presence of alkali carbonates during sintering of KNN-S on its defect chemistry and fatigue behavior, KNN ceramic with sintering profile similar to KNN-S but having absence of alkali carbonates during sintering were synthesized as well. After sintering, samples were characterized for their crystallographic phase using Panalytical X-ray diffractometer with Kα radiation. To perform the electric measurements, gold electrodes were sputtered on different shaped samples, followed by firing at 500°C. Dielectric measurements were performed using a multi-frequency LCR meter HP 4287A. Low-field piezoelectric coefficient (d_{33}) values were measured by using YE 2730 A d_{33}-meter. The polarization vs. electric field hysteresis curves were measured using Radiant ferroelectric tester based on Sawyer – Tower bridge concept. Electromechanical coupling coefficients (k_p & k_{31}) and piezoelectric coefficient (d_{31}) were determined using resonance – anti-resonance technique using HP 4192A impedance analyzer. Piezoresponse force microscopic (PFM) studies were performed using Bruker Dimension Icon system.

6.2.3 Result and Discussion

According to the previous investigations, KNN ceramic powder was calcined in the temperature range of 800°C - 950°C for 2h – 5h.[18,23] Calcination at temperatures lower than 800°C results in presence of broad peaks in x-ray diffraction pattern, suggestive of chemically non-homogeneous solid solution.[18] But since the melting points of two carbonates lie in the temperature range of 800°C – 900°C, loss of alkali ions cannot be ruled out during calcination, prior to chemical

reaction among them. This loss may further lead to defect formation and hence diminishing of piezoresponse.

To minimize the loss of alkali ions during calcination, in the present study efforts were made to decrease the calcination temperature of KNN. Figure 6.2 (a) – (c) illustrates the x-ray diffraction patterns of calcined KNN powder at temperatures 550°C, 600°C and 850°C respectively for 2 hours. It is evident that KNN powder calcined at temperature as low as 600°C formed a perovskite phase without the presence of any noticeable unreacted precursors, whereas powder calcined at 550°C showed the presence of such phases. Hence, for the present work, KNN powder calcined at 600°C was used for further processing. The minor chemical non-homogeneity evident from the presence of broad XRD peaks could be taken care of during sintering. Considering the disadvantages of previously used sintering additives described earlier, [30] sodium and potassium carbonates were used as sintering additives. These two carbonates release the CO_2 at temperature > 400°C and forms alkali oxides, which melts at 850°C – 900°C. Formation of a melt about 200°C - 300°C below the sintering temperature is desired condition for a sintering additive to be effective. Along with facilitating the liquid phase sintering, sodium and potassium carbonates have advantage that the diffusion of Na and K is not problematic. In addition, presence of the thin layer of sodium and potassium oxides[155] (Na_2O and K_2O) between KNN particles is also expected to reduce the volatilization of alkali elements.

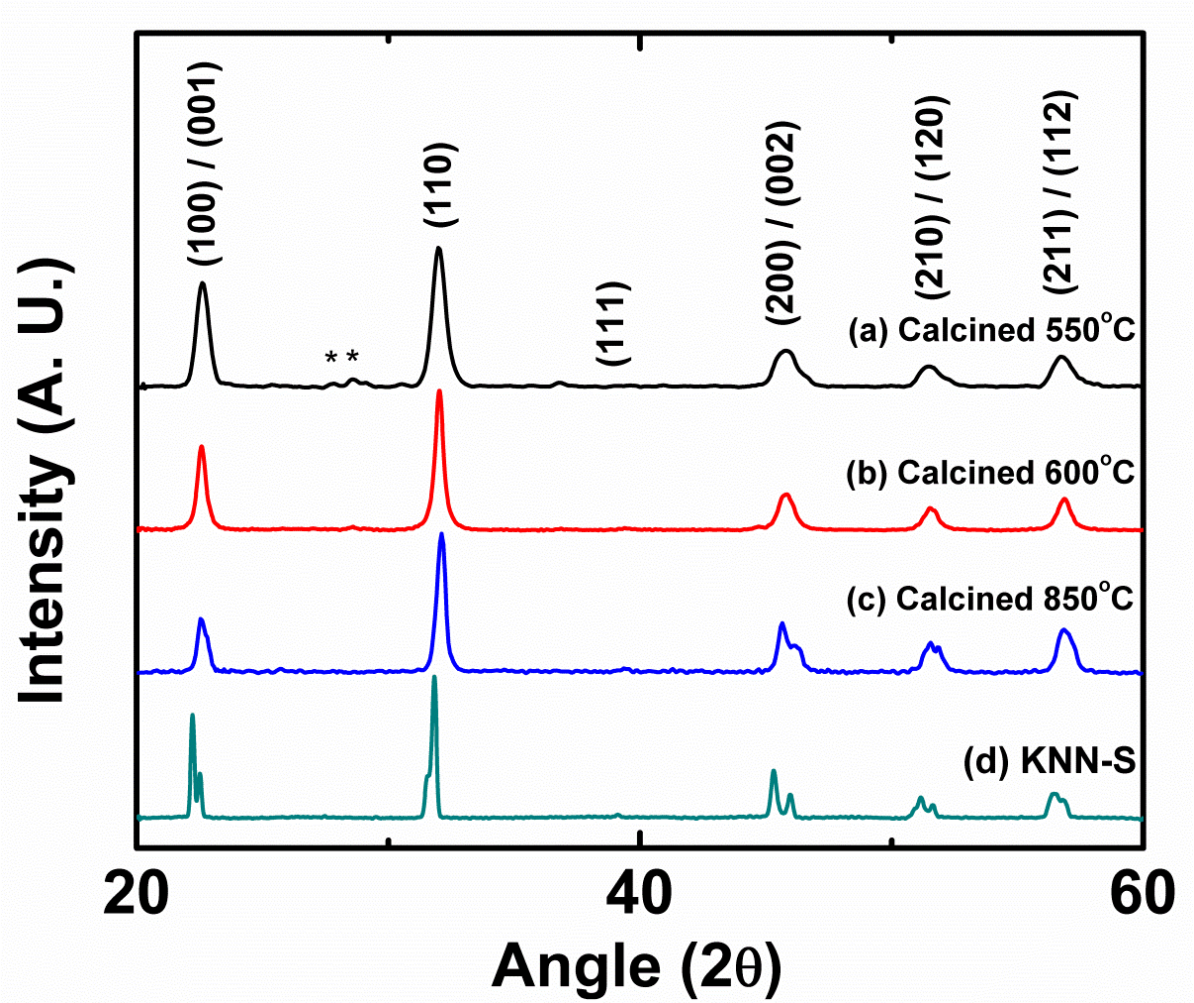

Figure 6.2 X-ray diffraction plots of KNN ceramics calcined at (a) 550°C, (b) 600°C, (c) 850°C, and (d) Sintered KNN-S ceramic.

Good wetting ability and solubility of base matrix with the melt is the primary requirement for the effectiveness of any additive in liquid phase sintering.[27, 155, 167, 168] First stage of LPS, resulting in more efficient packing of matrix particles due to capillary action of melt, requires good wetting of matrix particles with melt. This stage begins with the melt formation and is completed within 10-40 minutes. In the second stage of LPS, good solubility of matrix particles in melt helps in faster diffusion of the smaller particles to positions of lower energy, and hence improved shape accommodation.[168] To confirm the effectiveness of alkali oxides on these

two fronts, KNN samples with and without the presence of sintering additives were heated to 1080°C followed by immediate cooling without holding at this temperature for any amount of time (to be referred as 0 minute sintering, hereafter). Presence of alkali carbonates as sintering additives improved the density of KNN ceramic from 66% to 75% for sample sintered at 1080°C for 0 minute (Figures 6.3 (a) and (b)), confirming the advantage of presence of melt during first stage of LPS. Figures 6.3 (c) and (d) show the microstructures of samples sintered for 2 hours at 1130°C, with and without the sintering additives. Since third stage of LPS is also governed by solid state sintering phenomenon, any difference in the microstructure of these ceramics can only be attributed to the second stage of LPS. Two samples were found to have respective densities of 75% and 91% of theoretical density of KNN. It is important to note that the KNN sample sintered without any additive has grain size up to 10μm in contrast to 2μm grain size for ceramic sintered with alkali additives. This observation suggests that in addition to better grain accommodation in first step of sintering, presence of alkali oxide melt also helps in densification by inhibiting the grain growth of KNN ceramic at the second stage of LPS. In case of perovskite oxides, grain growth is normally controlled by the slowest diffusing cations and deficiency of A-site ions can play a significant role.[169] Also, presence of melt can increase the activation energy for grain growth and lead to smaller grain size.[170] Hence, inhibition of grain growth by the presence of melt in second stage of LPS could be either due to of the reduction of A-site vacancies or due to the increase in grain growth activation energy. But in spite of impeded grain growth, presence of alkali melts could not provide density higher than 91% of theoretical density of KNN.

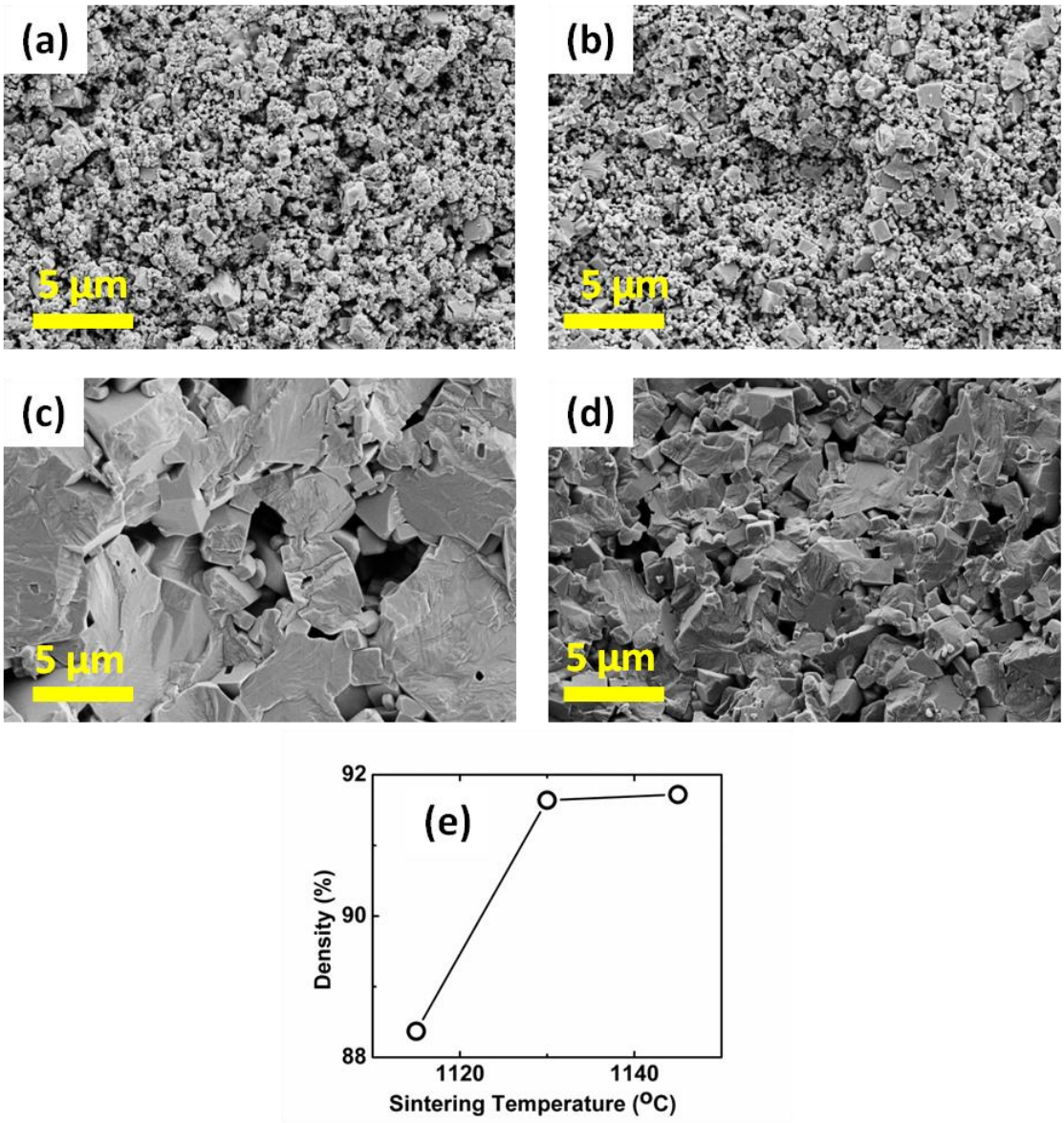

Figure 6.3 SEM images showing the microstructure of KNN ceramic sintered by conventional sintering technique at (a) 1080°C, 0 minute and (c) 1130°C, 2h. KNN ceramic sintered with the presence of alkali carbonates during sintering at (b) 1080°C, 0 minute (d) 1130°C, 2h (e) Variation of density of KNN ceramic with sintering temperature.

. Figure 6.3(e) shows the variation of density with the sintering temperature in the temperature range of 1115°C – 1145°C, suggesting that the saturation occurs at 92 % by use of alkali carbonates as sintering additives at sintering temperature of 1145°C. Along with kinetic drive, rapid evaporation of alkali oxides at higher temperatures could be playing an important role in rapid grain growth and saturation of density in the temperature range of 1130°C – 1145°C. Grain growth during densification is the inseparable part of the sintering process during each of the three steps. But in the first two steps of sintering, presence of a continuous pore network prevents the rapid grain growth.[171] On the other hand, in the third stage of sintering absence of continuous pore network leads to the onset of rapid grain growth.[171] According to the theoretical calculations performed on ceramics, the maximum density up to which this onset can be delayed is 92%.[172, 173] At densities higher than this, pores become isolated and hence rapid grain growth occurs.[172]

To suppress the grain growth further to achieve higher density for KNN ceramic, a two-step sintering technique was employed along with the use of alkali carbonates as sintering additives. Recently, two-step sintering has been proven to be an effective tool to achieve high density in ceramics with controlled grain growth in the final stage of sintering.[171, 174, 175] Though originally this method was proposed for sintering nano-ceramics, but the phenomenon holds equally well in the other scenarios where grain growth needs to be controlled while enhancing the density. This technique utilizes the presence of continuous pore network between particles to inhibit the grain boundary migration and hence grain growth. In this method, sample is heated to a high temperature for a small time period in order to achieve a density higher than > 70%, which preserves the desired pore – grain geometry in order to retard the grain boundary migration in the second step of sintering at relatively lower temperature. Hence the kinetic

difference between grain boundary diffusion and grain boundary migration leads to densification during second step without any significant grain growth.[171, 174, 176] This phenomenon is found to be equally valid for the sintering of ceramics in the presence of liquid phase.[177]

To employ the two-step sintering technique, KNN ceramic with 0.5 mole% of alkali carbonates were sintered according to the heating profile shown in Figure 6.4 (a). During the first step, samples were heated to 1160°C for 5 minutes while in the second step sintering was done for two hours in the temperature range of 1125°C – 1135°C. Figure 6.4 (b) shows the microstructure of ceramic after the first step (1160°C, 5 minutes), which was found to have density of 85% - 89%. This value of density is lower than the critical value of density for pore isolation in order to prevent the onset of rapid grain growth. Figures 6.4 (c) illustrates the microstructures and temperature (T_2) vs. density profile of samples sintered after two step sintering with 1125°C < T_2 < 1135°C. Consistent with the dense microstructures, the profile demonstrates that a density as high as > 99% could be achieved by this two-fold sintering technique . KNN ceramic sintered at T_2 = 1130°C and having density > 99 % of theoretical density of KNN (KNN-S) were characterized for their ferroelectric, piezoelectric and fatigue behavior in order to reveal the effect of higher density.

In order to compare the different properties with normal solid state sintered KNN, ceramic samples were sintered in the temperature range 1040°C – 1120°C. Among these, ceramic sintered at 1100°C was found to have highest density of 92% of theoretical density of KNN and hence chosen for electrical characterization (KNN-N).[152] KNN- ceramic sintered with heating profile of KNN-S but having absence of alkali carbonates during sintering were characterized for fatigue behavior.

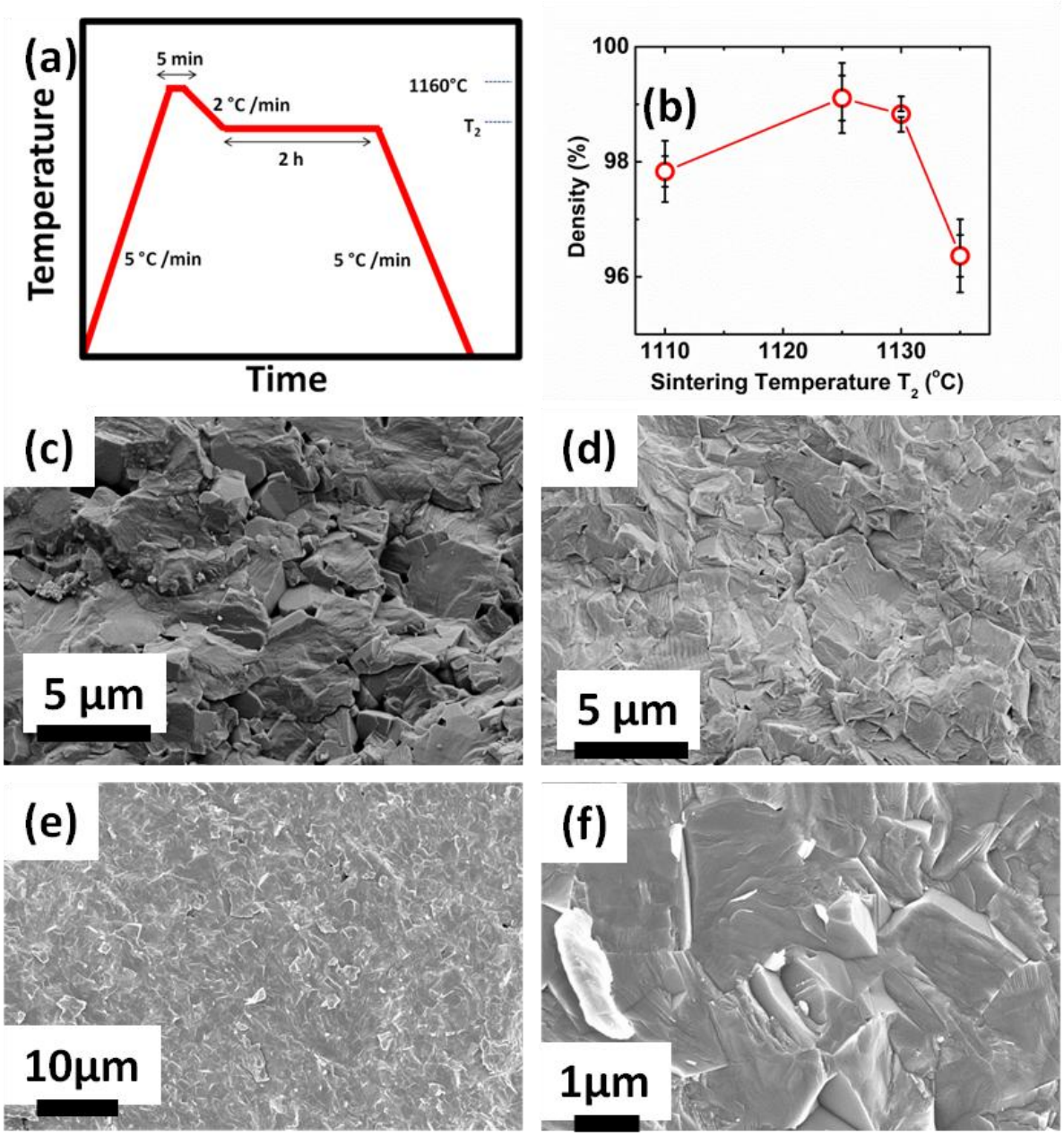

Figure 6.4 Sintering profile and microstructures used for KNN-S ceramics (a) heating profile (b) variation of density of KNN-S ceramic with temperature T_2 (c) microstructure of KNN ceramic sintered at 1160 °C for 5 minutes (d), (e) and (f) microstructure of KNN-S ceramic for T_2 = 1130°C at different magnifications.

Figure 6.5 (a) shows the ferroelectric loops (P-E) measured for KNN-S and KNN-N at 70 kV/cm. As illustrated, KNN-S and KNN-N were found to have similar values of coercive field and remanent polarization. Figures 6.5 (b) illustrates the current density vs. electric field (J-E) plots obtained for two samples in the electric field range of ± 50 kV/cm. Drops in current density values close to coercive fields indicates the dominance of displacement over leakage current in

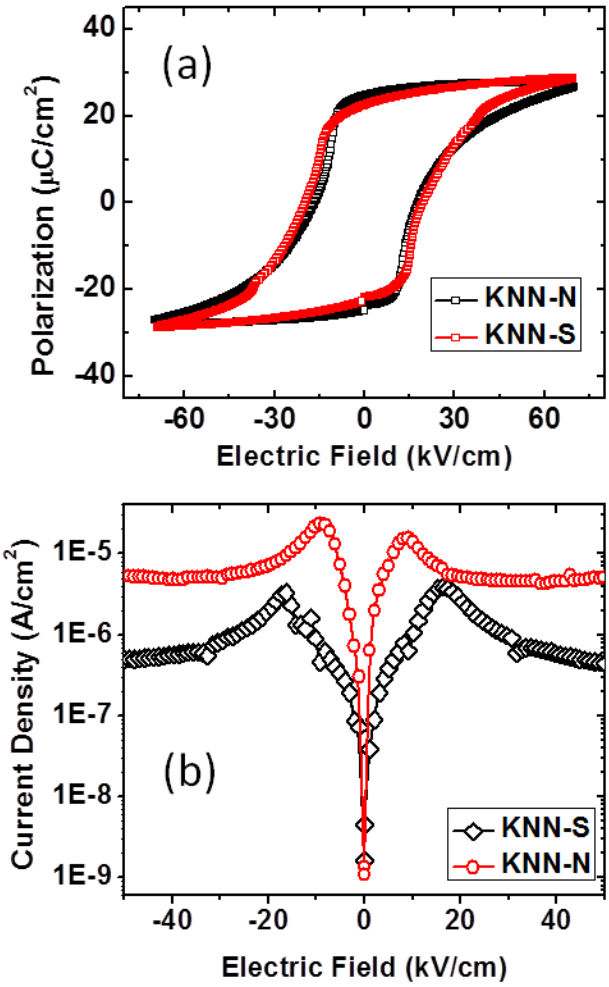

Figure 6.5 (a) P-E and (b) I-V characteristics for KNN-S and KNN-N ceramics

these samples at lower electric fields. Contrary to the ferroelectric loops, KNN-N was found to have peak in current density at lower field as compared to KNN-S. At fields much higher than coercive field of two samples (~ 50 kV/cm), when leakage current is expected to dominate over displacement current, an order of magnitude lower current density for KNN-S confirms their higher resistivity as compared to KNN-N. This observation confirms the hypothesis that presence of alkali oxide melt during sintering of KNN ceramic not only helps in achieving higher densification but also reduces the defect formation. At room temperature both the samples were found to have similar values of dielectric constants with dielectric loss being slightly higher for KNN-S. Dielectric anomalies at higher temperatures are indicative of first orthorhombic / monoclinic to tetragonal transition at 200°C followed by the tetragonal to cubic one at 395°C.

Table 6.1 lists the dielectric, ferroelectric and piezoelectric coefficients obtained for KNN-S and KNN-N samples. For comparison, values of these parameters are also listed for KNN ceramics sintered by non-conventional techniques like hot pressing (KNN-HP) and spark plasma sintering (KNN-SPS).[4, 38] For conventionally sintered ceramics, highest density achieved by sintering at 1100°C was about 92% of theoretical density. In contrast, the two-fold sintering technique developed in this study resulted in density > 99 % of theoretical density of KNN, similar to densification achieved by non-conventional sintering techniques like HP and SPS. This high density and the reduced concentration of A-site defects resulted in significant improvement in different electromechanical coefficients for KNN-S, as compared to KNN-N. Low field longitudinal and length mode piezoelectric coefficients (d_{31} and d_{33}), and planer coupling coefficient (k_p) showed about a two-fold improvement in their values. Values of different piezoelectric coefficients for KNN-S are close to those achieved for HP and SPS sintered samples. Remanent polarization for KNN-S was about three times higher than that for KNN-

SPS. As mentioned earlier, high value of remanant and saturation polarization of KNN-N could be attributed to its softer nature. Interestingly, dielectric constant value for both KNN-N and KNN-S samples were found to be significantly smaller than those for KNN-HP and KNN-SPS. This difference could be attributed to the grain size effect in these ceramics, as KNN-SPS was previously reported to have very small grain size.

Table 6.1 Comparison of piezoelectric, dielectric and ferroelectric properties of KNN-S, KNN-N, KNN-SPS and KNN-HP ceramics

Sample	**KNN-S**	**KNN-N**	**KNN-SPS**	**KNN-HP**
Density (%)	> 99	92	> 99	98.8
K (1 kHz)	323	312	606	420
Loss (1 kHz)	0.038	0.023	0.036	-
T_{o-t} (°C)	200	200	-	-
T_c (°C)	395	395	395	-
E_c (kV/cm)	19	16	13	-
P_r (μC/cm^2)	22	32	6.5	-
d_{33} (pC/N)	150 - 160	80 - 90	148	160
- d_{31} (pC/N)	45	23	-	49
d_h (pC/N)	65	39	-	62
Q_M	-	-	-	240
k_p	0.45	0.24	-	0.45
k_{31}	0.23	0.16	-	0.27

Previously KNN based compositions have been reported to exhibit reduction of 80 % of ferroelectric polarization in only 20 cycles of electric field.[178]

To study the effect of high density and reduced defects in KNN-S ceramics on fatigue behavior, KNN-S, KNN-N and KNN-N′ ceramics were subjected to cyclic electric loading under the electric field at about twice of coercive field ($2E_c$) for 65 million cycles. Figure 6.6 (a) shows the variation of saturation and remnant polarization values with number of cycles for KNN-S ceramic electroded with silver. Polarization showed a little drop in first 500 cycles but became stable after that up to 30 K cycles. Interestingly, polarization starts increasing after about 30 K cycles and attains values even higher than initial magnitude. Also, after the measurements the surface of pellet was found to turn black at few points where silver electrodes disappeared. To reveal the origin of this observation, SEM images were taken on cross-section of the surface of pellet after fatigue measurement (Figure 6.6 (b)). It can be seen that the surface of sample had two kinds of microstructures, which might belong to KNN and silver. Also fractured surface of sample showed poor density as compared to sample before fatigue measurement (Figure 6.6 (c)). All these observations suggested the continuous diffusion of silver into the KNN ceramic during electric cycling. Previous investigations performed to study the diffusion of silver electrodes in the PZT have also shown high diffusivity and hence degradation of piezoresponse.[179] Since silver electroded KNN ceramics do not reveal their inherent fatigue behavior, gold electrode was sputtered on all three ceramics for fatigue behavior study.

Figure 6.7 shows the fatigue behavior of KNN-S, KNN-N and KNN-N′ ceramic samples with gold electrodes. Unlike silver, gold electrodes did not show any sign of diffusion into the ceramic pellet. On comparing the fatigue behavior of KNN-S and KNN-N ceramics (Figure 6.7 (a) and (b)), it can be seen that for equal number of electric cycles they show about 47% and

70% drop in polarization values respectively. The profile of polarization drop was different in the two ceramics. KNN-S showed a continuous drop while KNN-N showed better stability up to 20 K cycles followed by a logarithmic drop. It can be concluded from this observation that modified sintering technique developed in this study not only provided better electromechanical properties, but also delayed the logarithmic drop regime in fatigue behavior beyond 65 million cycles. To better understand the origin of better fatigue behavior of KNN-S, fatigue behavior of KNN-N′ ceramic was also studied. KNN-N′ sintered with similar heating profile as KNN-S, but had no presence of carbonates during sintering showed a drastic decrease in ferroelectric polarization after 20 K cycles and polarization loops were found to collapse after 100 K cycles.

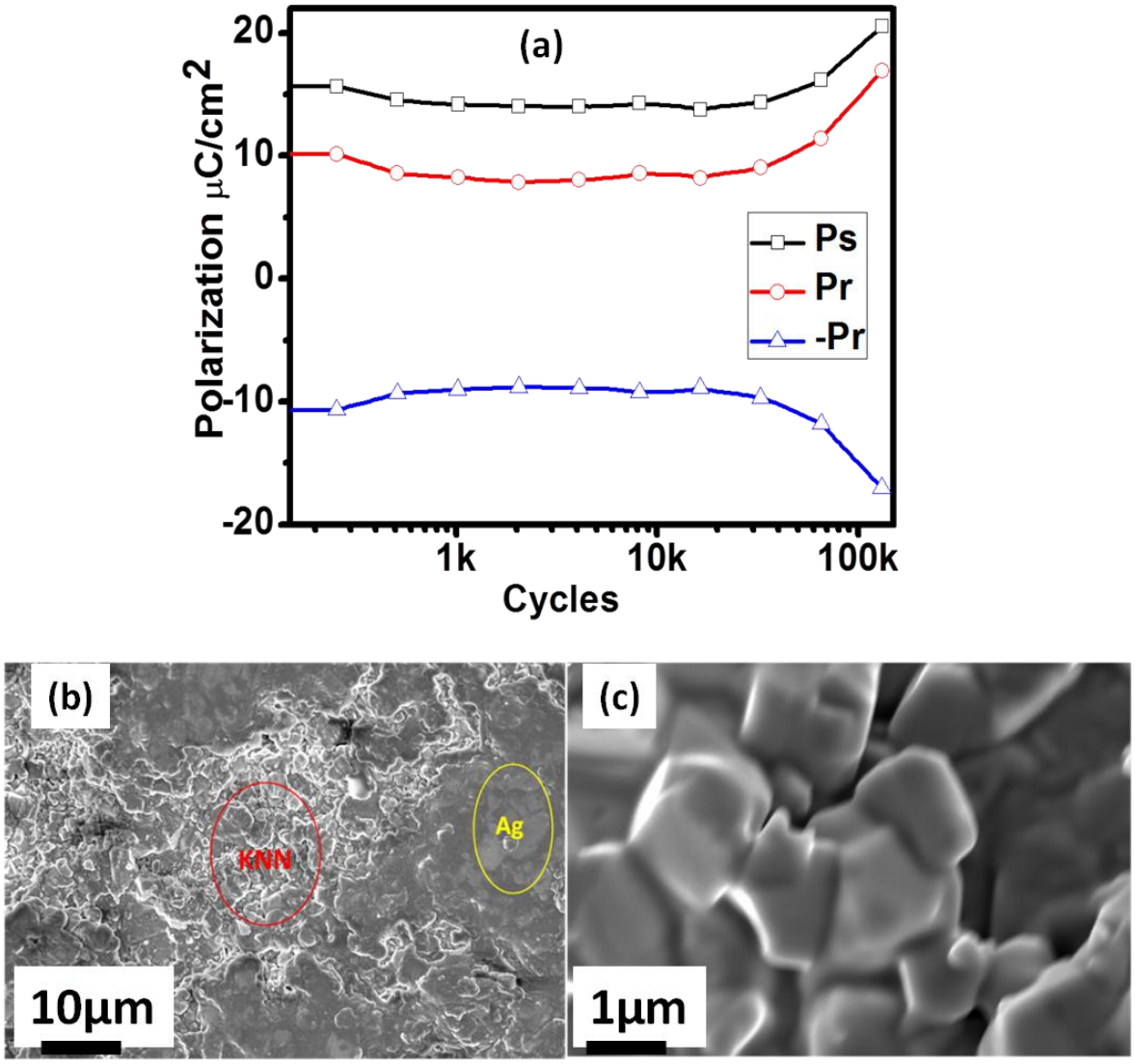

Figure 6.6 Fatigue behavior of silver electrode KNN ceramic (a) Variation of polarization values for KNN-S ceramic electrode with silver (b) and (c) micrographs showing the top electrode surface and fractured surface of ceramic after 200 K cycles of loading

Since KNN-N and KNN-N′ have similar densification, poor fatigue behavior of KNN-N′ could only be attributed to its higher sintering temperature and time, leading to higher evaporation of alkali elements. This higher evaporation resulted in A-site deficiency in lattice, simultaneously leading to oxygen ion vacancies in order to maintain the charge balance.[180] On

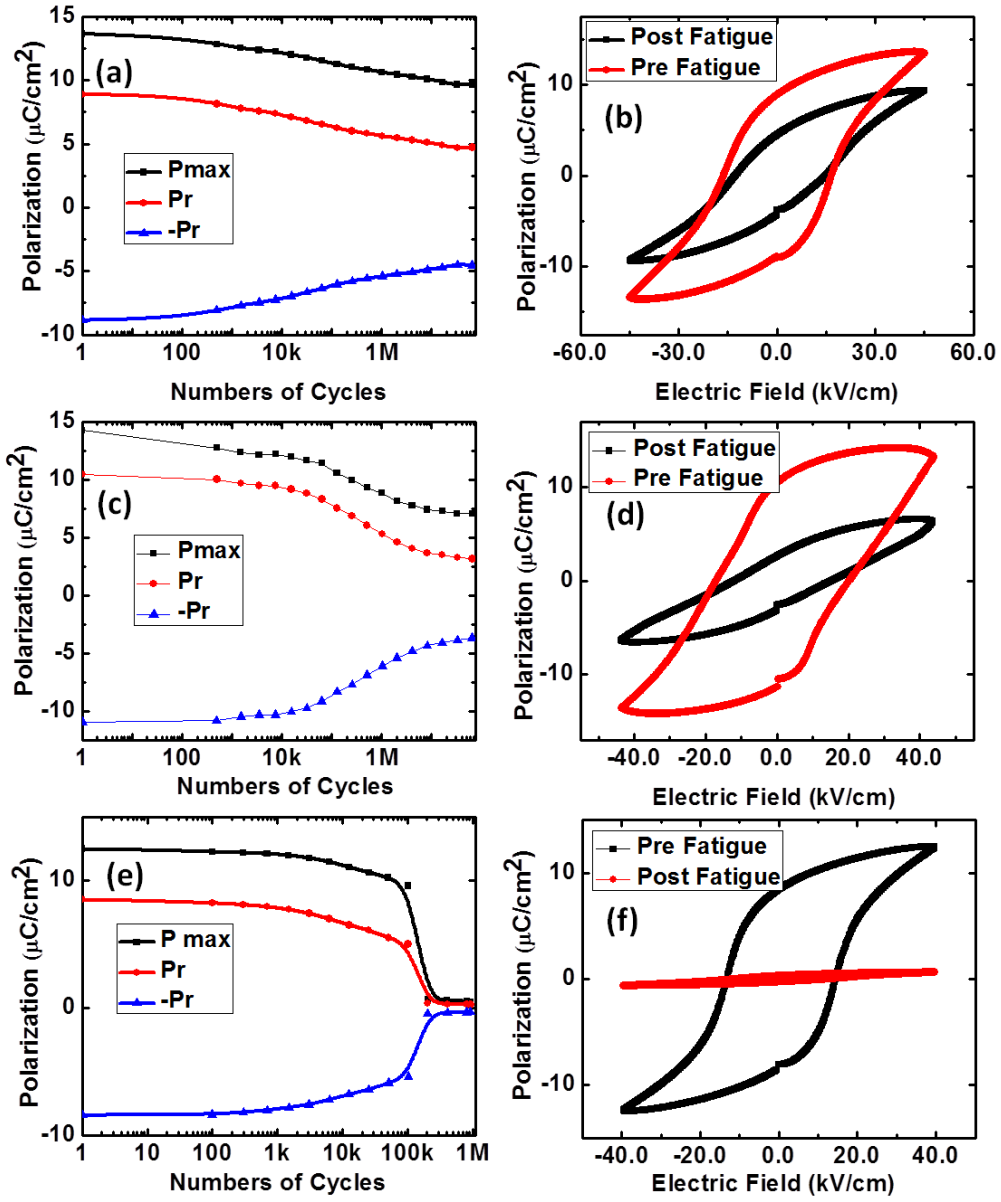

Figure 6.7 Fatigue behavior of gold electroded KNN ceramic (a), (c) and (e) Variation of ferroelectric polarization with numbers of cycles for KNN-S, KNN-N and KNN-N′ ceramics respectively (b), (d) and (e) Ferroelectric loops for KNN-S, KNN-N and KNN-N′ ceramics before and after fatigue.

the other hand for a KNN-S ceramic presence of alkali carbonates during sintering helped in limiting the defects up to some extent and hence developed a better fatigue behavior, consistent with our initial hypothesis.

To further elaborate the advantage of presence of alkali carbonates during sintering, impedance spectroscopic analysis was performed on KNN-S and KNN-N′ ceramics. Impedance data was collected in the temperature range of 25°C – 600°C in the frequency range of 100 Hz – 1 MHz. Due to high resistivity of ceramics, complex impedance plots in the ferroelectric regime (T < 400°C) could not be analyzed. Figure 6.8 (a), (c), (e) and (b), (d) (f) showed the real, imaginary and complex impedance plots for two ceramics. These impedance values were normalized according to the dimensions of the two samples. Only one semicircle can be seen in the complex impedance plots, which may belong to any of the three contributions, namely bulk, grain boundary and electrode – ceramic interface. By fitting the complex impedance plots to semicircles, corresponding values of capacitance (C) and resistance (R) were determined. To confirm that this semi-circle belongs to bulk contribution, 1/C values were plotted as a function of temperature for two ceramics according to Curie – Weiss law. Linear variation of 1/C with temperature (Figure 6.8 (g)) confirms that capacitance values follow the Curie – Weiss law and hence these semi circles belong to bulk contributions of KNN-S and KNN-N′ respectively. DC conductivity values for two ceramics ($\sigma = l/AR$) are plotted as function of 1000/T in Figure 6.8 (h). KNN-S not only shows about an order of magnitude improvement in resistivity, but also linear fit to the plots reveal the activation energy of conduction to be 1.4eV for KNN-S in contrast to 1 eV for KNN-N′. In perovskites, 1eV activation energy is generally attributed to the oxygen vacancy conduction, [181] and hence it can be concluded that KNN-S ceramic had lower concentration of oxygen vacancies, and which could be the origin of their better fatigue behavior.

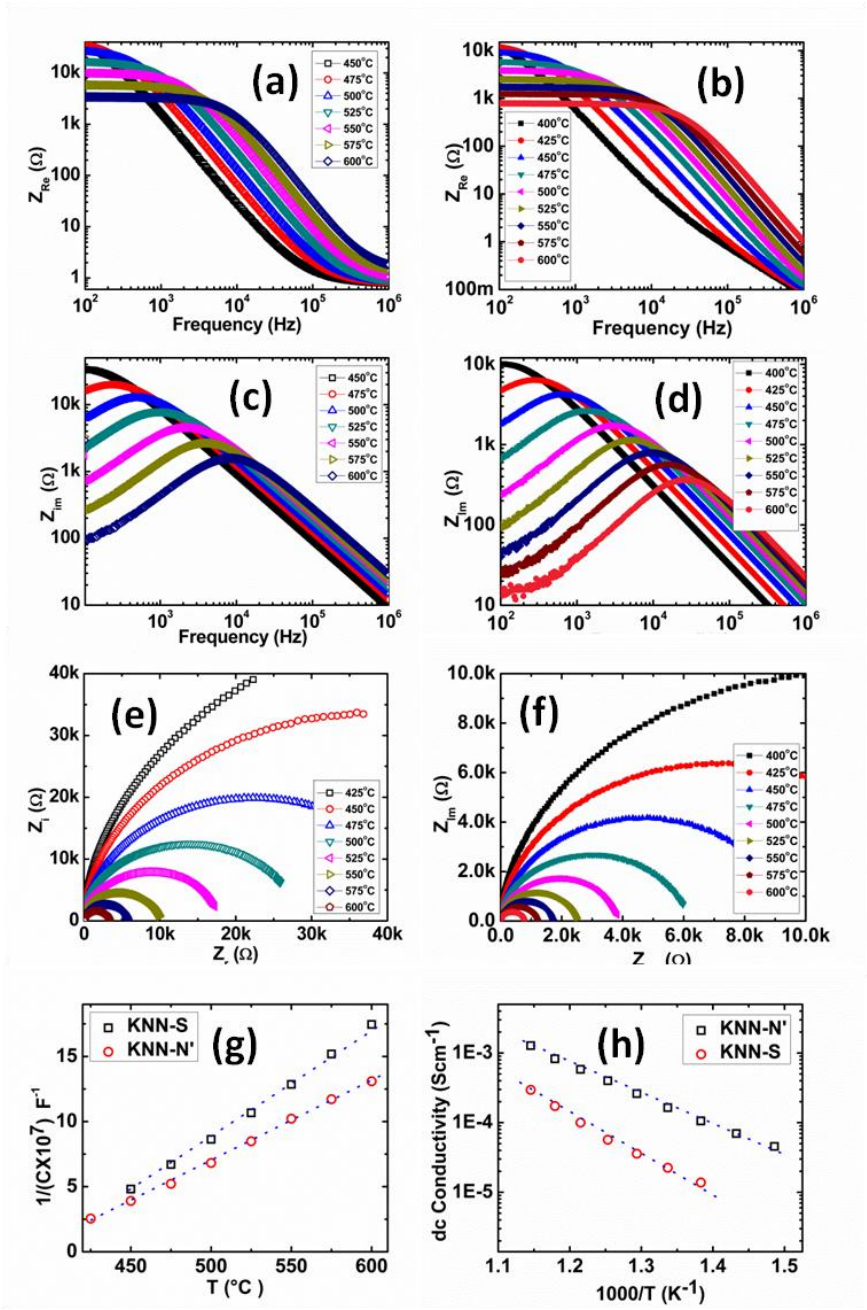

Figure 6.8 Real and imaginary parts of complex impedance as a function of frequency at different temperatures (a) and (c) KNN-S (b) and (d) KNN-N′. Complex impedance plots for (e) KNN-S and (f) KNN-N′ (g) Inverse of capacitance vs. temperature for KNN-S and KNN-N′ (bh) Conductivity vs. 1000/T for for KNN-S and KNN-N′

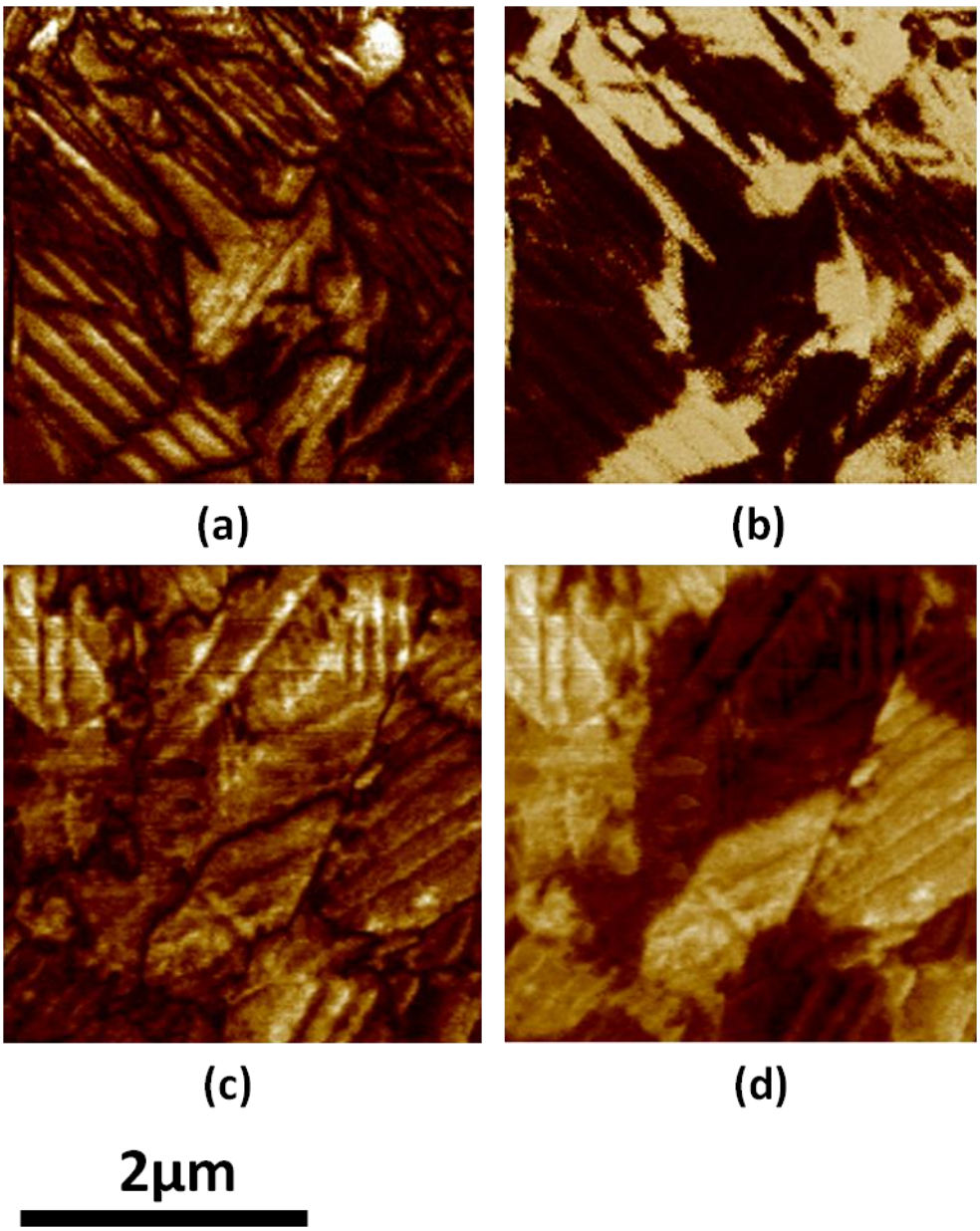

Figure 6.9 Piezoresponse force microscopy images for KNN-S and KNN-N′ respectively (a) and (c) amplitude and (b) and (d) phase.

To reveal any difference in domain structure of KNN-S and KNN-N′ ceramics, piezoresponse force microscopy (PFM) was performed on two samples. Figure 6.9 shows the amplitude and phase maps obtained for two ceramics. Both the samples show the presence of

stripe – like domains, consistent with the findings for the single crystals described in last chapter. There was no significant difference between the domain patterns of two types of ceramics.

6.2 Compositional Modification to KNN

6.2.1 Synthesis of KNN-NBT-BT ceramics

High Curie temperature (T_c) piezoelectric materials are highly desired for applications in actuators and transducers. In past few decades, $PbZr_xTi_{(1-x)}O_3$ (PZT) based compositions have dominated these applications because of its excellent piezoelectric properties and high Curie temperature (T_c) = 390°C.[4] One of the limitation of soft PZT as high temperature piezoelectric material is the thermal degradation of its electromechanical properties above 150°C.[4, 150] In addition, the toxic nature of lead-based compositions is also a concern.

Sodium potassium niobate $K_{0.5}Na_{0.5}NbO_3$ (KNN) having an orthorhombic crystal structure at room temperature is a possible alternative for high temperature applications having T_c close to 420°C.[4] However, presence of the orthorhombic to tetragonal transition at 200°C deteriorates the thermal stability of piezoelectric properties between room temperature (RT) and Curie point. In addition, the piezoresponse of KNN is much inferior to that of PZT and other lead-based compositions. In the last decade, doping with different A-site (Ca, Ba, Li etc.) and B-site (Ta, Nb, Ti etc.) elements has been reported to reduce the orthorhombic – tetragonal transition (T_{o-t}) close to room temperature, resulting in an improved room temperature piezoresponse.[71, 74, 150] But at the same time, the presence of T_{o-t} at room temperature results in a poor thermal behavior and the problem of reproducibility in piezoelectric properties.[166] By further lowering the T_{o-t}, it is possible to achieve the broad existence of the tetragonal region

from RT to T_c, which could impart good thermal stability of the piezoelectric properties. Very few studies have addressed the temperature variation of piezoelectric properties in this system and hence the thermal stability of KNN based ceramic compositions is not well understood. A study worth mentioning here is that by Zhang et al. which showed that small amount of $CaTiO_3$ incorporated into KNNLS ($K_{0.5}Na_{0.5}NbO_3$ - $LiSbO_3$) resulted in better thermal stability of the piezoelectric properties in the temperature ranging from - 60°C to 200°C.[150]

In this study we investigated the temperature dependent piezoelectric properties of ternary $(Na_{0.5}Bi_{0.5}TiO_3)_x$ – $(BaTiO_3)_y$ – $(Na_{0.5}K_{0.5}NbO_3)_{1-x-y}$ (xNBT - yBT- (1-x-y)KNN) compositions. The role of 90° domains and tetragonality was investigated to explain the observed stability of the piezoelectric response. Three components of this system $Na_{0.5}Bi_{0.5}TiO_3$ (NBT), $BaTiO_3$ (BT) and $Na_{0.5}K_{0.5}NbO_3$ (KNN) are well known piezoelectrics with Curie temperatures 320°C, 120°C and 420°C respectively. As it was reported previously that perovskite solid solutions have monotonous variation of Curie temperature with composition[182], thus KNN rich end was the obvious choice to achieve high Curie temperature. Moreover, to utilize the fact that any solid solution has its best piezoelectric properties for compositions close to MPB, efforts were made to find compositions close to morphotropic phase boundary (MPB) on KNN rich end of $(NBT)_x$ –$(BT)_y$ – $(KNN)_{1-x-y}$ system.

Figure 6.10 (a) shows the KNN rich ends of known binary phase diagrams of KNN-NBT and KNN – BT systems at room temperature. Both of these diagrams can be combined to give tentative ternary phase diagram of $(NBT)_x$ – $(BT)_y$ – $(KNN)_{1-x-y}$ system (Figure 6.10 (b)), showing the presence of a MPB close to KNN rich end. $(NBT)_x$ – $(BT)_y$ – $(KNN)_{1-x-y}$ ceramic samples were synthesized in compositions range $0.01 \leq x \leq 0.04$ and $0.01 \leq x \leq 0.03$ in order to find compositions with high piezoelectric properties.

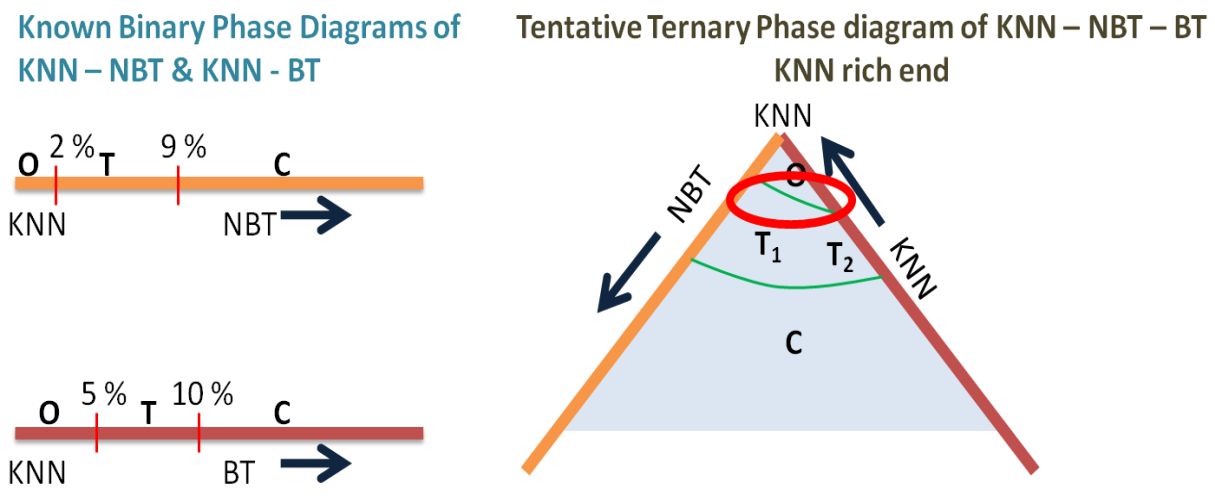

(a) (b)

Figure 6.10 Phase diagrams (a) known binary phase diagrams for KNN – NBT and KNN – BT systems (b) Tentative phase diagram of ternary KNN – NBT – BT system

6.2.1.1 Experimental Procedure

Since one of the components of (1-x-y)KNN-xNBT-yBT compositions (BT, calcination temperature 1350°C) has higher calcination temperature than the melting point of other (KNN, melting temperature 1200°C)[4], the mixed perovskite method was preferred to synthesize these ceramics. The compositions (1-x-y)KNN-xNBT-yBT with x = 0.025 y = 0.015 (C1), x = 0.03 y = 0.01 (C2), x = 0.01 y = 0.03 (C3), x = 0.015 y = 0.015 (C4), x = 0.035 y = 0.01 (C5), x = 0.04 y = 0.01 (C6), x = 0.03 y = 0.02 (C7), x = 0.0125 y = 0.0125 (C8), x = 0.03 y = 0.015 (C9), x = 0.035 y = 0.015 (C10)), x = 0.04 y = 0.015 (C11)), x = 0.035 y = 0.0125 (C12)), x = 0.035 y = 0.0075 (C13)) and x = 0.0375 y = 0.0125 (C14) were synthesized in two steps. In the first step, KNN and NBT ceramics were synthesized by mixed-oxide method. For KNN precursors K_2CO_3, Na_2CO_3 and Nb_2O_5, while for NBT precursors Bi_2O_3 and Ti_2O_5 (Alfa Aesar, purity > 99 %) were calcined at temperatures 850°C and 900°C respectively. In the second step, appropriate amounts

of these two components along with commercially available $BaTiO_3$ were ball milled and calcined at 850°C to achieve the desired KNN-NBT-BT stoichiometry. Table 6.2 lists the compositions for all fourteen ceramics compositions synthesized, along with the abbreviations. Samples of different sizes were compacted and subjected to cold isostatic pressure of 20 kPa before muffled sintering at 1080°C. To perform the electrical measurements, silver nanoparticles based conductive paste was painted on these samples followed by firing at 650°C.

6.2.1.2 Results and Discussion

The room temperature crystal structures of these samples were determined by X ray diffraction analysis (Cu Kα radiation). Figure 6.11 (a) shows the X ray diffraction patterns of ceramic samples between 2θ values 20° and 60°. All the samples crystallized in the perovskite phase without any significant fraction of impurity. As expected, careful observation of (110), (111) and (200) peaks suggested that all the samples crystallized either in orthorhombic or tetragonal structure, confirming these compositions to be close to morphotropic phase boundary (MPB). Figure 6.11 (b) showed the peak splitting of (200), suggesting that three samples namely C3, C6 and C14 had orthorhombic symmetry while rest belonged to the tetragonal symmetry.

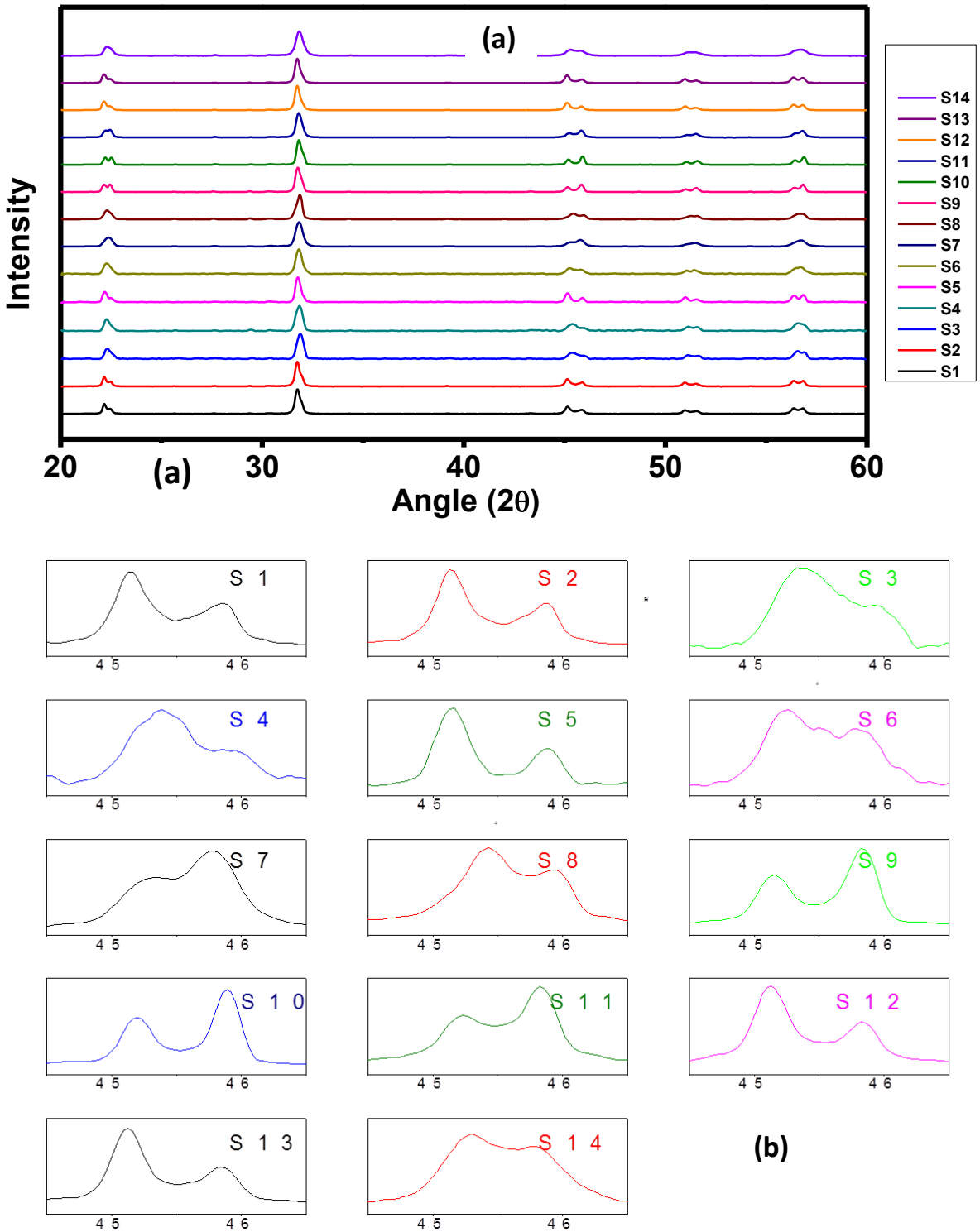

Figure 6.11 X-ray diffraction patterns for KNN – NBT – BT ceramics (a) in the 2theta range of 20° – 60° and (b) splitting of (200) peaks.

Pure as well as BT doped KNN samples have been reported to have problem of low sinterability. This problem not only leads to low electromechanical coupling but also affects the process of poling.[50] Sintering additives used to remove this problem often lead to decrease in piezoelectric response. In contrast to these compositions, KNN – NBT – BT ternary systems had no such problem of sinterability and all the samples exhibited dense microstructure. The microstructure of one of the samples (C2) is shown in Figure 6.12, indicating the presence of bimodal grains. Such bimodal grains in KNN ceramics have been observed previously and appear due to minor fluctuation in composition.[183]

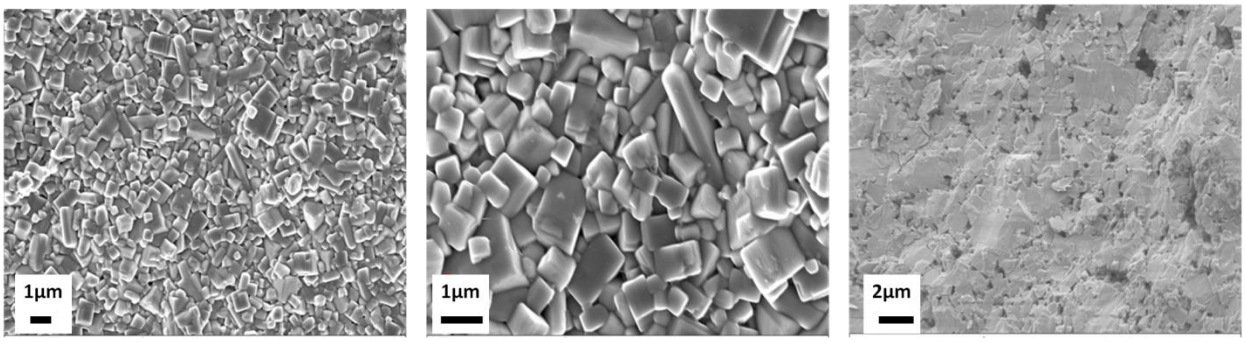

(a) (b) (c)

Figure 6.12 (a) & (b) Bimodal grains present in the microstructure of sample (C2). (c) Fractured surface of same pellet showing dense and uniform ceramic

For piezoelectric characterization samples were poled at the electric field of 4 kV/mm in the silicon oil bath at room temperature. Effect of high temperature poling was checked for one of the samples (C5) but it did not make any major difference on the piezoelectric coefficient. Table 6.2 lists the low field piezoelectric coefficient and remanent polarization values for all the compositions. For better illustration of the variation of piezoresponse with composition, three

Table 6.2 Piezoelectric coefficient and remanent polarization values for all the KNN-NBT-BT compositions

x (mole%)	**y (mole%)**	**d_{33}**	**Abbreviation**
0.025	0.015	132	C1
0.03	0.01	87	C2
0.01	0.03	47	C3
0.015	0.015	53	C4
0.035	0.01	210	C5
0.04	0.01	104	C6
0.03	0.02	112	C7
0.0125	0.0125	112	C8
0.03	0.015	148	C9
0.035	0.015	182	C10
0.04	0.015	145	C11
0.035	0.0125	130	C12
0.035	0.0075	110	C13
0.0375	0.0125	150	C14

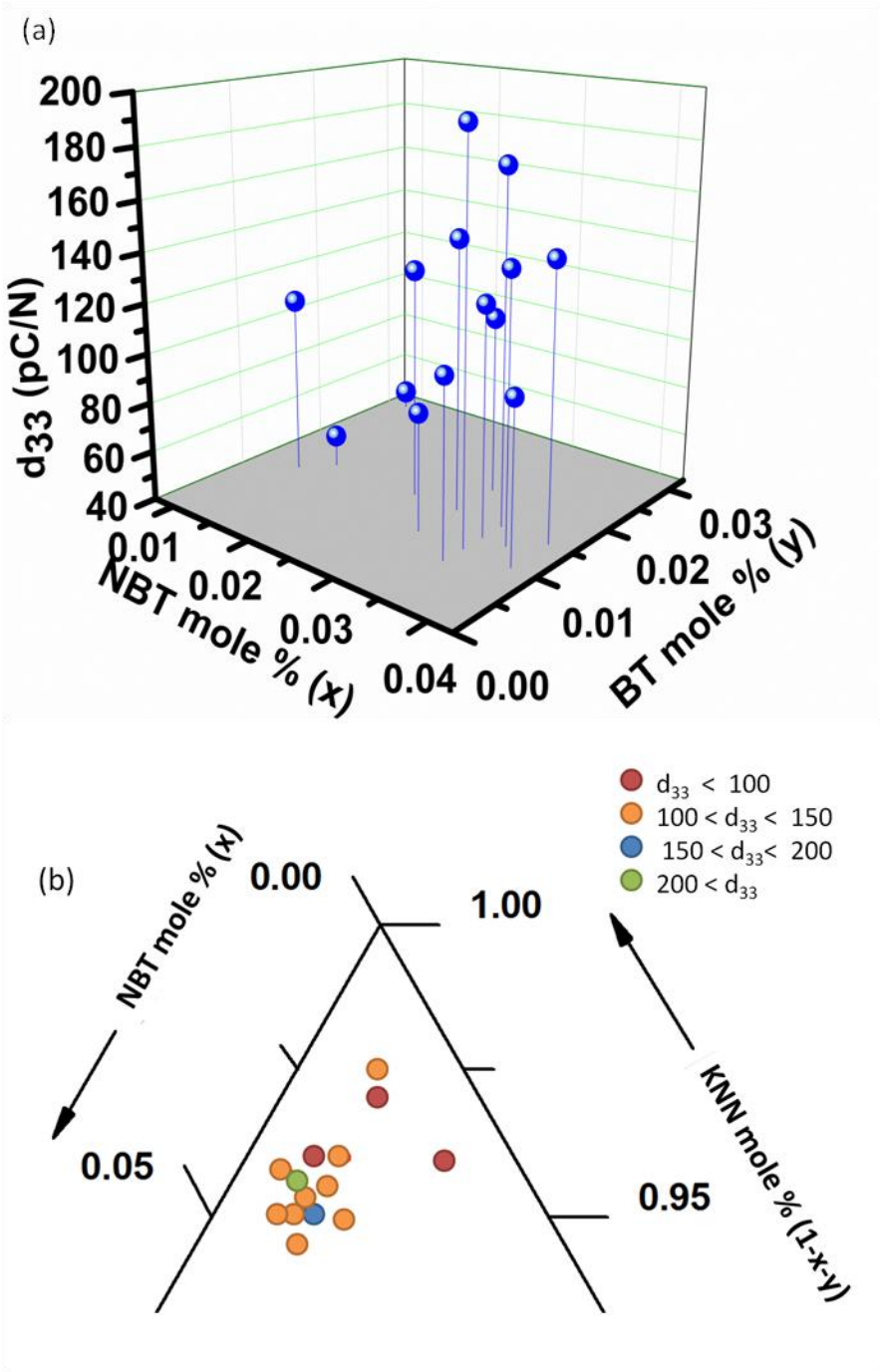

Figure 6.13 Variation of piezoelectric coefficient with amount of NBT (x) and BT (y) (a) 3D plot (b) Ternary Diagram

dimensional (3D) plot is drawn for d_{33} as a function of x and y (% concentration) (Figure 6.13).

The composition C5 has the highest piezoelectricity with d_{33} value 210 pC/N.

Five of these compositions C5, C9, C10, C11 and C14 having highest values of piezoelectric coefficients among others were chosen for further detailed analysis. From now onwards, these compositions are abbreviated as S1, S2, S3, S4 and S5 respectively.

For better illustration of evolution of crystallographic tetragonal phase, X-ray diffraction (XRD) patterns of all the (S1 – S5) ceramic samples with 2θ values between 20° - 60° are again shown in Figure 6.14.

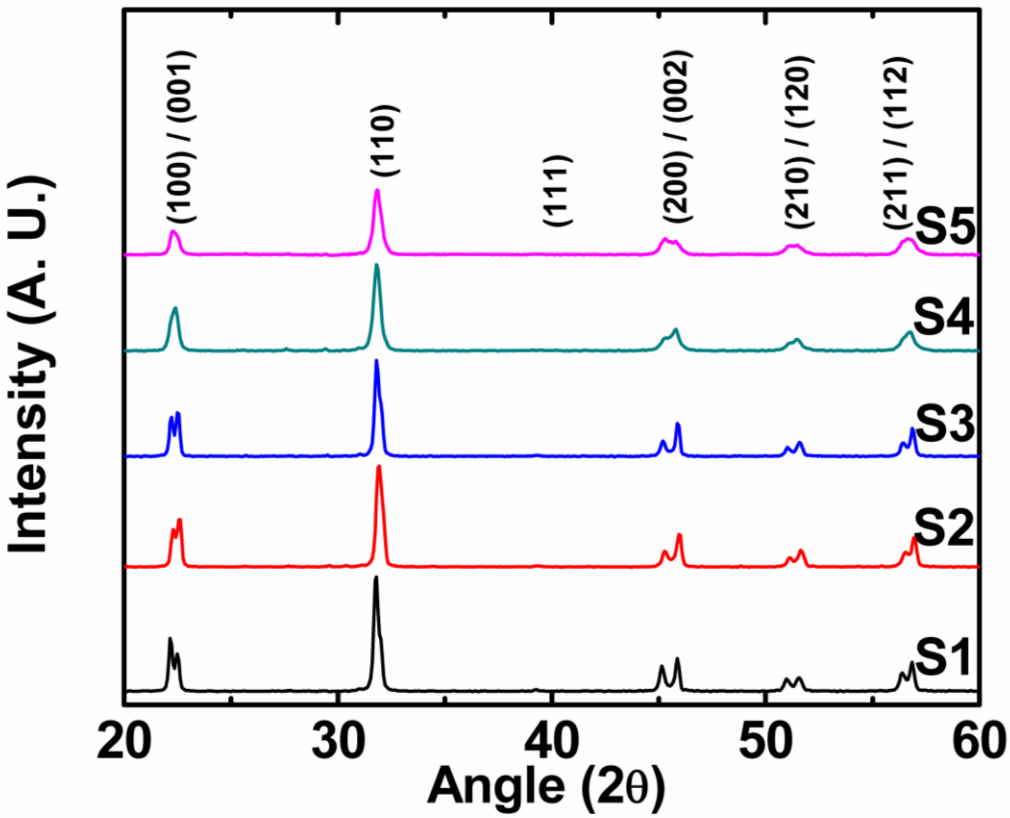

Figure 6.14 X-ray diffraction patterns of KNN-NBT-BT samples showing presence of perovskite phase without any noticeable amount of secondary phase (Reprint from reference 149 © 2013 American Institute of Physics).

Minor peaks existing in the 2θ range of 25° – 30° for S2 and S4 compositions could be attributed to the tetragonal tungsten bronze phase which is common to appear during synthesis of alkali niobates[35] Tetragonality of these compositions was determined using the peak positions of $(200)_{pc}$ / $(002)_{pc}$ as listed in Table 6.3. Samples S1 and S4 were found to exhibit the largest and smallest values of tetragonality (c/a – 1) having values of 0.0147 and 0.0103 respectively. Longitudinal piezoelectric coefficients (d_{33}) of these compositions exhibited similar trend as that of tetragonality. Room temperature dielectric measurements conducted at 100 Hz also suggested the high dielectric constant values for compositions S1, S2 and S3 with high tetragonality. Planar electromechanical coupling coefficients determined using resonance – anti-resonance technique were found to have values in the narrow range of 0.29 – 0.32. The composition S1 was found to have hydrostatic piezoelectric coefficient (d_h) value of 84 pC/N, which is comparable to the values obtained for lead-based piezoelectric compositions such as APC841 and APC855 (APC International Ltd.). Figure 6.15 (a) shows the P-E loops for all the compositions. Electric field and frequency were kept same for all the samples having values of 70 kV/cm and 200 Hz respectively. Saturated ferroelectric loops confirm the high resistive nature of these samples, with sample S1 having highest remanent polarization value of 18.3 μC/cm^2.

To reveal the phase transition behavior, temperature dependent dielectric measurements were performed in the range of - 60°C to 500°C. As can be seen in Figure 6.15 (b), all the samples were found to have orthorhombic - tetragonal (T_{o-t}) and tetragonal - cubic phase transition temperatures close to 0°C and 330°C respectively. It is interesting to note that compositional modifications to KNN shift the T_{o-t} by about 200°C in contrast to shift in T_c by only about 90°C, giving a broad temperature span of about 330°C without any phase transformation. This kind of behavior is quite unique for KNN-based compositions. Except for

few lithium incorporated compositions like KNNLS ($K_{0.5}Na_{0.5}NbO_3$ - $LiSbO_3$) and KNLN ($K_{0.5}Na_{0.5}NbO_3$ - $LiNbO_3$), most of the other compositions reported in literature maintain the temperature span of 200°C or lower between T_{o-t} and T_c.[46]

Careful observation of dielectric constant profiles in the tetragonal regime revealed that the compositions having high tetragonality at room temperature (S1, S2 and S3) showed better stability as compared to those with lower tetragonality (S4 and S5). To exemplify, the compositions S1 and S4 having tetragonality values of 0.0147 and 0.0103 showed 0.76% and 18% variation in dielectric constant in the temperature range of 0°C – 200°C. The dielectric constant of a polar perovskite composition can be given as sum of intrinsic and extrinsic contributions.[184] Intrinsic contribution come from the relative displacements of ions within unit cell while on the other hand extrinsic contribution results from the domain wall motion under electric field. The extrinsic contribution increases with temperature due to higher mobility of domain walls at higher temperature. On the other hand intrinsic contribution to dielectric constant decreases with temperature due to decrease in tetragonality.[184] Experimental as well as theoretical results obtained for hard and soft PZTs suggest that the extrinsic contribution to dielectric properties is about 67% – 70% of total response at room temperature.[184, 185] Since extrinsic contribution dominates at room temperature and increases sharply with temperature in contrast to intrinsic contribution, the dielectric constant shows a net increase with temperature.[184, 185]

To understand the temperature dependent dielectric behavior, temperature dependent XRD analysis was conducted on two samples with extreme tetragonality values (S1 and S4). Figure 6.15 (c) shows the variation of tetragonality of these samples in the temperature range of 30°C – 350°C, calculated using peak positions of (200) / (002) reflections. It can be seen that S1 having

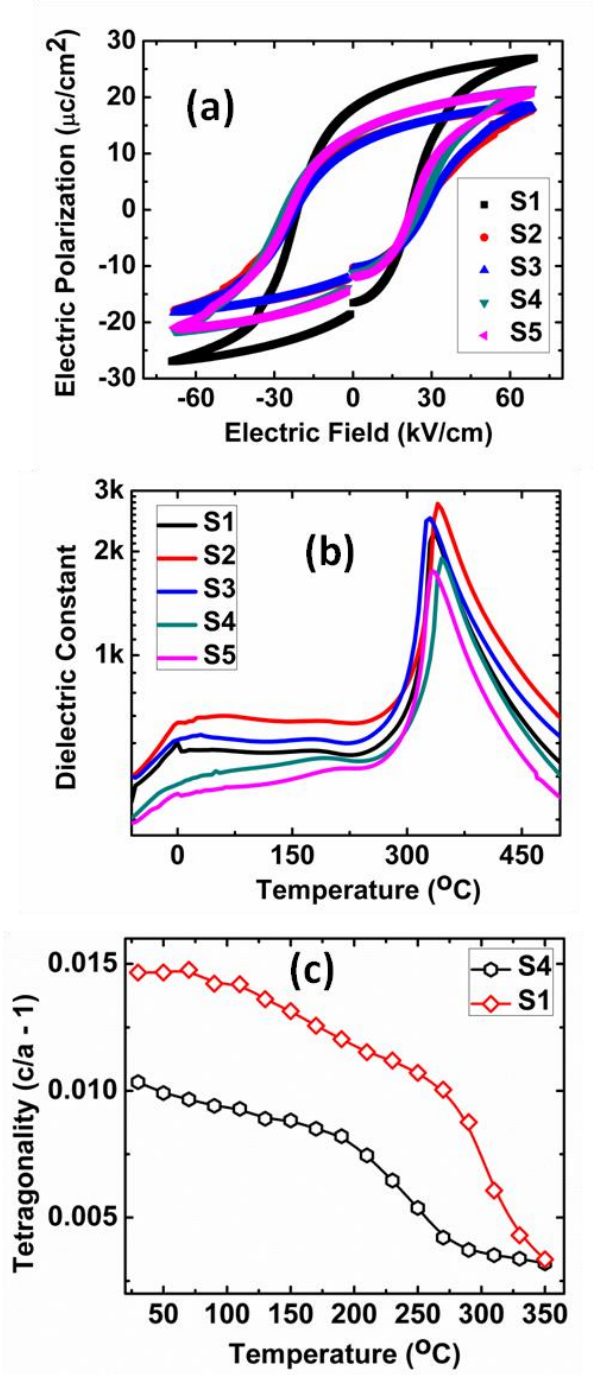

Figure 6.15 Characterization of compositions S1 and S4 (a) P-E loops (b) dielectric constant vs. temperature plots obtained for KNN-NBT-BT samples (c) variation in tetragonality with temperature (Reprint from reference 149 © 2011 American Institute of Physics).

Table 6.3 Different piezoelectric, dielectric and ferroelectric properties of S1, S2, S3, S4 and S5 ceramics.

Sample	S1	S2	S3	S4	S5
Composition (x, y)	0.035, 0.01	0.03, 0.015	0.035, 0.015	0.04, 0.015	0.0375, 0.0125
Tetragonality (c/a - 1)	0.0147	0.0133	0.0143	0.0103	0.0105
K (100 kHz)	531	644	583	398	440
Loss (100 kHz)	0.038	0.041	0.036	0.06	0.051
T_{o-t} (°C)	0	11	-5	8	0
T_c (°C)	329	333	327	339	333
P_r (μC/cm^2)	18.3	12	11.6	13.5	13.7
d_{33} (pC/N)	210	148	182	145	150
- d_{31} (pC/N)	63	-	-	48	-
d_h (pC/N)	84	-	-	49	-
K_p	0.32	0.3	0.3	0.29	0.29
K_{31}	0.21	-	-	0.17	-
Δd_{31} (%)	24	-	-	25	-
ΔK_p (%)	31	-	-	4	-
ΔK_{31} (%)	19	-	-	0.5	-

high tetragonality at room temperature maintains the dominance over low tetragonality sample S4 in the entire temperature range. Thus, stability of dielectric constant in high tetragonality compositions could be explained if the decrease in intrinsic contribution with temperature is

quantitatively comparable to increase in extrinsic contribution in the temperature span of 0°C – 200°C.

Considering the role of domain contribution in dielectric behavior of tetragonal compositions, previous studies suggest that 180° domains cannot respond to low fields at which dielectric measurements were performed.[184] Theoretical calculations conducted for tetragonal compositions suggests that the domain wall energy for 180° domains is on the order of 10 ergs/cm^2 in contrast to 3 ergs/cm^2 for 90° domains.[186] It has been found in the case of $BaTiO_3$ that 180° domains started responding to electric field only when the applied field magnitude was comparable to that of coercive field.[186] Thus, low extrinsic contribution to dielectric constant only indicates the inability of 90° domains in responding to the changes in external electric field. Since only 90° domains can contribute to the piezoelectric properties, this hypothesis is consistent with comparatively low values of piezoelectric coefficients (d_{33}, d_{31}, k_p & k_{31}) in KNN-NBT-BT ceramics as compared to other KNN modified compositions having PPB close to RT.[74, 150]

Contribution of domain walls to piezoelectric properties depend on their width as well as their dynamics under electric field.[124, 135] For example, theoretical calculations conducted for 90° domains in two dimensional (2D) $BaTiO_3$ single crystal using time dependent Ginzburg – Landau (TDGL) model suggest about threefold increase in low field longitudinal piezoresponse (d_{33}) by decreasing the domain size from 22.6 nm to 4.5 nm. Altering piezoelectric coefficients by controlling the domain wall mobility is a well-established procedure for lead-based piezoelectrics.[4] To understand the 90° domain dynamics in KNN-NBT-BT ceramics, scaling

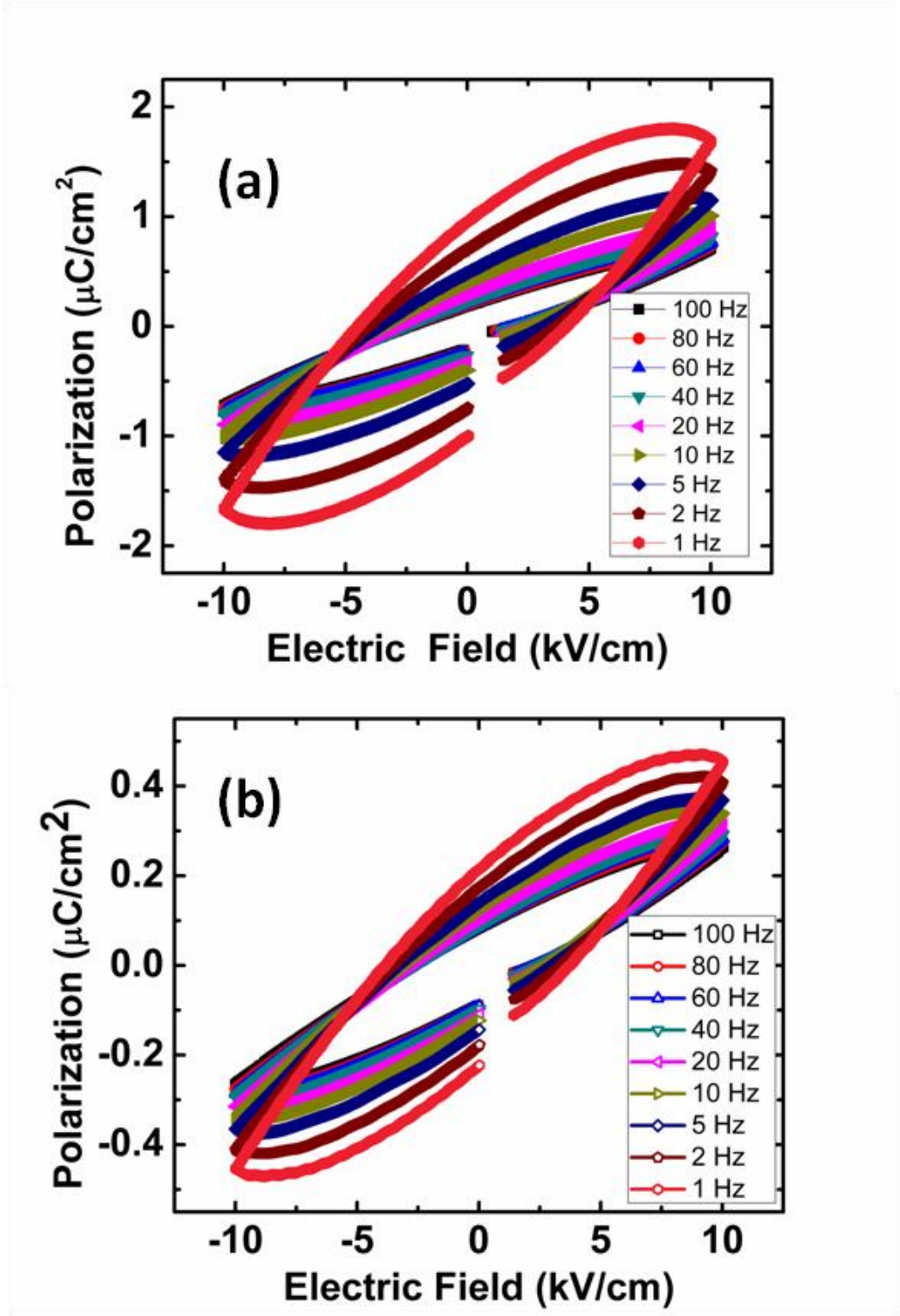

Figure 6.16 Ferroelectric loops obtained for (a) S1 and (b) S4 compositions at sub-coercive field

analysis was conducted on samples S1 & S4. In this analysis, area under the ferroelectric loops is related to frequency (*f*) and electric field amplitude (*E*) according to Equation 6.1. This concept was first developed for magnetic materials but holds good for ferroelectrics as well.[107, 124, 187]

$$\langle A \rangle \propto f^m E^n \tag{6.1}$$

The exponent m in this relation is a measure of switching time of domains while n represents the ability of domains to respond to changes in electric field direction. Theoretical calculations suggest the values of these parameters to be -1 and 2 respectively for magnetic materials.[100] Though very few ferroelectric materials follow these values[104], dynamic scaling remains an effective tool to study the domain dynamics. Since we are interested in understanding the ability of 90° domains in responding to the electric field, present analysis focuses on determining the value of parameter n only. Also this analysis was conducted at low fields ($E < E_c/2$), as 180° domain walls do not respond at low electric fields and thus the ferroelectric response would be mainly from 90° domains.[186]

Ferroelectric loops were measured for S1 and S4 for various possible combinations of electric field values ranging from 1 kV/cm – 10 kV/cm and frequencies in the span of 1 Hz – 100 Hz. Figure 6.16 shows the ferroelectric loops for two ceramic samples at different frequencies at electric field of 10 kV/cm. Values of area under loops for different frequencies and electric field is listed in appendix 1. Area under these loops was calculated and its variation with electric field at different frequencies can be seen in Figure 6.17 (a) and (b) for these two compositions. All these curves were fitted to the equation $\langle A \rangle \propto E^n$ providing the values of n ranging from 2.5 – 2.8 for two compositions at different frequencies, suggesting the similar dynamic behavior of domains. Analysis conducted on tetragonal ferroelectric $BaTiO_3$ ceramic and single crystal at sub-coercive field gives the values of parameter n to be 3.64 and 4.16 respectively.[104, 107] These

values are clearly higher as compared to the one obtained for KNN-NBT-BT compositions and hence it can be concluded that 90° domains in KNN-NBT-BT ceramics exhibit slower switching, consistent with the hypothesis. To ensure the role of any size difference of domains in determining the piezoresponse of two compositions S1 and S4, piezoresponse force microscopy was conducted. Phase contrast images obtained for S1 and S4 are shown in Fig. 3 (c) and (d) respectively, showing the presence of stripe-like domains for both the compositions having thickness of about 200 nm and extending through the grains with dimensions of 1-2 μm. Hence similar to the dynamic behavior given by magnitude of parameter "n", size of ferroelectric domains is not expected to play preferred role in determining the piezoelectric properties in any of these two compositions. In this scenario, these two compositions are expected to exhibit similar extrinsic contribution to piezoresponse. Thus, the superior piezoresponse of high tetragonality composition can be attributed to its higher intrinsic contribution.

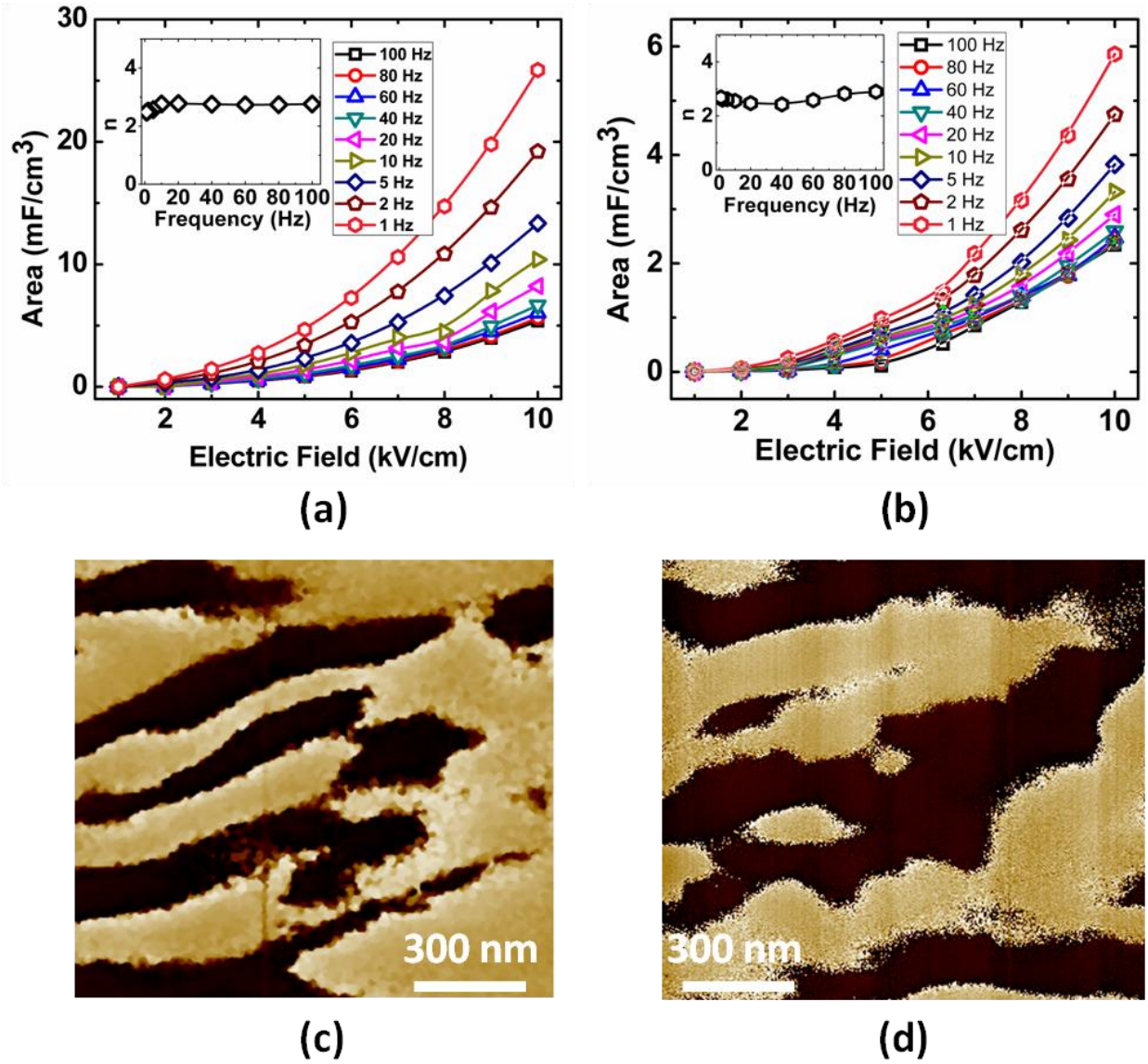

Figure 6.17 Dynamic behavior and size of domains for S1 and S4 (a) and (b) Area under ferroelectric loops vs. electric field at different frequencies for S1 and S4. Inset of figures show the values of parameter n at different frequencies for two compositions, (d) and (e) Piezoresponse force microscopy (PFM) phase images of samples S1 and S4 respectively (Reprint from reference 149 © 2011 American Institute of Physics).

This hypothesis can be further understood by noticing the phenomenological expression given by Equation 6.2, suggesting that piezoresponse varies with tetragonality and dielectric constant.[186, 188]

$$d_{33} = 2\varepsilon_o\varepsilon_{33}\,[Q(c/a - 1)]^{1/2} \qquad (6.2)$$

Where Q is the electrostriction coefficient, and ε_o and ε_{33} represent the permittivity of free space and dielectric material respectively.

Figure 6.18 shows the variation of piezoelectric coefficient (d_{31}) and electromechanical coupling coefficients (k_{31}, k_p) with temperature for compositions having highest and lowest values of tetragonality. For most of the tetragonal piezoelectric compositions reported in literature, an increase in piezoelectric properties was observed with temperature due to dominance of the extrinsic contribution which increases due to enhanced domain wall mobility at higher temperatures.[189, 190] But in the present case, composition S1 having prominence of intrinsic contribution, showed small drop in all three parameters with temperature, suggesting a decrease in tetragonality with temperature leading to poorer intrinsic contribution. On the other hand composition S4 having low tetragonality and hence more balanced intrinsic and extrinsic contributions, showed almost no variation in the electromechanical coupling coefficient k_{31} and k_p, and small increase in d_{31}. Both of these observations are consistent with our hypothesis about the role of intrinsic and extrinsic contributions to piezoelectric properties. Table 6.3 lists the percent variation of three electromechanical parameters for two compositions. If we compare the variation of piezoelectric parameters with various lead-based compositions used in devices for high temperature applications, our compositions definitely exhibit better thermal stability.[189, 190]

For example, both soft and hard PZT ceramics show about 50 % change in d_{31} values in contrast to about 24 % variation in KNN-NBT-BT ceramics for the same temperature range.[189]

In summary, KNN-NBT-BT ceramics were characterized for the thermal stability of piezoelectric parameters in the broad tetragonal region. Slow dynamics of 90° domains in these compositions leads to moderate values of piezoelectric coefficients at room temperature but at the same time provided higher thermal stability. This work provides significant insight towards the temperature dependent behavior of piezoelectric coefficients along with the role of intrinsic and extrinsic contributions in tetragonal compositions of KNN-based compositions. It can be concluded that by controlling the mobility of 90° domains in tetragonal compositions, piezoelectric compositions with good thermal stability of piezoresponse can be designed.

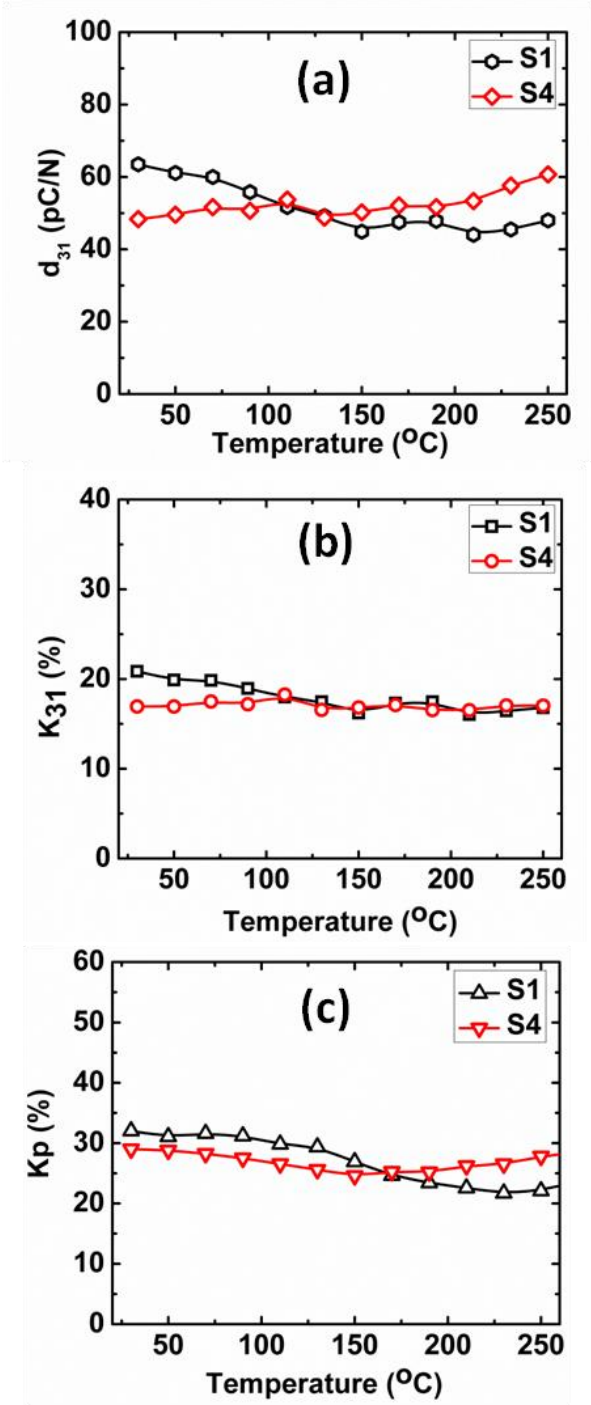

Figure 6.18 Variation of piezoelectric coefficients (a) d_{31} (b) k_{31} and (c) k_p with temperature (Reprint from reference 149 © 2011 American Institute of Physics).

.

6.2.2 Synthesis of multiferroic KN-BF ceramics

6.2.2.1 Experimental Work

In this study, the goal was to explore the magnetoelectric properties in alkali niobate based compositions. $(KNb)_x(BiFe)_{1-x}O_3$ (KNBF) ceramics were synthesized using mixed oxide method. High purity chemicals of composition Bi_2O_3, Fe_2O_3, Nb_2O_5 and K_2CO_3 were ball milled in ethanol medium for 24 hours and calcined at 850°C. Calcined powders went through second ball milling for 24 hours in ethanol medium to reduce the particle size. After drying the powders, pellets of diameter 12 mm were pressed followed by cold isostatic pressing at 20 kPa. These pellets were sintered at temperature 1000°C – 1100 °C to get dense KNBF samples. Silver electrodes were fired on the pellets in order to perform electrical measurements.

6.2.2.2 Results and Discussion

The piezoelectric response of KNBF sample with $0 < x < 1$ is shown in Figure 6.19. The highest magnitude of piezoelectric constant was found to be 9 pC/N. This peak in piezoelectric coefficient was found for composition close to $x = 0.5$ thus all further measurements were concentrated for this composition only. It is clear that none of the compositions in this system have any significant magnitude of piezoresponse. Figure 6.20 shows the XRD pattern of optimum composition confirming the presence of perovskite peaks. Minor splitting in (111) peak suggested that this composition belongs to the rhombohedral crystal structure.

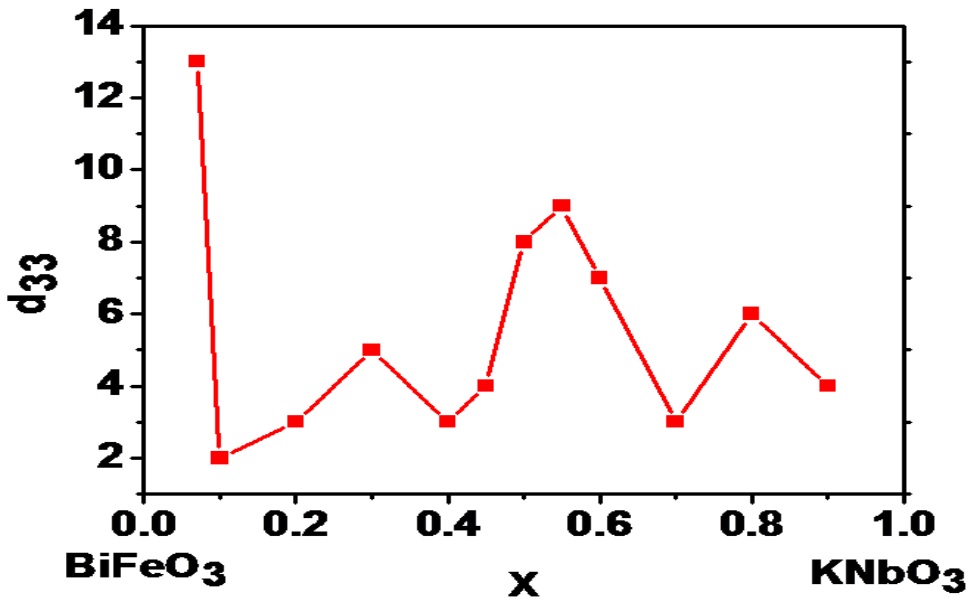

Figure 6.19 Variation of piezoelectric coefficient (d_{33}) of KNBF samples with composition

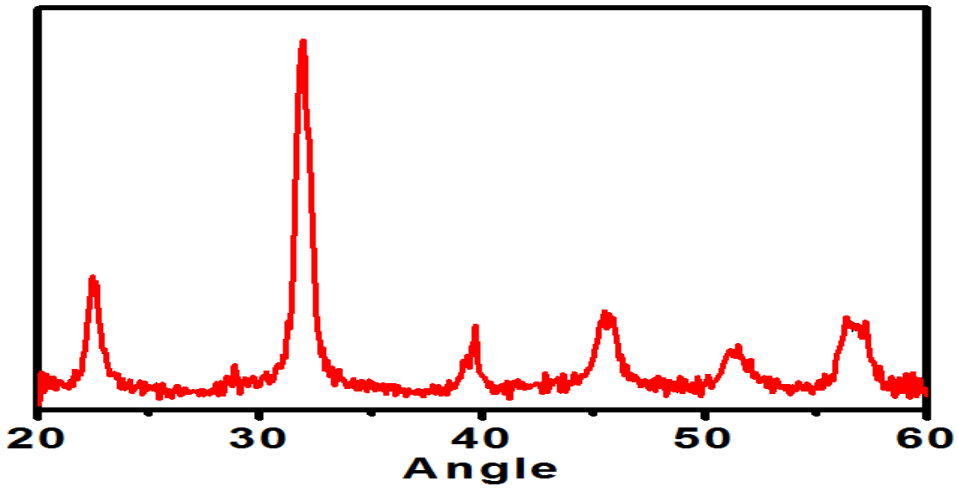

Figure 6.20 XRD pattern of $(KBi)_{0.5}(FeNb)_{0.5}O_3$ ceramic sample

Since $BiFeO_3$ based compositions have the problem of high leakage, KNBF sample is characterized for its conduction behavior at room temperature. Leakage current measurements showed at least three orders of magnitude improvement in resistivity as compared to the reported resistivity values of BF. For a bulk ceramic sample three conduction mechanisms, namely

Frenkel Poole conduction, space charge limited conduction and Schottky barrier conduction are possible. These three mechanisms can be differentiated from each other by comparing the variation of current as a function of applied field. Equation 6.3 gives the mathematical formulations for all three conduction mechanisms.

Space Charge Limited Conduction $J \alpha V^2$

Schottky barrier Conduction $J/T^2 \alpha V^{1/2}$ …. (6.3)

Frenkel Poole Conduction $\sigma \alpha V^{1/2}$

To identify which of these mechanisms dominate the conduction in KNBF samples, leakage current vs. voltage graphs were plotted. These plots are shown in Figure 6.21 and nonlinear behavior for all of them suggested that none of these mechanisms solely dominates the conduction in KNBF sample, rather they all contribute to it.

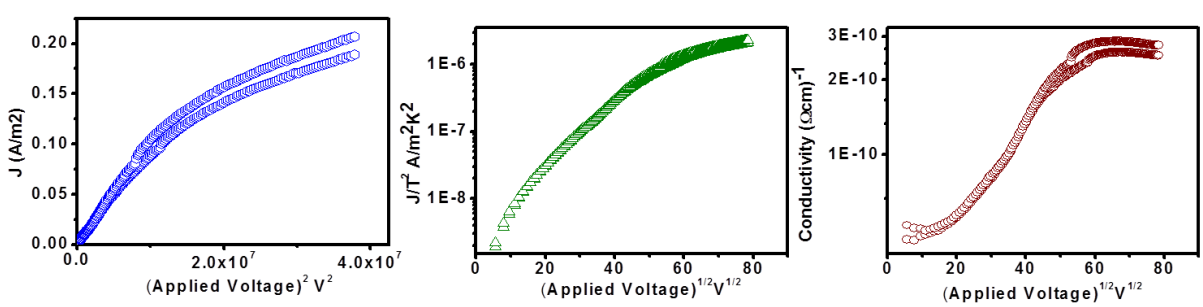

(a) (b) (c)

Figure 6.21 Leakage current plots according to (a) Space Charge conduction (b) Schottky barrier conduction, and (c) Frenkel Poole conduction.

High conductivity in BF was due to the formation of Fe^{+2} ions and oxygen ion vacancies generated due to following reactions:

$$2Fe^{3+} + O^{2-} \rightarrow 2Fe^{2+} + {}^{1}/_{2}\, O_2 + V_O^{2+}$$

$$2Bi^{3+} + 3O^{2-} \rightarrow Bi_2\, O_3 + 2V_{Bi}^{3-} + 3\, V_O^{2+} \qquad (6.4)$$

To understand the highly resistive behavior of KNBF ceramics, XPS analysis was performed as shown in Figure 6.22.

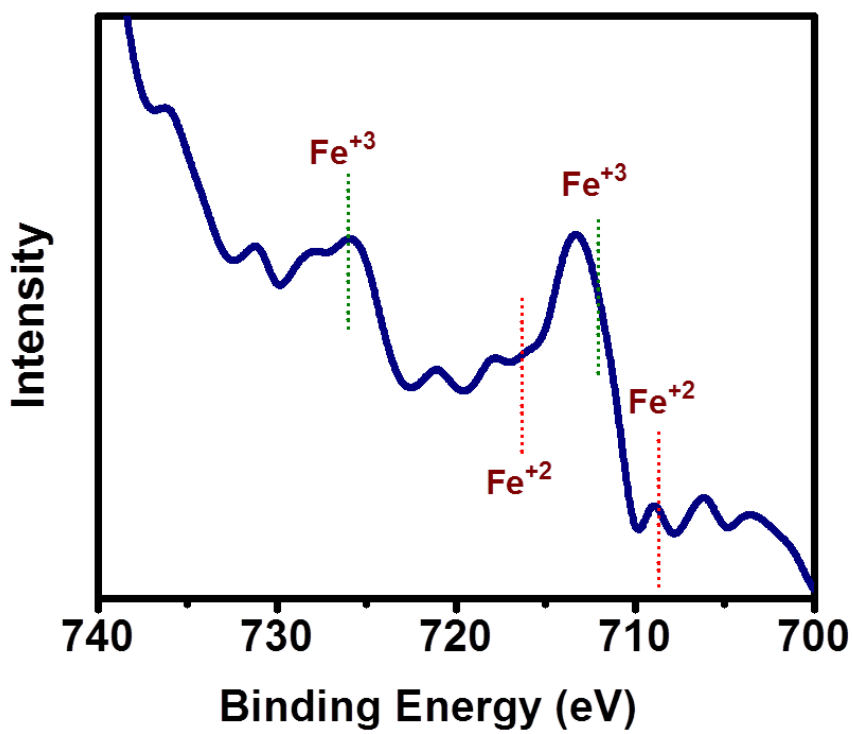

Figure 6.22 XPS spectra of KNBF sample showing the absence of Fe^{+2} ions in the sample.

In this figure, absence of peaks at positions of Fe^{+2} ions, confirms the suppression of charge fluctuation of Fe^{+3} ions and explains the high resistivity of these samples. To reveal the multiferroic nature of KNBF sample, ferroelectric and magnetic measurements were performed.

Figure 6.23 shows the ferroelectric loop obtained on the sample confirming its ferroelectric behavior. Remanent polarization value was found to be ~ 10 μC/cm^2.

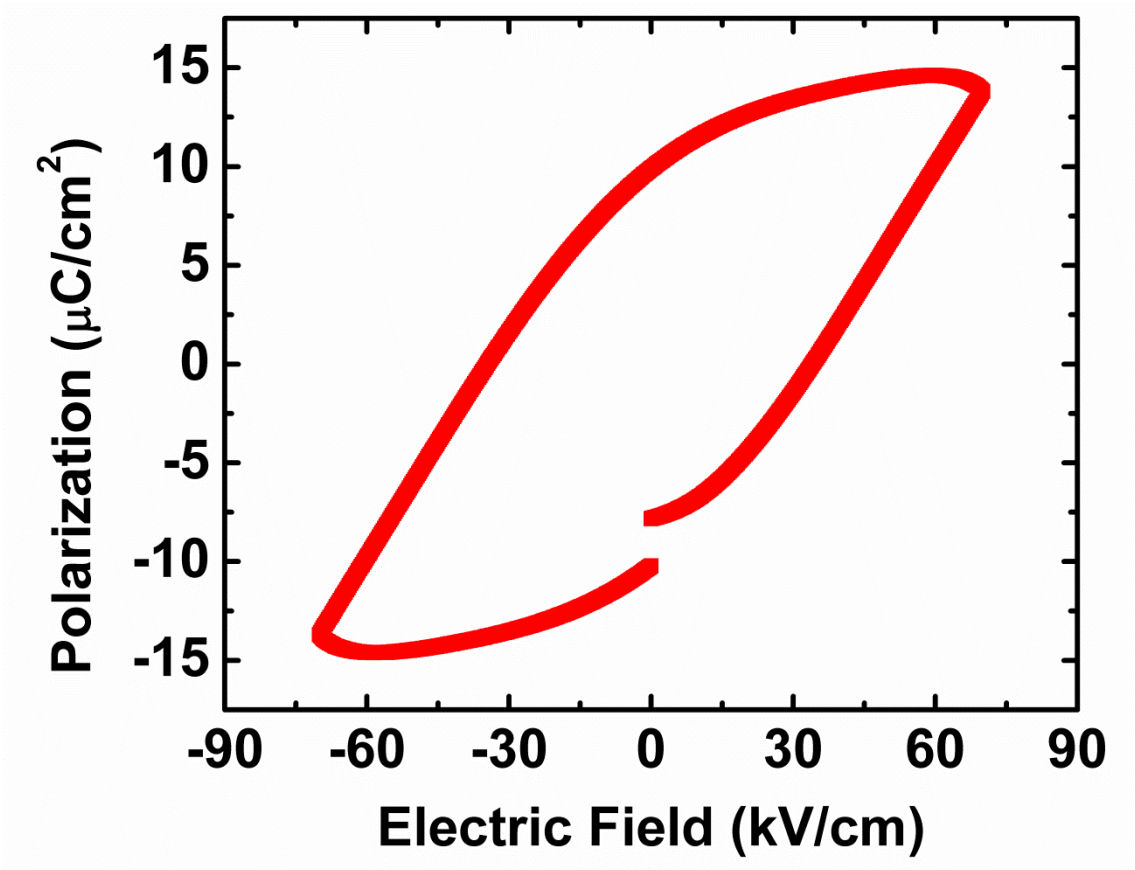

Figure 6.23 Ferroelectric loop for KNBF sample showing the remnant polarization value to be 10 μC/cm^2

Zero Field Cooled (ZFC) KNBF50 composition showed antiferromagnetic behavior at different temperatures (Figure 6.24), having near linear variation of magnetization with field. Slight opening of antiferromagnetic loop can be seen with remnant magnetization value of 3.57 x 10^{-3}emu/gm at room temperature.

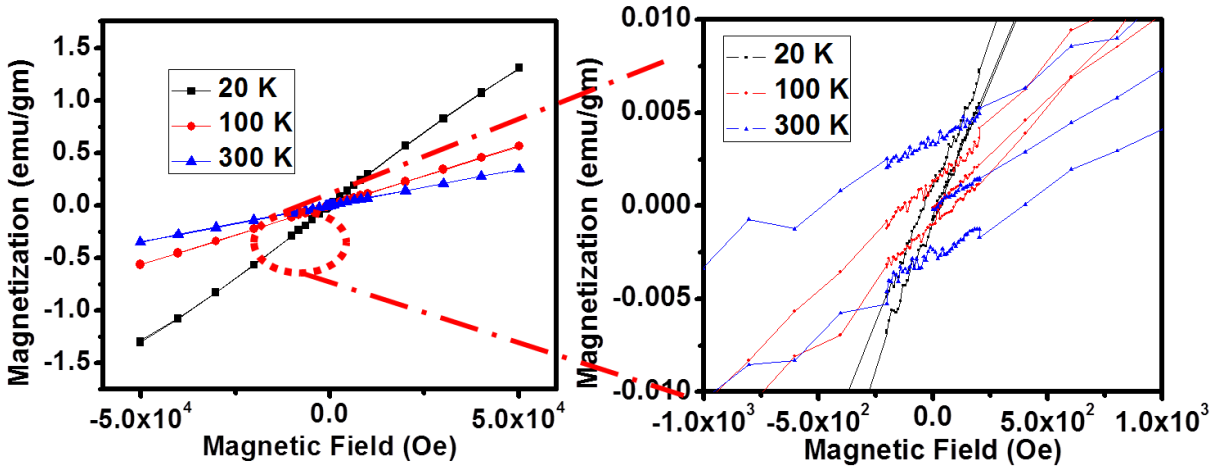

(a) (b)

Figure 6.24 Magnetic field vs. magnetization curves obtained for KNBF sample (a) at different temperatures (b) showing the magnified view of figure (a)

These results indicate that KNBF sample with x = 0.5 have multiferroic properties however more work is required to improve their performance and demonstrated direct magnetoelectric coupling.

Chapter 7

Synthesis and Characterization of {100} oriented $K_{0.5}Na_{0.5}NbO_3$ ceramics

7.1 Anisotropy in Piezoelectric Materials

Synthesis of oriented piezoelectric ceramics is an effective way to exploit the anisotropic nature in order to achieve enhanced properties in crystalline materials.[191] The anisotropic nature of piezoelectric materials is dependent on their crystal structure and varies with temperature.[191, 192] Mathematically, piezoelectric coefficient being a third rank tensor can be represented as proportionality constant between polarization (P) and stress (X), as shown in Equation 7.1. Due to the symmetric nature of stress tensor X, the number of unique elements in piezoelectric tensor is reduced to eighteen.[120] The piezoelectric tensor can be transformed from one coordinate system to another through Equation 7.2, where a_{ij} is the second order transformation matrix.[120]

$$P_j = d_{jkl}X_{kl} \tag{7.1}$$

$$d'_{imn} = a_{ij}a_{mk}a_{nl}d_{jkl} \tag{7.2}$$

For KNN, having orthorhombic crystal structure with mm2 point group, the longitudinal piezoelectric constant can be written as:[192]

$$d'_{333} = d'_{33} = Cos\theta[(d_{15} + d_{31})Sin^2\theta Sin^2\varphi + (d_{24} + d_{32})Sin^2\theta Cos^2\varphi + d_{33}Cos^2\theta] \tag{7.3}$$

where (φ, θ, ψ) are the Euler's angles. By knowing the values of d_{15}, d_{31}, d_{24}, d_{32} and d_{33} piezoelectric coefficient surface can be drawn. For $BaTiO_3$, one of the well studied piezoelectric materials belonging to mm2 point group symmetry at ~ 0 °°C, anisotropic d_{33} surface is shown in Figure 7.1.

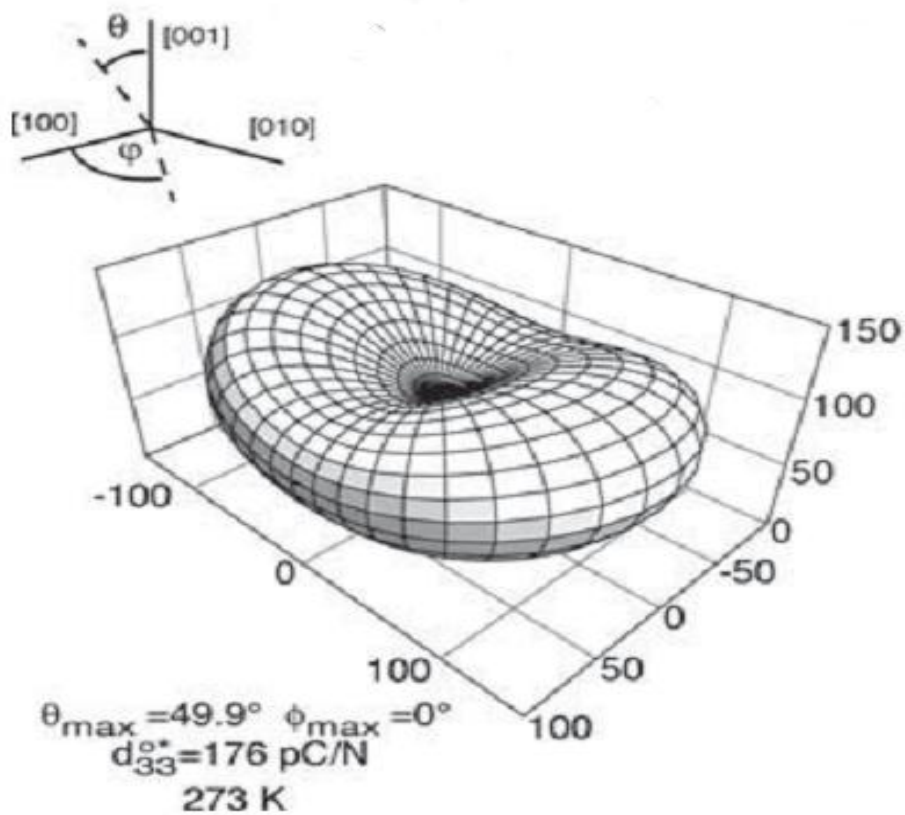

Figure 7.1 Geometric representation of longitudinal piezoelectric coefficient surface in $BaTiO_3$ (Reprint from reference 192 © 2006 Springer).

It is clear from the Figure 7.1 that the direction of maximum d_{33} lies about 50 degrees away from $[001]_o$ direction towards $[100]_o$, which is close to pseudo cubic [010] direction. Hence piezoelectric compositions having mm2 point group have highest value of longitudinal

piezoelectric coefficient close to pseudo cubic <100> direction. Due to the different values of piezoelectric coefficients appearing in Equation 7.3, small deviation from this orientation cannot be ruled out for different mm2 compositions. To exploit this anisotropy in KNN, template grain growth method was employed to synthesize the <100> oriented KNN ceramic. These textured samples were also interesting for fundamental investigations as they provide opportunity to understand the domain engineered configuration.

7.2 Experimental Procedure

7.2.1 Synthesis of seed crystals

To maintain a favorable thermodynamic and kinetic condition for 146emplate grain growth, synthesis and selection of a template is one of the most important steps.[193] A suitable template usually has four basic characteristics: (1) it should have same crystallographic structure as the matrix and a very small lattice mismatch (< 15%) to reduce the activation energy for nucleation and growth, (2) It should have an anisotropic morphology like a whisker or platelet so that it can be oriented under an applied shear force during tape casting, (3) It should have a suitable size because the driving force for the 146emplate grain growth is decided by the size difference between the template particles and matrix grains and (4) It should have good thermodynamic stability of the seed in the matrix else it can lead to secondary phase formation.

The appropriate template has the whisker or platelet morphology and is ideally of the same composition as matrix. Hence, high aspect KNN crystals were synthesized by a two step process and used as the seed for TGG.[194] This two step process was a slight modification to the one described earlier and was optimized for preparing $NaNbO_3$ seeds.[194, 195] In the first step,

$Bi_{2.5}Na_{1.75}K_{1.75}Nb_5O_{18}$ (BNKN) crystals with layered perovskite structure were grown by molten salt method using sodium chloride as a flux. According to the molecular formula of BNKN, stoichiometric amounts of alkali carbonates, niobium and bismuth oxide (purity > 99%, Alfa Aesar) were ball milled in ethanol medium for 24 hours along with the flux salt NaCl. The amount of flux taken for this crystal growth was double of the base precursors. After drying the mixture at 80°°C it was loaded in a platinum crucible and heated to 1200°°C in a conventional box furnace. After holding at 1200°°C for two hours, it was cooled to room temperature with the rate of 2°C/min. This salt – BNKN mixture was stirred in hot water to dissolve the salt, followed by careful leaching. This process was repeated many times to assure the complete removal of salt from BNKN crystals. Figure 7.2 shows the microstructure of BNKN crystals. It can be seen that these crystals have high aspect ratio with lateral dimensions about 10 μm – 20μm and thickness about 500 nm. Also, absence of any small particles confirms the complete removal of flux from the seed crystals.

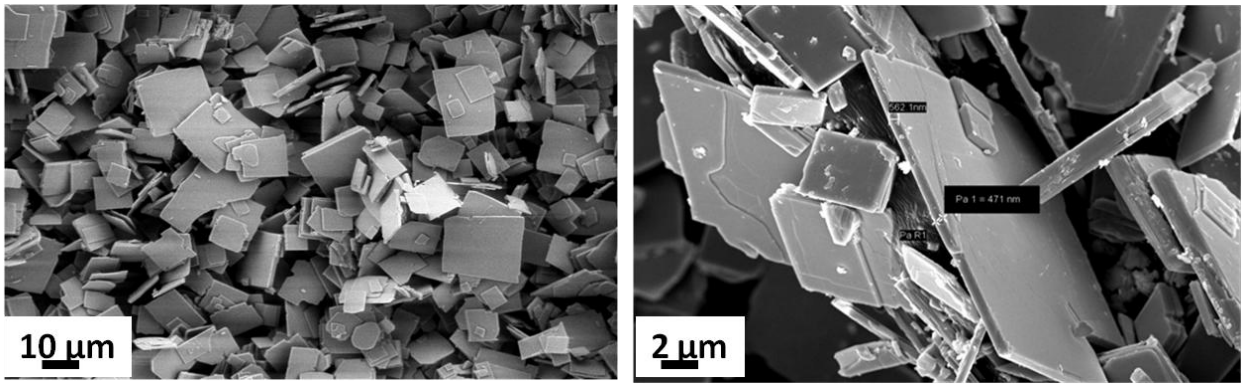

Figure 7.2 High aspect ratio BNKN crystals: (a) top view, and (b) cross-section image of one of the crystal showing its thickness to be about 500 nm.

In the second step of the process, BNKN crystals were further reacted with alkali carbonates at 1020°°C in the NaCl medium to convert the BNKN particles to perovskite KNN. A schematic diagram showing this conversion is shown in Figure 7.3.

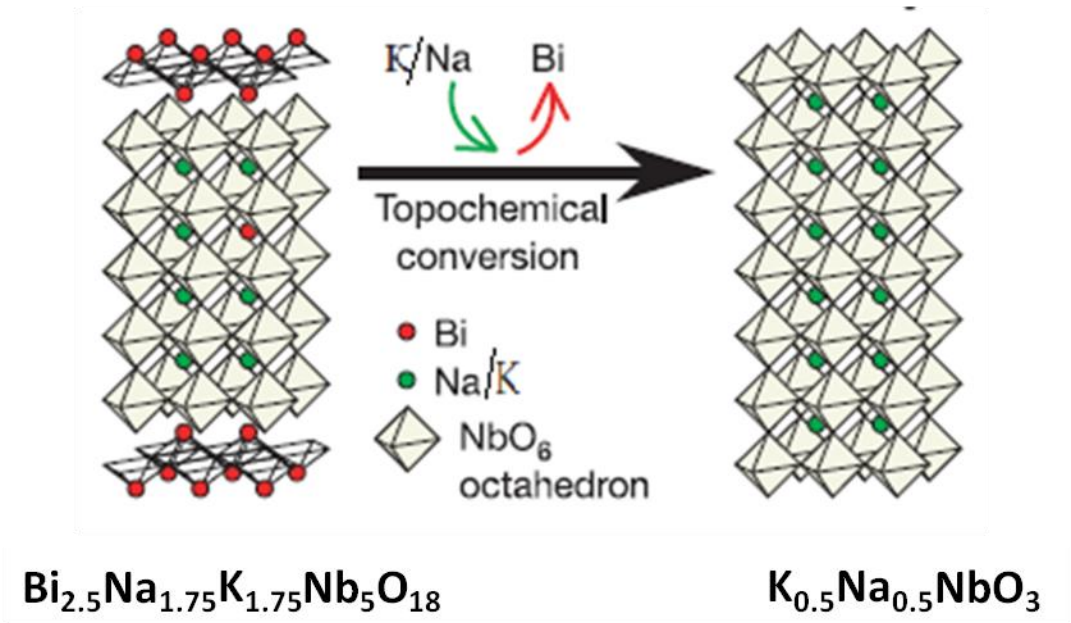

Figure 7.3 Conversion of KNBN crystals to perovskite KNN (Reprint from reference 82 © 2004 Nature Publishing Group).

During this substitution reaction the high aspect ratio of crystals was maintained. To avoid a rapid substitution reaction to take place, which may destroy the high aspect ratio of seeds during this step, the precursors were heated very slowly (2°°C /min) to the desired temperature, followed by natural cooling in order to achieve BNKN crystals of desired size. To remove the flux and bismuth oxide from seed crystals, alternative leaching was done few times with hot water and nitric acid, both being good solvents for NaCl and bismuth oxide respectively. Following chemical reactions (Equation 7.5) provide the chemical transformation taking place in these two steps.

Step 1

$$0.875K_2CO_3 + 0.875Na_2CO_3 + 1.25Bi_2O_3 + 2.5Nb_2O_5 \rightarrow Bi_{2.5}Na_{1.75}K_{1.75}Nb_5O_{18} + 1.75CO_2$$

Step 2

$$Bi_{2.5}Na_{1.75}K_{1.75}Nb_5O_{18} + 0.375K_2CO_3 + 0.375Na_2CO_3 \rightarrow 5K_{0.5}Na_{0.5}NbO_3 + 1.25Bi_2O_3 + 0.75CO_2 \quad (7.5)$$

Figure 7.4 shows the SEM image of KNN seeds along with X-ray diffraction pattern. Presence of peaks belonging to only perovskite phase confirms the complete transformation of layered perovskite structure of KNBN crystals to perovskite KNN, while high aspect ratio of seeds is maintained. Energy dispersive X-ray (EDX) analysis conducted on seed particles confirmed the absence of any traceable amount of bismuth ions. The analysis also showed small deviation of K/Na ratio from unity (Figure 7.5). Since the second step of seed formation consisted of substitution of bismuth ions by sodium and potassium from already crystallized particles, this small deviation in composition can be explained.

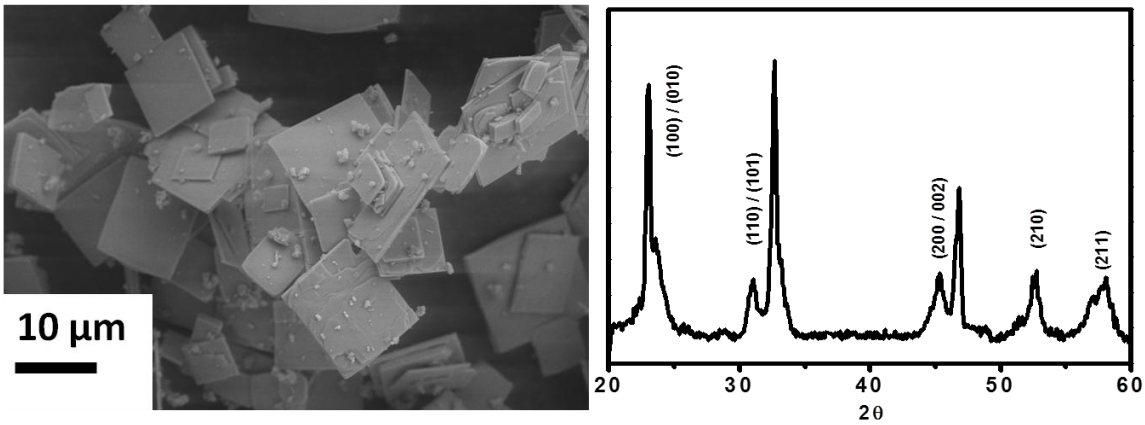

(a) (b)

Figure 7.4 BNKN crystal (a) SEM image and (b) XRD pattern of KNN seed crystals showing their high aspect ratio and presence of perovskite peaks.

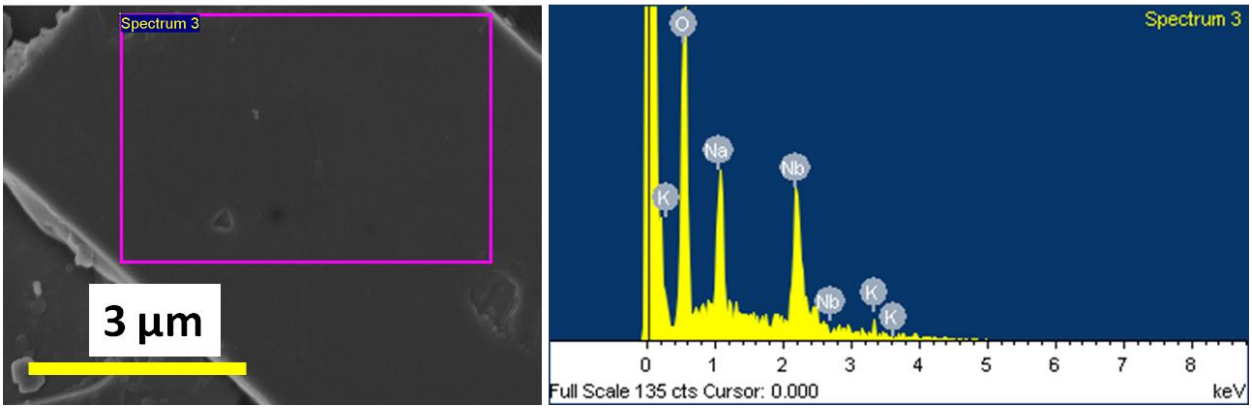

(a) (b)

Figure 7.5 EDX analysis on KNN seed crystal (a) 5µm x 3µm of crystal subjected to EDX analysis and (b) Energy spectrum showing absence of peaks belonging to bismuth ions.

The matrix KNN ceramic was prepared by conventional solid state synthesis process. Stoichiometric amount of sodium carbonate, potassium carbonate and niobium oxide (all from

Alfa Aesar with > 99% purity) were ball milled in ethanol medium for 24 hours, before calcining at 850°C for 90 minutes. After calcination, the KNN powder was ball milled again for 24 hours in ethanol medium to get small particle size and improve the sinterability. To further overcome the inherent problem of low sinterability of KNN, two different approaches described in next section were employed.

7.2.2 Templated Grain Growth (TGG) of KNN ceramic

The process flow of TGG method is schematically described in Figure 7.6 (a) – (f). In the first step, KNN ceramic along with the desired amount of sintering additives are ball milled for 24 hours with 60 wt % of binder and 100 wt% of alcohol to achieve homogeneous slurry. This step was followed by ultrasonic mixing of 10 wt% of KNN seed crystals to the slurry and stirring at room temperature. Besides avoiding the breaking of seeds ultrasonic mixing also helps in achieving uniform distribution of seeds in the matrix KNN powder. This final slurry was tape casted to form a thick film of thickness 500μm. This tape was allowed to dry for 6 hours at room temperature in order to vaporize alcohol used as a solvent during preparation of the slurry. After drying, this tape was cut into dimensions about 3 cm x 3 cm, followed by stacking and hot pressing. During hot pressing the stack of tapes was kept under the pressure of 1000 psi at 80°C for 15 minutes, followed by natural cooling to room temperature to avoid any crack formation. This laminated green body was cut in desired size followed by binder burn out at 400°C to get the porous KNN ceramic with aligned seeds. To avoid any crack formation and re-alignment of seed crystal during binder burn out process, heating was conducted at very slow speed (1°C/ min). These porous samples were subjected to cold isostatic pressure of 20 kPa before two step sintering according to the profile shown in Figure 7.6 (b) at T_2 = 1125°C for 6 hours. During

sintering, along with densification, small KNN particles start growing on larger KNN seeds to minimize the total surface energy of the system. This process is known as Ostwald ripening. During Ostwald ripening, small KNN particles follow the same growth orientation as seed crystals, and hence resulting in the formation of the (100) textured ceramic.

7.2.2.1 Use of $K_{5.4}Cu_{1.3}Ta_{10}O_{29}$ (KCT) as sintering additive

To overcome the problem of low sinterability, a number of sintering additives have been used in random KNN ceramics. In most of the cases, these additives improve the sinterability on the cost of either piezoelectric properties or transition temperatures. Among these additives, $K_{5.4}Cu_{1.3}Ta_{10}O_{29}$ (KCT) is one of the most effective sintering additives that improve the sinterability of KNN by liquid phase sintering. Liquid phase sintering not only facilitates higher density but also lowers the sintering temperature. Incorporation of only 0.38 mole % of KCT to KNN has been reported to result in > 99% density in KNN ceramics with improved piezoelectric properties.[46]

$K_{5.4}Cu_{1.3}Ta_{10}O_{29}$ (KCT) was synthesized by solid state synthesis route using high quality precursors (Alfa Aesar, > 99% purity) copper oxide, potassium carbonate and tantalum oxide. Weighted amount of precursors were ball milled for 24 hours in ethanol followed by calcination at 1100°C. For this study 0.38 mole % KCT was ball milled with KNN ceramic during second ball milling after calcination.

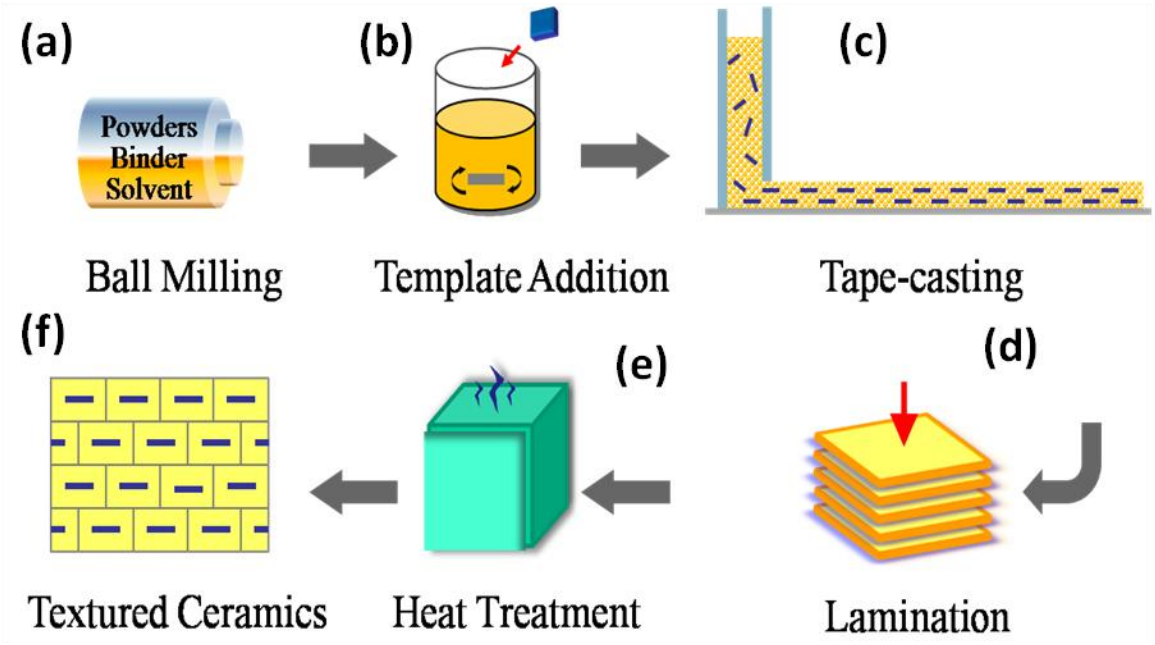

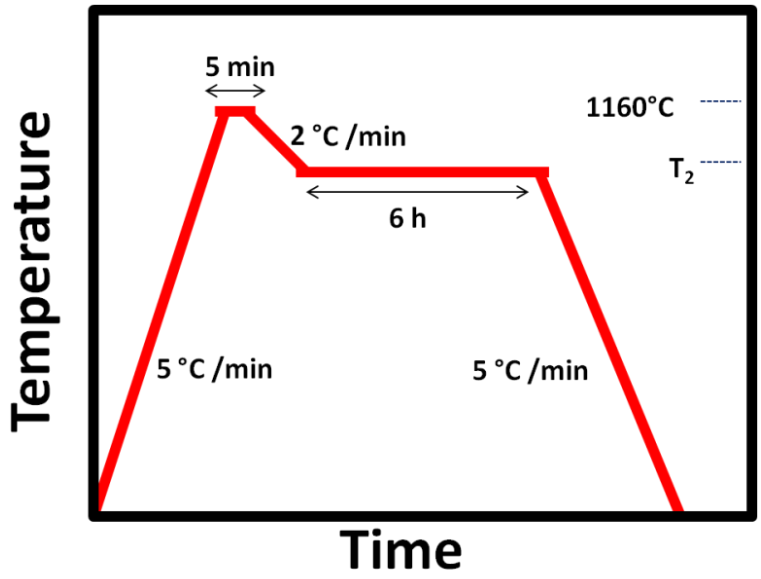

(g)

Figure 7.6 Schematic diagram for TGG process (a) – (f) showing different steps during tape casting process (g) Sintering profile used for synthesis of textured ceramics.

7.2.2.2 Use of Alkali Carbonates as sintering additives

As described in the last chapter, use of sodium and potassium carbonates having melting points lower than the sintering temperature of KNN not only provides an opportunity for liquid phase sintering but also avoids addition of foreign element to the lattice. Similar concept of using alkali carbonates as the sintering additive was used for texturing KNN ceramic. In this process, 1 mol% of alkali carbonate was added to the calcined KNN ceramic during second ball milling, prior to the preparation of slurry.

7.3 Results and Discussion

After sintering, samples were characterized for their crystallographic phase, orientation, microstructure and electric properties. Panalytical X-ray diffractometer was used to conduct the x-ray diffraction analysis. Radiant ferroelectric tester based on Sawyer – Tower bridge concept was used for ferroelectric characterization. Low field longitudinal piezoresponse was measured by using APC d_{33} meter.

7.3.1 KNN textured ceramics sintered with KCT

Phase analysis of sintered KNN samples was done by X-ray diffraction. Presence of only perovskite phase peaks (Figure 7.7) confirmed the formation of complete solid solution of KCT with KNN, in agreement with the previous reports. High intensity of pseudo cubic {l00} peaks confirmed the high degree of texturing in the desired orientation.

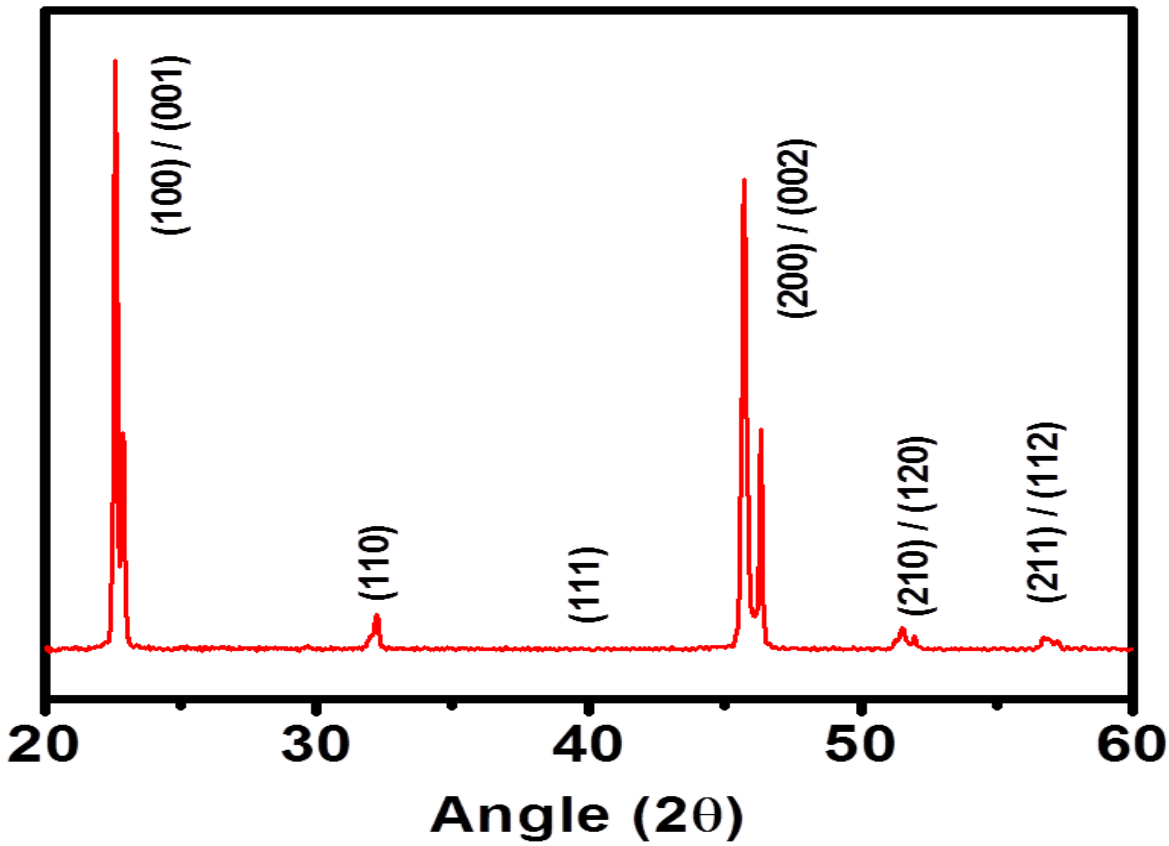

Figure 7.7 XRD pattern of textured KNN-KCT ceramic showing absence of any traceable impurity phase along with high degree of texturing.

Quantitatively, the degree of texturing is expressed in terms of Lotgering factor, given in Equation 7.6.

$$F_{00l} = (P_{00l} - P_0)/(1 - P_0) \tag{7.6}$$

where

$P_{00l} = \sum I_{00l} / \sum I_{hkl}$ And $P_0 = \sum I^0_{00l} / \sum I^0_{hkl}$

where $\sum I_{00l}$ and $\sum I_{00l}^{0}$ represents the sum of intensities of all {100} family peaks in textured and random ceramics, while $\sum I_{hkl}$ and $\sum I_{hkl}^{0}$ represents the sum of intensities of all peaks in textured and random samples respectively.

The lotgering factor calculated using Equation 7.6, was found to be 89%. The density of sintered samples was found to be 4.55 gm/cm^3 which was close to the theoretical density of KNN (4.51 gm/cm^3) and can be explained by accounting for the minor presence of comparatively heavier atoms like tantalum and copper. Figure 7.8 shows the SEM images at different magnifications for the surface normal to the tape casting direction. Consistent with the measured density by the Archimedes principle, the microstructure confirmed the presence of densely packed cubical grains of KNN.

The dielectric response of samples was investigated as a function of temperature to reveal the possible shifts in the two transition temperatures due to the incorporation of KCT in KNN lattice. Figure 7.9 shows the variation of dielectric permittivity and loss with temperature at 100 kHz. Associated with To-t and Tc respectively, the presence of a shoulder and peak at 180°C and 390°C confirmed a slight decrease in the two temperatures compared to pure KNN. This observation was consistent with what has been reported previously for random KNN-0.38 % KCT samples.[46]

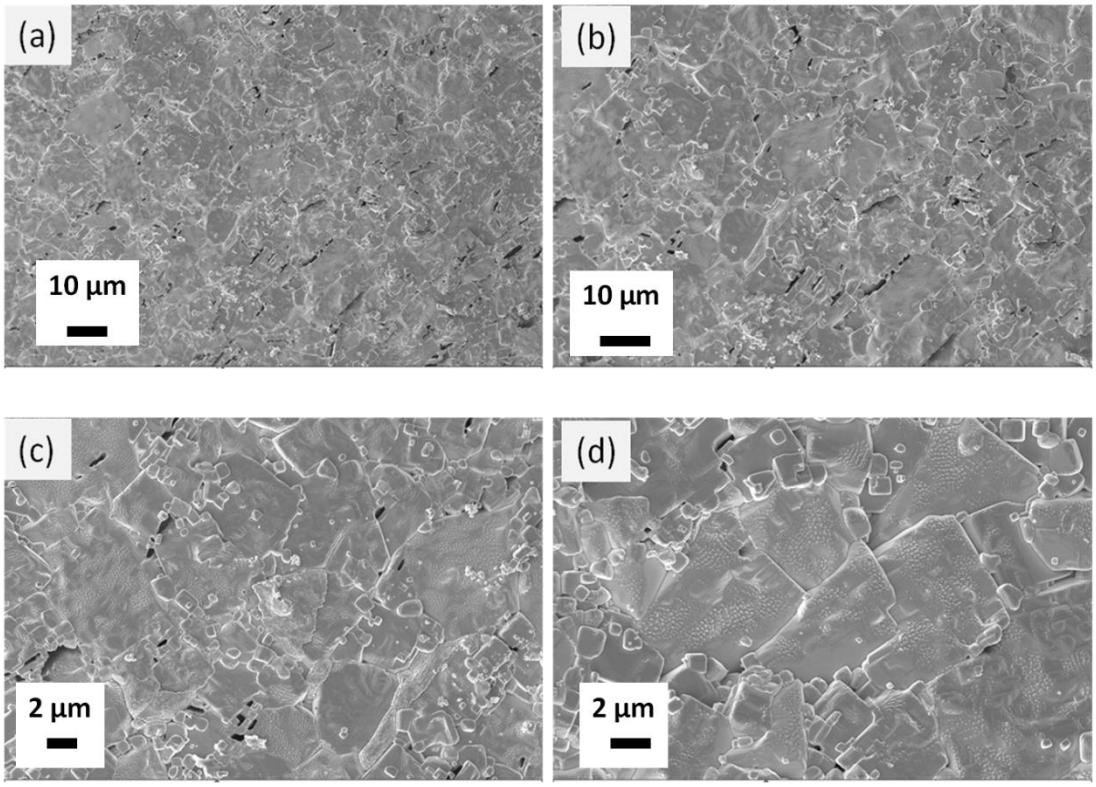

Figure 7.8 SEM images showing presence of aligned grains of KNN (a) – (d) at different magnifications.

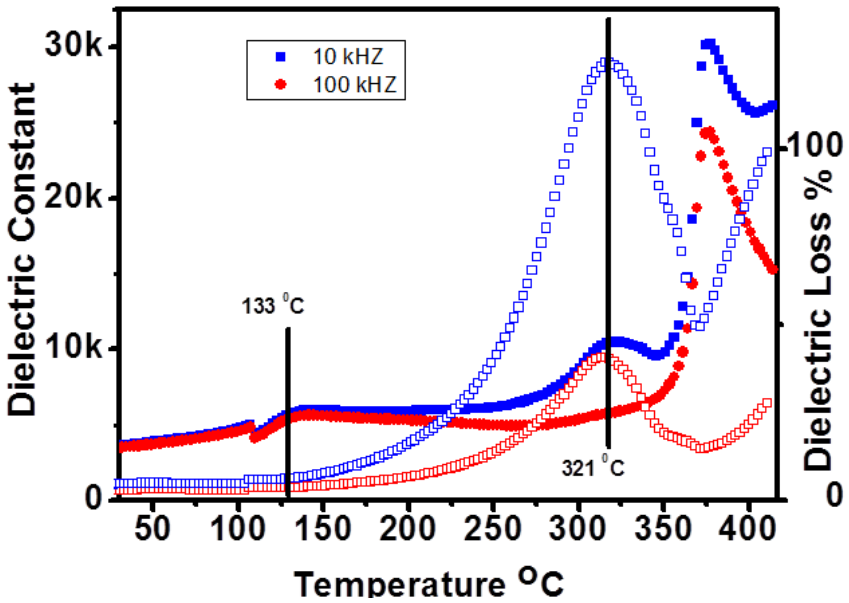

Figure 7.9 Temperature vs. dielectric constant plots for textured KNN-KCT ceramic.

P-E loops were obtained for random and textured samples as shown in Figure 7.10. The well saturated ferroelectric loop confirmed the absence of any significant leakage. The remanent polarization and coercive field values were found to be 18 μC/cm^2 and 17 kV/cm respectively. Almost equal values of remnant polarization for random and textured samples suggested that the highest polarization direction was not the same as pseudo cubic (100).

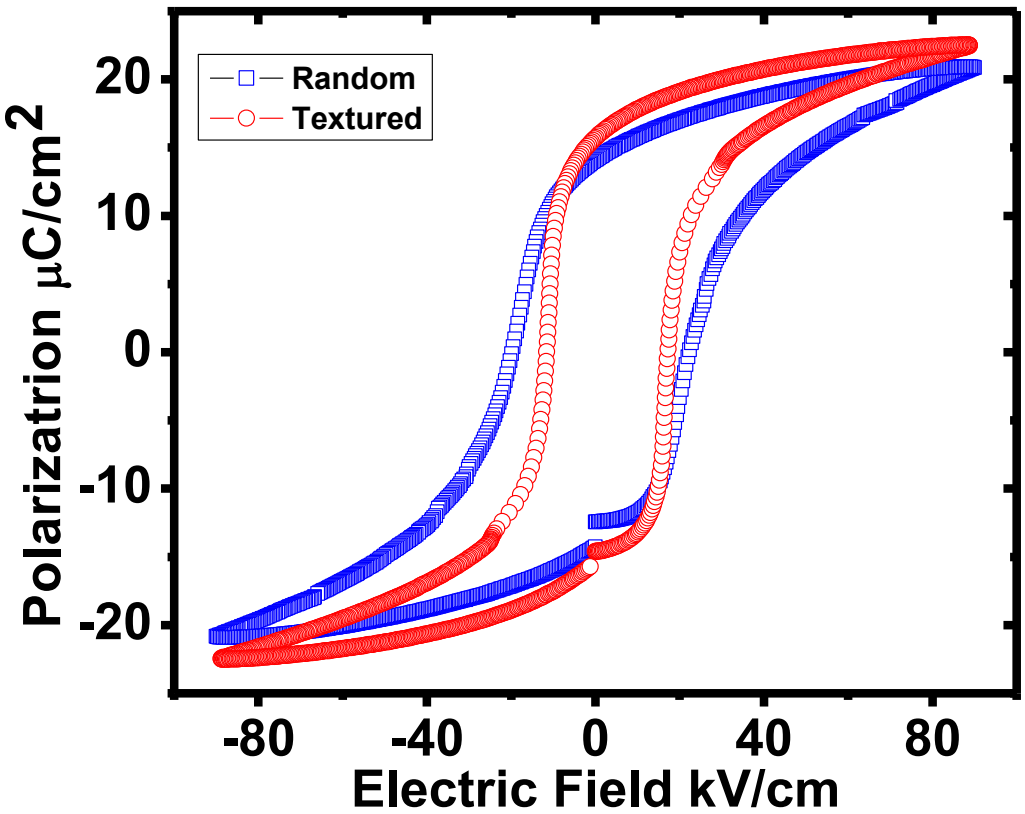

Figure 7.10 Ferroelectric loops obtained for random and textured KNN- KCT ceramics.

The piezoelectric coefficients obtained for random and textured ceramics were found to be 212 pC/N and 135 pC/N respectively, indicating an improvement of about 50% in the piezoresponse. This value of d_{33} is comparatively high as compared to the textured KNN samples synthesized

with $NaNbO_3$ seed and CuO as sintering additive (d_{33} ~ 145). Table 7.1 lists the values of different parameters of interest.

Table 7.1 Comparison of ferroelectric and piezoelectric properties of random and textured KNN-KCT ceramics.

	Random	**Textured**
$\mathbf{T_{O-T}}$	133℃	133℃
$\mathbf{T_c}$	321℃	321℃
$\mathbf{P_r}$ **(50Hz)**	17 μC/cm^2	18 μC/cm^2
$\mathbf{E_c}$	17 kV/cm	15 kV/cm
$\mathbf{d_{33}}$	212 pC/N	135 pC/N

7.3.2 KNN textured ceramics sintered with alkali carbonates

As described in Chapter 1, there are many studies conducted on KNN based compositions textured with different sintering additives. However, texturing of pure KNN ceramic still remains a challenge. Addition of sintering additives affects the magnitude of piezoelectric properties and temperature dependent behavior. In this study, where the intention was to conduct a comparative study among textured, random ceramics and single crystals, high quality pure KNN textured samples were desired. Figure 7.11 shows the XRD pattern of textured KNN sample sintered with alkali carbonates as sintering aid. Lotgering factor, calculated according to Equation 7.6, was found to be about 87 %.

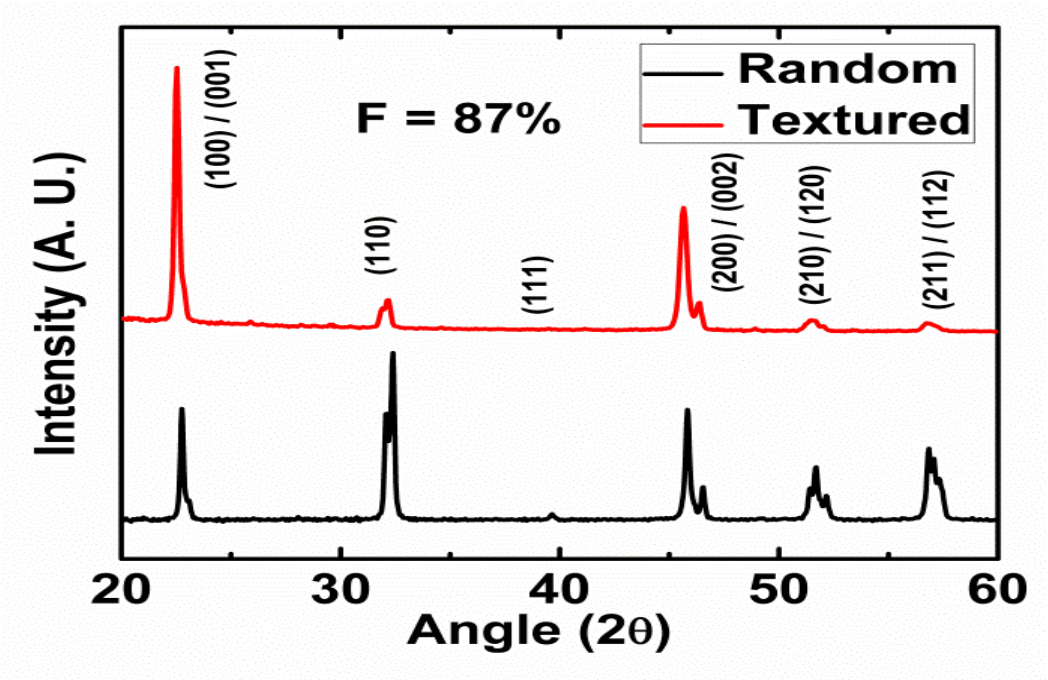

Figure 7.11 XRD pattern of KNN random and textured sample with about 87% lotgering factor.

The dielectric constant vs. temperature behavior is shown in Figure 7.12. Values of orthorhombic to tetragonal (200°C) and tetragonal to cubic (395°C) transition temperatures were quite similar to the values found for random ceramic samples.

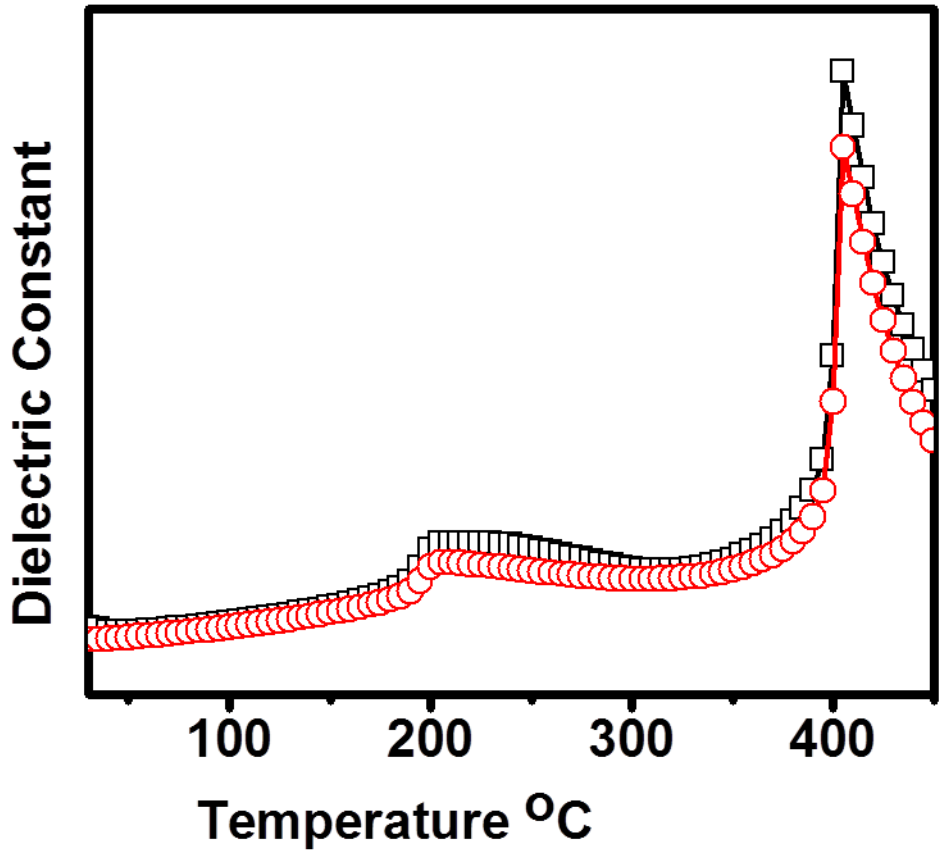

Figure 7.12 Temperature vs. dielectric constant plot showing the two transition temperature values to be about 200 °C and 395°C.

To perform the piezoelectric measurements, these textured samples were poled at the field of 5 kV/mm for one hour at 120°C. Low field value of longitudinal piezoelectric constant was found to be 170 - 180 pC/N, as compared to 100 – 110 pC/N for a random ceramic sample sintered under the same conditions (1135°C, 6 hours). These values of piezoelectric coefficients were lower than that found for a random ceramic sintered at 1130°C for 2 hours. This discrepancy was attributed to the higher sintering time required for achieving high degree of texturing in these samples. Figure 7.13 shows the ferroelectric loop obtained for highly textured sample showing remnant polarization value to be 20 μC/cm^2. This value is similar to the one measured for random ceramic sample. This observation is consistent with the finding for textured KNN- KCT

ceramic as (100) is not the highest polarization direction for KNN. The coercive field of textured ceramic was higher (40 kV/cm), as compared to its random counterpart (30 kV/cm).

Table 7.2 Comparison of ferroelectric and piezoelectric properties of random and textured KNN ceramics.

	Random	**Textured**
$\mathbf{T_{O\text{-}T}}$	200℃	395℃
$\mathbf{T_c}$	200℃	395℃
$\mathbf{P_r}$ **(50Hz)**	20 μC/cm^2	20 μC/cm^2
$\mathbf{E_c}$	30 kV/cm	40 kV/cm
$\mathbf{d_{33}}$	100 - 110 pC/N	170 – 180 pC/N

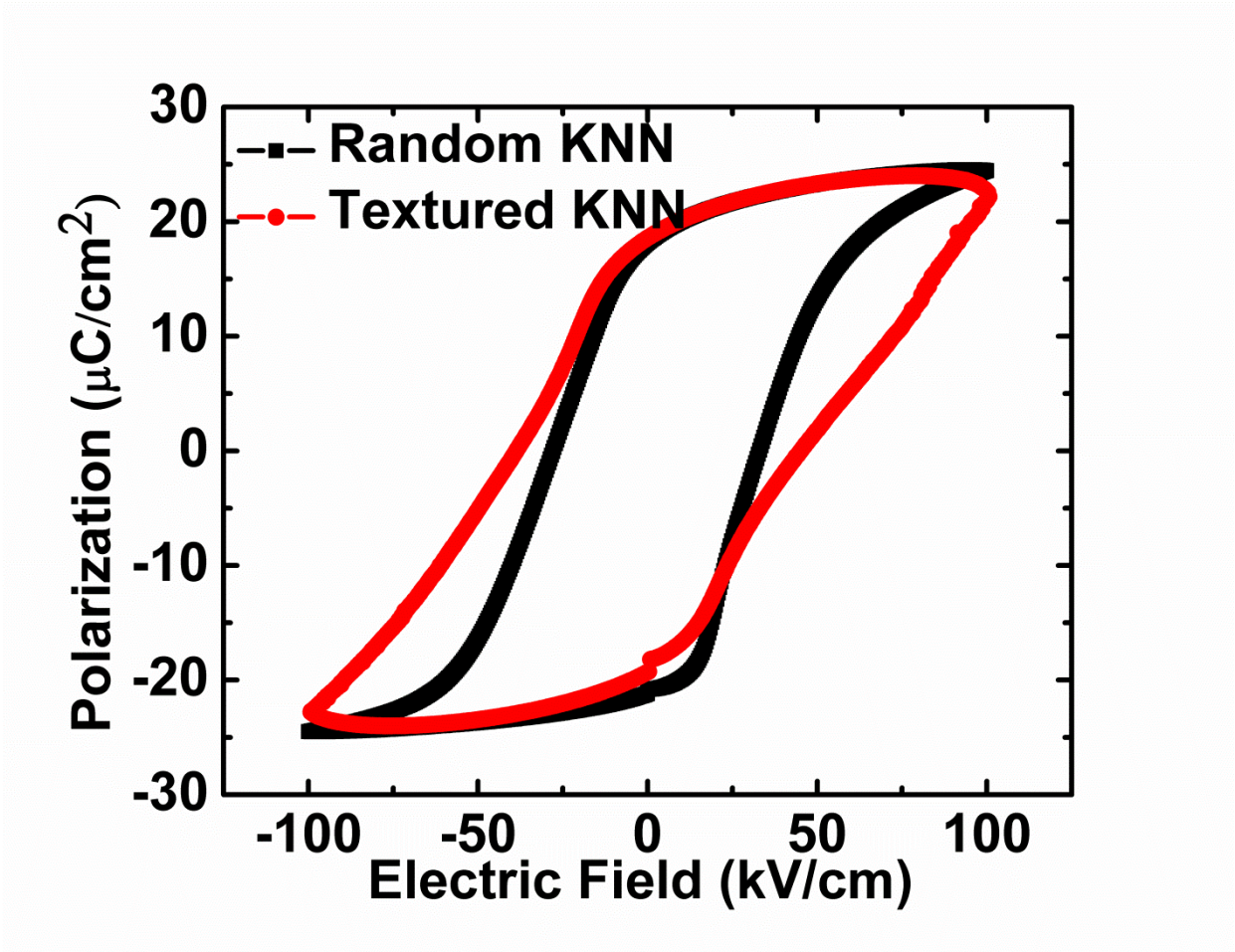

Figure 7.13 P –E loop obtained for random and textured KNN ceramic samples.

Other than crystallographic orientation, domain morphology and dynamics play an important role in determining the piezoelectric activity. To reveal these two aspects of textured KNN ceramic with respect to the random counterpart, samples were subjected to piezoresponse force microscopy (PFM) and switching spectroscopy (SS-PFM) analysis. Figure 7.14 shows the PFM amplitude and phase images for random and textured ceramics. It was observed that textured KNN ceramic had domain size in the range of 5μm - 8μm in contrast to the random ceramic that had domains of size 1μm - 3μm. Domain size play a profound role in determining the magnitude of coercive field as well as ferroelectric and electromechanical

response.[137, 196] Theoretical as well as experimental studies have confirmed the requirement of higher electric fields to switch the larger size domains.[197] Higher coercive field of textured KNN ceramic, as illustrated in Figure 7.13, could be attributed to its larger domain size.

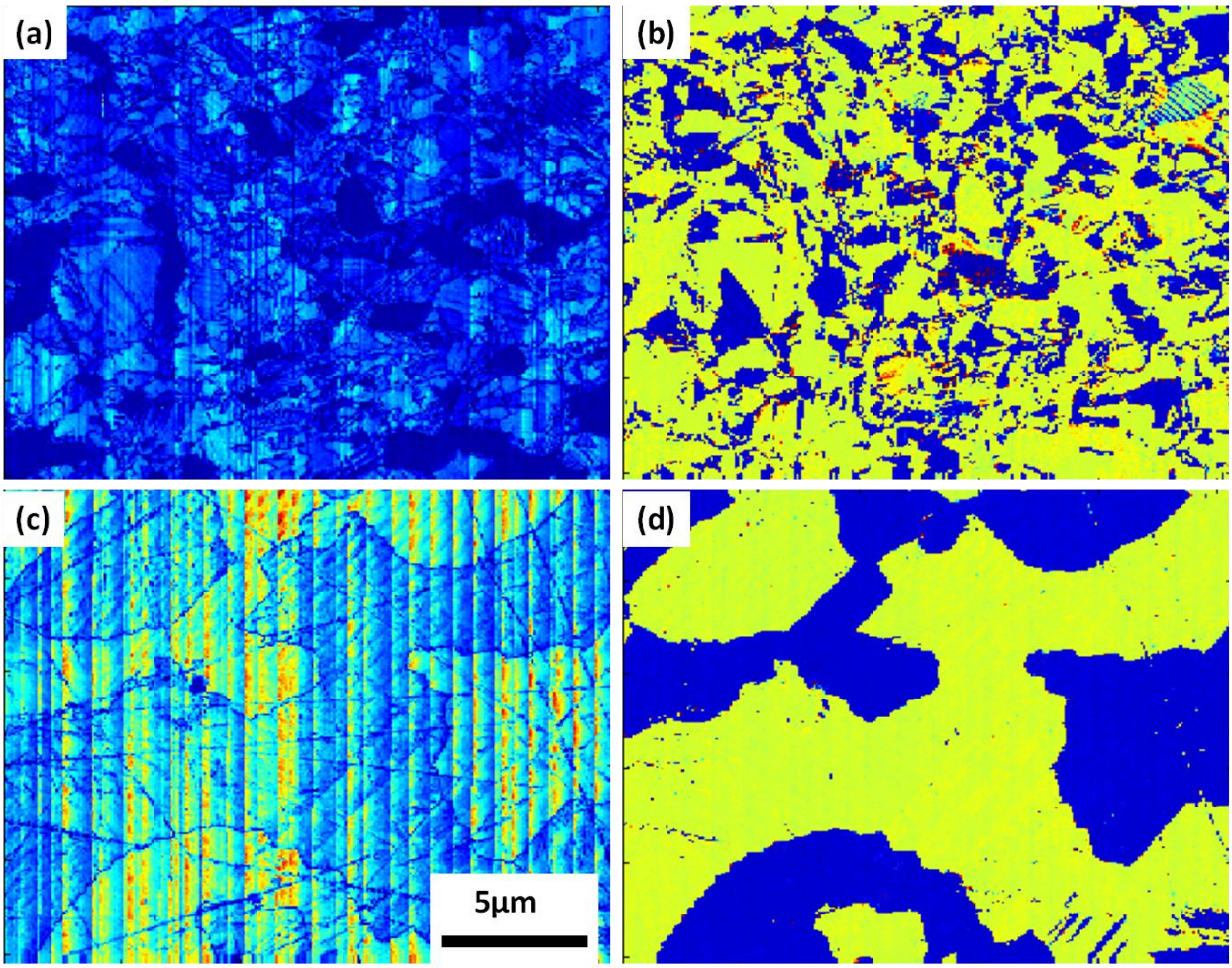

Figure 7.14 Domain structure of random and textured KNN ceramics (a) and (c) amplitude (b) and (d) phase.

Switching spectroscopy is an effective tool to determine the local switching behavior and piezoresponse of a ceramic.[198] In this technique piezoresponse is measured locally within a single domain and thus the response is independent of domain size. Figure 7.15 illustrates the local piezoresponse behavior of random and textured KNN ceramics. Two samples used for this

study were of equal thickness (90μm) and triangular voltage pulse of amplitude of 70 V was applied to capture the hysteresis loop. To avoid any discrepancy due to the statistical fluctuations, each of these loops for two ceramics were averaged over ten loops obtained from the same domain. In the case of the textured and random ceramics, the area of the ceramic switched under each of these points was 500 nm x 500 nm and 250 nm x 250 nm.

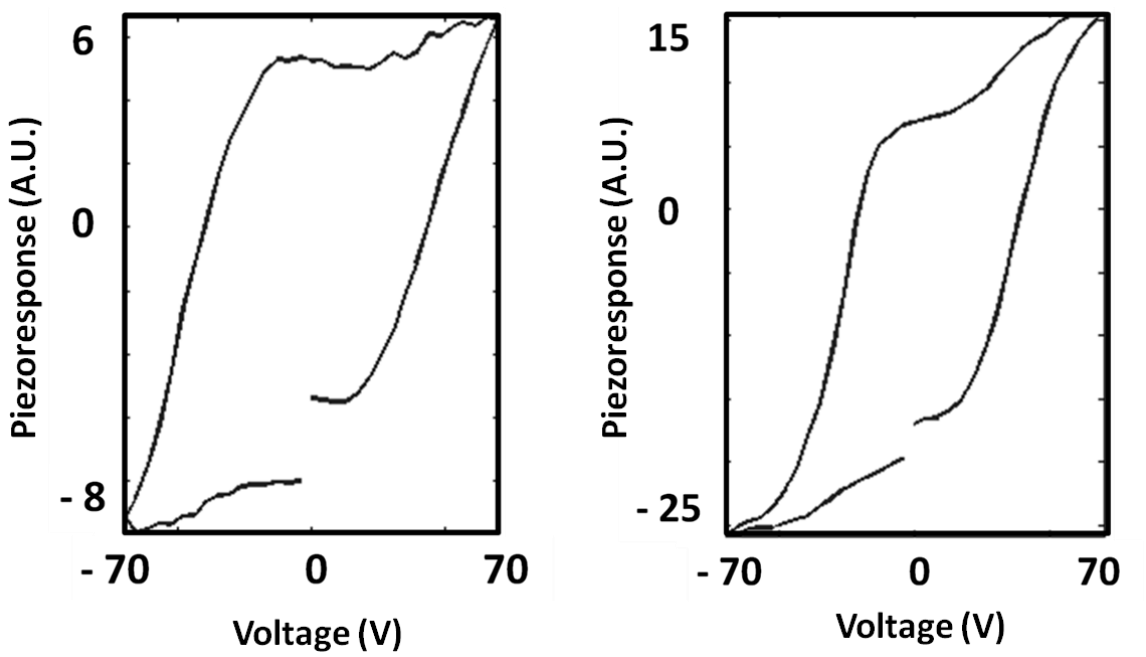

(a) (b)

Figure 7.15 Local piezoresponse of KNN (a) random and (b) textured ceramic.

Two interesting observations were made about these switching loops. Firstly, contrary to the bulk behavior, the random ceramic had higher coercive field as compared to the textured ceramic. This behavior was attributed to the role of the seed crystal in the textured ceramic as presence of any defect site tends to decrease the coercive field value. On the other hand the amplitude of piezoresponse in textured ceramics was about 2.5 times higher than that for random

ceramic. In contrast, the bulk piezoresponse of the textured ceramic only 1,5 times higher than that of random ceramic. This observation again could be attributed to the lower corecive field of the textured ceramic at a local scale.

In summary, textured KNN ceramics were synthesized using $K_{5.4}Cu_{1.3}Ta_{10}O_{29}$ (KCT) and alkali carbonates. Textured KNN-KCT ceramic having lotgering factor of 88% showed an improvement of about 50% in low field longitudinal piezoresponse (d_{33}), while ferroelectric polarization and coercive field values remain to be same. KNN ceramic textured using newly developed two-fold sintering technique also showed a similar improvement (50%) in piezoresponse. PFM analysis performed on these samples revealed the domain size to be 5µm - 8µm in contrast to random counterpart having domain size of 1µm - 3µm. In contrast to bulk piezoresponse, switching spectroscopy analysis (SS-PFM) suggests a two and half time improvement in local piezoelectric response for textured ceramic.

Chapter 8

Accomplishments and Future Work

8.1 Accomplishments

In this thesis, detailed crystallographic, domain structure and dynamic behavior of domains was studied by conducting detailed using KNN single crystal, textured ceramic and random ceramic. Important findings of this thesis are summarized as follows:

1. High leakage current has been a concern for KNN single crystals grown by variety of crystal growth techniques. This low resistivity of crystals limits the ferroelectric and piezoelectric characterization on these crystals. The results in thesis led to the conclusion that the high leakage current in KNN crystals is due to the presence of high concentration of oxygen ion vacancies. The solution to resolve this problem was identified as annealing the as-grown crystals in air. This additional annealing step in the synthesis process resulted in the high resistivity of crystals and hence they could be poled. Dynamic behavior of the domains was established by analyzing the ferroelectric behavior of high resistivity crystals under the varying electric field and frequency.
2. The crystallography of compositions close to x = 0.5 in the $(K_xNa_{1-x})NbO_3$ phase diagram has been a point of controversy in the literature. X-ray and neutron diffraction studies have provided different results probably due the close proximity of the lattice parameters. In this thesis, optical birefringence was used to determine the crystallographic nature of KNN crystals on either side of x =0.5. This investigation, independent of the lattice

parameter suggested that the potassium-deficient side had the monoclinic structure while the potassium rich side had the orthorhombic structure. This study further revealed the variation of the domain size of KNN single crystals across x = 0.5 phase boundary that improved the understanding of their role in governing the structure – property relationship.

3. Contrary to the findings of the optical birefringence study for macroscopic symmetry, pair distribution function analysis suggested the crystal structure of KNN to be monoclinic across x = 0.5. It is an important finding as few other complex perovskite ferroelectrics were also found to have different crystallographic behavior at local level than that in the bulk indicating the importance of probe size.
4. Practical application of KNN has been restricted by its poor sinterability and fatigue behavior. In this work, a modified two-fold sintering technique was developed that resulted in >99% density and improved fatigue behavior.
5. KNN-NBT-BT compositions were synthesized in order to study the thermal stability of piezoresponse in KNN based materials. It was demonstrated that the competing nature of the intrinsic and extrinsic contributions over the wide range of temperature lead to the reduction in the slope of the piezoelectric properties. A wide operating regime with temperature independent response was obtained.
6. To study the role of anisotropy in determining the local domain dynamics, textured KNN ceramic was synthesized. PFM analysis performed on textured ceramics revealed that the presence of seed crystals not only affected the domain size but also their local switching behavior. More work is required to make general conclusions but based on our current data this material has significant promise.

8.2 Future Work

1. Optical and pair distribution function analyses suggested the contrary crystallographic behavior of KNN crystals of composition close to x = 0.5. Detailed diffraction studies with varying probe sizes needs to be performed to confirm the findings of this study. The length scale at which the analysis is being conducted is vital in concluding the structure.
2. This study analyzed the domain structure of KNN at millimeter length scale and at the micrometer scale through optical birefringence and piezoresponse force microscopy. These investigations could be extended by conducting systematic TEM study in order to reveal the nano-scale domain morphology. Combined information at different length scales can be used in conjunction with the diffraction results to construct a clear picture of crystallography and its role in controlling the response in these materials.
3. A modified sintering technique was developed that led to the synthesis of high density KKN ceramics. These dense ceramics exhibited better piezoresponse and fatigue behavior. These ceramics provide opportunity to explore the deterministic role of microstructure towards piezoelectric behavior.
4. A high lotgering factor of 88% was achieved in the textured KNN ceramic. Efforts can be made to further improve the degree of texturing by making modification in the processing technique.

References

[1] B V Hiremath and R Newnham C Z Rosen, Key Papers in Physics : Piezoelectricity. (1992).

[2] K Uchino, Ferroelectric Devices, Second edition. (CRC Press, 2009).

[3] Y Xu, Ferroelectric Materials and their Applications. (Elsevier Science, 1991).

[4] B Jaffe, W R Cook, and H L Jaffe, Piezoelectric ceramics. (Academic Press, London; New York, 1971).

[5] H Kim, Y Tadesse, and S Priya, in Energy Harvesting Technologies, edited by S Priya and D J Inman (Springer US, 2009), pp. 3.

[6] S Priya, Journal of Electroceramics **19** (1), 167 (2007).

[7] E Hollenstein, D Damjanovic, and N Setter, Journal of the European Ceramic Society **27** (13-15), 4093 (2007).

[8] E Ringgaard, T Wurlitzer, and W W Wolny, Ferroelectrics **319** (1), 97 (2005).

[9] L Egerton and D M Dillon, Journal of the American Ceramic Society **42** (9), 438 (1959).

[10] V J T and K W Hang, Journal of Applied Physics **39** (10), 4749 (1968).

[11] L Wu, J L Zhang, C L Wang, and J. C. Li, Journal of Applied Physics **103** (8) (2008).

[12] J. Tellier, B. Malic, B. Dkhil, D. Jenko, J. Cilensek, and M. Kosec, Solid State Sciences **11** (2), 320 (2009).

[13] K Wang and J - F Li, Applied Physics Letters **91** (26), 262902 (2007).

[14] D W Baker, P A Thomas, N Zhang, and A M Glazer, Applied Physics Letters **95** (9) (2009).

[15] N Zhang, A M Glazer, D Baker, and P A Thomas, Acta Crystallographica Section B **65** (3), 291 (2009).

[16] D W Baker, P A Thomas, N Zhang, and A M Glazer, Acta Crystallographica Section B **65** (1), 22 (2009).

[17] A Glazer, Acta Crystallographica Section B **28** (11), 3384 (1972).

[18] P Bomlai, P Wichianrat, S Muensit, and S J Milne, Journal of the American Ceramic Society **90** (5), 1650 (2007).

[19] C - W Ahn, C -S Park, R Dittmer, S - H Hong, and Shashank Priya, Journal of Materials Science **45** (14), 3961 (2010).

[20] J Bernard, A Bencan, T Rojac, J Holc, B Malic, and M Kosec, Journal of the American Ceramic Society **91** (7), 2409 (2008).

[21] N M Hagh, B Jadidian, and A Safari, Journal of Electroceramics **18** (3), 339 (2007).

[22] D Jenko, A Bencan, B Malic, J Holc, and M Kosec, Microscopy and Microanalysis **11** (06), 572 (2005).

[23] C -W Ahn, C – S Park, C –H Choi, S Nahm, M - J Yoo, H –G Lee, and S Priya, Journal of the American Ceramic Society **92** (9), 2033 (2009).

[24] T A Skidmore and S J Milne, Journal of Materials Research **22** (08), 2265 (2007).

[25] Y Wang, D Damjanovic, N Klein, E Hollenstein, and N Setter, Journal of the American Ceramic Society **90** (11), 3485 (2007).

[26] H - L Du, F - S Tang, Z - M Li, W - C Zhou, S -B Qu, and Z - B Pei, Transactions of Nonferrous Metals Society of China **16** (Supplement 2), s462 (2006).

[27] R M German, *Sintering theory and practice*. (Wiley, New York, 1996).

[28] X Pang, J Qiu, K Zhu, and J Luo, Journal of Materials Science **46** (7), 2345 (2011).

[29] C W Ahn, M Karmarkar, D Viehland, D H Kang, K S Bae, and S Priya, Ferroelectrics Letters Section **35** (3-4), 66 (2008).

[30] D M Lin, K W Kwok, and H L W Chan, Journal of Physics D-Applied Physics **41** (4) (2008).

[31] R E Jaeger and L Egerton, Journal of the American Ceramic Society **45** (5), 209 (1962).

[32] H Du, Z Li, F Tang, S Qu, Z Pei, and W Zhou, Materials Science and Engineering: B **131** (1-3), 83 (2006).

[33] P Zhao, B - P Zhang, and J - F Li, Scripta Materialia **58** (6), 429 (2008).

[34] R Zuo, J Rödel, R Chen, and Longtu Li, Journal of the American Ceramic Society **89** (6), 2010 (2006).

[35] Y Wang, D Damjanovic, N Klein, and N Setter, Journal of the American Ceramic Society **91** (6), 1962 (2008).

[36] Y Zhen and J - F Li, Journal of the American Ceramic Society **89** (12), 3669 (2006).

[37] A Castro, B Jiménez, T Hungría, A Moure, and L Pardo, Journal of the European Ceramic Society **24** (6), 941 (2004).

[38] J F Li, K Wang, B P Zhang, and L M Zhang, Journal of the American Ceramic Society **89** (2), 706 (2006).

[39] L Egerton and C A Bieling, Ceram. Bull. **47** (1151) (1968).

[40] G H Haertling, Journal of the American Ceramic Society **50** (6), 329 (1967).

[41] M Kosec and D Kolar, Materials Research Bulletin **10** (5), 335 (1975).

[42] I Smeltere, M Dambekalne, M Livinsh, M Dunce, A Mishnov, and V Zauls, Integrated Ferroelectrics: An International Journal **108** (1), 46 (2009).

[43] C -W Ahn S - H Park, S Nahm and J – S Song, Jpn. J. Appl. Phys. **43**, L1072 (2004).

[44] Z Li, G Xu, Y Li, A Sun, L Duan, J Jiang, and P Cui, Physica B: Condensed Matter **405** (1), 296 (2010).

[45] M Matsubara, T Yamaguchi, K Kikuta, and S Hirano, Japanese Journal of Applied Physics Part 1-Regular Papers Short Notes & Review Papers **43** (10), 7159 (2004).

[46] M Matsubara, T Yamaguchi, K Kikuta, and S Hirano, Japanese Journal of Applied Physics Part 1-Regular Papers Short Notes & Review Papers **44** (1A), 258 (2005).

[47] E Li, H Kakemoto, S Wada, and T Tsurumi, Journal of the American Ceramic Society **90** (6), 1787 (2007).

[48] D Lin and et al., Journal of Physics D: Applied Physics **41** (4), 045401 (2008).

[49] C W Ahn, S Nahm, M Karmarkar, D Viehland, D H Kang, K S Bae, and S Priya, Materials Letters **62** (20), 3594 (2008).

[50] K Y, K Matsumoto, T Karaki, and M Adachi, Journal of the American Ceramic Society **93** (11), 3823 (2010).

[51] I T Seo, K H Cho, H Y Park, S J Park, M K Choi, S Nahm, H G Lee, H W Kang, and H J Lee, Journal of the American Ceramic Society **91** (12), 3955 (2008).

[52] R - A Eichel, E Erunal, M D Drahus, D M Smyth, J V Tol, J Acker, H Kungl, and M J Hoffmann, Physical Chemistry Chemical Physics **11** (39), 8698 (2009).

[53] B C Park, I K Hong, H D Jang, V D N Tran, W P Tai, and J - S Lee, Materials Letters **64** (14), 1577 (2010).

[54] Z Li-Mei et al., Chinese Physics Letters **26** (12), 127701 (2009).

[55] Y P Guo, K Kakimoto, and H Ohsato, Materials Letters **59** (2-3), 241 (2005).

[56] Y P Guo, K Kakimoto, and H Ohsato, Japanese Journal of Applied Physics Part 1-Regular Papers Short Notes & Review Papers **43** (9B), 6662 (2004).

[57] Y P Guo, K Kakimoto, and H Ohsato, Solid State Communications **129** (5), 279 (2004).

[58] Y P Guo, K Kakimoto, and H Ohsato, Applied Physics Letters **85** (18), 4121 (2004).

[59] R Zuo and C Ye, Applied Physics Letters **91** (6), 062916 (2007).

[60] R Zuo, C Ye, and X Fang, Journal of Physics and Chemistry of Solids **69** (1), 230 (2008).

[61] R Zuo, X Fang, and C Ye, Applied Physics Letters **90** (9), 092904 (2007).

[62] Y Saito and H Takao, Ferroelectrics **338** (1), 17 (2006).

[63] B - Q Ming, J – F Wang, P Qi, and G - Z Zang, Journal of Applied Physics **101** (5), 054103 (2007).

[64] H - Y Park, K - H Cho, D - S Paik, S Nahm, H - G Lee, and D - H Kim, Journal of Applied Physics **102** (12), 124101 (2007).

[65] S B Lang, W Zhu, and L E Cross, Ferroelectrics **336** (1), 15 (2006).

[66] Y Dai, X Zhang, and G Zhou, Applied Physics Letters **90** (26), 262903 (2007).

[67] R Zuo and J Fu, Journal of the American Ceramic Society **94** (5), 1467 (2011).

[68] Y Guo, K - I Kakimoto, and H Ohsato, Applied Physics Letters **85** (18), 4121 (2004).

[69] H Du, W Zhou, F Luo, D Zhu, S Qu, and Z Pei, Applied Physics Letters **91** (20), 202907 (2007).

[70] Q Zhang, B - P Zhang, H – T Li, and P - P Shang, Journal of Alloys and Compounds **490** (1-2), 260 (2010).

[71] G Z Zang, J F Wang, H C Chen, W B Su, C M Wang, P Qi, B Q Ming, J Du, and L M Zheng, Applied Physics Letters **88** (21) (2006).

[72] D M Lin, K W Kwok, K H Lam, and H L W Chan, Journal of Applied Physics **101** (7) (2007).

[73] Y Wang et al., Journal of Physics D: Applied Physics **41** (24), 245401 (2008).

[74] H L Du, W C Zhou, F Luo, D M Zhu, S B Qu, and Z B Pei, Applied Physics Letters **91** (20) (2007).

[75] C Lei and Z G Ye, Applied Physics Letters **93** (4) (2008).

[76] K -H Cho, H -Y Park, C -W Ahn, S Nahm, K Uchino, S - H Park, H - G Lee, and H -J Lee, Journal of the American Ceramic Society **90** (6), 1946 (2007).

[77] V Bobnar, M Kosec, M Hrovat, J Bernard, B Malic, J Holc J. Mater. Res. **19** (6), 1849 (2004).

[78] C - W Ahn, C - H Choi, H - Y Park, S Nahm, and S Priya, Journal of Materials Science **43** (20), 6784 (2008).

[79] C – H Choi, C - W Ahn, S Nahm, J - O Hong, and J – S Lee, Applied Physics Letters **90** (13), 132905 (2007).

[80] H Y Park, C W Ahn, H C Song, J H Lee, S Nahm, K Uchino, H G Lee, and H J Lee, Applied Physics Letters **89** (6) (2006).

[81] C - S Park C - W Ahn, D Viehland, S Nahm, D - H Kang, K - S Bae, and S Priya, Jpn. J. Appl. Phys. **47**, 8880 (2008).

[82] Y Saito, H Takao, T Tani, T Nonoyama, K Takatori, T Homma, T Nagaya, and M Nakamura, Nature **432** (7013), 84 (2004).

[83] Y Chang, S Poterala, Z Yang, and G L Messing, Journal of the American Ceramic Society **94** (8), 2494 (2011).

[84] Y Chang, S F Poterala, Z Yang, S Trolier-McKinstry, and G L Messing, Applied Physics Letters **95** (23), 232905 (2009).

[85] Y Chang, S F Poterala, Z Yang, S Trolier-McKinstry, and G L Messing, JOURNAL OF MATERIALS RESEARCH **25** (4) (2010).

[86] H Takao, Y Saito, Y Aoki, and K Horibuchi, Journal of the American Ceramic Society **89** (6), 1951 (2006).

[87] Y Yan, K - H Cho, and S Priya, Journal of the American Ceramic Society **92** (7), 1607 (2009).

[88] H Yilmaz, S Trolier-McKinstry, and G L Messing, Journal of Electroceramics **11** (3), 217 (2003).

[89] Y K, Y Noguchi, and M Miyayama, Applied Physics Letters **89** (14), 142910 (2006).

[90] D Lin, Z Li, S Zhang, Z Xu, and X Yao, Journal of the American Ceramic Society **93** (4), 941 (2010).

[91] J G Fisher, A Bencan, M Kosec, S Vernay and D Rytz, Journal of the American Ceramic Society, 2008, **91**, 1503-1507.

[92] H UrsiC, A BenCan, M Skarabot, M Godec and M Kosec, Journal of Applied Physics, 2010, **107**, 033705.

[93] A Bencan, E Tchernychova, M Godec, J Fisher, and M Kosec, Microscopy and Microanalysis **15** (5), 435 (2009).

[94] D Lin, Z Li, S Zhang, Z Xu, and X Yao, Solid State Communications **149** (39-40), 1646 (2009).

[95] S Gupta and S Priya, Applied Physics Letters **98** (24), 242906 (2011).

[96] H Y Hwang, Nat Mater **4** (11), 803 (2005).

[97] K W Browall, O Muller, and R H Doremus, Materials Research Bulletin **11** (12), 1475 (1976);

[98] K M Rabe, C H Ahn, and J M Triscone, *Physics of ferroelectrics : a modern perspective*. (Springer, Berlin; New York, 2007).

[99] D Maurya, N Wongdamnern, R Yimnirun, and S Priya, Journal of Applied Physics **108** (12), 124111 (2010).

[100] T K Song, Journal of the Korean Physical Society **46** (1), 5 (2005).

[101] M Rao, H R Krishnamurthy, and R Pandit, Physical Review B **42** (1), 856 (1990).

[102] M Rao and R Pandit, Physical Review B **43** (4), 3373 (1991).

[103] Y Y Guo et al., Journal of Physics: Condensed Matter **21** (48), 485901 (2009).

[104] R Yimnirun, Y Laosiritaworn, S Wongsaenmai, and S Ananta, Applied Physics Letters **89** (16), 162901 (2006).

[105] N Wongdamnern, A Ngamjarurojana, Y Laosiritaworn, S Ananta, and R Yimnirun, Journal of Applied Physics **105** (4), 044109 (2009).

[106] M Acharyya and B K Chakrabarti, Physical Review B **52** (9), 6550 (1995).

[107] B Pan, H Yu, D Wu, X H. Zhou, and J - M Liu, Applied Physics Letters **83** (7), 1406 (2003).

[108] A Ngamjarurojana, N Wongdamnern, S Ananta, Y Laosiritaworn, R Yimnirun, Key Engineering Materials **421-422**, 4 (2010).

[109] N Wongdamnern, N Triamnak, M Unruan, K Kanchiang, A Ngamjarurojana, S Ananta, Y Laosiritaworn, and R Yimnirun, Physics Letters A **374** (3), 391 (2010).

[110] J M Liu, H L W Chan, C L Choy, and C K Ong, Physical Review B **65** (1), 014416 (2001).

[111] B Noheda, D E Cox, G Shirane, R Guo, B Jones, and L E Cross, Physical Review B **63** (1), 014103 (2000.

[112] B. Noheda, J. A. Gonzalo, L. E. Cross, R. Guo, S. E. Park, D. E. Cox, and G. Shirane, Physical Review B **61** (13), 8687 (2000).

[113] G Xu, H Luo, H Xu, and Z Yin, Physical Review B **64** (2), 020102 (2001).

[114] B Noheda, D E Cox, G Shirane, J Gao, and Z G Ye, Physical Review B **66** (5), 054104 (2002).

[115] B Noheda, Z Zhong, D E Cox, G Shirane, S E Park, and P Rehrig, Physical Review B **65** (22), 224101 (2002).

[116] S Gorfman, A. M. Glazer, Y. Noguchi, M. Miyayama, H. Luo, and P. A. Thomas, Journal of Applied Crystallography **45** (3), 444 (2012).

[117] M Ahtee and A W Hewat, Acta Crystallographica Section A **34** (2), 309 (1978)

[118] M Ahtee and A M Glazer, Acta Crystallographica Section A **32** (3), 434 (1976).

[119] A M Glazer, N Zhang, A Bartasyte, and D S Keeble, Journal of Applied Crystallography **43** (6), 1305 (2010).

[120] J F Nye, *Physical properties of crystals*. (Clarendon Press, Oxford, 1957), p.322 p.

[121] R E Newnham, *Properties of materials : anisotropy, symmetry, structure*. (Oxford University Press, Oxford; New York, 2005).

[122] User Manual, Metripol Birefringence System, Oxford.

[123] M Geday, J Kreisel, A M Glazer, and K Roleder, Journal of Applied Crystallography **33** (3-2), 909 (2000).

[124] A M Glazer, J G Lewis, and W Kaminsky, Proceedings: Mathematical, Physical and Engineering Sciences **452** (1955), 2751 (1996).

[125] D Vanderbilt and M H Cohen, Physical Review B **63** (9) (2001).

[126] C - W Ahn, C – S Park, D Viehland, S Nahm, D - H Kang, K - S Bae, and S Priya, Japanese Journal of Applied Physics **47** (12), 8880 (2008).

[127] J Erhart, Phase Transitions **77** (12), 989 (2004).

[128] J Erhart and W Cao, Journal of Applied Physics **94** (5), 3436 (2003);

[129] J Sapriel, Ferroelectrics **13** (1), 459 (1976).

[130] J Sapriel, Physical Review B **12** (11), 5128 (1975).

[131] K Aizu, Journal of the Physical Society of Japan **28** (3), 706 (1959).

[132] J Fousek and V Janovec, Journal of Applied Physics **40** (1), 135 (1969).

[133] K Aizu, Physical Review B **2** (3), 754 (1970).

[134] F Bai, J Li, and D Viehland, Applied Physics Letters **85** (12), 2313 (2004)

[135] R Ahluwalia, T Lookman, A Saxena, and W Cao, Physical Review B **72** (1), 014112 (2005).

[136] S Wada, K Muraoka, H Kakemoto, and T Tsurumi, Materials science & engineering. B, Solid-state materials for advanced technology **120** (1), 186 (2005).

[137] K Yako, H Kakemoto, T Tsurumi, and S Wada, Materials science & engineering. B, Solid-state materials for advanced technology **120** (1-3), 181 (2005).

[138] S A Mabud and A M Glazer, Journal of Applied Crystallography **12** (1), 49 (1979).

[139] D Zekria, A M Glazer, V Shuvaeva, J Dec, and S Miga, Journal of Applied Crystallography **37** (4), 551 (2004).

[140] M Paturzo, L Aiello, F Pignatiello, P Ferraro, P D Natale, M D Angelis, and S D Nicola, Applied Physics Letters **88** (15), 151918 (2006).

[141] A Ziębińska, D Rytz, K Szot, M Górny, and K Roleder, Journal of Physics: Condensed Matter **20** (14), 142202 (2008).

[142] C L Jia, A Thust, and K Urban, Physical Review Letters **95** (22), 225506 (2005).

[143] M Takagi and T Ishidate, Solid State Communications **113** (7), 423 (2000).

[144] J Harada, J D Axe, and G Shirane, Physical Review B **4** (1), 155 (1971).

[145] Y Yamada, G Shirane, and A Linz, Physical Review **177** (2), 848 (1969.

[146] M F Wong and K Zeng, Journal of the American Ceramic Society **94** (4), 1079 (2011).

[147] K Aizu, Journal of the Physics Society Japan **28** (3), 706 (1959).

[148] T Egami and S J L Billinge, Underneath the Bragg peaks : structural analysis of complex materials, Pergamon, Kiddington, Oxford, UK; Boston, 2003.

[149] S Gupta and S Priya, Applied Physics Letters **102** (1), 012906 (2013.

[150] S Zhang, R Xia, and T R Shrout, Applied Physics Letters **91** (13), 132913 (2007).

[151] P Palei, M Pattanaik, and P Kumar, Ceramics International **38** (1), 851 (2012).

[152] S Priya and S Nahm, *Lead-free piezoelectrics*. (Springer, New York; London, 2011).

[153] B Guiffard, E Boucher, L Eyraud, L Lebrun, and D Guyomar, Journal of the European Ceramic Society **25** (12), 2487 (2005).

[154] M Kosec, B Malič, A Benčan, and T Rojac, in *Piezoelectric and Acoustic Materials for Transducer Applications*, edited by Ahmad Safari and E. Koray Akdoğan (Springer US, 2008), pp. 81.

[155] M N Rahaman, *Ceramic processing*. (CRC/Taylor & Francis, Boca Raton, FL, 2007).

[156] J Svoboda, H Riedel, and R Gaebel, Acta Materialia **44** (8), 3215 (1996.

[157] N Liu, K Wang, J – F Li, and Z Liu, Journal of the American Ceramic Society **92** (8), 1884 (2009).

[158] X J Lou, Journal of Applied Physics **105** (2) (2009).

[159] M Dawber and J F Scott, Applied Physics Letters **76** (25), 3801 (2000).

[160] D C Lupascu and U Rabe, Physical Review Letters **89** (18), 187601 (2002).

[161] E L Colla, D V Taylor, A K Tagantsev, and N Setter, Applied Physics Letters **72** (19), 2478 (1998).

[162] S Zhang, J Luo, F Li, R J Meyer Jr, W Hackenberger, and T R Shrout, Acta Materialia **58** (10), 3773 (2010).

[163] W L Warren, D Dimos, B A Tuttle, R D Nasby, and G E Pike, Applied Physics Letters **65** (8), 1018 (1994).

[164] D C Lupascu, *Fatigue in ferroelectric ceramics and related issues*. (Springer, Berlin; New York, 2004).

[165] E A Patterson and D P Cann, Ultrasonics, Ferroelectrics and Frequency Control, IEEE Transactions on **58** (9), 1835 (2011).

[166] S Zhang, R Xia, H Hao, H Liu, and T R Shrout, Applied Physics Letters **92** (15), 152904 (2008).

[167] S J L Kang, (Woodhead Publishing Limited, 2011), pp. 110.

[168] R M German, *Liquid phase sintering*. (Plenum Press, New York, 1985).

[169] P Babilo and S M Haile, Journal of the American Ceramic Society **88** (9), 2362 (2005).

[170] D Dey and R C Bradt, Journal of the American Ceramic Society **75** (9), 2529 (1992).

[171] X - H Wang, P - L Chen, and I W Chen, Journal of the American Ceramic Society **89** (2), 431 (2006).

[172] I W Chen, G N Hassold, and D J Srolovitz, Journal of the American Ceramic Society **73** (10), 2865 (1990).

[173] P - L Chen and I W Chen, Journal of the American Ceramic Society **79** (7), 1801 (1996).

[174] I W Chen and X H Wang, Nature **404** (6774), 168 (2000).

[175] X H Wang, X Y Deng, H - L Bai, H Zhou, W - G Qu, L T Li, and I W Chen, Journal of the American Ceramic Society **89** (2), 438 (2006).

[176] K Lu, Int. Mater. Rev. **53** (1), 21 (2008).

[177] Y - I Lee, Y - WKim, M Mitomo, and D - Y Kim, Journal of the American Ceramic Society **86** (10), 1803 (2003).

[178] P Winotai, N Udomkan, and S Meejoo, Sensors and actuators. A. Physical. **122** (2), 257 (2005).

[179] G S Kulikov, R S Malkovich, E A Skoryatina, V P Usacheva, T A Shaplygina, S F Gafarov, and T D Dzhafarov, Ferroelectrics **144** (1), 61 (1993.

[180] G C Mather, S Garcia-Martin, D Benne, C Ritter, and U Amador, Journal of Materials Chemistry **21** (15), 5764 (2011).

[181] J J Dih and R M Fulrath, Journal of the American Ceramic Society **61** (9-10), 448 (1978).

[182] C L Wang C Arago, J A Gonzalo, Ferroelectrics **337**, 233 (2006).

[183] C W Ahn et al., Journal of Physics D: Applied Physics **42** (21), 215304 (2009).

[184] Q M Zhang, H Wang, N Kim, and L E Cross, Journal of Applied Physics **75** (1), 454 (1994).

[185] X L Zhang, Z X Chen, L E Cross, and W A Schulze, Journal of Materials Science **18** (4), 968 (1983).

[186] F Jona and G Shirane, *Ferroelectric crystals*. (Pergamon Press, Oxford; New York, 1962).

[187] T Leist, T Granzow, W, and J Rodel, Journal of Applied Physics **108** (1), 014103 (2010).

[188] L Pintilie, I Vrejoiu, D Hesse, G LeRhun, and M Alexe, Physical Review B **75** (22), 224113 (2007).

[189] F Li, Z Xu, X Wei, and X Yao, Journal of Physics D: Applied Physics **42** (9), 095417 (2009).

[190] S Zhang, J Luo, W Hackenberger, and T R Shrout, Journal of Applied Physics **104** (6), 064106 (2008).

[191] M Budimir, D Damjanovic, and N Setter, Journal of Applied Physics **94** (10), 6753 (2003).

[192] D Damjanovic, M Budimir, M Davis, and N Setter, Journal of Materials Science **41** (1), 65 (2006).

[193] S Trolier-McKinstry, G L Messing, C Duran, S Kwon, B Brahmaroutu, P Park, H Yilmaz, P Rehrig, K Eitel, E Suvaci, M Seabaugh, M, and K Oh Critical Reviews in Solid State and Material Sciences **29**, 45 (2004).

[194] M Cao, W Wang, F Li, H Hao, Z Yu, and H Liu, Ferroelectrics **404** (1), 39 (2010).

[195] Y Yan, D Liu, W Zhao, H Zhou, and H Fang, Journal of the American Ceramic Society **90** (8), 2399 (2007).

[196] W Cao and C A Randall, Journal of Physics and Chemistry of Solids **57** (10), 1499 (1996).

[197] D - T Le, S – J Kwon, N - R Yeom, Y - J Lee, Y- H Jeong, M - P Chun, J - H Nam, J – H Paik, B - I Kim, and J - H Cho, Journal of the American Ceramic Society **96** (1), 174 (2013).

[198] S Jesse, A P Baddorf, and S V Kalinin, Applied Physics Letters **88** (6), 062908 (2006).

Appendix 1

(A) Area Under ferroelectric loops for $K_{0.5}Na_{0.5}NbO_3$ Single Crystals -

E. Field (kV/cm)	Area under ferroelectric loop (mF/cm3)					
	200 Hz	**100 Hz**	**80 Hz**	**60 Hz**	**40 Hz**	**20 Hz**
4	0.90	1.09	1.13	0.66	1.67	1.56
6	3.90	4.53	5.04	6.14	5.38	7.48
8	13.77	17.23	9.37	9.55	11.49	17.08
10	26.12	32.67	35.24	39.88	44.47	62.01
12	68.16	85.30	90.47	97.89	111.19	136.65
14	137.71	165.57	170.57	178.23	197.64	226.19
16	234.24	263.90	267.38	274.04	291.16	316.98
18	341.10	365.14	364.64	368.57	376.95	394.11
20	0.07	453.63	450.22	449.92	451.69	461.45
22	539.97	533.25	523.77	522.99	516.62	518.58
24	618.53	599.95	586.08	576.82	572.83	571.78
26	700.07	662.45	653.18	645.32	633.61	620.90
28	768.05	723.23	710.29	700.31	686.91	667.98
30	827.91	778.83	759.47	744.67	732.78	714.96
32	884.62	826.96	805.94	789.49	773.96	753.94
34	943.09	873.95	853.49	836.89	812.83	793.28
36	993.43	922.58	895.37	869.98	856.44	824.99

38	1045.95	975.76	944.79	918.00	897.64	868.53
42	1107.48	1063.93	1064.12	1070.28	1050.48	1012.17
46	1229.89	1167.18	1169.26	1164.38	1151.03	1110.88
50	1300.25	1238.85	1209.86	1181.86	1155.49	1112.16
54	1489.87	1441.45	1531.15	1373.77	1333.97	1291.40

E. Field (kV/cm)	**Area under ferroelectric loop (mF/cm3)**				
	10 Hz	**8 Hz**	**6 Hz**	**4 Hz**	**2 Hz**
4	1.91	2.06	2.26	2.60	3.48
6	10.16	11.25	12.98	15.93	25.26
8	26.20	30.35	35.97	44.92	63.69
10	84.28	94.03	106.29	122.19	154.11
12	166.29	178.98	192.61	212.30	244.90
14	258.88	272.16	285.67	301.92	329.59
16	339.80	352.31	352.31	374.31	395.35
18	409.40	417.89	427.13	436.17	449.04
20	468.51	477.84	483.17	488.81	492.70
22	522.84	526.79	528.47	530.36	532.16
24	570.24	572.67	572.86	572.52	580.25
26	615.10	616.87	618.93	617.56	618.47
28	663.40	664.90	661.97	658.42	651.46
30	700.32	700.85	698.26	693.18	685.90
32	738.58	739.89	736.59	729.39	722.74
34	771.71	771.99	769.95	765.62	751.32

36	807.00	805.51	801.84	796.17	787.95
38	843.39	841.75	836.96	827.82	813.49
42	983.14	972.39	955.23	931.97	885.51
46	1070.36	1065.00	1052.73	1018.71	974.37
50	1083.79	1080.89	1073.64	1063.69	1044.23
54	1243.13	1231.41	1208.06	1173.54	1114.95

(B) Area Under ferroelectric loops for S1 Ceramic -

E. Field (kV/cm)	**Area under ferroelectric loop (mF/cm3)**								
	100 Hz	**80 Hz**	**60 Hz**	**40 Hz**	**20 Hz**	**10 Hz**	**5 Hz**	**2 Hz**	**1 Hz**
1	0.00	0.00	0.00	0.00	0.00	0.00	0.00	0.00	0.00
2	0.00	0.00	0.00	0.00	0.00	0.00	0.30	0.44	0.60
3	0.25	0.26	0.28	0.31	0.40	0.53	0.70	1.05	1.43
4	0.48	0.50	0.54	0.64	0.79	1.02	1.35	2.01	2.75
5	0.81	0.86	0.93	1.06	1.36	1.74	2.28	3.39	4.66
6	1.29	1.40	1.50	1.71	2.12	2.73	3.57	5.27	7.25
7	2.00	2.07	2.24	2.50	3.17	4.04	5.27	7.74	10.59
8	2.83	3.02	3.23	3.23	3.61	4.50	7.44	10.84	14.73
9	3.97	4.12	4.51	4.95	6.15	7.82	10.11	14.63	19.81
10	5.37	5.62	6.04	6.65	8.21	10.39	13.35	19.21	25.87

(C) Area Under ferroelectric loops for S4 Ceramic -

E. Field (kV/cm)	**Area under ferroelectric loop (mF/cm3)**								
	100 Hz	**80 Hz**	**60 Hz**	**40 Hz**	**20 Hz**	**10 Hz**	**5 Hz**	**2 Hz**	**1 Hz**
1	0.00	0.00	0.00	0.00	0.00	0.00	0.01	0.01	0.01
2	0.01	0.01	0.02	0.01	0.02	0.02	0.03	0.05	0.06
3	0.03	0.04	0.04	0.05	0.05	0.06	0.08	0.12	0.25
4	0.08	0.11	0.13	0.30	0.34	0.37	0.41	0.50	0.56
5	0.11	0.17	0.40	0.54	0.59	0.64	0.71	0.84	0.98
6	0.72	0.70	0.76	0.82	0.88	0.96	1.06	1.31	1.47
7	0.85	0.91	0.99	1.05	1.14	1.24	1.42	1.78	2.18
8	1.28	1.31	1.40	1.38	1.57	1.79	2.02	2.61	3.16
9	1.81	1.77	1.78	1.95	2.18	2.43	2.84	3.55	4.36
10	2.34	2.38	2.47	2.59	2.90	3.32	3.83	4.75	5.86

Appendix 2

(A) Determination of Orientation Histogram for KNN crystals –

To plot the orientation histograms for KNN crystals, orientation false color images obtained by the Metripol birefringence system were used. Each of this false color images was obtained for the area of 2.5 X 1.9 mm^2 of crystal with the resolution of 1360 X 1024 pixels. Hence, each of these 1392640 (1360 X 1024) pixels was representing the orientation of optical indicatrix for the area of about 3.4 μm^2 of crystal. The orientation of optical indicatrix for each pixel was represented by ϕ, having value between 0° – 180°. For the present study twenty four (three x = 0.4, 0.5 and 0.6 crystals studied at eight temperatures) such false color images were converted to the ϕ matrices. Each of these matrices in Microsoft excel sheet when converted to Microsoft word, occupied about 3000 pages and hence practically impossible to be included in this thesis. Also due to the limitation of Microsoft excel worksheet, histogram for 1392640 numbers could not be created at a time. Hence each of these matrices was splitted in 56 parts and histograms are created for all of them separately with the bin size of 1°. Finally, all these fifty six histograms were compiled together to get the desired orientation histograms for the crystal area of 2.5 X 1.9 mm^2. Following tables show the distribution of ϕ values for three crystals in the range of 0° – 180° with the bin size of 1°.

(B) Distribution of orientation angle for x = 0.4 crystal -

Bin	Temperature (°C)							
	30	**80**	**130**	**180**	**230**	**280**	**330**	**380**
0° - 1°	2017	970	552	1564	2744	4535	5526	11097
1° - 2°	1784	934	520	1527	2848	4733	5753	10684
2° - 3°	1650	834	535	1519	2987	4742	5916	10377
3° - 4°	1573	821	476	1538	2900	4729	5986	9741
4° - 5°	1471	746	448	1533	3012	4873	6120	8983
5° - 6°	1316	718	441	1559	2927	4990	6075	8416
6° - 7°	1283	623	442	1564	2967	5000	6441	7901
7° - 8°	1120	635	390	1545	3043	5002	6373	7650
8° - 9°	947	603	392	1541	3014	4862	5892	6733
9° - 11°	898	629	352	1474	3161	4703	5540	6500
11° - 12°	887	560	392	1480	3107	4447	5395	6262
12° - 13°	902	572	376	1461	2990	4230	4878	5746
13° - 14°	832	554	354	1479	3029	4034	4675	5454
14° - 15°	812	526	345	1415	2970	3831	4730	5028
15° - 16°	773	525	328	1470	2864	3783	4552	4776
16° - 17°	800	546	362	1456	2769	3725	4362	4445
17° - 18°	759	537	337	1438	2622	3421	3945	4075
18° - 20°	734	594	353	1476	2500	3258	3997	3730
20° - 21°	737	568	339	1473	2352	3225	3885	3526
21° - 22°	676	638	333	1470	2394	3079	3766	3307
22° - 23°	717	653	323	1436	2368	3050	3583	3206
23° - 24°	688	678	327	1421	2300	2816	3465	3100
24° - 25°	697	677	315	1360	2210	2685	3503	3209
25° - 26°	718	722	304	1387	2184	2630	3366	3087
26° - 27°	681	766	322	1478	2163	2644	3486	3074
27° - 28°	681	892	367	1434	2116	2450	3277	3001
28° - 30°	668	950	345	1469	2083	2475	3197	2854
30° - 31°	688	956	346	1471	2066	2576	3126	2858
31° - 32°	654	1010	353	1464	2029	2427	3083	2827
32° - 33°	626	970	377	1483	2051	2374	2952	2681
33° - 34°	653	938	398	1490	2071	2346	2883	2776
34° - 35°	647	886	361	1601	2069	2411	2738	2725

35° - 36°	719	815	359	1540	2037	2435	2772	2639
36° - 37°	624	738	454	1580	2087	2198	2830	2637
37° - 39°	682	685	424	1628	2045	2371	2774	2598
39° - 40°	685	723	433	1635	2086	2394	2757	2699
40° - 41°	721	727	450	1664	2233	2512	2793	2664
41° - 42°	757	713	471	1648	2209	2513	2836	2688
42° - 43°	787	751	514	1712	2196	2578	2891	2684
43° - 44°	753	799	502	1711	2340	2628	3048	2660
44° - 45°	845	797	571	1779	2353	2646	3124	2656
45° - 46°	816	796	587	1758	2305	2737	3159	2646
46° - 47°	866	776	663	1818	2587	2876	3381	2970
47° - 49°	915	870	716	1880	2830	2917	3302	2948
49° - 50°	937	905	732	1960	2916	2988	3410	2933
50° - 51°	950	913	755	2076	3042	3133	3302	3036
51° - 52°	985	995	874	2119	3220	3229	3532	3087
52° - 53°	1069	998	906	2215	3387	3413	3777	3356
53° - 54°	1084	1035	979	2167	3426	3509	3889	3449
54° - 55°	1096	1031	1071	2343	3812	3922	4013	3764
55° - 56°	1243	1305	1358	2509	4527	4382	4329	4063
56° - 58°	1252	1272	1423	2620	4644	4640	4442	4043
58° - 59°	1285	1433	1547	2730	5067	4926	4584	4066
59° - 60°	1350	1551	1643	2811	5298	5641	4825	3913
60° - 61°	1421	1668	1832	3078	5590	6014	5156	4066
61° - 62°	1552	1863	1940	3438	6036	6524	5232	3900
62° - 63°	1621	2074	2073	3604	6644	6784	5352	4062
63° - 64°	1792	2315	2267	3799	7052	7414	5367	4161
64° - 65°	1892	2534	2447	4284	7463	7585	5462	4232
65° - 66°	2383	3387	3328	5526	8799	7787	5515	4392
66° - 68°	2530	3811	3653	6309	9105	7915	5606	4492
68° - 69°	2597	4096	4192	6896	9443	8320	5739	4565
69° - 70°	2803	4739	4659	7490	9847	8378	5977	4723
70° - 71°	3027	5298	5274	8131	10308	8474	6025	4828
71° - 72°	3331	5940	6153	8607	10119	8434	6172	5004
72° - 73°	3661	6556	7032	9493	10242	8271	6503	4954
73° - 74°	3849	7072	7836	9822	10460	8436	6477	4897
74° - 75°	5352	9624	9878	10679	10146	8385	6678	5374

75° - 77°	6072	10058	10356	10650	10143	8148	6643	5636
77° - 78°	6852	11004	10840	10739	9969	8323	6783	5645
78° - 79°	7746	11456	11340	10994	9923	8075	6891	5943
79° - 80°	8400	12128	11564	11013	10068	8046	6857	6180
80° - 81°	9067	12782	11803	11125	10090	8311	6921	6408
81° - 82°	9863	13130	12075	11429	10136	8181	7010	6868
82° - 83°	11042	13509	12596	11470	10086	8323	6983	7107
83° - 84°	11520	13523	12522	11400	10043	8248	7200	7293
84° - 85°	13449	13266	12771	11644	9805	8196	7673	8313
85° - 87°	14146	13060	12944	11839	9837	8338	8011	8834
87° - 88°	14358	12898	12858	11603	9649	8622	8185	9400
88° - 89°	14460	12776	12857	11509	9798	8662	8433	10203
89° - 90°	14686	12476	12537	11224	9752	8906	8683	11200
90° - 91°	14734	12368	12312	11100	9449	8893	9285	11994
91° - 92°	14787	12125	12202	10790	9546	8825	9644	12684
92° - 93°	14649	11711	12017	10888	9307	9053	10086	13920
93° - 94°	13735	11087	11606	10459	9834	9729	11411	18600
94° - 96°	13193	10984	11616	10620	9670	9964	12037	19655
96° - 97°	12939	10582	11533	10428	9856	10483	12905	21037
97° - 98°	12648	10218	11534	10308	9823	10744	13485	21863
98° - 99°	12095	10084	11419	10177	9919	11061	14216	21920
99° - 100°	11894	9530	11398	10015	10077	11263	15092	21323
100° - 101°	11439	9309	11306	9850	10099	11671	16171	20110
101° - 102°	11037	9085	11419	9894	10223	12117	17217	18759
102° - 103°	10904	8781	11443	9575	10173	12333	18018	17103
103° - 104°	10021	8430	11121	9409	10795	13874	19819	14174
104° - 106°	9488	8364	11324	9341	11052	14539	19993	13421
106° - 107°	9440	8239	11274	9168	11486	14918	20424	12397
107° - 108°	8918	8409	11158	9140	11671	15073	19866	11659
108° - 109°	8869	8157	11099	8961	11884	15175	18278	10802
109° - 110°	8530	8259	11178	8902	12209	15197	17728	10218
110° - 111°	8506	8374	11012	8921	12468	15621	16441	9725
111° - 112°	8249	8046	11094	8869	12650	15227	15421	9299
112° - 113°	7989	7890	11152	8945	12918	13590	13417	8796
113° - 115°	7810	7956	11191	8719	13207	13283	12690	8579
115° - 116°	7924	8057	11258	8884	13436	12637	12250	8538

116° - 117°	7714	7923	11257	9001	13314	12376	11986	8548
117° - 118°	7717	8103	11484	9046	12985	11983	11497	8476
118° - 119°	7574	7974	11208	9132	12892	11365	10989	8651
119° - 120°	7615	8123	11562	9162	12468	10974	10669	8502
120° - 121°	7494	8382	11577	9233	12428	10691	10059	8454
121° - 122°	7454	8291	11905	9300	11983	10184	9772	8487
122° - 123°	7354	8532	12151	9507	11252	9654	9450	8814
123° - 125°	7259	8557	12260	9864	11408	9628	9561	8853
125° - 126°	7441	8585	12519	9791	11050	9495	9562	9114
126° - 127°	7396	8660	12726	10114	10935	9306	9817	9180
127° - 128°	7377	8904	13066	10256	10835	9525	9692	8900
128° - 129°	7392	8825	13297	10414	10657	9601	9593	8715
129° - 130°	7476	9138	13619	10847	10568	9715	9678	8703
130° - 131°	7644	9264	13763	11198	10506	9427	9692	8489
131° - 132°	7946	9935	14937	12040	10756	9699	9952	8249
132° - 134°	8300	10317	15344	12509	10898	10071	10217	7723
134° - 135°	8249	10606	15707	13003	10974	10594	10272	7911
135° - 136°	8470	10762	16345	13762	11143	10758	10098	7396
136° - 137°	8655	11218	16949	14150	11636	10944	10011	7094
137° - 138°	8787	11710	17290	14433	11675	11523	10260	6974
138° - 139°	8923	12337	17688	15315	12452	11879	10470	6755
139° - 140°	9198	13001	18388	15674	12918	11947	10573	6356
140° - 141°	9315	13750	19933	16105	13428	12465	9749	6090
141° - 142°	9634	14845	20262	17587	14234	12733	9557	5898
142° - 144°	10527	15457	21133	18896	14468	12911	9269	5555
144° - 145°	10878	15912	21357	19564	14568	13089	8875	5429
145° - 146°	11168	16600	22352	20703	14780	12967	8342	5361
146° - 147°	11868	16740	22847	21314	14842	12301	7736	5450
147° - 148°	12041	17655	23229	21656	14188	11380	7361	5309
148° - 149°	12533	18578	22945	22395	13890	10391	6490	5064
149° - 150°	13202	19414	23034	22730	13150	9501	5893	5069
150° - 151°	13971	20595	22498	22902	12385	8213	5082	4792
152° - 153°	16312	23294	18683	19972	8974	5623	4119	4885
153° - 154°	16938	24286	16923	17880	7417	5132	3930	4968
154° - 155°	17824	24842	14709	15337	6031	4583	3762	4796
155° - 156°	18674	25230	11978	12670	5213	4562	3562	4804

156° - 157°	19551	25189	9540	10488	4525	4272	3380	4769
157° - 158°	20560	24362	7214	8425	4118	4004	3303	4731
158° - 159°	21131	23904	5424	6849	3773	3917	3321	4696
159° - 160°	22104	22416	4231	5943	3654	3769	3231	4515
160° - 161°	23276	15612	2350	3673	3097	3436	3091	4455
161° - 163°	23473	12489	1947	3392	3001	3453	2999	4401
163° - 164°	22796	9693	1699	2944	2801	3411	3047	4637
164° - 165°	22291	7727	1541	2755	2797	3350	3038	4747
165° - 166°	20720	6309	1336	2578	2852	3424	3008	5020
166° - 167°	19181	5200	1299	2371	2722	3454	3021	5182
167° - 168°	17261	4181	1160	2184	2793	3621	3125	5457
168° - 169°	15018	3640	1053	2076	2685	3639	3188	5913
169° - 170°	12769	3099	1002	2015	2599	3655	3158	6195
170° - 172°	7437	2160	896	1752	2604	3749	3473	6952
172° - 173°	6189	1936	874	1675	2536	3605	3527	7226
173° - 174°	5423	1734	810	1604	2509	3957	3610	7664
174° - 175°	4596	1590	768	1604	2621	4031	3702	8288
175° - 176°	4023	1501	737	1586	2517	4024	3791	9273
176° - 177°	3459	1381	741	1614	2559	4156	3822	9789
177° - 178°	3023	1322	720	1509	2523	4213	4101	10288
178° - 179°	2770	1277	703	1605	2624	4317	4462	10717
179° - 180°	2098	1041	581	1500	2810	4530	5232	10996

(C) Distribution of orientation angle for x = 0.5 crystal -

Bin	**Temperature (°C)**							
	30	**80**	**130**	**180**	**230**	**280**	**330**	**380**
0° - 1°	15671	10640	10574	13045	12097	17988	8047	24370
1° - 2°	10840	7222	7022	8687	8060	12229	5533	18070
2° - 3°	11310	6966	6892	8544	7976	12047	5594	17452
3° - 4°	11505	7026	6862	8634	7877	10858	5445	15505
4° - 5°	12298	6885	6752	8467	7693	10050	5525	14302
5° - 6°	12412	6882	6637	8470	7717	8975	5465	12656
6° - 7°	12965	6761	6572	8250	7575	8323	5455	11396
7° - 8°	13590	6883	6531	8298	7509	7762	5578	10789

8° - 9°	14315	6816	6570	8086	7272	7367	5525	10357
9° - 11°	16770	6790	6469	7482	6963	6675	5932	8938
11° - 12°	17274	6593	6411	7581	6632	6524	5771	8528
12° - 13°	18017	6692	6354	7590	6530	6412	5967	7986
13° - 14°	18800	6604	6353	7276	6236	6352	6109	7756
14° - 15°	19680	6773	6373	7267	6209	6003	6201	7415
15° - 16°	20764	6479	6409	6927	5949	5916	6312	7230
16° - 17°	21379	6539	6115	6940	5753	5732	6445	6887
17° - 18°	22325	6539	6343	6927	5630	5772	6573	6661
18° - 20°	23603	6504	6367	6542	5308	4971	6935	5760
20° - 21°	23811	6623	6300	6354	5232	5064	7008	5552
21° - 22°	22853	6631	6390	6474	5055	4949	7080	5300
22° - 23°	22432	6589	6122	6127	4986	5052	7299	5186
23° - 24°	20673	6424	6305	6119	4849	4979	7450	4924
24° - 25°	19127	6642	6346	5905	4803	4871	7695	4739
25° - 26°	17197	6789	6342	5886	4750	4828	7692	4533
26° - 27°	14958	6508	6232	5845	4718	4688	8132	4495
27° - 28°	12827	6759	6463	5734	4450	4740	8228	4252
28° - 30°	7540	6719	6414	5652	4466	4623	8900	3890
30° - 31°	6322	6880	6502	5545	4396	4710	9235	3735
31° - 32°	5463	6871	6373	5526	4407	4630	9444	3609
32° - 33°	4614	6758	6353	5357	4447	4573	9750	3452
33° - 34°	4012	6778	6517	5289	4318	4724	10275	3541
34° - 35°	3505	6820	6350	5179	4483	4534	10852	3405
35° - 36°	3046	6949	6209	5230	4507	4595	11220	3400
36° - 37°	2783	6667	6458	5290	4467	4664	11341	3234
37° - 39°	2078	6517	6137	5042	4675	4643	13952	3072
39° - 40°	2030	6603	6115	5078	4631	4687	14619	2998
40° - 41°	1773	6504	5933	5066	4810	4538	14824	3004
41° - 42°	1638	6286	5863	4894	4711	4726	13898	2951
42° - 43°	1533	6270	5718	5102	4947	4539	12585	2777
43° - 44°	1438	6091	5593	5071	4971	4623	11612	2862
44° - 45°	1303	6022	5491	4937	5127	4599	10883	2814
45° - 46°	1253	5880	5483	5152	5086	4607	10510	2781
46° - 47°	1081	5939	5352	5138	5212	4709	9914	2808
47° - 49°	932	5569	5000	5178	5397	4606	8912	2822

49° - 50°	878	5240	5004	5280	5360	4681	8602	2785
50° - 51°	877	5434	5019	5289	5558	4639	8351	2722
51° - 52°	879	5375	4930	5261	5523	4627	7982	2877
52° - 53°	819	5177	4833	5287	5453	4743	7736	2799
53° - 54°	786	5153	4694	5444	5423	4622	7405	2716
54° - 55°	761	4886	4788	5475	5614	4600	7180	2814
55° - 56°	781	4935	4870	5605	5600	4661	7113	2802
56° - 58°	737	4965	4688	5535	5566	4711	6346	2920
58° - 59°	692	4895	4736	5505	5456	4715	6204	2858
59° - 60°	708	4881	4633	5593	5398	4800	5970	3037
60° - 61°	644	4831	4571	5627	5385	4905	5864	2982
61° - 62°	699	4927	4675	5519	5304	4841	5798	3029
62° - 63°	668	4949	4660	5556	5340	4999	5595	3198
63° - 64°	659	4902	4669	5576	5357	4936	5585	3112
64° - 65°	709	4690	4773	5369	5420	5030	5258	3220
65° - 66°	656	4851	4561	5549	5277	5032	5280	3255
66° - 68°	654	4765	4621	5277	5299	5197	4963	3457
68° - 69°	652	4902	4653	5330	5362	5514	4904	3455
69° - 70°	663	4826	4697	5171	5236	5529	4990	3657
70° - 71°	605	4982	4670	5011	5266	5721	4889	3867
71° - 72°	592	4987	4693	5179	5339	5766	4835	3825
72° - 73°	609	4932	4821	5029	5435	5862	4741	3828
73° - 74°	626	5008	4839	5128	5392	6107	4750	4048
74° - 75°	701	5106	4852	5084	5398	6196	4711	4178
75° - 77°	591	5158	4871	4928	5963	6645	4645	4653
77° - 78°	643	5264	5083	5019	5840	6699	4435	4850
78° - 79°	657	5356	5116	5012	6100	6989	4417	4840
79° - 80°	698	5390	5229	4927	6172	7143	4485	5019
80° - 81°	731	5394	5257	4992	6216	7302	4313	5432
81° - 82°	762	5512	5279	4997	6372	7506	4463	5510
82° - 83°	720	5560	5237	4832	6477	7561	4325	5645
83° - 84°	819	5570	5314	4929	6612	7819	4414	6019
84° - 85°	790	5753	5327	4945	6824	8131	4339	6364
85° - 87°	842	5827	5278	4787	7207	8880	4400	7362
87° - 88°	923	5951	5511	5035	7297	9181	4302	7471
88° - 89°	932	5810	5709	4936	7668	9594	4435	7931

89° - 90°	955	6097	5652	5010	7652	10000	4450	8531
90° - 91°	987	6083	5641	4977	8033	10315	4329	8782
91° - 92°	1073	6159	5833	5112	8171	10566	4439	9583
92° - 93°	1109	6022	5859	5111	8345	10616	4482	10642
93° - 94°	1128	6238	5723	5176	8929	10573	4525	12304
94° - 96°	1256	6329	5792	5237	10675	10463	4465	19197
96° - 97°	1271	6223	5925	5234	11131	10322	4480	18877
97° - 98°	1314	6305	6065	5299	10736	10447	4638	16925
98° - 99°	1395	6241	6074	5380	10090	10177	4554	15161
99° - 100°	1453	6271	6159	5268	9807	10228	4723	13574
100° - 101°	1585	6505	6360	5450	9730	10103	4567	12832
101° - 102°	1647	6485	6206	5437	9550	9910	4781	12078
102° - 103°	1801	6447	6306	5490	9415	9799	4897	11557
103° - 104°	1885	6528	6475	5376	9631	9606	4938	11010
104° - 106°	2377	6619	6810	5596	9501	9169	5128	9903
106° - 107°	2560	6616	6753	5782	9212	8894	5195	9486
107° - 108°	2623	6689	6738	5843	9133	8802	5346	9058
108° - 109°	2846	6862	6950	5844	9258	8519	5336	8911
109° - 110°	3084	6753	7065	5890	8986	8392	5413	8611
110° - 111°	3383	6876	7166	5922	9321	8319	5545	8153
111° - 112°	3676	7046	7137	5990	9042	8365	5747	8489
112° - 113°	3896	7301	7273	6155	9031	8187	5839	8275
113° - 115°	5345	7459	7834	6396	8887	7640	6292	7416
115° - 116°	6047	7640	7994	6327	8700	7415	6341	7427
116° - 117°	6852	7756	8083	6517	8761	7367	6625	7239
117° - 118°	7648	7843	8454	6557	8626	7193	6838	7153
118° - 119°	8315	8126	8521	6763	8386	7209	6969	7020
119° - 120°	8899	8195	8801	6528	8494	7045	7388	6851
120° - 121°	9598	8471	8956	6685	8359	7027	7690	6570
121° - 122°	10731	8630	9125	6864	8350	7030	7728	6612
122° - 123°	11349	8607	9512	6945	8358	6806	8165	6638
123° - 125°	13237	9215	9878	7245	8071	6592	8761	6241
125° - 126°	13810	9415	9888	7282	8073	6547	9248	6158
126° - 127°	13919	9621	10229	7542	8045	6738	9535	5942
127° - 128°	14075	9430	10122	7533	8007	6597	10069	6168
128° - 129°	14328	9817	10105	7624	7936	6502	10394	5971

129° - 130°	14328	9755	10149	7779	7912	6632	10786	5923
130° - 131°	14434	9979	10188	7997	7910	6571	11363	5858
131° - 132°	14422	9952	10488	8199	7895	6647	11629	5963
132° - 134°	13485	9865	10154	8407	7727	6542	13574	5836
134° - 135°	12888	9725	10275	8603	7960	6593	13143	5695
135° - 136°	12652	9758	10302	8712	7750	6488	12579	5736
136° - 137°	12306	9628	10209	9040	7789	6485	11610	5811
137° - 138°	11749	9512	10116	9141	7727	6516	10655	5803
138° - 139°	11584	9526	9818	9159	7668	6576	10286	5917
139° - 140°	11096	9279	9746	9526	7740	6508	9881	5823
140° - 141°	10649	9267	9541	9456	7719	6639	9533	5871
141° - 142°	10658	9229	9799	9952	7740	6533	8900	5804
142° - 144°	9722	9011	9456	10229	7654	6466	7799	5950
144° - 145°	9257	8950	9228	10491	7857	6401	7935	5793
145° - 146°	9214	8871	9268	10533	7654	6448	7742	5887
146° - 147°	8715	9051	9229	10703	7665	6378	7618	6007
147° - 148°	8656	8920	9279	10740	7756	6446	7656	5833
148° - 149°	8457	8789	9062	10883	7578	6442	7434	5918
149° - 150°	8261	8804	9219	10991	7680	6496	7171	5925
150° - 151°	8065	8634	9069	11013	7450	6497	7334	5943
152° - 153°	7803	8635	8830	11062	7467	6643	6657	6204
153° - 154°	7711	8664	8988	11188	7576	6701	6624	6380
154° - 155°	7884	8548	8988	10972	7446	6809	6687	6247
155° - 156°	7576	8641	8963	10823	7428	6981	6463	6555
156° - 157°	7600	8651	9016	10781	7527	6900	6255	6681
157° - 158°	7538	8574	8990	10941	7369	7067	6165	6923
158° - 159°	7587	8461	8754	10472	7522	7032	6103	6875
159° - 160°	7427	8222	8872	10565	7493	7113	6159	7177
160° - 161°	7472	8339	8812	10229	7460	7328	6194	7320
161° - 163°	7369	8078	8571	10114	7430	7670	5900	8083
163° - 164°	7366	8133	8643	10063	7477	7577	5600	8347
164° - 165°	7493	8110	8520	9970	7490	7577	5591	8632
165° - 166°	7619	7945	8465	9672	7572	7835	5630	8808
166° - 167°	7546	8054	8549	9659	7581	7939	5669	8753
167° - 168°	7605	7913	8627	9590	7691	8049	5618	9008
168° - 169°	7649	7813	8351	9472	7632	8150	5439	9162

169° - 170°	7744	7806	8341	9451	7671	8252	5462	9260
170° - 172°	8180	7711	8070	9140	7919	8973	5424	10273
172° - 173°	8518	7670	7893	9226	7966	9242	5384	10538
173° - 174°	8480	7670	7922	8969	7967	9426	5354	10669
174° - 175°	8722	7576	7894	9030	7916	9387	5529	11341
175° - 176°	8893	7403	7863	9005	8073	9934	5601	11709
176° - 177°	9069	7317	7616	8823	8103	10097	5420	12327
177° - 178°	9108	7318	7551	9025	8129	10297	5341	12971
178° - 179°	9376	7375	7526	8756	8166	10664	5299	13272
179° - 180°	14779	10657	10864	12948	12179	17124	8271	21898

(D) Distribution of orientation angle for x = 0.6 crystal -

Bin	**Temperature (°C)**							
	30	**80**	**130**	**180**	**230**	**280**	**330**	**380**
0° - 1°	2527	2664	3318	6028	22310	20564	26334	24304
1° - 2°	2480	2613	3231	3891	13219	20485	24983	25963
2° - 3°	2279	2607	3044	3833	12354	20025	22661	25899
3° - 4°	2317	2448	2983	3632	11371	18588	20136	23578
4° - 5°	2307	2394	3024	3567	10498	13583	17173	20278
5° - 6°	2250	2342	2779	3542	9645	12410	14702	17239
6° - 7°	2150	2250	2819	3338	8878	11522	13020	14772
7° - 8°	2234	2209	2782	3292	8117	10714	11466	12927
8° - 9°	2181	2240	2695	3398	7649	9628	8793	11580
9° - 11°	2178	2181	2759	3129	6193	8690	8177	10311
11° - 12°	2203	2109	2652	3017	6024	8217	7828	9261
12° - 13°	2185	2185	2675	2965	5683	7589	7400	7538
13° - 14°	2113	2138	2666	2933	5361	11241	7167	7142
14° - 15°	2161	2190	2544	2982	5201	10369	6698	6702
15° - 16°	2054	2131	2684	2935	5315	6406	6203	6510
16° - 17°	2116	2257	2597	2959	4864	6242	5970	6184
17° - 18°	2212	2144	2605	2896	4820	5954	8600	5755
18° - 20°	2143	2275	2664	2972	4744	5530	7762	5440
20° - 21°	2173	2308	2518	2843	4640	5255	5119	5355
21° - 22°	2289	2285	2690	2925	4519	4999	4887	4840

22° - 23°	2433	2284	2830	2968	4445	4818	4553	4615
23° - 24°	2452	2391	2826	2922	4351	4723	4466	4424
24° - 25°	2399	2458	2897	2858	4250	4414	4450	4294
25° - 26°	2637	2557	2957	2922	3929	4485	4259	4129
26° - 27°	2605	2655	2997	3041	3915	4308	4156	4007
27° - 28°	2757	2761	3000	3051	3805	4346	4069	3759
28° - 30°	2828	2741	3080	3361	3546	4213	3638	3831
30° - 31°	2979	2858	3460	3268	3490	4095	3629	5441
31° - 32°	3288	3014	3449	3373	3322	4014	3474	5281
32° - 33°	3441	3037	3633	3440	3414	3914	3372	3529
33° - 34°	3640	3200	3784	3608	3385	3526	3413	3440
34° - 35°	3828	3647	4060	3743	3297	3561	3349	3449
35° - 36°	3948	3904	4113	3782	3214	3563	3246	3400
36° - 37°	4189	4336	4430	3967	3098	3451	3298	3251
37° - 39°	4267	4449	4685	4487	3031	3461	3070	3202
39° - 40°	4678	4689	4969	4741	3008	3457	2975	3254
40° - 41°	5776	5050	6152	4928	2924	3422	3027	3168
41° - 42°	6222	5383	6575	5381	2910	3257	2891	3011
42° - 43°	6736	5929	7243	5635	2895	3281	2861	3050
43° - 44°	7464	7385	7755	5914	2844	3219	2906	3010
44° - 45°	8159	7979	8518	6632	2796	3122	2847	2998
45° - 46°	9328	8735	9554	7147	2811	3116	2813	2825
46° - 47°	9959	9415	10511	7629	2811	3129	2729	2847
47° - 49°	11102	10407	11650	10084	2772	2944	2801	2794
49° - 50°	12331	11584	16087	10925	2730	2894	2776	2768
50° - 51°	16551	12734	17557	11920	2737	2813	2740	2663
51° - 52°	18175	14584	19236	12827	2716	2840	2678	2688
52° - 53°	19380	16331	20535	13921	2605	2756	2822	2550
53° - 54°	20239	20615	21642	14841	2622	2778	2787	2433
54° - 55°	20391	21086	21532	15974	2665	2743	2690	2367
55° - 56°	19674	20081	20609	16525	2548	2717	2698	2406
56° - 58°	18328	18279	18854	15618	2640	2831	2503	2266
58° - 59°	17136	16576	16900	14632	2871	2831	2511	2343
59° - 60°	13327	14652	11188	13839	2812	2952	2429	2214
60° - 61°	11898	13156	9684	12481	2779	2845	2396	2229
61° - 62°	10702	11652	8468	11378	2894	3030	2387	2168

62° - 63°	9611	8457	7379	10272	2968	3096	2511	2144
63° - 64°	8664	7695	6691	8967	2934	3195	2613	2088
64° - 65°	7968	6964	5997	8148	2927	3148	2542	2061
65° - 66°	7189	6247	5380	7731	2983	3091	2630	2176
66° - 68°	6790	5912	4634	5737	3198	3181	2633	2261
68° - 69°	6197	5387	3632	5212	3188	3172	2529	2222
69° - 70°	4697	5118	3376	4796	3175	3173	2762	2341
70° - 71°	4509	4558	3079	4289	3419	3258	2601	2412
71° - 72°	4245	4334	2978	3919	3328	3509	2665	2468
72° - 73°	3892	3608	2774	3787	3475	3461	2611	2433
73° - 74°	3712	3351	2565	3366	3462	3524	2803	2530
74° - 75°	3633	3051	2448	3180	3527	3633	2873	2510
75° - 77°	3465	2959	2300	2763	3760	3638	3242	2801
77° - 78°	3365	2885	2270	2665	3741	3775	3309	2945
78° - 79°	2957	2730	1969	2574	3877	3748	3437	2842
79° - 80°	2864	2640	1896	2457	3851	3926	3463	3465
80° - 81°	2811	2491	1774	2235	3957	3959	3590	3470
81° - 82°	2625	2352	1730	2233	4143	4127	3745	3632
82° - 83°	2665	2244	1664	2132	4153	4220	3827	3890
83° - 84°	2443	2139	1692	2073	4371	4257	3930	3872
84° - 85°	2499	2161	1551	1980	4608	4300	4008	4177
85° - 87°	2373	2187	1482	1860	5682	4559	5067	4648
87° - 88°	2363	2101	1505	1724	6189	4894	5614	4892
88° - 89°	2258	2004	1471	1730	6645	5157	5825	6441
89° - 90°	2196	2044	1392	1820	7273	5542	6386	7044
90° - 91°	2279	2071	1390	1612	7927	7336	7007	8166
91° - 92°	2137	2018	1377	1603	8804	8156	7827	9397
92° - 93°	2133	1966	1362	1703	9864	9663	8515	10972
93° - 94°	2248	1899	1307	1560	10840	10899	9150	12965
94° - 96°	2148	1987	1308	1521	13027	12615	12766	14844
96° - 97°	2061	2015	1291	1530	13710	14024	13483	17345
97° - 98°	2210	1966	1347	1506	13753	14659	14536	18918
98° - 99°	2190	2035	1376	1567	13610	15333	15223	19463
99° - 100°	2107	1981	1284	1488	13393	15559	14863	18561
100° - 101°	2201	1933	1329	1470	12842	13396	14473	17663
101° - 102°	2175	2081	1322	1466	12405	12280	13830	16265

102° - 103°	2248	2036	1383	1446	11464	11419	12983	15250
103° - 104°	2254	2000	1423	1462	10474	10292	11590	13762
104° - 106°	2306	2081	1459	1468	8329	9612	9396	12590
106° - 107°	2386	2150	1414	1515	8063	9050	9317	11304
107° - 108°	2550	2260	1543	1524	7774	8422	8624	8727
108° - 109°	2529	2224	1564	1606	7804	8148	8344	8230
109° - 110°	2707	2226	1574	1585	7542	7030	7963	7556
110° - 111°	2783	2396	1584	1710	7434	6912	7629	7065
111° - 112°	2855	2464	1642	1687	6945	6520	7321	6850
112° - 113°	2902	2391	1747	1643	6789	6528	6819	6499
113° - 115°	3009	2577	1616	1892	6448	6327	6155	6178
115° - 116°	3166	2708	1820	1900	6450	6023	5902	6037
116° - 117°	3383	2814	1993	1888	6421	5901	5639	5891
117° - 118°	3601	2940	2069	1948	6325	5684	5591	5561
118° - 119°	3676	2955	2265	2064	6301	5583	5568	5326
119° - 120°	3877	3395	2347	2134	6214	5359	5458	5285
120° - 121°	4210	3560	2470	2175	6222	5355	5134	5233
121° - 122°	4148	3664	2613	2280	6168	5183	5057	5217
122° - 123°	4453	3851	2720	2369	6102	5230	5244	5152
123° - 125°	4591	4093	2848	2816	6313	5339	4976	4962
125° - 126°	4944	4459	3335	2949	6339	5406	5013	4980
126° - 127°	5977	4721	3665	3075	6312	5522	5095	5029
127° - 128°	6409	5133	3889	3255	6343	5504	5086	4801
128° - 129°	6925	5516	4185	3385	6398	5524	5050	4855
129° - 130°	7406	6710	4601	3739	6553	5368	5095	4939
130° - 131°	8057	7329	4999	3919	6489	5238	4978	4703
131° - 132°	8540	7848	5415	4133	6526	5350	4980	4933
132° - 134°	9479	8706	5981	5226	6620	5474	5234	4894
134° - 135°	10464	9593	6590	5525	6678	5522	5243	4848
135° - 136°	13835	10699	9339	6065	6817	5571	5242	4635
136° - 137°	15681	11686	10558	6562	6853	5672	5346	4854
137° - 138°	17416	13089	12027	7230	6802	5682	5325	4927
138° - 139°	19849	18748	13625	7976	6897	5922	5408	4888
139° - 140°	22202	20950	15817	9067	6782	5952	5679	4774
140° - 141°	25247	23917	18289	9807	6767	5998	5707	5013
141° - 142°	28237	27349	21264	11310	6796	5929	5839	4926

142° - 144°	31067	30938	24471	16650	6816	6096	5818	4941
144° - 145°	33228	34781	35617	19531	7014	6089	6036	5115
145° - 146°	30819	37298	37779	23224	6869	6134	6097	5339
146° - 147°	28344	38013	38160	27044	6799	6267	6150	5216
147° - 148°	25103	36977	36820	32205	7063	6476	6181	5237
148° - 149°	22607	27168	34939	35930	7307	6668	6130	5306
149° - 150°	20386	23857	31563	39167	7246	6643	6108	5325
150° - 151°	18041	20626	28576	40494	7217	6661	6366	5279
152° - 153°	16096	18222	25432	32947	7489	6717	6354	5383
153° - 154°	14676	16175	22694	29654	7541	6833	6414	5430
154° - 155°	10745	14131	16582	25868	7918	6970	6564	5525
155° - 156°	9557	12586	14609	23312	7883	7141	6315	5623
156° - 157°	8871	11356	13306	20531	8081	7006	6764	5731
157° - 158°	7947	8450	11981	18389	8207	7107	6790	5906
158° - 159°	7451	7827	10812	16410	8223	7298	6795	6051
159° - 160°	7013	7205	9948	15022	8535	7338	6924	5941
160° - 161°	6322	6627	9030	13403	8869	7410	7250	6055
161° - 163°	5868	6154	8344	10741	9640	7805	7841	6307
163° - 164°	8453	5973	6940	10000	10124	7933	8265	6345
164° - 165°	7718	5476	6282	8944	10539	8017	8312	6813
165° - 166°	4775	5203	6095	8538	11392	8196	8653	6935
166° - 167°	4519	7347	5827	7974	11822	9316	8981	7250
167° - 168°	4211	6795	5503	7560	12469	9996	9415	7414
168° - 169°	4054	4267	5042	7124	13634	10541	9715	7815
169° - 170°	3805	3998	4851	6723	14377	11369	10522	8106
170° - 172°	3682	3931	4610	5901	18456	12400	12641	8466
172° - 173°	3595	3607	6726	5567	19352	13245	13810	9095
173° - 174°	3309	3595	6286	5277	19812	14478	14958	9778
174° - 175°	2937	3429	3868	5238	20040	15506	16118	13268
175° - 176°	2991	3269	3788	5029	19749	16506	17770	14430
176° - 177°	2843	3155	3734	4759	19510	19437	19560	15889
177° - 178°	2704	2852	3537	4645	19066	19895	20764	17947
178° - 179°	2709	2699	3494	4299	18136	20129	22371	19975
179° - 180°	2610	2743	3452	6449	25167	19922	23571	21884